

**Flux Pump based field excitation for a High
Temperature Superconducting synchronous
generator**

Ravichandra

A thesis submitted to

Auckland University of Technology

in fulfilment of the requirements for the degree of

Doctor of Philosophy (PhD)

2017

School of Engineering, Computer and Mathematical Sciences

Abstract

High-Temperature Superconductors (HTS), first discovered in 1986, have proven to be a potential replacement for their low-temperature counterparts, the Low-temperature superconductors (LTS). HTS materials exhibit the superconducting behaviour (zero resistance against current) at a practically realizable high temperature above absolute zero ($>30\text{K}$).

Applications like Magnetic Resonance Imaging (MRI) and Nuclear Magnetic Resonance (NMR), which require very high magnetic fields, are finding HTS to be a viable alternative to LTS. Research and development of second generation high temperature superconducting (HTS) wires and tapes in the last decade has made HTS based coils and wires a possibility which is suitable for power applications like transmission cables, transformers, generators and motors.

The HTS power applications are expected to capture a substantial amount of market in few years to come-owing to their high power density capability. An HTS generator is one such potential application. Although HTS generators and motors have been designed since quite some time, the designs are still evolving, and the materials in use in these applications are still being researched and the applications are yet to be commercially established.

Flux pump offers a unique way of magnetizing a superconductor. In a type 2 HTS flux pump, a quasi-dc emf is induced across the stator of the flux pump thus making it a potential source. By the application of flux pump to a rotating machine, there is a fair amount of success in avoiding the thermal link between cryogenic and non-cryogenic environments, with this the associated thermal loading on the cryogenic system is significantly reduced. Such a system design involves a lot of

critical design factors. This thesis aims at investigating the effects of flux pump based pulsating field excitation and the stator design effects on the Total Harmonic Distortion(THD) of the induced voltage in a 10 kW proof-of-concept HTS rotor synchronous generator.

This thesis focuses on the performance of an HTS generator integrated with mechanically rotating HTS flux pump. The experiments are conducted to investigate for flux pump as a viable alternative to DC excitation of the field in a synchronous generator. A mechanical HTS flux pump applies a homo-polar magnetic field to an HTS tape acting as the stator and is soldered to the HTS coil of the rotor; this arrangement avoids a physical, thermal link between cryogenic and non-cryogenic environment, and has been proven feasible.

Experiments were conducted on two different types of flux pump systems, to study the influence of a rotating homo-polar magnetic rotor on a type 2 HTS tape. The HTS tape acting as the stator in both the types of flux pumps was excited at different frequencies and current measured through field using a hall sensor. The V-I characteristics for various frequencies at different separation distances between the rotor magnets and HTS stator in both the types of flux pump were analysed and were found to be consistent and followed a similar trend in both the cases.

A Finite Element Model (FEM) of the proof-of-concept flux pump integrated 10 kW HTS generator, modelled geometrically in SOLIDWORKS, was developed in ANSYS. The boundary conditions, time stepping and meshing, was carried out to provide a reasonable accuracy to carry out the THD performance analysis. Different winding configurations and geometrical placements were also modelled

to improve the THD performance; such a trial with the actual system being uneconomical.

This research has provided some benchmark results towards the development of an MW range flux pump integrated HTS wind turbine generators.

In conclusion, this thesis reports:

(1) The experimental study carried out on two different types of HTS flux pumps, designed to study the magnetisation of Yttrium Barium Cupric Oxide (YBCO) tape using a mechanically rotating homopolar magnet system. Consistent V-I characteristics were observed for both the types.

(2) Finite Element Modelling (FEM) based analytical study of the harmonic performance of a flux pump integrated proof-of-concept HTS generator. FEM based analysis of the synchronous generator incorporating such a flux pump was carried out for focusing on the stator design and THD performance of the synchronous generator. The results indicate that flux pump can be utilized as an alternative for DC field excitation in HTS rotating machinery, the thesis also contributes towards the practical analysis of proof-of-concept flux pump integrated 10 kW HTS Generator being developed by Robinson Research Institute, VUW.

The flux pump operation has been studied by various expert groups, our work on a warm rotor flux pump model based study of a flux pump integrated HTS generator is first of its kind. This research work fills the gap between the machine design aspects and an innovative application of flux pump technology and thus aids in optimised design of the machine.

Acknowledgements

I would not have been able to complete this thesis without the generous support of the beautiful people around me. First, I would like to thank my supervisor Prof Dr Krishnamachar Prasad for providing me with an opportunity to undertake this work and for his continuous support throughout these years. I would like to acknowledge his patience and commitment in guiding me to the finishing line by gently nudging my ideas towards clarity and form. Also, big thanks to my secondary supervisor Prof Dr Tek Tjing Lie for his continuous support and thoughts regarding the work despite his busy schedule.

This research could have never been possible without the incredible support from my additional supervisor, well known for his numerous projects and publications, Dr R. A. Badcock, Robinson Research Institute, VUW. I would also like to render my thanks to Dr C.W. Bumby for his consistent support all through.

I am thankful to AUT and the School of Engineering who supported this research in many ways. In particular, Head of research Prof Dr Zhan Chen for ensuring continuous PGR9/lunchtime seminar meetings for research scholars and general advice in making a successful PhD journey. My sincere thanks also go to the school manager, postgraduate coordinator and the administrative staff for arranging me a comfortable working space and taking care of the rest.

I thank Dr Zhenan Jiang, Hae-Jin Sung and Michael Davies for their help in making my test rigs, experimentation at RRI, VUW and continuous support throughout the work at RRI. Thanks also go to my research colleagues for the valuable discussions during my studies. Thanks must also go to dear friends for

their help and support. I also thank all my teachers and my extended family for making me who I am today.

I thank my mother Geeta, for her love and being there for me during my ups and downs through my life, my father Hanumanth Rao, sister Rajeshree and my loving in-laws for being there whenever I needed them.

Finally, my heartfelt thanks to my lovely wife Roopa, for patiently putting up with me during all of my tantrums during these years and my toddler boy Vishwas Roorav who has put all my stresses away with the cutest smile I could ever imagine.

List of Publications

Over the course of this research, the following papers are published. Though covered by this thesis, they form an additional body of work (Appendix-A) the reader may wish to refer.

Journal papers:

- “Design Improvisation for Reduced Harmonic Distortion in a Flux Pump-Integrated HTS Generator.” *Energies* journal, MDPI, August 2017.
- “Through-Wall Excitation of a Magnet Coil by an External-Rotor HTS Flux Pump.” *IEEE Transactions on Applied Superconductivity* 26(4): 1-5. 2016.

Conference papers:

- “Flux pump for HTS rotating machinery applications.” *PowerTech*, 2015 IEEE Eindhoven.
- “FEM and performance analysis of 10 kW HTS generator with flux pump excitation,” 2016 IEEE International Conference on Power System Technology (POWERCON), Wollongong, NSW, 2016.

Table of Contents

| | |
|---|------|
| Abstract..... | i |
| Acknowledgements..... | iv |
| List of Publications | vi |
| Table of Contents..... | vii |
| List of Figures..... | x |
| List of Tables | xiii |
| Attestation of authorship..... | xiv |
| Chapter 1. Overview..... | 1 |
| 1.1 Introduction..... | 1 |
| 1.2 Background..... | 3 |
| 1.3 Rationale | 4 |
| 1.4 Significance..... | 5 |
| 1.5 Structure of the thesis..... | 7 |
| Chapter 2. Literature Review..... | 9 |
| 2.1 High Temperature Superconductivity..... | 9 |
| 2.2 HTS Rotating Machinery..... | 13 |
| 2.3 Excitation System and Thermal link..... | 15 |
| 2.3 Flux pump..... | 16 |
| 2.4 Why Flux pump?..... | 18 |
| 2.5 Flux pump applied to HTS Rotating machines..... | 23 |
| 2.6 Finite Element Modelling..... | 24 |
| 2.7 Conclusions..... | 26 |
| Chapter 3. Flux pump..... | 27 |
| 3.1 Introduction..... | 27 |
| 3.2 Design of Experiments..... | 29 |
| 3.2.1 Experimental Process..... | 30 |
| 3.2.2 Apparatus used in the experiments on flux pumps | 31 |
| 3.2.3 Procedure outline | 32 |
| 3.3 Calibration of Hall sensor | 34 |
| 3.4 Sampling frequency | 37 |
| 3.5 Speed setting..... | 37 |
| 3.6 Cold Rotor Flux Pump (Gen 1)..... | 39 |
| 3.6.1 Introduction..... | 39 |
| 3.6.2 Experimental results and observations..... | 40 |
| 3.6.3 Excitation frequencies..... | 43 |

| | | |
|------------|--|----|
| 3.6.4 | Remarks | 47 |
| 3.7 | Warm rotor Flux pump (Gen 2a) | 48 |
| 3.7.1 | Introduction..... | 48 |
| 3.7.2 | Experimental results and observations..... | 51 |
| 3.7.3 | Excitation frequencies (Lower range: 12 Hz, 24.75 Hz, 54.75 Hz and 111 Hz) | 52 |
| 3.7.4 | 111 Hz at various separations | 54 |
| 3.7.5 | 223.5 Hz at various separations | 55 |
| 3.7.6 | 448.5 Hz at various separations | 56 |
| 3.7.7 | Remarks | 59 |
| 3.8 | Equivalent Circuit Model..... | 60 |
| 3.8.1 | I-V curves..... | 62 |
| 3.8.2 | Dynamic Resistance | 65 |
| 3.9 | Comparative performance analysis of Gen 1 and Gen 2a..... | 67 |
| 3.10 | Concluding Remarks..... | 69 |
| Chapter 4. | Finite Element Modelling | 71 |
| 4.1 | Introduction..... | 71 |
| 4.2 | Basic Modelling..... | 73 |
| 4.2.1 | Magnet and Stator wire | 73 |
| 4.2.2 | Permanent Magnet Synchronous Generator..... | 76 |
| 4.2.3 | Salient Pole Synchronous generator model..... | 79 |
| 4.3 | Observations | 85 |
| Chapter 5. | 10 kW HTS Generator | 86 |
| 5.1 | Introduction..... | 86 |
| 5.1.1 | Modelling and Simulation Methodology | 86 |
| 5.1.2 | Geometric modelling..... | 87 |
| 5.1.3 | Stator modelling..... | 88 |
| 5.1.4 | Symmetric Reduction..... | 89 |
| 5.1.5 | ANSYS 3D to 2D..... | 89 |
| 5.1.6 | Properties Assignment | 90 |
| 5.1.7 | Excitation assignment | 91 |
| 5.1.8 | Result Collection..... | 91 |
| 5.2 | FEM study of HTS generator..... | 92 |
| 5.2.1 | System Modelling | 92 |
| 5.2.2 | Field Excitation Inputs..... | 96 |
| 5.2.3 | Performance analysis | 97 |
| 5.2.4 | Field pattern analysis | 98 |

| | | |
|-----------------|---|-----|
| 5.2.5 | Excitation Frequency | 101 |
| 5.2.6 | Harmonic Analysis..... | 102 |
| 5.3 | Concluding Remarks..... | 107 |
| Chapter 6. | Stator Design and Separate Excitation effects | 108 |
| 6.1 | Introduction..... | 108 |
| 6.2 | Performance Analysis | 109 |
| 6.3 | Design considerations | 110 |
| 6.4 | Stator Design..... | 111 |
| 6.4.1 | Stator Yoke Material | 112 |
| 6.4.2 | Winding Pitch Factor (K_p)..... | 112 |
| 6.4.3 | Load configuration..... | 114 |
| 6.5 | Results and Observations | 115 |
| 6.6 | Stator Design Improvisation | 124 |
| 6.6.1 | Stator Design 1 | 124 |
| 6.6.2 | Stator Design 2..... | 125 |
| 6.7 | Results and Observations | 127 |
| 6.8 | Separate Excitation | 131 |
| 6.9 | Results and Observations | 132 |
| 6.10 | Effect of Imbalance on Torque | 140 |
| 6.10.1 | Torque plot using condition (a)..... | 141 |
| 6.10.2 | Torque plot using condition (b) | 142 |
| 6.11 | Concluding Remarks..... | 144 |
| 6.11.1 | Stator Design..... | 144 |
| 6.11.2 | Separate Excitation | 145 |
| Chapter 7. | Conclusions and Future Work..... | 149 |
| 7.1 | Conclusions..... | 149 |
| 7.2 | Future Work..... | 152 |
| References..... | | 153 |
| Appendices..... | | 163 |

List of Figures

| | |
|---|----|
| Fig. 2. 1 Temperature dependence of Bax-La5-Cu5-O5 (3-y) with x (Ba)=1 (upper curve) and x(Ba)=0.75(lower curve) (Bednorz <i>et al.</i> , 1986)..... | 9 |
| Fig. 2. 2 Magnetic field lines..... | 10 |
| Fig. 2. 3 Typical Slip ring and brush assembly representation. | 15 |
| Fig. 2. 4 Block diagram illustrating thermal link between cryogenic and non-cryogenic environment with the use of conventional excitation system. | 16 |
| Fig. 2. 5 (a) CAD model and (b) Experimental model of Flux pump for HTS magnet (Hoffman <i>et al.</i> , 2011). | 19 |
| Fig. 2. 6 Plots of (a) Ramping up of current in the flux pump single stator vs multiple stator (b) Ramping up of current in the flux pump stator at different frequencies (Hoffman <i>et al.</i> , 2011)..... | 20 |
| Fig. 2. 7 Plot of current vs voltage in the HTS flux pump (Hoffmann <i>et al.</i> , 2011). | 21 |
| Fig. 2. 8 Plots of (a) Current, (b)Voltage against time and (c) Current vs. Voltage (c) of an HTS flux pump. (Jiang <i>et al.</i> , 2014) | 22 |
| Fig. 2. 9 Double helix HTS rotor with Flux pump (Ishmael <i>et al.</i> , 2008) | 23 |
| Fig. 3.1 Field interaction between rotor magnets and stator of the flux pump. | 28 |
| Fig. 3.2 Cold rotor flux pump diagrammatic representation..... | 29 |
| Fig. 3.3 Warm rotor flux pump diagrammatic representation..... | 29 |
| Fig. 3.4 Block diagram illustrating flux pump experimental process..... | 30 |
| Fig. 3.5 A. Hall probe and coil (old arrangement, Courtesy: Robinson Research Institute) | 32 |
| B. Hall probe and coil (new arrangement)..... | 32 |
| Fig. 3.6 Hall probe..... | 33 |
| Fig. 3.7 Hall Effect equivalent circuit..... | 34 |
| Fig. 3.8 Calibration of the Hall sensor. | 35 |
| Fig. 3.9 Schematic diagram of the measurement system. | 35 |
| Fig. 3.10 Hall voltage vs. Coil current..... | 36 |
| Fig. 3.11 Closed-loop angular position control using DC motor and angle feedback from a servo-type potentiometer (Hughes & Drury, 2013)..... | 38 |
| | 39 |
| Fig. 3.12 Gen 1 Flux pump test rig..... | 39 |
| Fig. 3.13 Rotor Magnets and HTS stator of Gen 1 Flux pump | 39 |
| Fig. 3.14 Voltage (598 Hz) across the HTS stator during flux pump operation. .. | 41 |
| Fig. 3.15 The averaged current for 1 mm separation and 598 Hz. | 42 |
| Fig. 3.16 Steady state current ripple (598 Hz). | 42 |
| Fig. 3.17 Normalized FFT of the Voltage (598 Hz) across the HTS stator. | 43 |
| Fig. 3.18 Current ramp up at different frequencies for a separation of 1mm..... | 44 |
| Fig. 3.19 Time-averaged current and voltage profile of HTS flux pump at 298 Hz for a separation of 1mm. | 45 |
| Fig. 3.20 Time-averaged current and voltage profile of HTS flux pump at 598 Hz for a separation of 1mm. | 45 |
| Fig. 3.21 Rate of rise of current vs frequencies for a separation of 1mm..... | 46 |
| Fig. 3.22 Warm rotor flux pump (CAD Model)..... | 49 |

| | |
|---|----|
| Fig. 3.23 (a) 3D view of the warm rotor flux pump, set up for further experimentation, the composite cryostat bath, and the HTS coil. (b) A cross-sectional view of the cryostat wall and flux pump rotor and stator showing magnetic circuit formed between the rotor and the stator (Bumby <i>et al.</i> , 2016)... | 50 |
| Fig. 3.24 Warm rotor flux pump (Actual Model)..... | 51 |
| Fig. 3.25 Current ramp up at different frequencies for a separation 4 mm..... | 53 |
| Fig. 3.26 Current ramp up at 111Hz for various separation distances..... | 54 |
| Fig. 3.27 Steady state current ripple of 111 Hz at 4mm separation | 54 |
| Fig. 3.28 Current ramp up at 223.5 Hz for various separation distances..... | 55 |
| Fig. 3.29 Steady state current ripple of 223.5 Hz at 4mm separation..... | 56 |
| Fig. 3.30 Current ramp up at 448.5 Hz for various separation distances..... | 56 |
| Fig. 3.31 Time-averaged voltage across flux pump stator at 448.5 Hz for various separation distances. | 57 |
| Fig. 3.32 Steady state current ripple of 448.5 Hz at 4 mm separation..... | 58 |
| Fig. 3.33 Rate of rise of current vs frequencies for a separation of 4 mm..... | 58 |
| Fig. 3.34 Electrical equivalent circuit of a dynamic flux pump (Jiang <i>et al.</i> , 2014). | 60 |
| Fig. 3.37 I-V curves of flux pump experiment with Gen 2a test rig (Bumby <i>et al.</i> , 2016). | 64 |
| Fig. 3.38 Dynamic resistance versus frequency | 66 |
| Fig. 4.1 Magnet and Ferromagnetic Yoke | 73 |
| Fig. 4.2 Flux Interaction..... | 74 |
| Fig. 4.3 Flux Interaction-Magnified view | 74 |
| Fig. 4.4 AirX-12 pole permanent magnet generator model | 77 |
| Fig. 4.5 Permanent magnet synchronous generator model pie section..... | 77 |
| Fig. 4.6 Voltage and flux linkage output plots of permanent magnet synchronous generator..... | 78 |
| Fig. 4.7 Output from the reference document | 78 |
| Fig. 4.8 RMxpvt model..... | 79 |
| Fig. 4.10 ANSYS MAXWELL 2D model of the 12-pole generator developed using RMxpvt..... | 81 |
| Fig. 4.11 Phase A voltage and field current profile with a DC field current excitation of 14.484A..... | 82 |
| Fig. 4.12 Phase A voltage and field current profiles with a DC voltage excitation of 65mV. | 82 |
| Fig. 4.13 Phase A voltage profile and Field current profile with 240 Hz FP excitation (inset figure) | 83 |
| Fig. 5.1 Simulation Methodology-Flow Diagram. | 86 |
| Fig. 5.2 Model of the HTS rotor with flux pump integration ANSYS 3D model. | 87 |
| Fig. 5.3 HTS Generator-ANSYS Model..... | 88 |
| Fig. 5.4 ANSYS MAXWELL 3D FEM pie model of HTS generator..... | 89 |
| Fig. 5.5 2D Model of the Pie section. | 90 |
| Fig. 5.6 Mesh plot of pie section of the 2D FEM Model..... | 94 |
| Fig. 5.7 Gen 1 FP Voltage output. | 96 |
| Fig. 5.8 Gen 2a FP Voltage output. | 97 |
| Fig. 5.9 Gen 2a FP Voltage refined output (Courtesy: Robinson Research Institute). | 97 |

| | |
|--|-----|
| Fig. 5.10 Field pattern with ferromagnetic stator at $t = 0$ s..... | 99 |
| Fig. 5.11 Field pattern with ferromagnetic stator at $t = 10$ ms..... | 100 |
| Fig. 5.12 Field pattern with the G-10 stator..... | 101 |
| Fig. 5.13 Field current increase versus the excitation frequency..... | 102 |
| Fig. 5.14 Open circuit phase voltage plots with steel stator..... | 103 |
| Fig. 5.15 Open circuit phase voltage plots with the G-10 stator..... | 103 |
| Fig. 5.16 FFT of Phase A voltage plot for steel stator..... | 104 |
| Fig. 5.17 FFT of Phase A voltage plot for the G-10 stator..... | 105 |
| Fig. 6.1 2D Model of stator design 1 | 111 |
| Fig. 6.2 (a) Full pitch, (b) 5/6 pitch and (c) 2/3 pitch..... | 113 |
| Fig. 6.3 ANSYS field pattern with G-10 Stator Yoke..... | 115 |
| Fig. 6.4 ANSYS plot of induced 3-phase voltage..... | 116 |
| Fig. 6.5 Normalised FFT plot of Induced Phase Voltage at rated load and (a) pitch = 5/6. (b) pitch = 2/3..... | 118 |
| Fig. 6.6 Field current oscillations with the loading condition..... | 120 |
| Fig. 6.7 The variation of THD with material, pitch and load configuration..... | 121 |
| Fig. 6.8 2D model with stator design 1 | 124 |
| Fig. 6.9 2D model with stator design 2..... | 125 |
| Fig. 6.10 2D field pattern with stator design 1 | 128 |
| Fig. 6.11 Field pattern around stator conductors with stator design 1..... | 129 |
| Fig. 6.12 2D field pattern with stator design 2..... | 129 |
| Fig. 6.13 Field pattern around stator conductors with stator design 2..... | 130 |
| Fig. 6.14 Field pattern with an imbalance current of 5A (95A-90A) in adjacent coils..... | 133 |
| Fig. 6.15 Field pattern with an imbalance current of 10A (95A-85A) in adjacent coils..... | 133 |
| Fig. 6.16 Field pattern with an imbalance current of 95A (95A-0A) in adjacent coils..... | 134 |
| Fig. 6.17 Phase voltage plots with an imbalance current of 5A (95A-90A) in adjacent coils | 134 |
| Fig. 6.18 Phase voltage plots with an imbalance current of 10A (95A-85A) in adjacent coils | 135 |
| Fig. 6.19 Phase voltage plots with an imbalance current of 95A (95A-0A) in adjacent coils | 135 |
| Fig. 6.20 Phase voltage plot of one phase separated, with an imbalance current of 95A (95A-0A) in adjacent coils | 135 |
| Fig. 6.21 The variation of THD with increased imbalance..... | 137 |
| Fig. 6.22 THD (%) versus Imbalance condition(s) | 138 |
| Fig. 6.23 Torque response comparison for various conditions of imbalance considering mechanical transient..... | 141 |
| Fig. 6.24 Initial torque transients under different imbalance conditions..... | 142 |
| Fig. 6.25 Steady state torque ripples under lower imbalance conditions..... | 142 |
| Fig. 6.26 Torque response comparison for various conditions of imbalance without considering mechanical transient..... | 143 |

List of Tables

| | |
|--|-----|
| Table 2.1 Comparison between T_c of type I and type II superconductors (C. P. Poole, 2000)..... | 12 |
| Table 2. Comparison between 3 finite element packages..... | 25 |
| Table 3.1. Frequencies and distances at which the voltage and current in the HTS stator of a cold rotor flux pump were recorded. | 40 |
| Table 3.2 Frequencies and distances at which the voltage and current in the HTS stator of a warm rotor flux pump were recorded. | 52 |
| Table. 3.3 Gen 2a Frequency versus dynamic resistance for the separation distance of 7.5 mm calculated from Fig. 3.37 (Bumby et al., 2016). | 64 |
| Table. 3.4 Gen 1 Frequency versus dynamic resistance for a separation distance of 1 mm | 65 |
| Table. 3.5 Gen 2a Frequency versus dynamic resistance for a separation distance of 4 mm | 65 |
| Table. 3.6 Gen 1 and Gen 2a current ramp up the comparison for a separation distance of 4 mm..... | 67 |
| Table 4.1. 20kVA model setup quantities..... | 80 |
| Table 4.2 Comparison of THDs for the conventional design | 83 |
| Table 5.1. HTS Generator Parameters | 93 |
| Table 5.2. FEM Simulation Parameters..... | 95 |
| Table 5.3. THD Comparison between Steel and G-10 Stator | 105 |
| Table 6.1. Winding Pitch Factor..... | 114 |
| Table 6.2. No-Load-THD (V_{ph}) | 117 |
| Table 6.3. Rated Load-G-10 Stator -2/3 Pitch..... | 119 |
| Table 6.4. Star-Delta -G-10 Stator -2/3 Pitch..... | 119 |
| Table 6.5. Star-Star -G-10 Stator -2/3 Pitch-RL Load..... | 122 |
| Table 6.6. Star-Delta -G-10 Stator -2/3 Pitch-RL Load..... | 123 |
| Table 6.7. THD Comparison between Design 1 and Design 2 | 127 |
| Table 6.8. THD Comparison between R Load and RL Load with Design 2 | 128 |
| Table 6.9. Imbalance current and Corresponding No-Load THD values for design 2 | 136 |
| Table. 7.2 Machine configuration..... | 145 |

Attestation of authorship

I hereby declare that this submission is my own work and that, to the best of my knowledge and belief, it contains no material previously published or written by another person (except where explicitly defined in the acknowledgements), nor material which to a substantial extent has been submitted for the award of any other degree or diploma of a university or other institution of higher learning.

Auckland

Signature  _____

Chapter 1. Overview

1.1 Introduction

The HTS based rotating electric machines namely, generators and motors, can be examined based on high performance because of recently developed advanced HTS wires, which have high critical current and low AC loss. Windings using HTS materials generate less heat than copper windings. In addition, liquid nitrogen, the common cryogenic coolant is a good electrical insulant (McConnell *et al.*, 2000). From refrigeration perspective, HTS materials have higher reliability, and lesser cost and thus are better than low-temperature superconducting materials (LTS) (Mehta *et al.*, 1997).

In this research work, the generator in consideration is HTS wind generator because the wind energy generation is very promising and is growing at a rapid pace; by 2020, wind energy generation is expected to cater to 12% of the world's electricity consumption. For wind turbine generator with capacity >5 MW, use of HTS materials avoids critical issues like larger size, higher costs of foundations and connections per unit of generation.

The application of HTS materials in wind turbine generator will reduce the size of the generator by more than 50% (Lewis *et al.*, 2007; Lukasik *et al.*, 2011; Karmaker *et al.*, 2015; Liang *et al.*, 2016). In this research, the field coils on the rotor of the generator are HTS material in the racetrack form. HTS field coils would be able to provide high air gap field without the use of iron core, and the generator can be operated at low wind speeds. Higher field generation by the rotor field coils will also lead to a reduction in copper windings on the non-HTS stator side of the generator (Liang *et al.*, 2016).

HTS technology though efficient, potential, reliable and beneficial, the actual implementations must be preceded by modelling and analytical studies on the desired applications. This research work focusses on one such potential application of HTS - Flux pump based excitation of an HTS generator. With the use of flux pump for exciting the HTS rotor of an HTS generator can, the physical link between the cryogenic and non-cryogenic environment can be completely avoided, subsequently reducing the load on the cryogenic environment. In addition, it is a pre-requisite to understand the fundamental HTS generator design aspects that can facilitate the development of practical designs by industry. The design and performance of proof-of-concept prototype(s) of flux pump integrated HTS generator needs to be examined and verified critically before practical implementation of the machine design, as the capital cost involved in such implementations is high at this point. The predicted performance and reliability of a flux pump integrated HTS generator is proposed to be verified through experimentation and finite element analysis.

The ultimate purpose is, to contribute on to the following objectives.

- The behaviour of two different types of flux pumps when used as excitation source for an HTS rotor.
- The harmonic performance of HTS generator with flux pump excitation under various conditions.
- Design modifications of HTS generator to reduce harmonic distortion.
- Preliminary torque imbalance studies are conducted, to act as a precursor to the mechanical optimisation of the machine before and after prototype testing.

1.2 Background

The phenomenal growth of High-Temperature Superconducting (HTS) materials has put tremendous focus on the design and development of reliable and cost-effective superconductivity based electric equipment. Due to their dynamic structure, the design of HTS based rotating electric machines pose additional challenges.

The current carrying capacity of any conductor is characterised by the engineering critical current density (J_c) as a function of the temperature and magnetic field as experienced by the windings. The HTS materials have a high value of J_c as against the conventional conductors (SuperPower HTS-2G wire: J_c of $\sim 2.66 \text{ A/mm}^2$ per amp of operating current). The machine design considerations also change with the usage of HTS materials in place of conventional conductors. In addition, it is necessary to develop a good understanding of the non-conventional generator design concepts to provide the basis for developing prototypes and benchmarks for wind power industry, to implement HTS applications commercially.

In America, more than 1/4th of the losses in the power system are due to the resistive heating in the conventional power equipment (Mehta, *et al.*, 1997). Voltage consistency in the electrical network, over a wide range of load conditions, can be well achieved by the use of HTS based equipment in the electrical network (McConnell, *et al.*, 2000; Reis, *et al.*, 2002). Hence, the development of HTS materials based equipment will save energy substantially, thus reducing costs.

1.3 Rationale

In recent days, the high demand for power recently has called in for efficient and non-conventional ways of supplying reliable and cost effective power. The important challenges in HTS generator's design are to withstand thermal runaway (quench), loss minimization and cryogenic system optimisation.

The flux pump integrated HTS generator needs to fulfil all the standard requirements to integrate well into the existing system. The performance and reliability of the new proposed design and its benefits have to be convinced to the engineering community and manufacturers through analysis, simulation and prototype testing, but also through field tests for actual commercialization to be successful.

The work in the thesis uses a combination of experimentation and simulation-based analyses to contribute towards the design and development of a flux pump integrated proof-of-concept 10 kW HTS generator. The adaptation of standard harmonic specifications for generator into the evaluation determines the performance of the flux pump integrated HTS generator against a conventional generator. During the project evolution, different configurations of flux pump integrated HTS generator designs are considered. By further investigations, the performance of the flux pump integrated HTS generator for different load configurations, better harmonic performance, stability and safe operating envelope are analysed.

1.4 Significance

A few significant objectives form the foundation for this work. The first is to develop a good understanding of two different configurations of flux pump operation and then using finite element modelling (FEM) study a flux pump integrated HTS generator design issue for improving the THD performance of the generator to meet the prescribed standards.

THD limit as specified in IEEE STD 519- 2014 is 5% for a bus voltage < 69 kV at the point of common coupling and the permitted limit is 8% for lower voltage generation < 1 kV. The final commercial product based on the proof-of-concept generator considered in this research will be a flux pump integrated MW class wind turbine HTS generator, and the generated voltage levels for this generator are expected to be > 1 kV and < 69 kV. For this class of generation, the maximum limit of THD is 5% as per the prescribed standard.

The research focuses on understanding the critical parameters, the operation of flux pump integrated HTS generators, and model the generator, study output under a range of conditions; improvise design to meet the prescribed standard THD limits. The broad understanding of flux pump integrated HTS generator capabilities that have evolved will benefit the ongoing project and power industry at large.

In summary, the significant contributions of the work are as follows:

1. Experimental study of cold rotor flux pump (Gen 1) to understand the nature of flux pump excitation for a configuration with rotor and stator both in the cryogenic temperature.
2. Design and experimental study of warm rotor flux pump (Gen 2a) to emulate the HTS generator excitation system at the laboratory scale.

3. Finite element modelling and study of the proof-of-concept 10kW HTS generator, focussing on the stator design and harmonic performance of the generator. The inputs to the field system of the generator were the results obtained in objective two.

1.5 Structure of the thesis

This thesis contains seven main chapters. The first chapter is the overview, which presents the background of the research, describes the rationale and significance behind the accomplished research work and provides the structure of the thesis.

Chapter 2 is a literature review that provides an overview of the development of superconductors. The literature review briefly accounts for the development of LTS and HTS superconductors, superconducting generators and the need for flux pumps. Finally, the chapter discusses the significant benefits of the application of flux pumps for exciting the field windings of an HTS generator. It also describes the review of various software packages necessary for finalising the best-suited software package to achieve the study objectives.

Chapter 3 starts with an overview of a dynamic mechanical flux pump. The chapter presents the operation principle of the flux pump. The descriptions of Gen 1 flux pump, experimental procedure and description of Gen 2a flux pump are discussed in detail. The results obtained in Gen1, Gen 2a flux pump is reported, compared, and the relevance of the observed results to the overall research objective is discussed in detail.

Chapter 4 presents the analysis of the application of FEM in the current work. Chapter 4 begins with the description on ANSYS and RMxpert. The analysis continues with a discussion on different features available in ANSYS that are relevant to the research work.

Chapter 5 proceeds with the description on the FEM of 10 kW HTS generator and the no-load results are discussed focussing on harmonic analysis.

Chapter 6 deals with the description and analysis of stator design and the influencing parameters in the stator design that affect the performance of the HTS generator in grid connected or standalone operation. This chapter also touches upon the effects of current imbalance in the field coils because of separate excitation and thermal runaway of coils during operation.

Chapter 7 discusses the summary of results and conclusions of the research based on the results, observations and analysis carried out during the course of research, discussed in the chapters 3 to 5. The chapter also comments upon the future scope and enhancement possibilities based on the undertaken research.

Chapter 2. Literature Review

This section highlights important technologies, which form the basis for the proposed research, and identifies the area wherein the technologies under discussion can be suitably applied to solve identified issues.

2.1 High Temperature Superconductivity

H K Onnes discovered superconductivity in Mercury in 1911. It was discovered that mercury exhibited zero resistivity at 4.2 K; this temperature is considered as critical temperature for mercury. The critical temperature is very low for other known simple alloys like Nb and metals like Mercury. Müller and Bednorz (Bednorz *et al.*, 1986) discovered materials exhibiting superconductivity above 30 K.

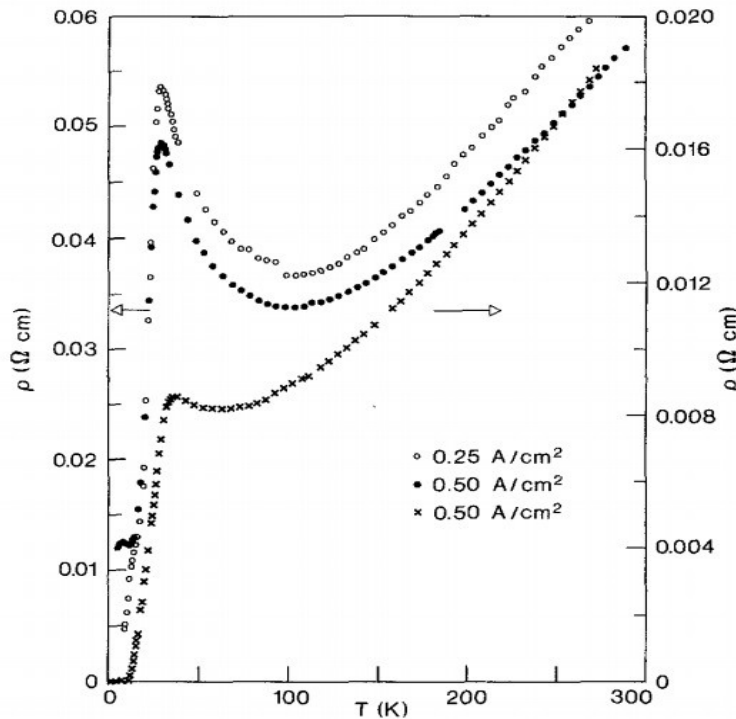


Fig. 2. 1 Temperature dependence of Bax-La5-Cu5-O5 (3-y) with x (Ba)=1 (upper curve) and x(Ba)=0.75(lower curve) (Bednorz *et al.*, 1986).

The temperature dependence of the resistivity of Barium Cuprate compounds observed by Bednorz and Muller is as shown in Fig. 2.1. In 1987, Wu *et al.*, discovered the cuprate superconducting material YBaCuO or generally termed as YBCO, which has 91 K as T_c (critical temperature), 14 K higher than the boiling point of liquid nitrogen i.e. 77 K (Wu *et al.*, 1987).

Broadly, superconducting materials are classified into:

1. LTS: Low temperature superconducting materials ($T_c < 30$ K)
2. HTS: High temperature superconducting materials ($T_c > 30$ K)

The application of superconducting materials is fairly dependent on their critical temperature.

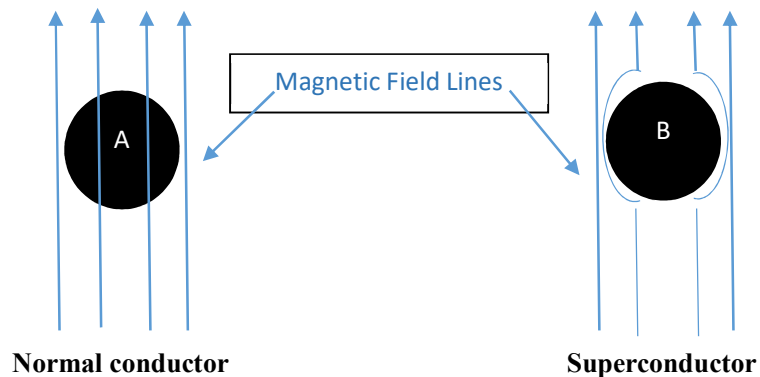


Fig. 2. 2 Magnetic field lines.

Meissner effect (see Fig. 2.2.s A and B), the explanation for the expelling of magnetic field and London equations are used to explaining the behaviour of Type-I superconductors, and the Ginzburg-Landau theory is a powerful tool for the analysis of Type-II superconductors (Cyrot, 1973). Type II commercial wires: 1G-BSCCO (Bismuth Strontium Calcium Copper Oxide) and 2G-YBCO (Yttrium Barium Copper Oxide).

Meissner effect explains the expelling of magnetic field for Type-I superconductors below B_c and for Type II superconductors below B_{c1} (Kim et al., 1963; Bean, 1964; Bondarev, 2015).

Table 1.1 shows the comparison between Type I and Type II superconductors with their corresponding critical temperatures. In a Type I superconductor, the field strength value, known as the critical field (H_c), will cause the superconductor to transition to a normal conducting state. Below H_c , the field is completely excluded from the material and it is fully superconducting. However, at H_c and beyond, there is no superconducting state, the field fully penetrates and the superconductor transitions to a normal conductor. In Type II superconductor, there are two critical fields H_{c1} and H_{c2} . For magnetic field $H < H_{c1}$, the properties are same as a Type I. Above H_{c1} , the applied field is not completely excluded out of the superconductor. However, the superconductor is still in superconducting state at this state as a phenomenon known as the mixed Meissner state occurs. Most applications use Type II superconductors.

Higher current density and advancement in manufacturing technology in providing long lengths of HTS wires have made magnet windings using HTS possible (Their higher operating temperature (77 K) lowers the cost of cryogenic maintenance. The upper critical fields YBCO and BSCCO are higher than LTS (NbTi and Nb₃Sn), which indicates that HTS materials can operate at much stronger fields than the LTS materials. The BSCCO wire is known as first generation (1G) HTS wire, and YBCO wire is known as the second-generation (2G) HTS wire. Though YBCO is difficult to fabricate it is preferred in manufacture of magnet windings as it performs better than BSCCO (Poole, 2000; Wolfus *et al.*, 2004).

With the successful commercialization of YBCO materials, high temperature superconductivity applications have been under the limelight of many research groups in the domain of superconductivity.

Table 2.1 Comparison between T_c of type I and type II superconductors (C. P. Poole, 2000).

| Type I | $T_c(K)$ | Type II | $T_c(K)$ |
|-------------------|----------|--------------------|----------|
| α -Hg | 4.15 | NbTi | 9.6 |
| β -Hg | 3.95 | Nb ₃ Sn | 18 |
| Ta | 4.48 | BSCCO | 89 |
| ZrB ₁₂ | 6.0 | YBCO | 91 |

LTS



HTS



The evolution extent of HTS materials has been great since their discovery, and few of their outstanding features have been applied commercially (Kalsi, 2005). The design of magnets using LTS is an old technology and dominates the Magnetic Resonance Imaging (MRI) applications to date. HTS magnets have also been designed and have proven to trap high strength magnetic fields (Murakami, 2003). The high current densities (10^6 - 10^8 A/m²) and high magnetic field capabilities (4-5 T) of the 2G HTS (YBCO) wires make them outstandingly ‘power dense’ (Murakami, 2003; Barnes *et al.*, 2005; Kalsi, 2011).

There are two kinds of HTS wires, which have been commercialised at present: BSSCO and YBCO. BSSCO is known as the first generation (1G) HTS wire and YBCO is the second-generation (2G) HTS wire. Based on shape, applications of YBCO can be classified into two broad categories: bulk application and film application.

Bulk applications include HTS flywheel, HTS maglev (Kim *et al.*, 2006; Wang *et al.*, 2002), bulk electric machine, particle separation, vibration isolation, etc..., Film applications include HTS coils, superconducting fault current limiters (FCL), superconducting cables, etc. (Jones, 2008; Lousberg *et al.*, 2008; Hazelton *et al.*, 2009; Jensen *et al.*, 2011).

2.2 HTS Rotating Machinery

HTS based generators were predicted to capture 50% of the rotating electrical machines market by 2020 (Mulholland, 2003). However, the prediction was too ambitious and unlikely to meet the expected market share by 2020, but low weight, small size and high efficiency are still some of the commercially attractive characteristics for electrical rotating machines using superconductors and extensive research is being carried out to further increase the market share.

Since long, LTS materials are in major use in various applications. Different types of machines have been studied and designed since 1960s (Qu *et al.*, 2013) and it is observed that HTS based rotating machinery possess better commercial possibility than LTS machines (Kalsi *et al.*, 2004; Jensen *et al.*, 2011; Min *et al.*, 2012).

Reliance Electric/Rockwell Automation is reportedly the first corporation to have started development of HTS motors in the USA. In 1996, a 200-hp motor was, built and tested, followed by a larger 1000-hp motor tested in the year 2000. Both motors were four-pole 60-Hz using conventional copper armatures with HTS field coils (Kalsi *et al.*, 2004). In 2002, Siemens developed and presented the results of 380 kW synchronous machine with HTS rotor windings. (Nick *et al.*, 2002). Different topologies of the superconducting generator for direct driven wind turbines have been reviewed taking into account many key parameters (Wang *et al.*,

2013). One of the claims in this work is that, when referred to the overall size, efficiency and drive train costs, the HTS generator concept is superior to Permanent Magnet Direct Drive Generator.

One of the most relevant HTS machines applications is the megawatt range synchronous machines for wind turbines and is near the commercial stage. Synchronous machines with HTS materials on rotor and copper stator winding are preferred, as the rotor winding are subjected to a constant magnetic field, the superconducting AC losses would, therefore, be zero. Whereas, if the stator winding were HTS experiencing current and magnetic field variations causing ripple field, would result in large AC losses (Appleton and Prothero, 1998).

The two classical types of synchronous generator often used in wind turbine industry are: 1. The wound rotor synchronous generator (WRSG). 2. The permanent magnet synchronous generator (PMSG), the WRSG is considered as the workhorse of the electrical industry (Ackermann, 2005). The HTS generator considered in this research has HTS rotor, and it is difficult to categorise it strictly as a PMSG or a WRSG.

In a conventional WRSG, the stator windings are connected directly to the grid, but the rotational speed is strictly fixed by the frequency of the supply grid. The rotor windings are excited using slip-ring and brush assembly or a brushless exciter. Few conventional wind turbine manufacturers like Enercon use the wind turbine concept Type D (WT 4), with a multipole (low-speed) WRSG and no gearbox but this results in a large and heavy generator (Ackermann, 2005). The problem of a large generator can be solved with the use of HTS materials. In this research, a proof of concept 10 kW HTS synchronous generator integrated with a flux pump has been studied and performance analysis with the flux pump based

field excitation has been carried out. For harmonic analysis, the harmonic performance of the generator without any power electronic interface has been carried out.

HTS materials application in rotating machinery puts significant advantages but also poses other additional design challenges predominantly in the domain of cryogenic design. It is observed that the design and development of HTS based motors are more common than HTS based generators. HTS based generators can help in generating high power per cubic volume for applications with space constraints.

2.3 Excitation System and Thermal link

The rotating electrical machinery (generators and motors) needs an excitation system to maintain a magnetic field to facilitate the conversion of mechanical energy to electrical energy or vice versa. Generally, the excitation system is a source of DC and a transmission system to deliver static DC to a dynamic rotating frame. Commutators and slip rings are the widely used conventional rotary electrical interfaces. Commonly, the slip ring arrangement (Fig. 2.3) is used, to excite the rotor windings in traditional generators and HTS based generators, but eventually, for HTS applications, it creates a physical, thermal link between the non-cryogenic and cryogenic environments of the system.

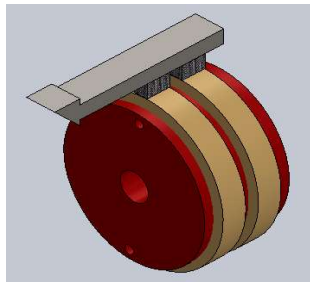


Fig. 2. 3 Typical Slip ring and brush assembly representation.

The common concern, raised in most of the work on HTS based applications, is the interaction between the cryogenic and non-cryogenic parts of the system. This interaction loads the cryogenic system with thermal load and results in significant amount of loss and reduces overall efficiency of the system (Jeong *et al.*, 2010). The efficiency can be improved by avoiding or reducing the thermal load on the cryogenic system.

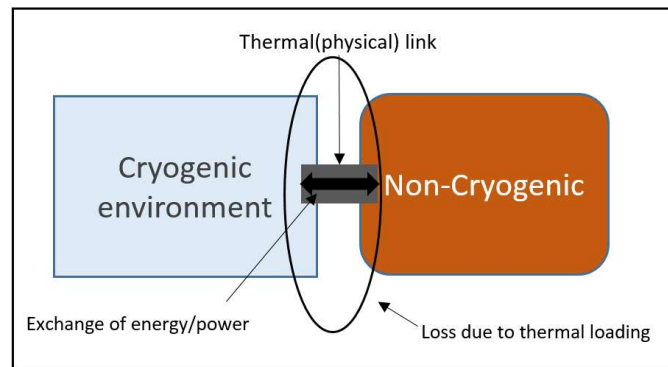


Fig. 2. 4 Block diagram illustrating thermal link between cryogenic and non-cryogenic environment with the use of conventional excitation system.

If the physical link between the cryogenic environment and the non-cryogenic environment is avoided, there will be considerable improvement in efficiency (see Fig. 2. 4 for illustration). A brushless exciter based on a superconducting flux pump can be one such measure to avoid the thermal link (Bumby *et al.*, 2016).

2.3 Flux pump

Superconducting magnet technology is widely used for various applications such as MRI, Nuclear Magnetic Resonance (NMR), accelerator technologies such as the large hadron collider (LHC), fusion technologies such as TOKAMAK, superconducting windings inside superconducting electric machines, magnetic levitation trains, superconducting magnetic energy storage system, *etc...* The superconducting coil can have either DC or transient transport current.

Superconductors can carry a very large persistent current without decay, which is ideal for use in DC magnets such as MRI and NMR magnets. Flux pumps have been in application for pumping flux and in turn injecting a current in superconductors.

According to Klundert *et al.*, (van de Klundert *et al.*, 1981), the basic schemes of flux pumps are: (i) flux compressors, (ii) dc dynamos and (iii) transformer rectifiers. The above mentioned work, describes the flux pumps utilizing conventional low temperature superconductors, since the HTS were discovered in 1986. However, the overall objective of LTS flux pump and an HTS flux pump, as the one in this research, remains the same.

The use of flux pumps to excite HTS coils for various applications has come a long way and evolved significantly. To be specific, the application of a flux pump as an excitation alternative for rotating machines has been proven and studied by various research groups across the world (Mawardi *et al.*, 1977; Ferendeci *et al.*, 1981; Muta *et al.*, 1992; Muta *et al.*, 2001; Ishmael *et al.*, 2008; Coombs *et al.*, 2008; Hoffmann *et al.*, 2011, 2012; Jiang *et al.*, 2014; Kulkarni *et al.*, 2015; Bumby *et al.*, 2016). The independent and novel finding of the voltage profile across the flux pump stator is our unique contribution. The study on the influence of flux-pump excitation on the induced voltage in a generator, as against a conventional DC excitation source is the first of its kind. Along with the nature of excitation, the load configuration and stator material have also been taken into consideration to make the research more comprehensive.

The HTS flux pump in this research work resembles a superconducting DC dynamo. However, the switching between superconducting and non-

superconducting state and creation of normal spots is not necessary due to the existence of flux flow regime in YBCO-Type II superconductors (Hoffman *et al.*, 2011). With this advantage, the application of flux pump has become technically feasible. It also provides foundation for the commercially viable superconducting applications exploiting the advantages of an HTS flux pump and have been dealt with in the following section.

2.4 Why Flux pump?

The feasibility of using superconductor materials for any application is dependent on the minimization of heat leak produced by current feed through and the dissipation in the normal parts of the current leads. In order to better commercialize the applications of superconducting systems, reduction of these losses is crucial. Flux pump is one potential method to achieve this (van de Klundert *et al.*, 1981; Hoffmann *et al.*, 2012).

For megawatt range HTS Rotating Machines, the windings can require currents of up to 400A. Since, the current is iteratively added into the HTS circuit using a flux pump, the required magnitude of the current to excite the coils may be achieved using a flux pump. The flux pump also compensates for the operating current decay of the HTS and ensures the stabilisation of the magnetic field (Bai *et al.*, 2010). Flux pump magnetizes a superconductor coil without a physical current feedthrough lead between the cryogenic and non-cryogenic parts of the system.

If suit-fitted properly for a rotating machine application, flux pump can resolve the problem of thermal link between the cryogenic and non-cryogenic environments. Application of flux pump to energize an HTS magnet with a current ramp rate of 0.44 A/s with a maximum current of 49 A in a 2.7 mH HTS coil has

been successfully demonstrated (Hoffmann *et al.*, 2011). It is also observed that the rate of rise of current is dependent on the number of tapes and also on the frequency of rotation of the flux pump (see Fig. 2. 5 a, b and Fig. 2. 6 a, b).

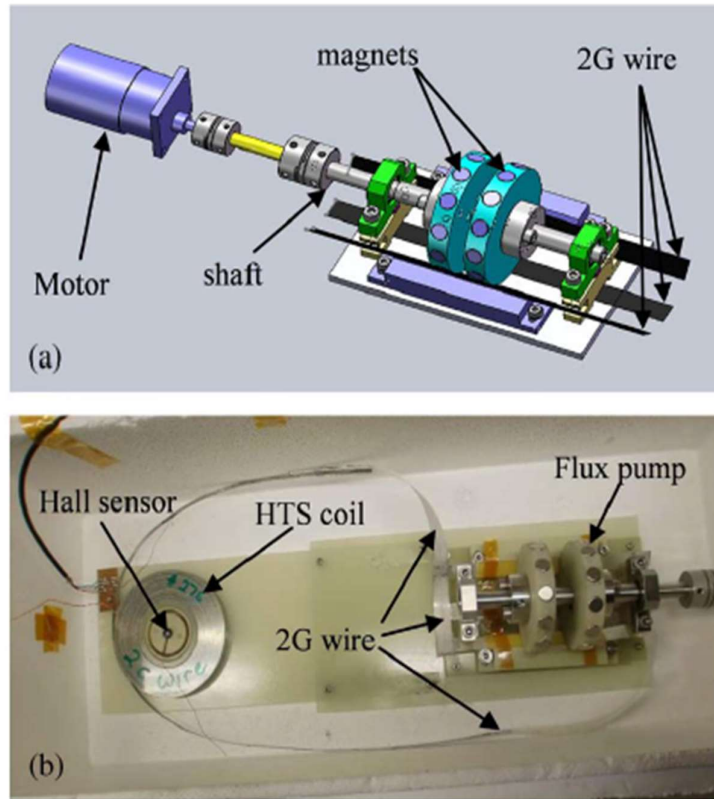


Fig. 2. 5 (a) CAD model and (b) Experimental model of Flux pump for HTS magnet (Hoffman *et al.*, 2011).

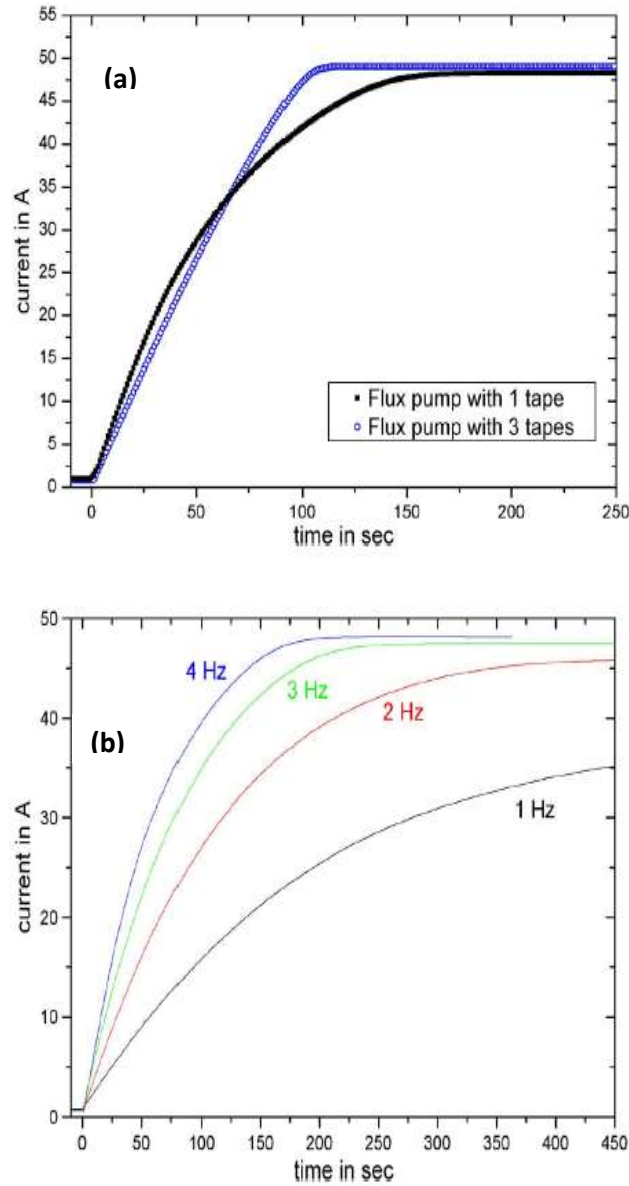


Fig. 2. 6 Plots of (a) Ramping up of current in the flux pump single stator vs multiple stator (b) Ramping up of current in the flux pump stator at different frequencies (Hoffman *et al.*, 2011).

A thermally actuated flux pump has been proposed by Coombs *et al.*, and the technique used enables the creation of a high magnetic field limited by the characteristic features of the superconductor and not the magnetizing system (Coombs *et al.*, 2008). The technique applied in the method used by Coombs *et al.*,

is on the surface plane of the superconductor and offers shaping and patterning of the magnetic field with use of multiple pumps on the surface of superconductor. The authors, however, have not commented on the suitability of this method to a HTS rotating machine. Though it is worth investigating, a simpler method proposed in (Hoffmann *et al.*, 2011), would conveniently solve the issue.

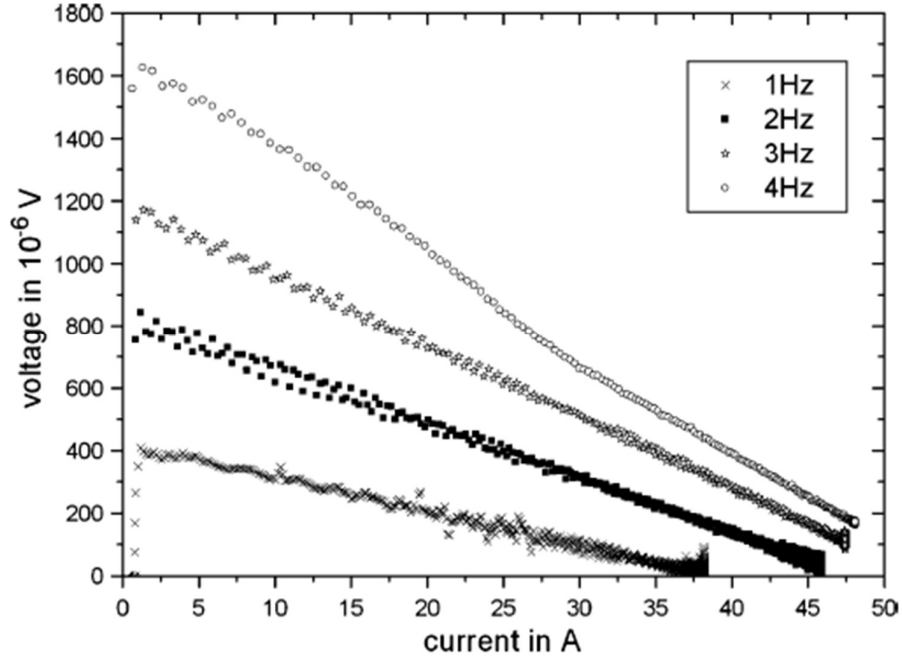


Fig. 2. 7 Plot of current vs voltage in the HTS flux pump (Hoffmann *et al.*, 2011).

The current vs voltage profile with a gap of 1 mm at different frequencies are as shown (Fig. 2.7). The results show that the rate of increase in current is dependent directly on frequency of the flux interaction.

Formulation of dynamic resistance model for a high temperature superconducting flux pump has been presented (Jiang *et al.*, 2014). From the voltage profile, it is evident that a net voltage (quasi DC emf) drop occurs across the Superconducting coil (Fig. 2.8b) The time dependent current I is given by Eq 2.1, (Jiang *et al.*, 2014).

$$I(t) = \frac{\Delta\phi}{\beta} \left(1 - \exp\left(\frac{-\beta f t}{L}\right) \right) \quad (2.1)$$

where,

$\Delta\phi$ = net flux change, β = constant defined by the design parameters of the flux pump, L = inductance of the coil, f = frequency and t = time.

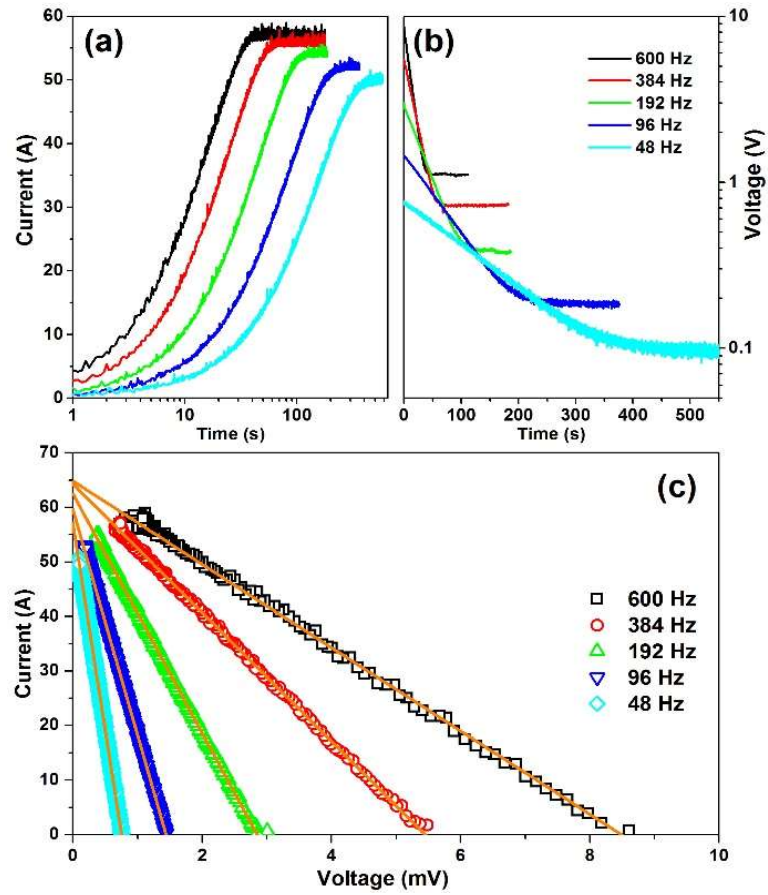


Fig. 2. 8 Plots of (a) Current, (b) Voltage against time and (c) Current vs.

Voltage (c) of an HTS flux pump. (Jiang *et al.*, 2014)

The results observed in previous works indicate that there is possibility to apply this technology for electrical rotating machines but a thorough study on the

variations in the field due to the current ripple, distortion in the voltage on the stator of the rotating machine is needed.

2.5 Flux pump applied to HTS Rotating machines

As mentioned in section 2.3, one of the design challenges is to maintain as much isolation as possible between the cryogenic and non-cryogenic environment in a superconducting application. This becomes far more complex when the superconducting application involves a dynamic component.

Works on improving the current leads from cryogenic environment to non-cryogenic environment have been carried out in the past. A method of thermal anchoring of the conduction-cooled current leads has been formulated and a decrease in the cooling load on the cryogenic system has been reported (Jeong *et al.*, 2010). Despite having reduced the load on the cryo-cooler, a thermal link exists and thermal loading does occur in this system.

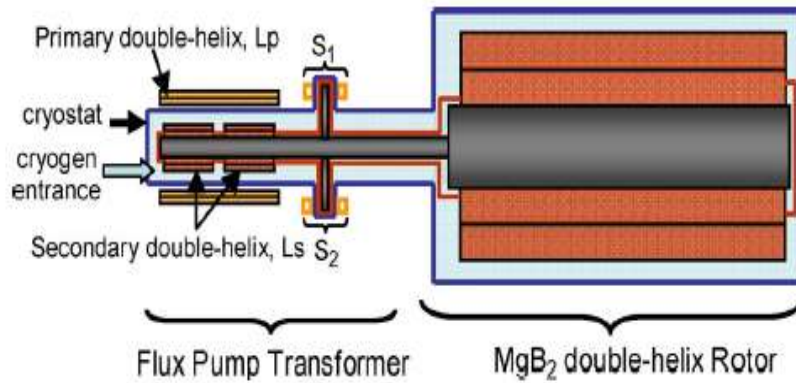


Fig. 2. 9 Double helix HTS rotor with Flux pump (Ishmael *et al.*, 2008)

A conceptual design (see Fig. 2. 9) of a double helix flux pump transformer based rotor excitation of a synchronous motor has been presented (Ishmael *et al.*, 2008). The practicality and commercial aspects of this design are inconclusive.

Hence, a more probable and practical approach towards utilizing the benefits of the flux pump would be to investigate the mechanical flux pump discussed in section 2.5 to excite the field windings of an HTS generator. Such an application would involve numerous design investigations to be carried out *viz.*, mechanical, electrical, cryogenic, economic *etc...* The scope of the thesis would be limited to electrical aspects of the design. Investigations are carried out to answer the feasibility of application of such a flux pump from perspective of electrical design.

The range of investigation is divided as follows:

1. Understand the flux pump operation with respect to voltage and current outputs.
2. Use the flux pump output (as voltage source) to a practical or near practical machine model and investigate the output parameters using FEM.

2.6 Finite Element Modelling

In order to design and develop an HTS machine, it is important to have the analysis and design beforehand to zero in on an optimal design, as the capital cost involved in prototype development and testing is higher.

Finite element modelling (FEM) method is a numerical technique that provides approximate solutions to partial differential equations governed boundary value problems. It divides a large problem into smaller parts by dividing the geometry. The simple equations that model these finite elements are then assembled into a larger system of equations that model the entire problem. FEM then uses calculus of variations to approximate a solution by minimizing an associated error function.

Thus, finite element method can be used to analyse the performance of systems where electromagnetic field can be calculated by representing the geometry of the system and from the field solution different quantities like voltage, current,

torque can be calculated. This approach is useful when studying generators. It is also observed in earlier works that FEM is resource intensive.

A comparative study (see Table 2.) between 3 different packages has also been reported earlier (Persarvet, 2011). As seen in Table 2, the programmability and ease of geometry generation with ANSYS MAXWELL makes it suitable to be used for the research objective of this thesis. The load circuit for the generator is implemented in MAXWELL Circuit Editor and integrated to the MAXWELL model.

Table 2. Comparison between 3 finite element packages.

| Criteria | Comsol | Flux2D | MAXWELL |
|--------------------------------------|----------|----------|----------|
| 1. Field and Circuit Coupling | Y | Y | Y |
| 2. Sliding Mesh Technique | Y | Y | Y |
| 3. Swing Equation Coupling | Y | Y | Y |
| 4. Parameter Optimization | Y | Y | Y |
| 5. CAD import | Y | Y | Y |
| 6. Model programmed control function | External | External | Internal |
| 7. Generate geometry from template | N | N | Y |

ANSYS MAXWELL can also be considered more suitable to study an engineering application as most of the physics principles and microscopic variations are taken care of and need not be explicitly applied for all the studies. In addition, most of the ANSYS based studies adopt adaptive refining and convergence, thus making the ANSYS based models more practical.

2.7 Conclusions

From the Literature review, it was found that flux pump could be investigated as an alternative to the conventional slip ring assembly to inject a DC current into the field winding of an HTS rotor. Study on the effects of flux pump based excitation on the performance of an HTS generator at the developmental stage is essential to improvise and implement such a design at a commercial level. This thesis reports on the accomplishments of the proposed task.

The research is carried out as follows:

1. An experimental study to understand the flux pump phenomenon.
2. FEM-based simulation and analysis to investigate the effects of flux pump excitation on the performance of a proof-of-concept 10 kW HTS generator.

Chapter 3. Flux pump

3.1 Introduction

In general, successful flux pumping occurs through the switching between superconducting and non-super conducting state (van de Klundert *et al.*, 1981). In case of Type II HTS stator, it can also be achieved through flux flow regime (Hoffmann, 2011). One of the generic governing equations of a dynamic flux pump (van de Klundert *et al.*, 1981) is as in Eq. 3.1.

$$\emptyset + L_c I = \text{const} \quad (3.1)$$

For a coil of inductance L_c , any change in the flux \emptyset results in a change in the current. If the constant in the above equation is denoted as k and the equation is rearranged for I , we would get Eq. 3.2.

$$I = \frac{-V}{2fL_c} + \frac{k}{L_c} \quad (3.2)$$

where V would be the voltage drop across the coil and f would be the frequency of change in the applied flux \emptyset .

The flux pump operation has been studied in detail by various research groups for smaller distances. Large distance operation of the dynamic flux pump in this research work depends on the dimension of the magnet. The correlation between the required field strength, size of the magnets, orientation of the magnets, type of superconducting stator, stator side yoke etc., which define the scalability of the flux pump concept, are under study by the associated research groups. However, from the experiments it is observed that, a larger magnet with the presence of a ferromagnetic yoke on the stator increases the distance at which successful flux pumping can be achieved.

The flux pump in this research is a mechanically rotating permanent magnet rotor with a Type II HTS stator, which operates with a local region in the mixed state (Hoffmann, 2011), without any normal zone as in case of superconducting dynamos (van de Klundert *et al.*, 1981). The rotor is rotated with a servomotor and the distance between the magnet and the HTS stator is variable. The measurements are done for different separation distances and at different frequencies.

The HTS wire used as the stator is Type II superconductor and has two critical fields, B_{c1} and B_{c2} , with B_{c1} being too low (~ 300 Gauss). At smaller distances, the field due to the NdFeB magnets causes the flux flow regime to exist and is also sufficient to make the HTS stator operate in a mixed state (*i.e.*, $>B_{c1}$ and $<B_{c2}$).

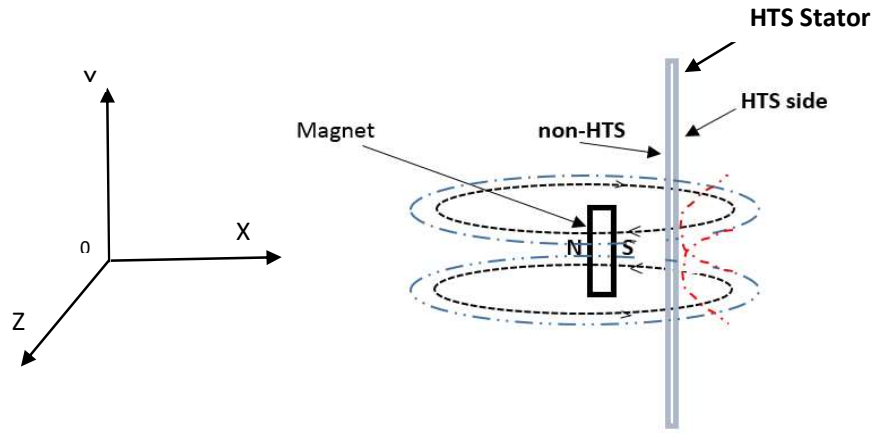


Fig. 3.1 Field interaction between rotor magnets and stator of the flux pump.

Figure 3.1 shows the interaction between the magnetic field lines and the HTS stator. When the magnet moves with respect to the HTS wire in the XZ-plane, the flux lines are cut by the HTS stator and a current is induced in the HTS stator and this form of interaction generates a quasi-DC emf across the HTS stator

and the current starts ramping up (Hoffmann *et al.*, 2011; Jiang *et al.*, 2014). In this phase of research, experiments have been carried out on two different types of flux pumps.

1. Cold rotor flux pump: Flux pump in which all the components including the rotor are at cryogenic temperature.
2. Warm rotor flux pump: Flux pump in which all the dynamic components are outside the cryogenic environment, mimicking the actual 10 kW proof-of-concept HTS generator.

3.2 Design of Experiments

The experimental study has developed a better understanding, of the phenomenon of occurrence of a net DC current across HTS stator in the flux pump. In order to accomplish the aforementioned objective, experiments were conducted, using two different configurations of flux pumps:

1. Cold rotor flux pump (Gen 1) (Fig 3.2)

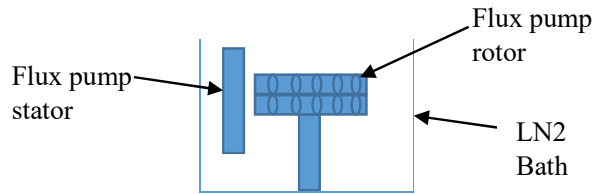


Fig. 3.2 Cold rotor flux pump diagrammatic representation

2. Warm rotor flux pump (Gen 2a) (Fig. 3.3)

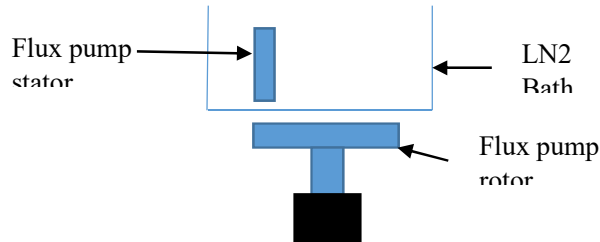


Fig. 3.3 Warm rotor flux pump diagrammatic representation

The experimental procedure for both the configurations is the same and discussed in section 3.2.1. The construction and design variations are discussed further in the corresponding sections.

3.2.1 Experimental Process

Figure 3.4 illustrates the experimental process with the flux pumps. As seen in the Fig 3.4, there are four important systems in the experimental process and there is one sub-system used for setting the distance of separation between the magnetic rotor and the HTS stator of the flux pump. The technical aspects of the systems are discussed here and the supporting data sheets are attached in Appendix-C.

For experimentation at cryogenic temperatures, slow cooling has to be carried out so that there is no thermal breakdown of equipment because of rapid cooling. The offsets for the amplifier are to be noted down once the cooling is complete and the offsets have to be compensated for in the recorded results. The procedure of cooling was followed every time the system had to be shifted from room temperature to the cryogenic temperature.

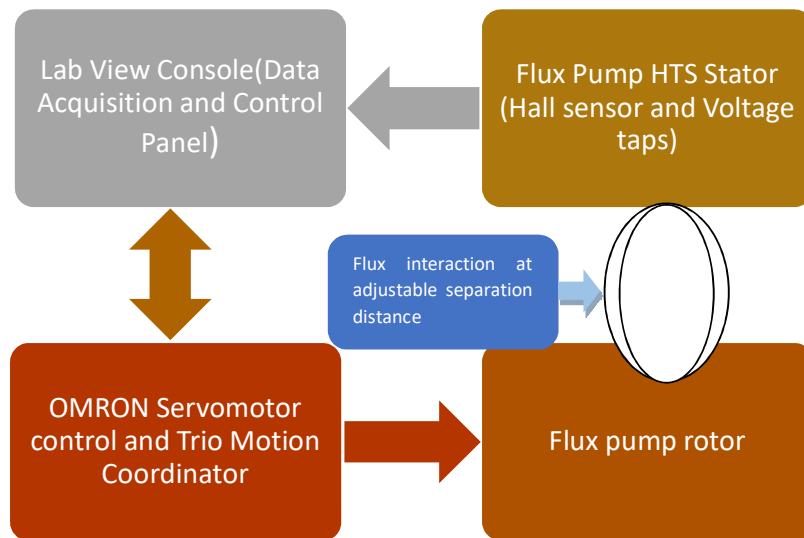


Fig. 3.4 Block diagram illustrating flux pump experimental process

3.2.2 Apparatus used in the experiments on flux pumps

- Test rig frame with distance adjustment
- Flux pump rotor magnets
- OMRON stepper motor driver
- TRIO motion coordinator
- 2G HTS coil
- Hall probe
- Shielded cables
- Lettech Amplifier
- NI-USB DAQ
- LabVIEW

3.2.3 Procedure outline

2G HTS coil and a Hall probe arrangement (Fig. 3.5 B and Fig. 3.6) are used to measure the current in the HTS stator. The coated conductor wire used as the stator is manufactured by Superpower Inc. (SF12100) and includes a 12 mm wide Hastelloy ribbon substrate upon which a 1 μm film of YBCO is deposited and coated with 2 μm of silver.

The old and new arrangements of the coil are shown in Fig. 3.5 A and Fig. 3.5 B, respectively. In the old arrangement used by Robinson Research Institute for previous experiments, only one of the available 7 Hall sensors on the probe was used to acquire data. In the new arrangement, all 7 sensors were used and shielded cables were used.

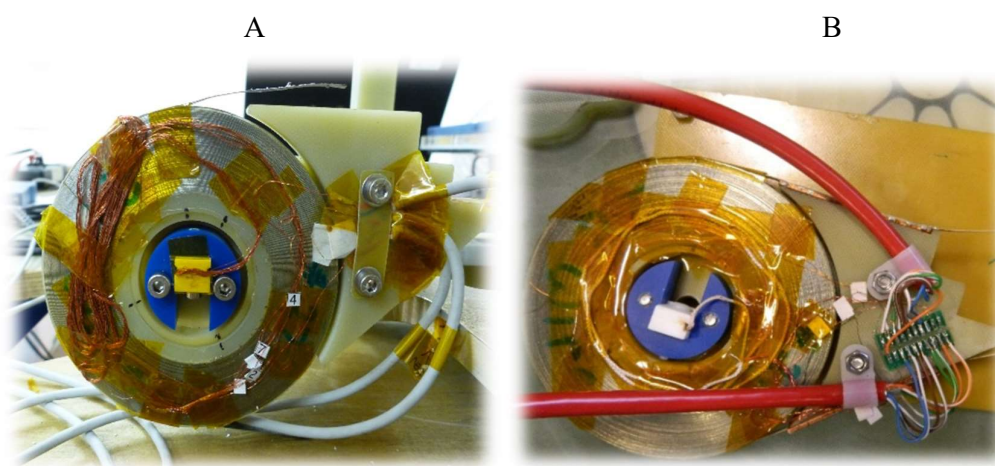


Fig. 3.5 A. Hall probe and coil (old arrangement, Courtesy: Robinson Research Institute)

B. Hall probe and coil (new arrangement)

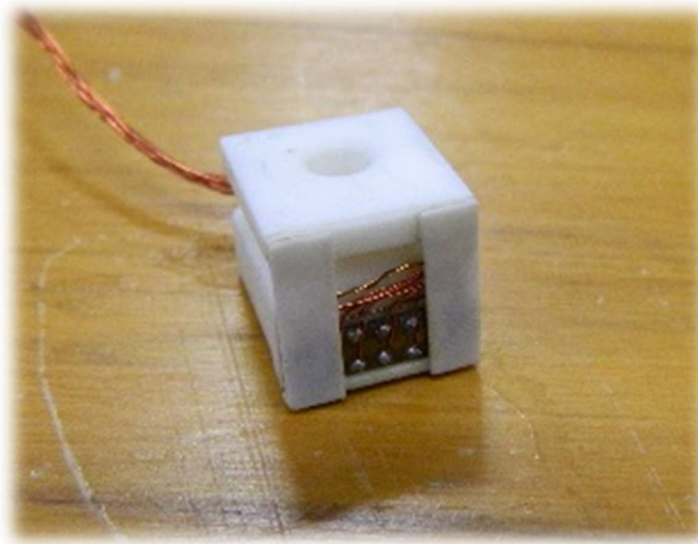


Fig. 3.6 Hall probe

Shielded cables were used to avoid any stray pick up from the surrounding. The Hall sensor voltage outputs are of the order of μV . Hence, the Lettech amplifier was used to amplify the voltage signals from the Hall sensor and these were recorded using NI Data acquisition cards (NI-6210 and NI-6215) and LabVIEW.

Flux pump rotor comprised of two co-aligned circular arrays of 12 permanent magnets (NdFeB N38) which were mounted on the outer circumference of a cylindrical FRP epoxy (G-10) holder. G-10 is a composite of epoxy and fibreglass and has lower thermal conductivity, (Van Sciver, 2012). Due to its lower thermal conductivity property, G-10 is a suitable material for most of the components in a cryogenic system. Bevel gear arrangement was used to vary the distance between the HTS stator and the rotor magnets.

OMRON driver and TRIO Motion coordinator were used to control the speed of servomotor coupled to the rotor of flux pump. LabVIEW and National Instruments data acquisition cards (NI-6210 and NI-6215) were used to start-stop the servomotor, acquire and save data.

3.3 Calibration of Hall sensor

Hall probe in consideration is an array of hall sensors that produce an output voltage in response to the magnetic field applied. It is a small piece of the semiconductor layer. Leads are connected to the midpoints of opposite sides as illustrated in Fig. 3.7.

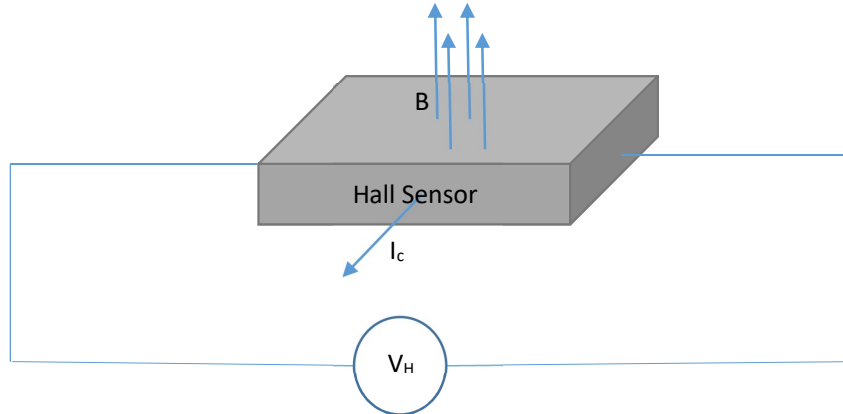


Fig. 3.7 Hall Effect equivalent circuit

With the control current flowing through the control current terminals, a voltage proportional to the perpendicularly applied magnetic field is produced across the hall sensor and it can be calibrated to measure the current flowing in a solenoid coil, which produces a corresponding magnetic field.

The output voltage V_H of the Hall probe is affected by the change in the angle between the vector of the magnetic flux lines and the sensing plane.(High Linearity Hall Probes for Room and Cryogenic Temperatures, 2007).

The Hall sensor was calibrated using a DC current supply (see Fig. 3.8). A known current was injected into the coil and the response of the Hall sensor was measured and logged. The currents were injected in steps, at an incremental step of 0.5 A till the critical current ($I_c = 55\text{A}$) of the coil. The measured values were then fit to a quadratic curve fit and the coefficients for each sensor were documented and input into the LabVIEW program.

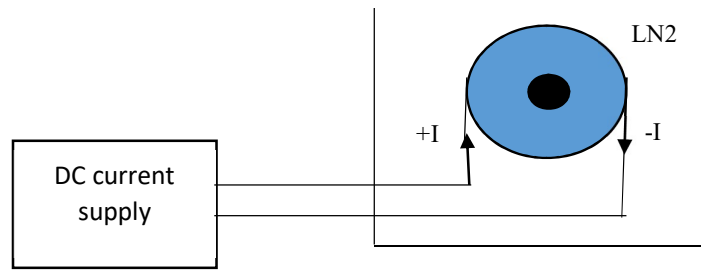
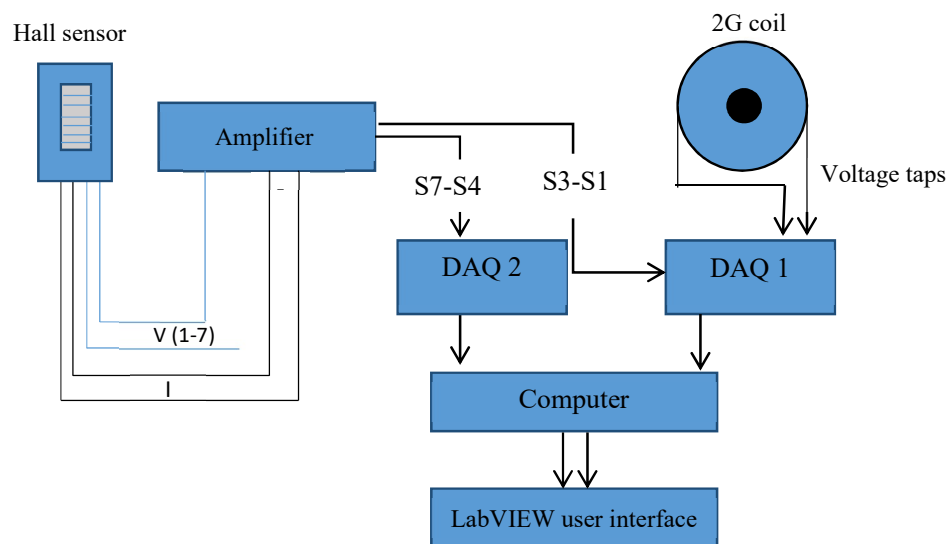


Fig. 3.8 Calibration of the Hall sensor.



S#, sensor output from the hall probe

Fig. 3.9 Schematic diagram of the measurement system.

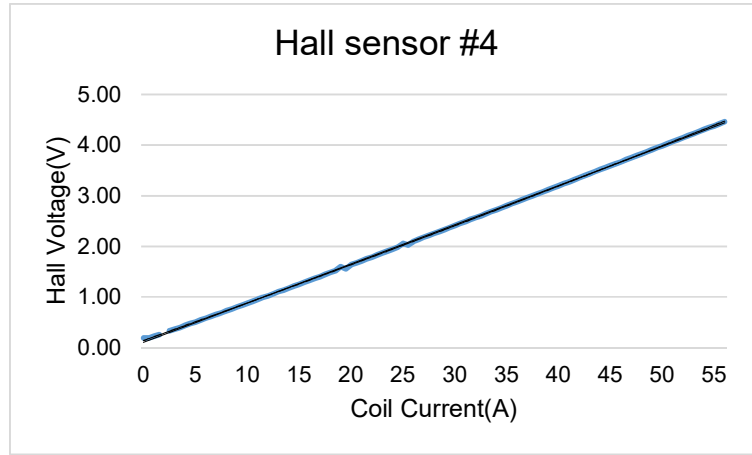


Fig. 3.10 Hall voltage vs. Coil current.

The schematic diagram of the measurement system indicating all the critical systems is as shown in Fig. 3.9. The response of Hall voltage against coil current for Hall sensor 4 is shown in Fig. 3.10 (response of other sensors have been provided in Appendix B- Additional results). The response is observed to be linear, but a quadratic fit for coil current against hall voltage by change of variables was obtained to have better accuracy. A quadratic fit for current measured using hall sensor 4 is shown in Eq. 3.3.

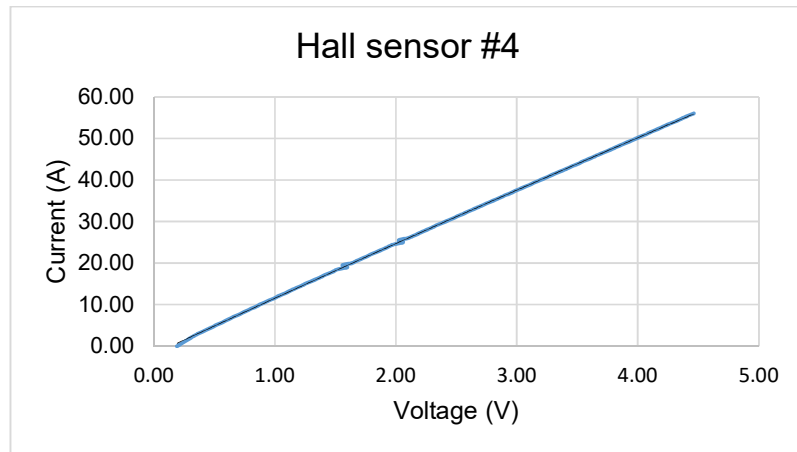


Fig. 3.10 Hall voltage vs. Coil current

$$i_4 = 0.167v^2 + 11.9v \quad (3.3)$$

3.4 Sampling frequency

The high rate of data acquisition was chosen to have sufficient resolution to aid in the time-resolved analysis of the data. Rather than using a flat high rate of data acquisition, the sampling frequency for data acquisition was selected according to the frequency of flux interaction.

The higher frequencies of 598 Hz and 298 Hz were measured at 50 KS/s per channel and 25 KS/s per channel, respectively. The lower frequencies of 148 Hz, 73 Hz, 33 Hz and 16 Hz were measured at 12.5 KS/s.

3.5 Speed setting

The speed of the rotor was set according to the required frequency of flux interaction between each magnet and the HTS stator, using Eq. 3.4.

$$N = \frac{60 * f}{P} \quad (3.4)$$

where N = speed of the rotor, f = frequency (Hz) and P = Number of magnets

The rotor of Gen1 flux pump contained 12 magnets. For example, to get a frequency of 598 Hz, the speed of the servomotor was programmed to rotate at 2990 rpm. 598 Hz was selected instead of 600 Hz to avoid resonance with the mains connected to various devices in the measurement system.

Servomotor was used to rotate the rotor. Servomotors are better suited for high acceleration/deceleration applications and in feedback based position control applications (see Fig. 3.11) (Hughes & Drury, 2013).

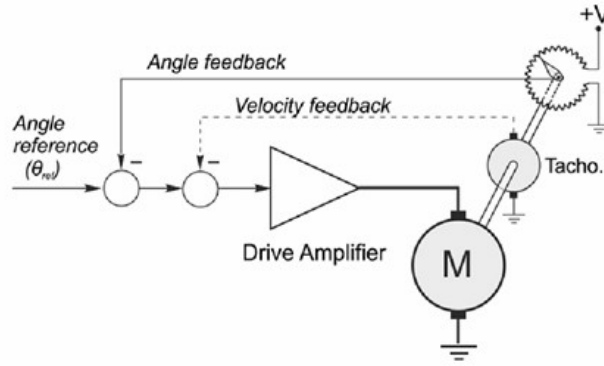


Fig. 3.11 Closed-loop angular position control using DC motor and angle feedback from a servo-type potentiometer (Hughes & Drury, 2013).

The control of the servo motor was through LabVIEW-TRIO Motion coordinator and Omron drive. It found out that the servo motor could be controlled using the CX-Drive software. As a computer needs to be connected while doing the experiments (to run LabVIEW), running the servo motor directly from CX-Drive would introduce no issues and would allow same motor controls as from the Trio.

To stop the motor immediately in case of emergencies, an emergency physical stop button was used. Distance between the HTS stator wire of the flux pump and the rotor magnets was set at 1 mm, 2 mm, 3 mm, 4 mm, 6 mm, 7 mm and 8 mm for Gen1 and 4 mm, 5 mm, 6 mm, 8 mm and 12 mm for Gen2a flux pump. The measurements were carried out for different frequencies.

3.6 Cold Rotor Flux Pump (Gen 1)

3.6.1 Introduction

Experiments were conducted on 'cold rotor flux pump', called so, as the entire rotor of the flux pump is in the cryogenic environment. Figs. 3.12 and 3.13 show the test rig of cold rotor flux pump (Gen 1). The aim of these experiments was to measure and record the voltage and current waveforms in the HTS stator when excited. The data was analysed to infer on the suitability of flux pump based rotor excitation. The experimentally recorded data was, later used as inputs in FEM based study discussed in chapters 4 and 5.

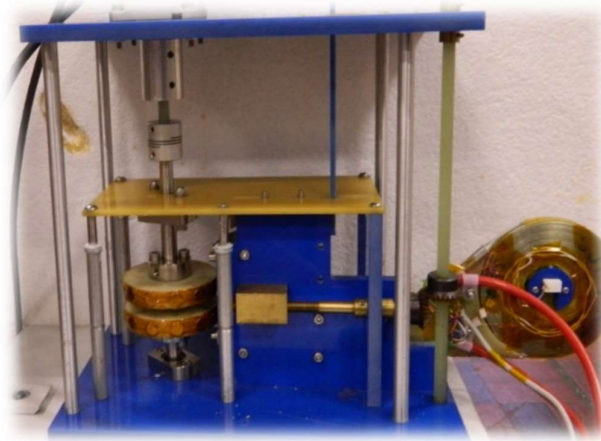


Fig. 3.12 Gen 1 Flux pump test rig.

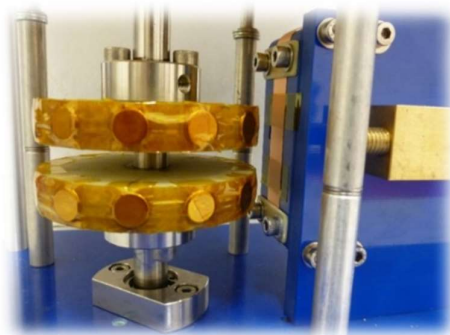


Fig. 3.13 Rotor Magnets and HTS stator of Gen 1 Flux pump

The current in the HTS stator and the voltage across the HTS stator were measured and recorded across various frequencies of flux interaction. The distance between the rotor and stator were set as tabulated in Table 3.1. The recorded data when analysed, provided the qualitative relationship between the current in the stator, the voltage across the stator, the frequency and the distance between the rotor and stator for the flux pump without a ferromagnetic yoke.

For higher distances, only higher frequencies were recorded as excitation with lower frequencies provided very low current and took very long time to ramp up, making the experiment impractical over the expected timeline.

Table 3.1. Frequencies and distances at which the voltage and current in the HTS stator of a cold rotor flux pump were recorded.

| Sl. No | Frequency (Hz) | Distances (mm) |
|--------|----------------|----------------|
| 1 | 298 | 1,2,3,4,6,8 |
| 2 | 148 | 1,2,3 |
| 3 | 73 | 1,2,3 |
| 4 | 33 | 1,2 |
| 5 | 16 | 1,2 |

3.6.2 Experimental results and observations

As discussed in section 3.3. The current in the HTS stator was measured using a solenoid coil and Hall sensor arrangement. The Hall sensor senses the variation in the magnetic field and provides a proportional voltage as the output and the magnitude of voltage is of the order of few mV. Lettech amplifier was used to amplify the Hall voltages. A high rate data acquisition system was designed using LABVIEW and NI-DAQ cards. The frequency of data acquisition was selected based on the frequency of flux interaction between the rotor and the stator of the

flux pump. The amplified Hall voltage signals were acquired by LABVIEW program via NI-DAQ cards and stored in TDMS file format to facilitate large data management.

In the experiment, the speed N of the flux pump rotor was set using Eq. 3.4. In order to avoid resonance with the line voltage, the frequency was set at 598 Hz and the corresponding speed was set at 2990 rpm for a 12 NdFeB magnets rotor. The voltage and current profiles observed are in agreement with the results reported earlier. The voltage across the HTS stator of flux pump is shown in Fig. 3.14. The voltage across the HTS stator is asymmetric over the reference line. The averaging of the voltage profile shown in Fig. 3.14 gives a non-zero value (Kulkarni *et al.*, 2015; Bumby *et al.*, 2016).

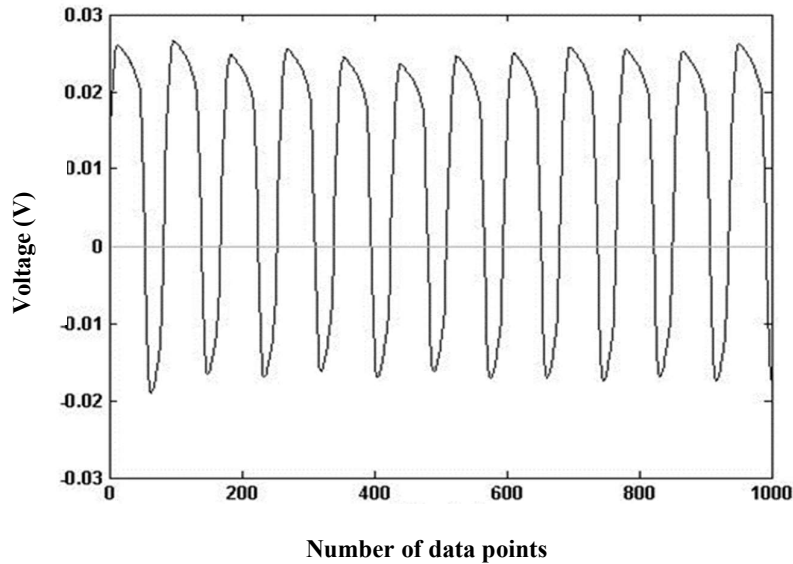


Fig. 3.14 Voltage (598 Hz) across the HTS stator during flux pump operation.

The averaged current for 1 mm separation and 598 Hz frequency is shown in Fig. 3.15. The ramp up rate is around 0.875 A/s. The maximum current reached is 52.5 A. The steady state is reached in ~65 s.

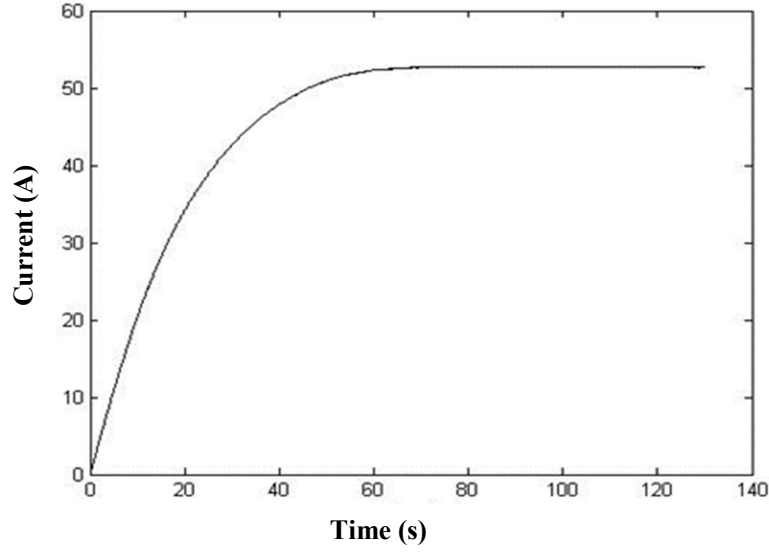


Fig. 3.15 The averaged current for 1 mm separation and 598 Hz.

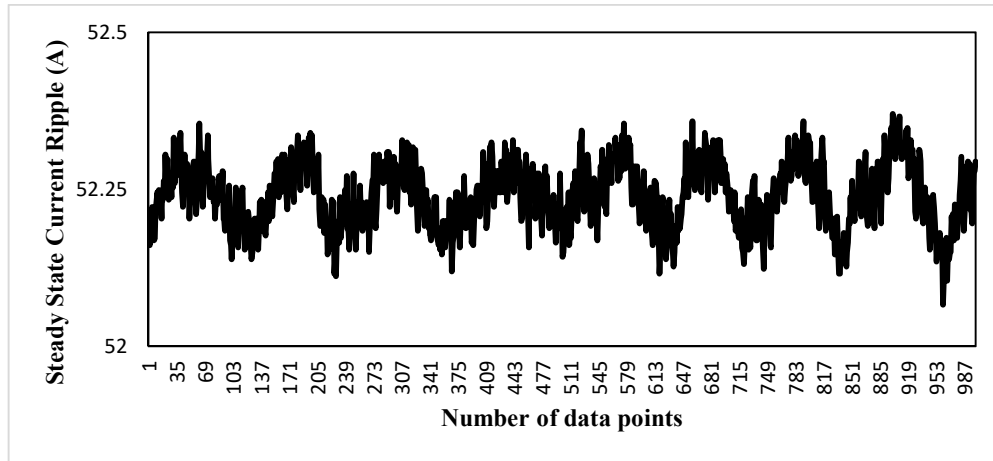


Fig. 3.16 Steady state current ripple (598 Hz).

From the current ripple (see Fig. 3.16), an overlap of the cycles is observed. The overlap of the waveforms can be because of high frequency of flux interaction or the cogging effect. The cogging effect is expected because of magnets passing by at a very close distance to the HTS stator. From the ripple in the waveform it can be expected that the field fluctuation would be similar to the current ripple, as the field due to a current carrying conductor is proportional to the current flowing

through it. Further experimentation and FEM studies are needed to critically analyze the field pattern and fluctuations in the field taking into account the shielding currents, demagnetizing and cross-magnetizing effects. The Fast Fourier Transform (FFT) of the voltage across HTS stator is shown in Fig. 3.17. The normalized FFT of the voltage signal across the HTS stator showed the presence of 2nd and 4th harmonics. The presence of even harmonics is due to the asymmetry in the voltage, reported by us for the first time. However, an interesting factor is the magnitude of the harmonics. The magnitude of 2nd and 4th harmonics are observed to be ~30% and ~4% of the fundamental, respectively. The 3rd harmonic is found to be much smaller than the 4th harmonic (Kulkarni *et al.*, 2015).

Further investigation and analysis with a larger data set have been carried out to draw on the relevant aspects of the designed study discussed in section 3.7.

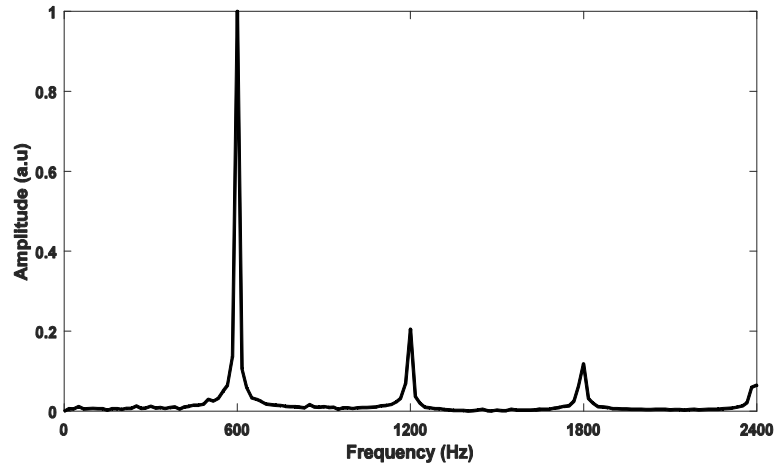


Fig. 3.17 Normalized FFT of the Voltage (598 Hz) across the HTS stator.

3.6.3 Excitation frequencies

The flux pump stator current is observed to be greatly affected by the frequency of excitation. The two important parameters of the stator current were quantified to understand the dependency.

- 1) The rate of rise of current (r).
- 2) Saturation current (I_{sat})

As mentioned earlier, the sampling rate for 298 Hz was 25 KS/s and for 598 Hz, it was 50 KS/s.

In Fig. 3.18, the time averaged stator current for various frequencies of excitation is plotted against time. From the plots, it is inferred that the rate of rise of current in the stator varies directly with the frequency of excitation of the flux pump. From the coil current graphs, it can be observed that the trend of current induced in the coil is an exponential curve.

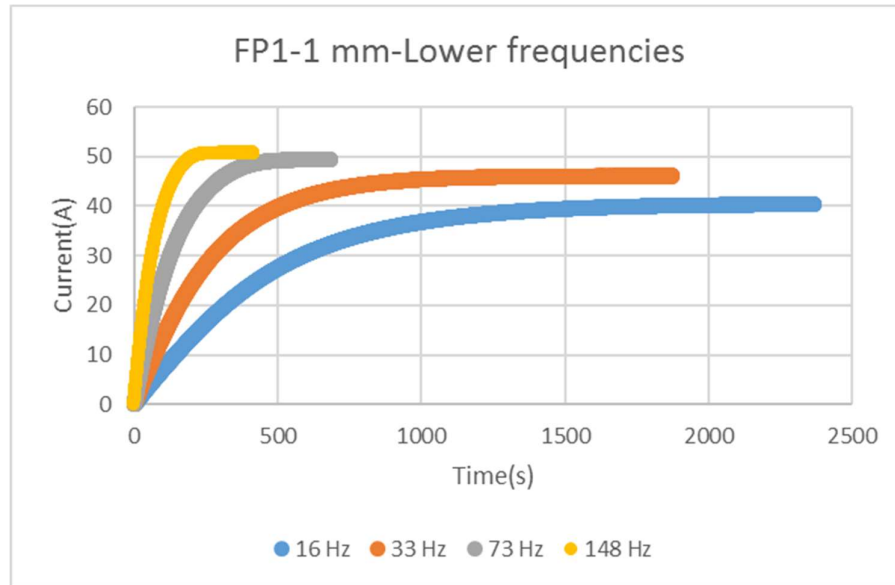


Fig. 3.18 Current ramp up at different frequencies for a separation of 1mm.

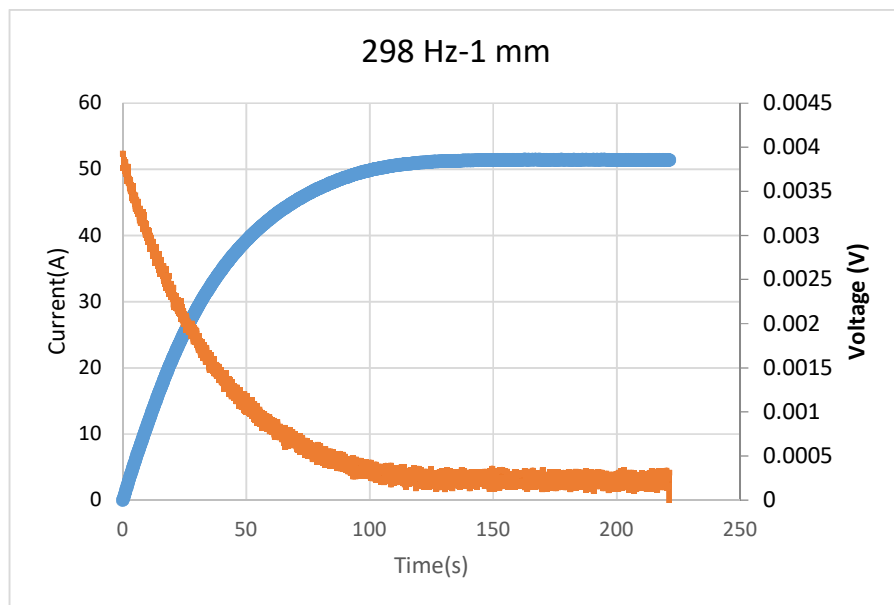


Fig. 3.19 Time-averaged current and voltage profile of HTS flux pump at 298 Hz for a separation of 1mm.

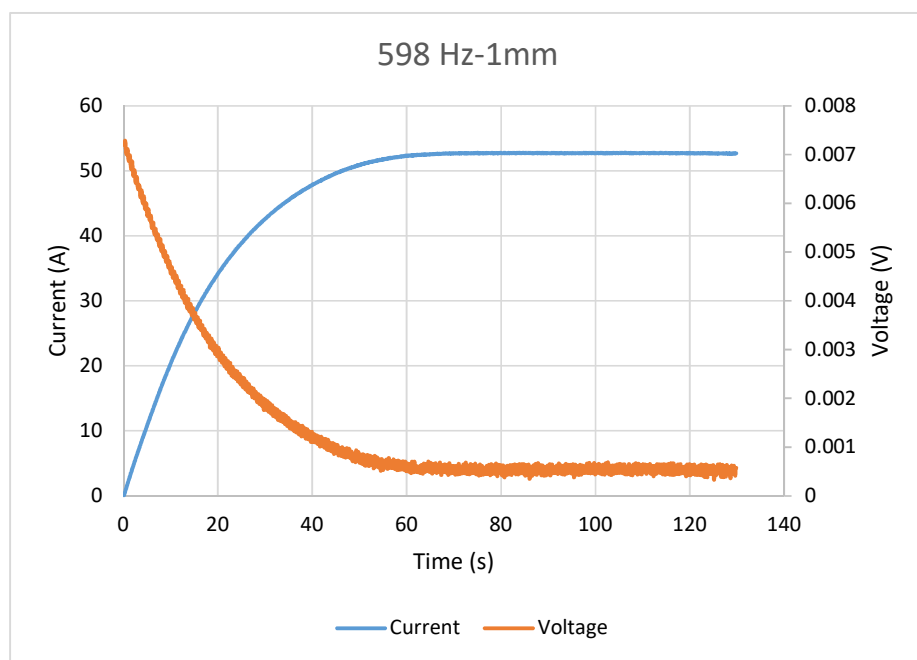


Fig. 3.20 Time-averaged current and voltage profile of HTS flux pump at 598 Hz for a separation of 1mm.

Using the data, an exponential fit with the following equation form can be obtained for current in each of Fig 3.19 and Fig 3.20 as in Eq. 3.5;

$$y = A \left(1 - e^{-\frac{x}{\tau}} \right) \quad (3.5)$$

where y is current (A), A is maximum current (A), x is time (s) and τ is the time constant (s)

From the coil voltage graph in Fig 3.19 and Fig 3.20, it can be observed that the trend of coil voltage is an exponential decay curve. Using the data, an exponential fit with the following equation form can be obtained as in Eq. 3.6.

$$y = C + (A \times (e^{-\frac{x}{\tau}})) \quad (3.6)$$

where, where y is coil voltage (mV), A is maximum coil voltage (mV), x is time (s), τ is the time constant (s) and C is the offset.

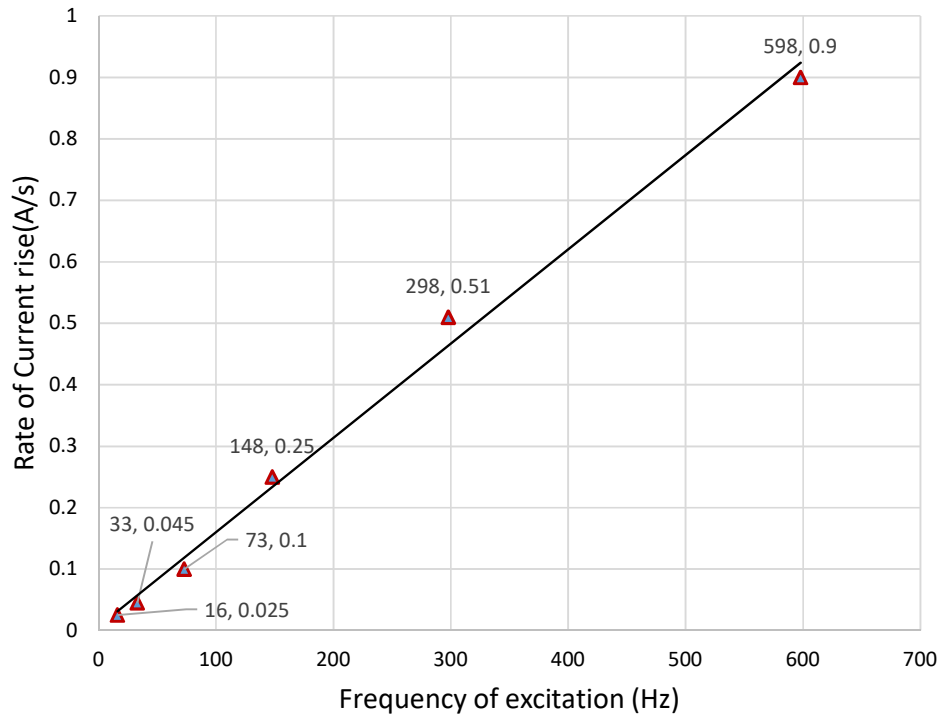


Fig. 3.21 Rate of rise of current vs frequencies for a separation of 1mm.

The plot of the rate of current rise with frequency (Fig. 3.21) is discussed further. However, the trends are found to be similar with all the frequencies.

From the results of Gen 1 flux pump experiments in magnetising a superconductor, it is clear that the flux pump can be utilised in generating the magnetic field in an HTS rotating machinery.

Some of the concerns that need to be addressed are as follows:

- a) An efficient magnetic circuit to bridge the magnetic flux between flux pump magnets and the superconductor.
- b) Harmonic analysis of the system in conjunction with the synchronous generator operating conditions.
- c) Stator design effects and effect of imbalance caused due to separately excited stators.

3.6.4 Remarks

An empirical formula for the rate of rise of current and its dependency on the shape and size of the magnets used in the flux pump and choice of material for the magnetic circuit are some of the aspects for improvising the design of the flux pump in order to suit-fit it to a rotating machinery application. Based on the literature review and results observed until now in this research work, it can be inferred that the application of flux pump is suitable for exciting rotor (HTS conductors) in a synchronous generator.

Studies are conducted on the warm rotor flux pump and the proof-of-concept 10 kW HTS generator to conclude on, the practical feasibility and performance of a flux pump integrated MW rating wind-based synchronous generator, are reported in further sections and chapters.

3.7 Warm rotor Flux pump (Gen 2a)

3.7.1 Introduction

The cold rotor flux pump (Gen 1) discussed in the previous section did not have a ferromagnetic yoke on the stator side of the flux pump. The presence of a ferromagnetic yoke has the advantage that the separation distance between the rotor and stator can be increased and practical width for cryogenic insulation can be more easily achieved. Thus, a warm rotor flux pump with a ferromagnetic yoke (iron) on the stator side was designed.

The cryostat of the warm rotor flux pump was designed by Fabrum solutions. The material used for the construction of the test rig was same as the material used to manufacture the rotating cryostat of the proof-of-concept 10 kW HTS generator. As a result, the heat leak of the cryostat could be monitored as well.

The warm rotor flux pump emulated the operating conditions of a flux pump integrated HTS generator at a laboratory scale. The warm rotor flux pump can be considered an experimental prototype of the flux pump integrated HTS rotor synchronous generator at laboratory scale. The analysis of results of the conducted experiment is expected to give a qualitative understanding of the application of flux pump for exciting the rotor coil in HTS rotor synchronous generator. The observations were expected to be extrapolated to the behaviour of flux pump for the 10 kW proof-of-concept HTS generator.

An iron stator yoke was placed directly upon the base of the cryostat above a thin (3 mm) section of the cryostat wall. A 12 mm wide coated-conductor stator wire was wrapped around the stator yoke and threaded through a hole to enable a closed electrical circuit to be formed through soldered connection to an HTS double pancake coil (DPC). The DPC was measured to have a critical current of

$I_c = 95$ A at the $1 \mu\text{Vcm}^{-1}$ criterion and had a measured inductance $L = 2.3$ mH. The stator wire was manufactured by Superpower Inc., and had a measured I_c at the $1 \mu\text{Vcm}^{-1}$ criterion of 292 A. An iron rotor disc (yoke) was placed opposite the stator yoke, but outside (beneath) the cryostat such that the composite cryostat wall was accommodated in the flux gap between the rotor and stator yoke. The rotor yoke housed 9 Nd-Fe-B (N42) permanent magnets which were arranged in a homopolar orientation with the axis of magnetisation directed across the flux gap. The CAD model of the warm rotor flux pump is shown in Fig. 3.22. Further, experiments were conducted using the warm rotor flux pump to realise the consistency of the results for different separation distances and excitation frequencies. The inner details of the warm rotor flux pump can be better visualised as shown in Fig. 3.23.

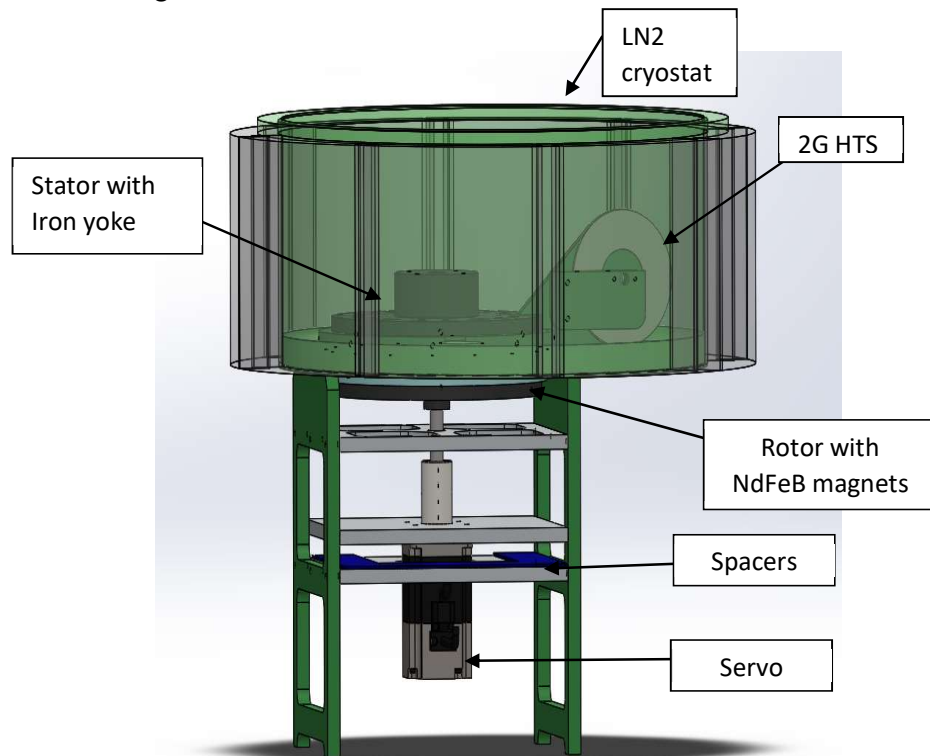


Fig. 3.22 Warm rotor flux pump (CAD Model).

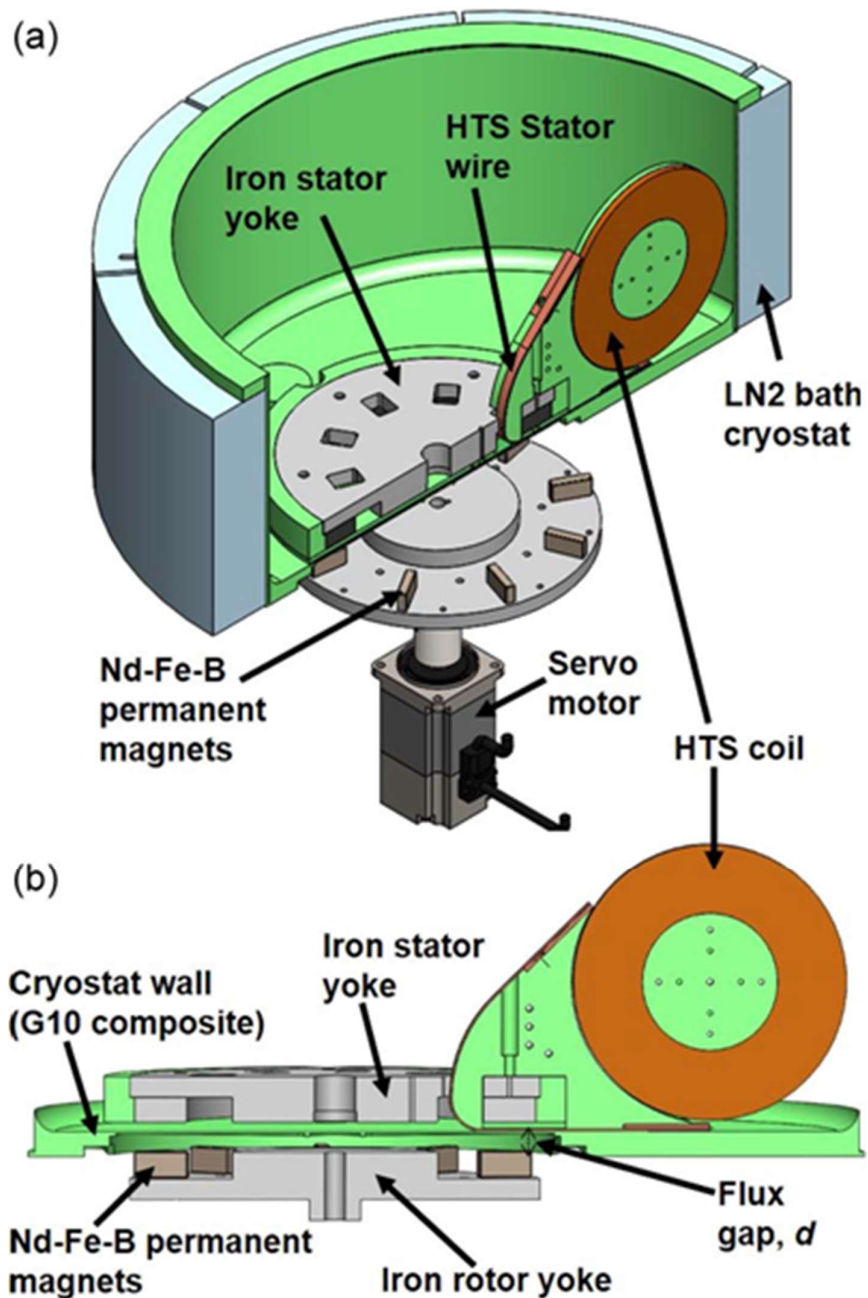


Fig. 3.23 (a) 3D view of the warm rotor flux pump, set up for further experimentation, the composite cryostat bath, and the HTS coil. (b) A cross-sectional view of the cryostat wall and flux pump rotor and stator showing magnetic circuit formed between the rotor and the stator (Bumby *et al.*, 2016).

Experiments were carried out on warm rotor flux pump with a ferromagnetic yoke on stator side for different gaps similar to those on cold rotor flux pump without a ferromagnetic yoke. The actual model is as shown in Fig. 3.24.

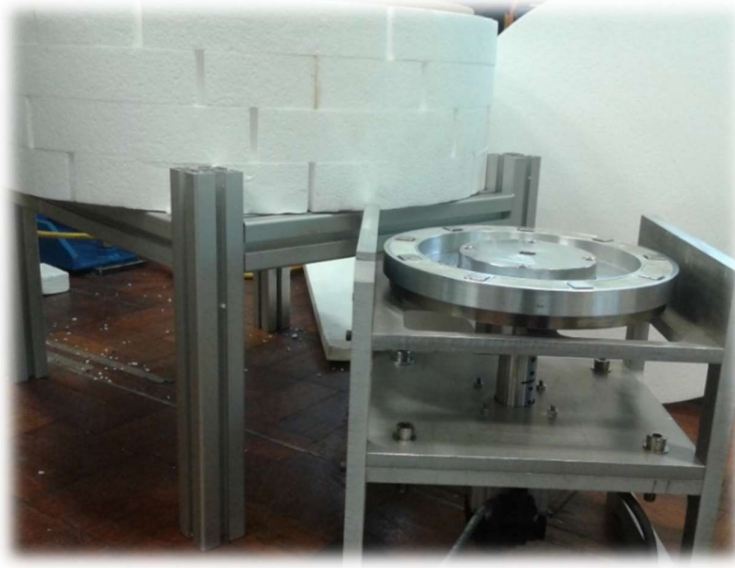


Fig. 3.24 Warm rotor flux pump (Actual Model).

3.7.2 Experimental results and observations

Current and voltage on the stator of the flux pump were recorded using Hall sensor and LabVIEW setup. Higher sampling rates (50 KS/s and 25 KS/s) were used for higher frequencies of 448.5 Hz and 223.5 Hz, respectively. For all other frequencies (111 Hz, 54.75 Hz, 24.75 Hz, 12 Hz) a fixed sampling rate of 12 KS/s was used. The minimum possible distance of separation between the flux pump rotor and the stator with the Gen 2a flux pump rig was 4 mm (4 times higher than the minimum separation possible with Gen 1). The current and voltage were similar in magnitudes to those attained using Gen 1. The stator voltage and current values were recorded for various separations and shown in Table 3.2.

Table 3.2 Frequencies and distances at which the voltage and current in the HTS stator of a warm rotor flux pump were recorded.

| Sl. No | Frequency(Hz) | Distances(mm) |
|--------|---------------|---------------|
| 1 | 448.5 | 4,5,6,8,12 |
| 2 | 223.5 | 4,5,6,8,12 |
| 3 | 111 | 4,5,6,8,12 |
| 4 | 54.75 | 4 |
| 5 | 24.75 | 4 |
| 6 | 12 | 4 |

Higher distances were chosen as the practical distances for a cryogenic insulation for a 10 kW rating machine is expected to be ~12 mm. For the lower frequencies, it was observed that the current ramp up rate was very small and the current saturation time was long and was deemed impractical. Thus, the measurements were only carried out for the minimum distance of 4 mm for lower frequencies.

3.7.3 Excitation frequencies (Lower range: 12 Hz, 24.75 Hz, 54.75 Hz and 111 Hz)

The speed of the servomotor was set to a calculated value (based on the number of magnets in the rotor) to obtain the desired frequency of magnetisation of the stator. The sampling rate of measurement was set at 12.5 KS/s for all these frequencies. The rate of rise of current and the saturation value of current are the key factors for the application of flux pump. The plots of current versus time for various separations and the nature of ripple at steady state for after time averaging are discussed now.

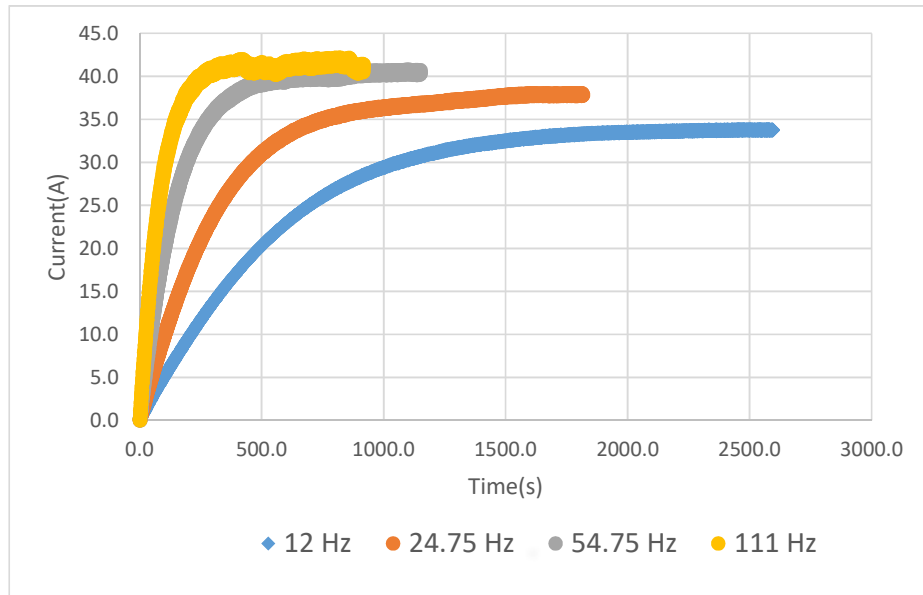


Fig. 3.25 Current ramp up at different frequencies for a separation 4 mm.

Fig. 3.25 shows the plots of time-averaged stator currents of Gen 2a- warm rotor flux pump for a separation of 4 mm, at various frequencies of excitation versus time. From the plots, in this case too, it infers that the rate of rise of current in the stator varies directly with the frequency of excitation of the flux pump.

3.7.4 111 Hz at various separations

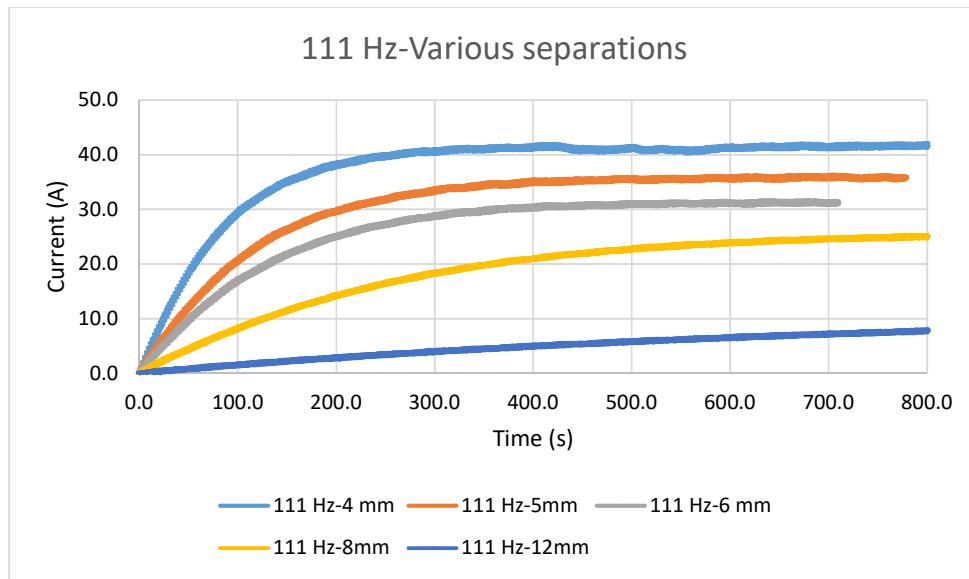


Fig. 3.26 Current ramp up at 111Hz for various separation distances.

In Fig. 3.26, the current ramp up at different separation distances for 111 Hz of excitation is shown.

Inference:

The peak-to-peak value of ripple current is observed to be ‘almost’ the same for all gaps. The peak-to-peak ripple for 4 mm separation varies between 0.8 A to 1 A (see Fig. 3.27).

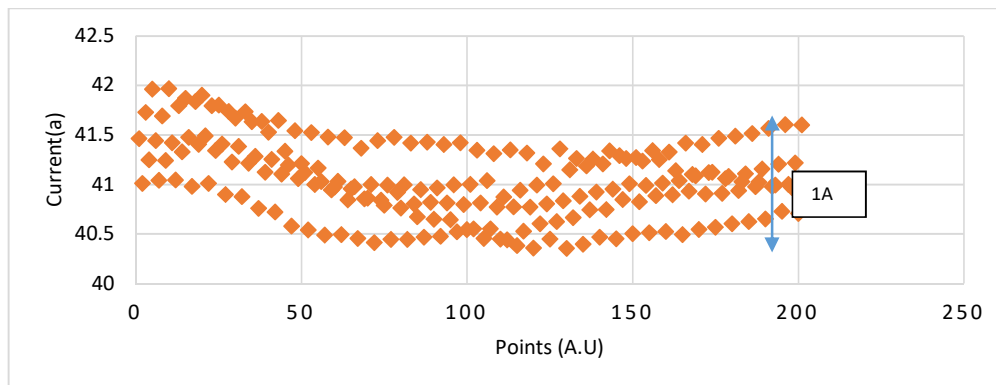


Fig. 3.27 Steady state current ripple of 111 Hz at 4mm separation

3.7.5 223.5 Hz at various separations

To know the effect of the change in frequencies, the frequencies were set to a value other than the one used for Gen 1 but the trend followed is found to be the same. The sampling rate for higher frequencies of 223.5 Hz and 448.5 Hz was set at 25 KS/s and 50 KS/s respectively and the response at these frequencies are shown separately in Figs. 3.28 and 3.30 respectively.

In Fig. 3.28, the current ramp up at different separation distances for 223.5 Hz of excitation is shown.

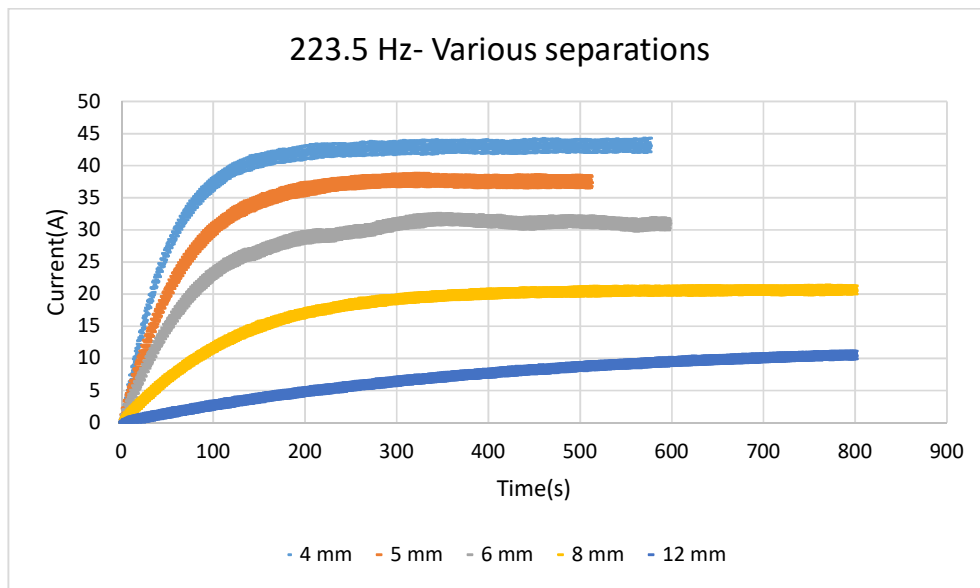


Fig. 3.28 Current ramp up at 223.5 Hz for various separation distances.

Inferences:

1. The peak-to-peak value of ripple current is observed to be 'almost' the same for all gaps.
2. The peak to peak ripple for 4 mm separation is around 2 A (see Fig. 3.29) and is higher than the one observed with 111 Hz, which implies higher frequency of magnetization results in a faster rise of current with almost same saturation current but introduces ripple current of higher magnitude.

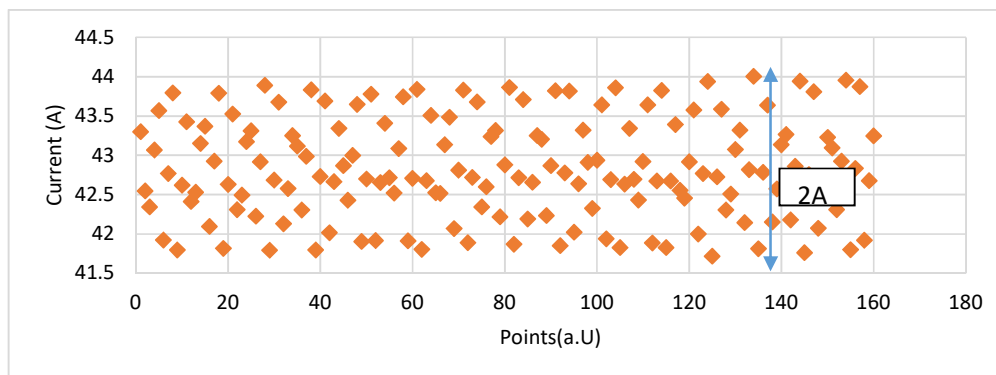


Fig. 3.29 Steady state current ripple of 223.5 Hz at 4mm separation

3.7.6 448.5 Hz at various separations

In Fig. 3.30, the current ramp up at different separation distances for 448.5 Hz of excitation is shown.

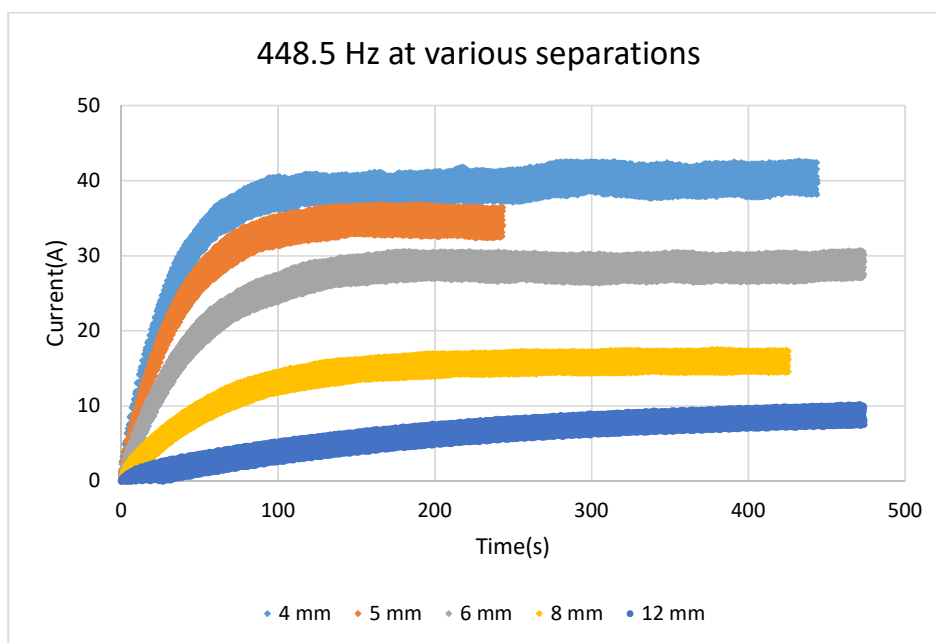


Fig. 3.30 Current ramp up at 448.5 Hz for various separation distances.

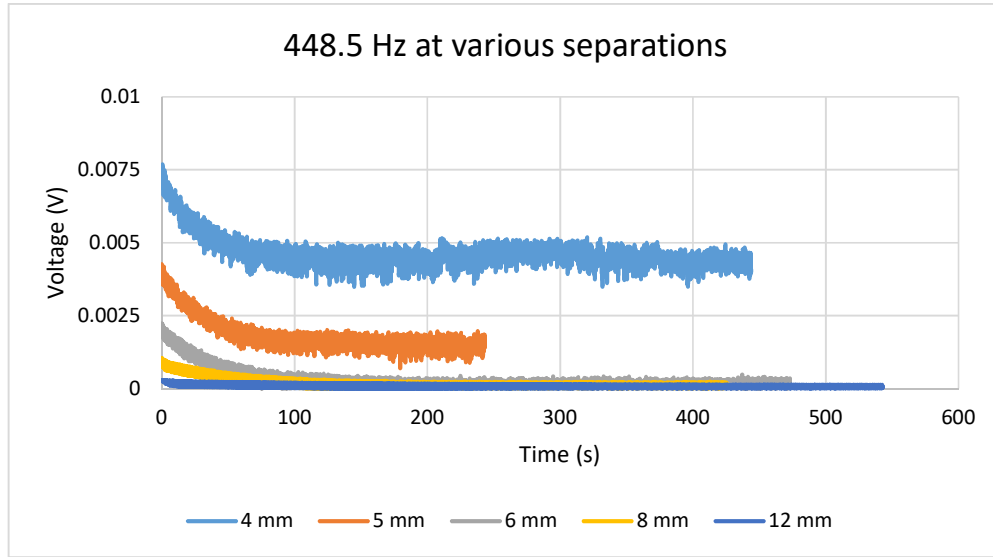


Fig. 3.31 Time-averaged voltage across flux pump stator at 448.5 Hz for various separation distances.

Inferences:

1. The time averaged voltage across flux pump (Fig. 3.31) follows the same trend as observed with Gen 1.
2. The peak-to-peak value of ripple current is ‘almost’ the same for all gaps.
3. The peak-to-peak ripple for 4 mm separation is around 4.2 A (see Fig. 3.32) and is higher than the one observed with 111 Hz and 223.5 Hz, which implies higher frequency of magnetization results in a faster rise of current, with almost same saturation current but introduces ripple current of higher magnitude.

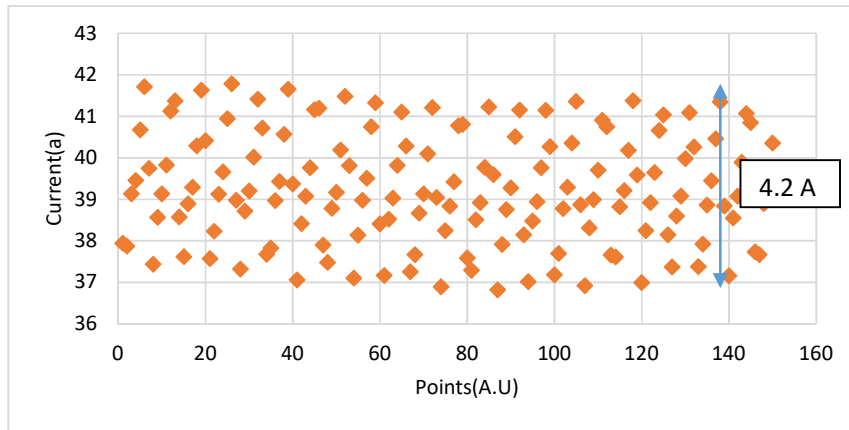


Fig. 3.32 Steady state current ripple of 448.5 Hz at 4 mm separation

The rate of rise of current in case of warm rotor flux pump follows the same trend as that of the cold rotor flux pump and the values for different frequencies of excitation for a 4 mm separation distance are as shown in Fig. 3.33.

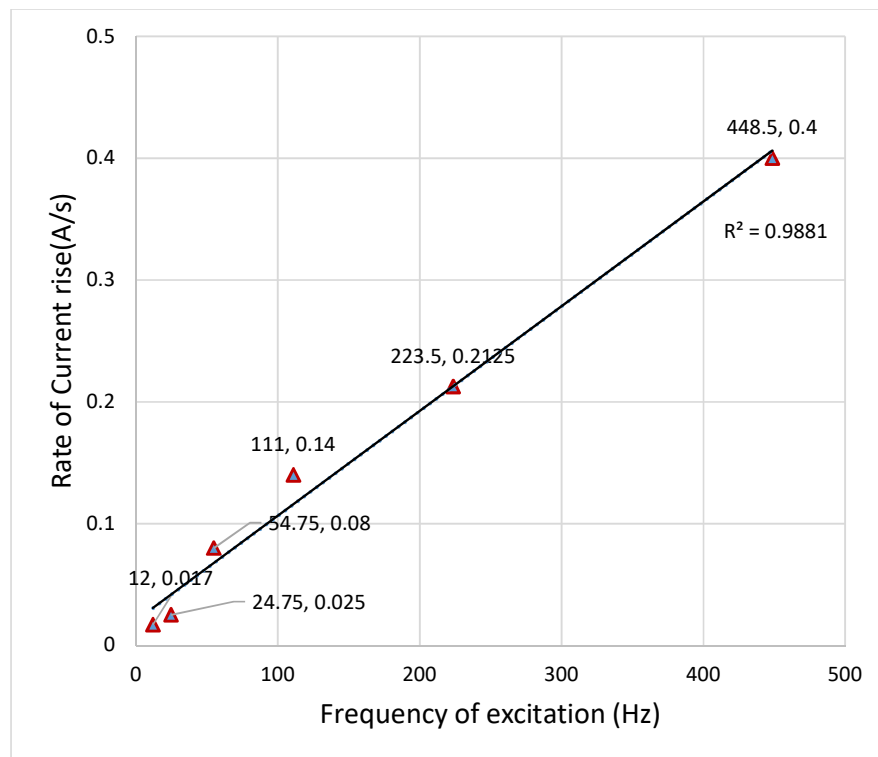


Fig. 3.33 Rate of rise of current vs frequencies for a separation of 4 mm.

3.7.7 Remarks

The rate of rise of current is observed to be proportional to the frequency of magnetisation. The saturation current is observed to be proportional at lower frequencies but with the higher 2 frequencies (in this category) the saturation current is almost the same and leads to a possibility of stator current becoming independent of the frequency of magnetization after a particular frequency. The cause for the aforementioned phenomenon needs further investigations, as it is now believed that there is a particular rate of magnetic fluxon generation (due to the magnetic flux of $>B_{c1}$ getting linked with the Type II HTS stator) and degeneration (due to resistive components in the circuit).

Fluctuations in steady state current are seen at 111 Hz. The reason for the fluctuations is not clear. The current ripple is observed to be higher at higher frequencies.

3.8 Equivalent Circuit Model

From the voltage and current plots of the cold rotor and warm rotor flux pumps discussed in sections 3.6 and 3.7 respectively, the voltage and current are found to vary consistently as in a DC RL circuit (see Figs. 3.18, 3.19, 3.20, 3.30 and 3.31) similar to ones reported by Jiang *et al.* (see Fig 2.8). The generic equations for current and voltage are as presented in Eq. 3.5 and Eq. 3.6.

Hence, it is inferred that the electrical equivalent circuit model for the flux pump in this research work, is in accordance with the one reported by Jiang *et al.* (Jiang *et al.*, 2014) as shown in Fig 3.34. The equivalent circuit model and the dynamic resistance parameter for the mechanical flux pump, similar to the one being used in this research, has been investigated and reported by Jiang *et al.* .,

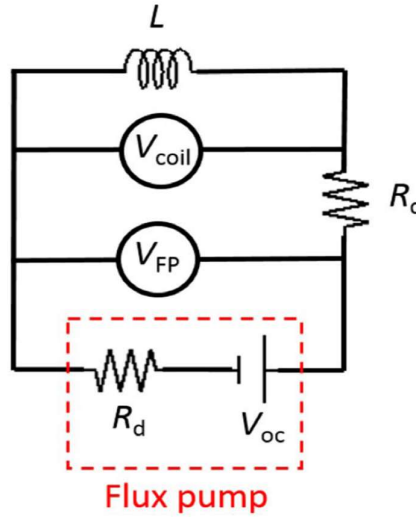


Fig. 3.34 Electrical equivalent circuit of a dynamic flux pump (Jiang *et al.*, 2014).

The equivalent circuit shown in Fig. 3.34 describes the behavior of a rotating HTS flux pump connected in series with a superconducting coil. Here R_c denotes the resistance of normal-conducting soldered joints between the coated conductor wires in the circuit, L is the inductance of the HTS coil, and V_{oc} is the

open-circuit voltage of the flux pump. It is, understood that, the internal resistance of the flux pump, R_d , is due to the effect of dynamic resistance within the superconducting stator.

From the output plots in section 3.6 and 3.7, generic governing equations could be derived and are as shown in Eq. 3.5 and Eq. 3.6 for current and voltage respectively. Similarly, from the equivalent circuit model (Fig. 3.34), the equation for measured output voltage (V_{fp}) from the flux pump experiment, for the similar configuration, conducted later to Gen 2a experiments in this work has been formulated as in Eq. 3.7 (Bumby *et al.*, 2016).

$$V_{fp} = V_{oc} - IR_d \quad (3.7)$$

where I is the current flowing in the circuit.

The evolution of the current described as in Eq. 3.8.

$$I = I_o \left(1 - e^{-\frac{(R_d + R_c)t}{L}} \right) \quad (3.8)$$

where t is the time since the flux pump started operating and I_o as in Eq. 3.9,

$$I_o = \frac{V_{oc}}{R_d + R_c} \quad (3.9)$$

Eq. 3.8 assumes that $I < I_{coil}$, the coil current. The voltage across the coil can be expressed similarly, as in Eq. 3.10,

$$V_{coil} = V_{oc} \left(e^{-\frac{(R_d + R_c)t}{L}} \right) \quad (3.10)$$

From Eq. 3.9, it has been inferred that the total resistance of the circuit limits the maximum current that can be injected into the coil during flux pump operation, $R_c + R_d$. The joint resistance R_c is obtained from the decay time constant, (L/R_c) of the current in the circuit once the flux pump has been turned off (as both R_d and V_{oc} are zero when there is no oscillating applied field).

For Gen 1 and Gen 2a flux pump, the joint contact resistances were $0.96 \mu\Omega$ and $1.1 \mu\Omega$ respectively and were stable over multiple cooling-warming cycles. Considering the output voltage of the flux pump as a function of current, the ramping response of flux pump discussed in sections, can be, clearly understood. V_{oc} is the open-circuit voltage and obtained from x-intercept and R_d from the gradient of each curve. As R_d varies with the frequency it can be, considered as the hysteretic loss (Oomen *et al.*, 1999; K. Ogasawara *et al.*, 1976; R. C. Duckworth *et al.*, 2011).

3.8.1 I-V curves

The gradient of the I-V curves provides the value of dynamic resistance and the value of the dynamic resistance is proportional to the operating frequency. The I-V curves for Gen 1 are shown in Fig. 3.35.

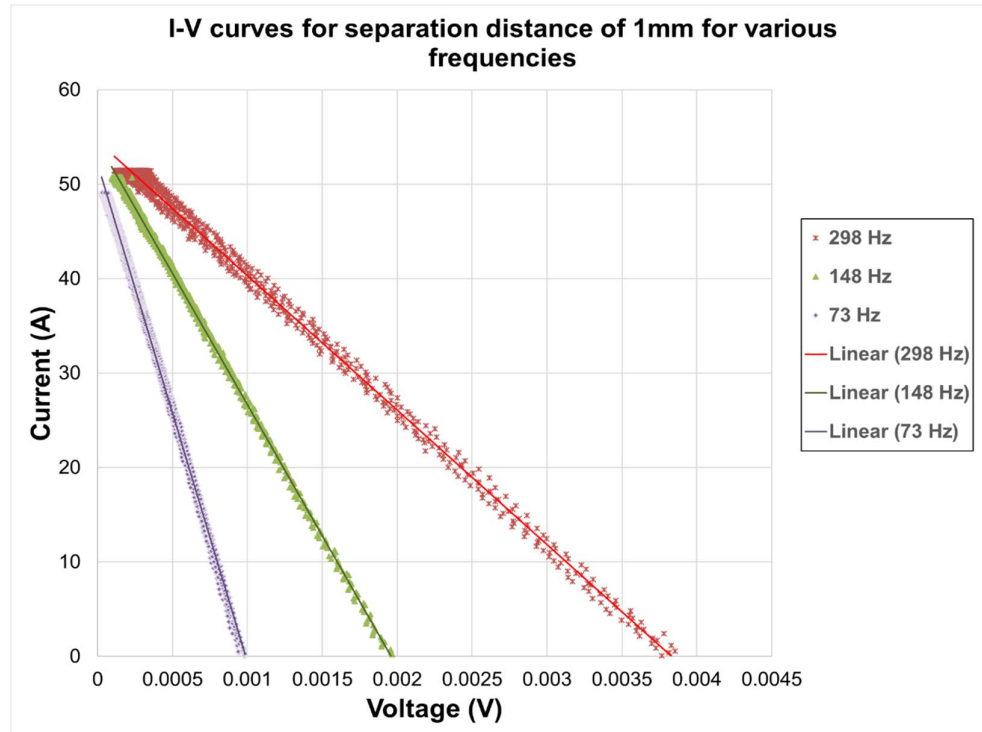


Fig. 3.35 I-V Curves of Gen 1

Along the same lines as Gen 1, the I-V curves obtained for Gen 2a flux pump are as shown in Fig. 3.36. Bumby *et al.*, have reported similar curves after further experimentation with the warm rotor flux pump and reproduced in Fig 3.37 for comparison. The intercept of each line on the y-axis of Fig. 3.35 and Fig. 3.36 gives the short-circuit current, I_{sc} can be mathematically put up as in Eq. 3.12.

$$I_{sc} = V_{oc} / R_d \quad (3.12)$$

I_{sc} represents the maximum current that the flux pump is capable of delivering to a fully superconducting circuit for which $R_c = 0 \Omega$. It is seen that for each fixed flux gap, I_{sc} is approximately independent of operating frequency. This is a general characteristic of HTS rotating flux pumps (Jiang *et al.*, 2014; Bumby *et al.*, 2016), which reflects that both V_{oc} and R_d are approximately proportional to the operating frequency, such that this dependency cancels in Eq. 3.12.

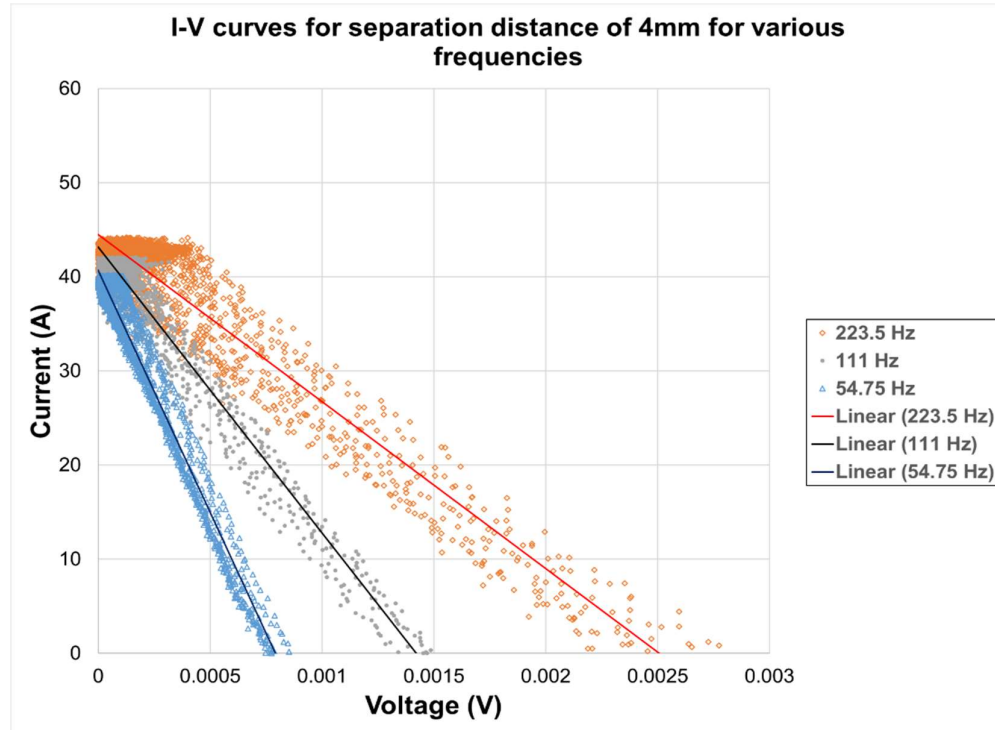


Fig. 3.36 I-V Curves of Gen 2a

One of the important findings in the works on Jiang *et al.* and Bumby *et al.* is the equivalent circuit model and deduction on dynamic resistance which is discussed briefly in the next section. The dynamic resistances for the corresponding frequencies from the I-V curves shown in Fig 3.37 are tabulated in Table. 3.3.

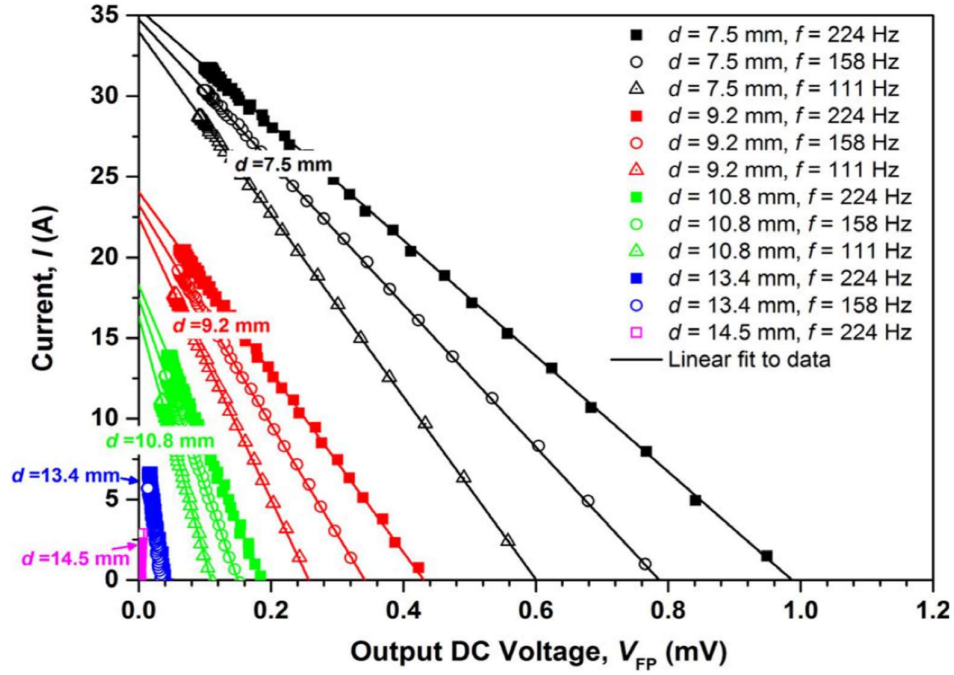


Fig. 3.37 I-V curves of flux pump experiment with Gen 2a test rig (Bumby *et al.*, 2016).

Table. 3.3 Gen 2a Frequency versus dynamic resistance for the separation distance of 7.5 mm calculated from Fig. 3.37 (Bumby *et al.*, 2016).

| Operating Frequency (Hz) | Dynamic resistance ($\mu\Omega$) |
|--------------------------|------------------------------------|
| 224 | 28.5 |
| 158 | 22.5 |
| 111 | 17.1 |

3.8.2 Dynamic Resistance

Dynamic resistance is a loss due to hysteresis caused by the interaction of the oscillating magnetic field applied by the rotor magnet with a DC transport current in the stator wire (Oomen *et al.*, 1999; Ogasawara *et al.*, 1976; Duckworth *et al.*, 2011). Table. 3.4 gives the dynamic resistance of Gen 1 flux pump at the corresponding operating frequencies obtained from the plots in Fig. 3.35. The values are in accordance with the values calculated from the plots in the work reported by Bumby *et al.*, (Table. 3.3).

Table. 3.4 Gen 1 Frequency versus dynamic resistance for a separation distance of 1 mm

| Operating Frequency (Hz) | Dynamic resistance ($\mu\Omega$) |
|--------------------------|------------------------------------|
| 298 | 69.1 |
| 148 | 36.3 |
| 73 | 17.9 |

The dynamic resistances of Gen 2a obtained from Fig. 3.36 for the corresponding frequencies are tabulated in Table. 3.5.

Table. 3.5 Gen 2a Frequency versus dynamic resistance for a separation distance of 4 mm

| Operating Frequency (Hz) | Dynamic resistance ($\mu\Omega$) |
|--------------------------|------------------------------------|
| 223.5 | 55.6 |
| 111 | 31.1 |
| 54.75 | 16.7 |

Fig. 3.38 gives the plot of dynamic resistances of Gen 1 and Gen 2a flux pump against frequency.

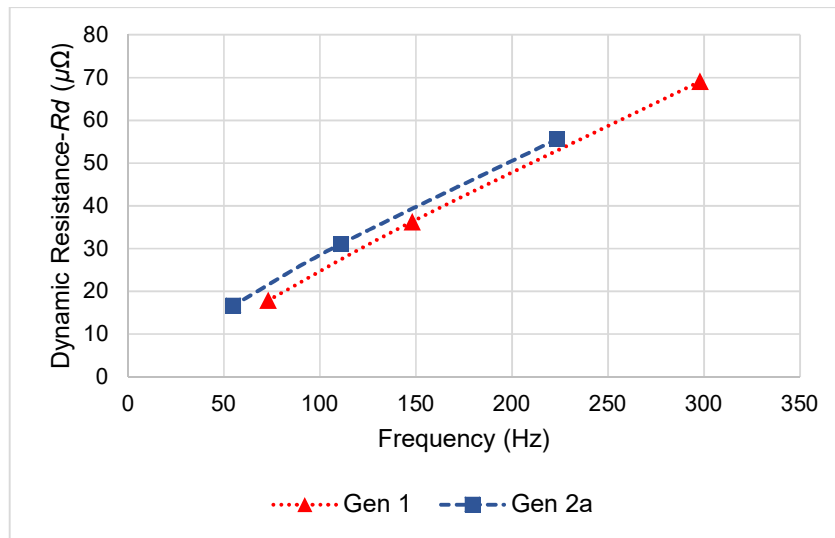


Fig. 3.38 Dynamic resistance versus frequency

The magnitude of dynamic and contact resistances are of the $\mu\Omega$ range and from the range of frequencies at which the flux pump will be operated, it can be said that the increase in dynamic resistance is not significant. Hence, for simulation purpose, the dynamic resistance and the contact resistance of the flux pump together can be lumped as source resistance of the flux pump. For a distance $>12\text{mm}$ it is suitably assumed as $10 \mu\Omega$ for the FEM simulations, though this magnitude of resistance does not affect the field pattern or the harmonic performance of the model, it is factored in to make the model more practical.

3.9 Comparative performance analysis of Gen 1 and Gen 2a

The experiments conducted using two different configurations of flux pump gave a good understanding of the working of the flux pump. The experimental study also formed the basis to analyse the suitability of flux pump to excite the field windings of a synchronous generator with an HTS rotor. The rate of rise of current and the current oscillations are important parameters to assure a stable field in the rotor of the generator. A stable field is one of the pre-requisite to ensure lesser THD.

The following Table. 3.5 gives a comparison of Gen 1 and Gen 2a current ramp up rates at different frequencies for the same distance of 4 mm with Gen 1 and Gen 2a flux pumps, the observations are expected to provide guidelines for practically implementable distances considering the cryogenic insulation.

Table. 3.6 Gen 1 and Gen 2a current ramp up the comparison for a separation distance of 4 mm.

| Gen 1 (without ferromagnetic yoke) | | | Gen 2a (with ferromagnetic yoke) | | |
|---|----------------------------|------------------------|---|----------------------------|----------------|
| Frequency (Hz) | Current Ramp up rate (A/s) | Time to reach 95 A (s) | Time to reach 95 A (s) | Current Ramp up rate (A/s) | Frequency (Hz) |
| 598 | 0.013 | 7307 | 237 | 0.4 | 448.5 |
| 298 | 0.0071 | 13380 | 447 | 0.2125 | 223.5 |
| 148 | 0.0048 | 19792 | 678 | 0.14 | 111 |

With the use of ferromagnetic core on the stator, the improvement in the ramp-up rate is significantly high (~28 times) than without a ferromagnetic core. However, the presence of a ferromagnetic core on the stator side of the flux pump

will increase the thermal mass of the HTS rotor and causes additional heat loss due to eddy current and hysteresis.

The time required for Gen 1 and Gen 2a flux pumps to achieve 95 A (the rated current of 10 kW HTS proof-of-concept prototype) is shown in Table 3.6. From linear extrapolation, the ramp up time for a flux pump configuration having the geometry and orientation of magnets as in Gen 2a flux pump and no ferromagnetic core on the stator side as in Gen 1, for a separation distance of around 12 mm, the time required would be ~ 20 to 24 hours.

The 20 to 24 hours' time required to ramp up to the rated current will also aid in slow cooling of the flux pump and HTS rotor set up. Thus, this configuration would be the best-suited flux pump configuration for integration with a synchronous generator. The optimisation of geometry and orientation of magnets form a basis for a further detailed study on improvement of flux pump performance and are out of the scope of this thesis.

3.10 Concluding Remarks

The rate of rise of current varies directly with the frequency of excitation in cold rotor flux pump and warm rotor flux pump. The saturation current in both the cases varies inversely with the distance of separation. An optimal frequency of operation would be an ideal way to minimize the peak to peak value of ripple current and calls for further experimentation.

Despite the reduction in the maximum output current, at increased flux gaps, in the warm rotor flux pump, the device is still capable of injecting current into the experimental circuit at wall thickness distance $d > 10$ mm. The result is significant because the mechanical strength and thermal performance of a composite cryostat wall are closely related to its physical dimensions. Wall thicknesses of more than 7.5 mm allow space for vacuum insulation in a G-10 composite cryostat wall.

In the case of the warm rotor flux pump, practical values of stator currents for an HTS application are achieved at higher separation distances. The reason is the presence of a ferromagnetic yoke on the stator side of the flux pump which causes flux concentration. In an HTS application, the presence of a heat source in the system or surroundings is to be avoided as much as possible to reduce the load on the cryogenic system.

The presence of a ferromagnetic yoke will lead to additional heat in the system due to eddy current and hysteresis. G-10 can be used as an alternative to the ferromagnetic yoke. G-10 is a composite of epoxy and fibreglass. It does not carry electrical current at all and for the most part has lower thermal conductivity (Van Sciver, 2012). Due to its lower thermal conductivity, G-10 is a suitable material for cryogenic applications. Another source of heat in the surroundings is the ferromagnetic yoke of the stator of the generator, conventionally used in the

synchronous generator. Using a non-ferromagnetic yoke (G-10) material as the stator of the generator would resolve the issue.

Unlike a stable DC excitation, the anomalous nature of the voltage excitation, as shown in Fig. 3.14, would lead to fluctuations in the flux pump stator current and would lead to changes in the field. The change in the field would reflect in the voltage generated by the synchronous generator. The effects of flux pump stator side ferromagnetic yoke, on the rate of rise of current and ripple current are analyzed.

A FEM based study to analyze the effect of the flux pump and other stator design considerations is discussed in chapters 5 and 6 of the thesis. As the plan is to use the flux pump technology for an HTS synchronous generator with a wind turbine, the quality of power would not be good if there is no stable field in the rotor coils and would need a customized power converter to make it usable, which may not be economical, else, with sufficient experimental and analytical proofs, it has to ensure that this would not be necessary. An analytical study based on FEM is conducted and is reported in the subsequent chapters of the thesis.

Chapter 4. Finite Element Modelling

4.1 Introduction

The research work involves analysis of a rotating electrical machine and the effect of a pulsating flux pump excitation on the performance of the machine. This chapter describes the advantages of Finite Element Analysis-modelling and simulation that needs to be carried out in order to, achieve the objectives of the research.

ANSYS MAXWELL and RMxpert software package are chosen, to carry out FEA. ANSYS MAXWELL is the premier electromagnetic field simulation software for engineers tasked with designing and analysing 2-D and 3-D electromagnetic and electromechanical devices, including motors, actuators, transformers, sensors and coils. MAXWELL uses the accurate finite element method to solve static, frequency-domain, and time varying electromagnetic and electric fields.

A key benefit of ANSYS MAXWELL is its automated solution process, which requires one to specify only the geometry, material properties and desired output. From this point, MAXWELL automatically generates an appropriate, efficient and accurate mesh for solving the problem. This proven automatic adaptive meshing process removes complexity from the analysis process, giving out a highly efficient, easy-to-use design flow.

ANSYS MAXWELL generates high fidelity, reduced-order models from the finite element solution for use in ANSYS Simplorer, a multi-domain system simulation software. This advanced functionality creates a powerful electromagnetics-based design flow that combines complex circuits with accurate

component models to design complete, high-performance electromechanical, mechatronic and power electronic systems.

ANSYS MAXWELL Circuit Editor is used, to implement the load circuit and the load circuit can be integrated as a part of excitation with the ANSYS MAXWELL model. The output of the simulation is stored as .csv file, which can be analysed in MSExcels and MATLAB conveniently (MAXWELL 3D and 2D Help Manuals, support.ansys.com).

4.2 Basic Modelling

Basic modelling was carried out to understand the flux interaction between a permanent magnet and a stator wire (HTS tape- built in perfect conductor model) with a ferromagnetic core on the HTS stator (Fig. 4.1), and was analyzed to understand the flux interaction between different surfaces in MAXWELL. The observations were as per the expectation and a simulation on permanent magnet synchronous generator was carried out to understand the transient magnetic analysis with rotation.

4.2.1 Magnet and Stator wire

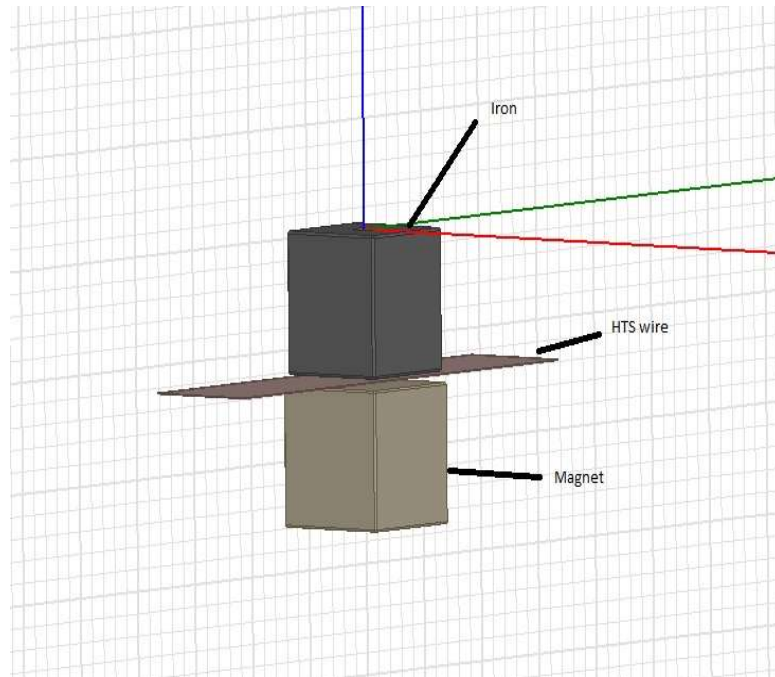


Fig. 4.1 Magnet and Ferromagnetic Yoke

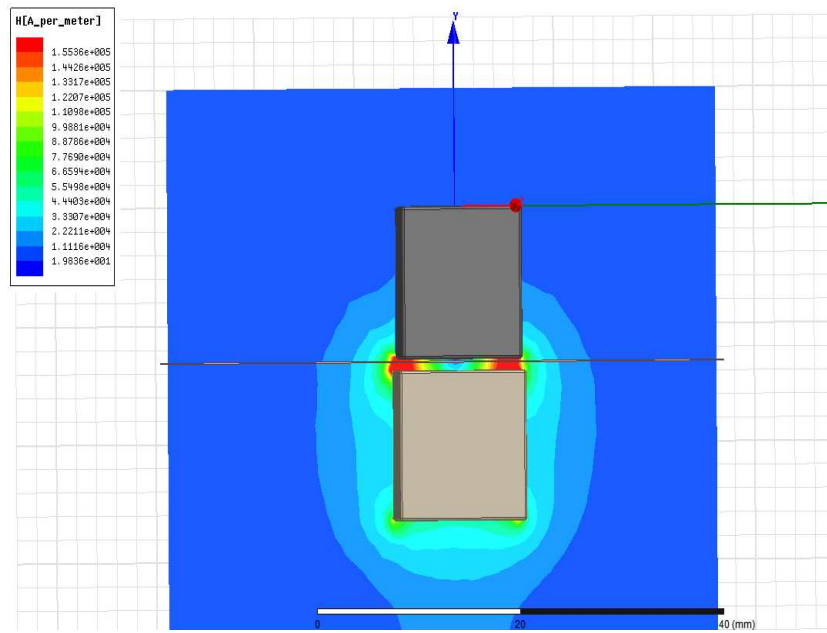


Fig. 4.2 Flux Interaction

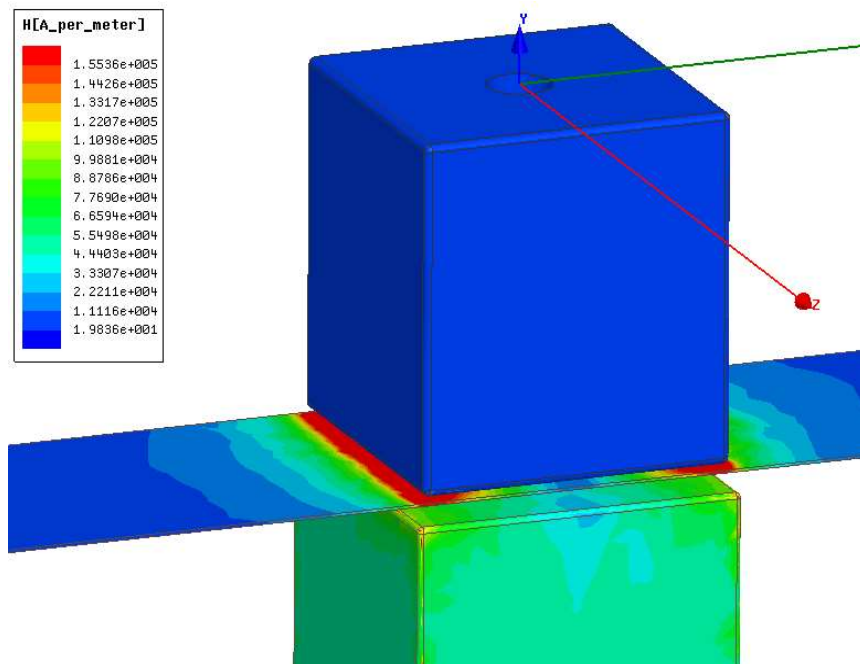


Fig. 4.3 Flux Interaction-Magnified view

Observations:

Presence of a ferromagnetic yoke, on the other side of the HTS tape, causes flux concentration. And as expected the flux lines are fringed at the edges and corners (see Fig. 4.2 and 4.3), this type of interaction with a Type II HTS tape is expected to create a field sufficient to drive the local points on the tape into mixed state thus causing flux pinning and driving a steady state current through the HTS tape.

If a coil made out of the Type-II HTS tapes and mounted as the field system of a generator, then a mechanically rotating flux pump with permanent magnets on the rotor could be, conveniently used, to excite the field system of the generator. However, the presence of a ferromagnetic yoke in the system will also cause additional losses in the form of eddy current and hysteresis.

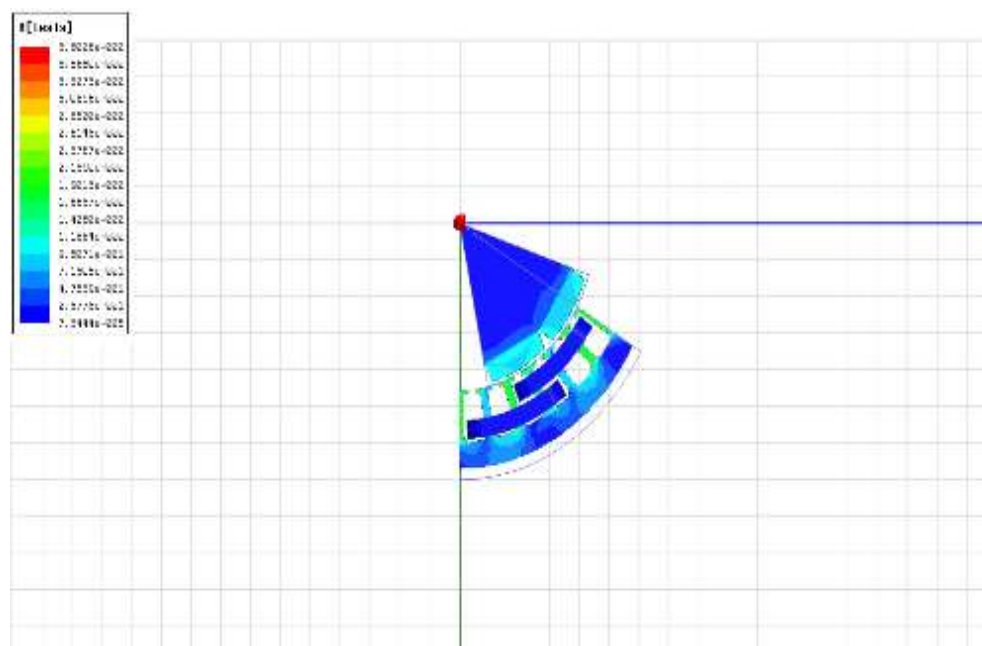
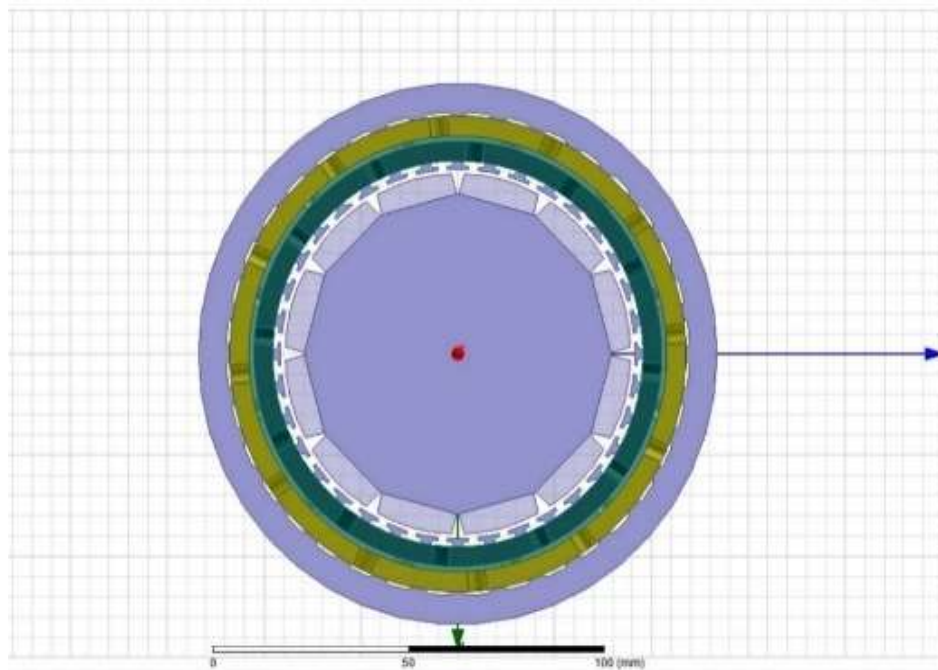
Alternatively, keeping all the geometry of the flux pump similar to Gen 2a flux pump, an air cored stator yoke will avoid the concern of eddy current and hysteresis. This thesis further investigates on the issues around the usage of non-ferromagnetic stator material.

4.2.2 Permanent Magnet Synchronous Generator

A 12-pole permanent magnet generator model was developed, to understand, the meshing and solution set up method for analysing the voltage profile on the stator conductors of the generator. The model was developed based on a document of North Arizona University, the model creation acted as precursor to the analysis of the actual 10 kW HTS generator model development and simulation. A FEM model (Fig. 4.4 and Fig. 4.5) of the Southwest Windpower Air-X generator was created and the results obtained were compared with the results provided in the NAU document (Fig. 4.6 and 4.7). The outputs were identical and hence verified the correctness of the simulation process.

For machine parts, ANSYS-RMxpert is used and for Electromagnetic modelling- ANSYS MAXWELL was used. The model was reduced to a pie section as the geometry is symmetric and the symmetric boundary conditions were used (Master and Slave). With the integration of RMxpert with ANSYS the development of rotating machine models in ANSYS is more flexible.

In MAXWELL 3D, common rotor and stator models created in RMxpert are through the user defined parameters, which are then to be custom designed geometrically and materials assigned as per the application.



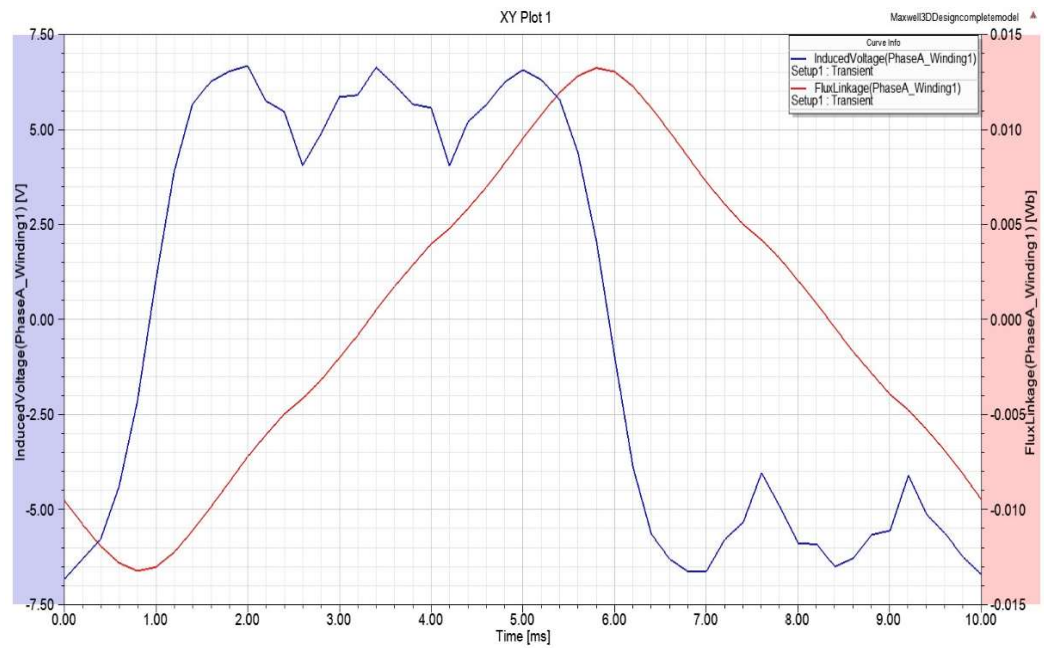


Fig. 4.6 Voltage and flux linkage output plots of permanent magnet synchronous generator

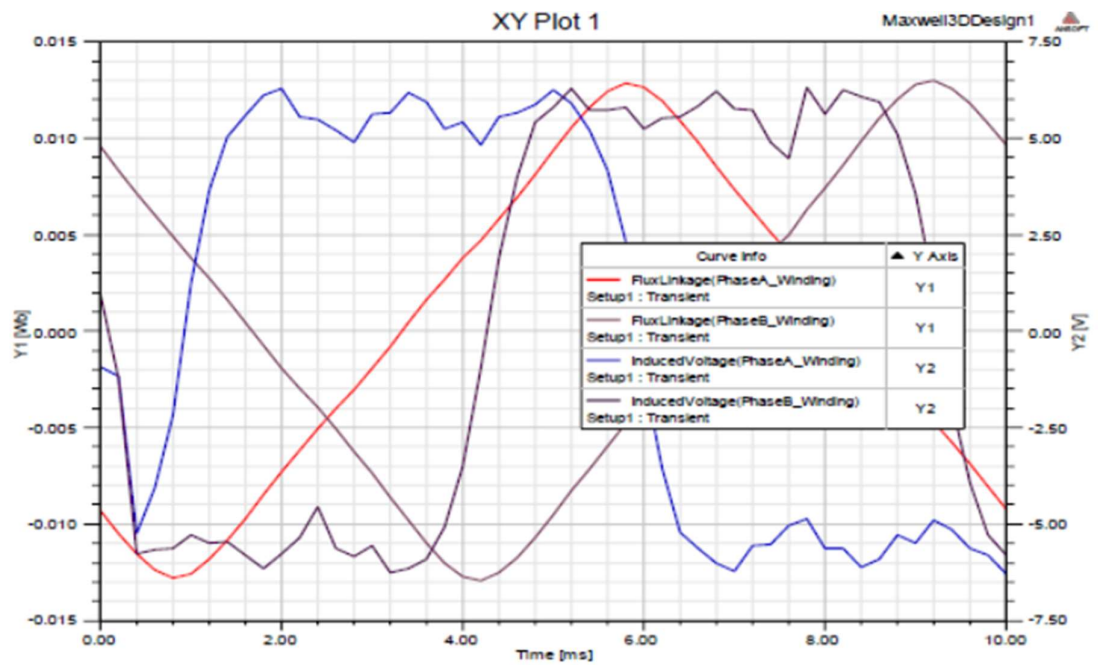


Fig. 4.7 Output from the reference document

4.2.3 Salient Pole Synchronous generator model

In order to understand the modelling and simulation associated with current and voltage excitations for the field windings of a generator, a salient pole synchronous generator model was developed and simulated. The steps of simulation were same as for the permanent magnet generator discussed in section 4.2.2. The only difference was that the field was generated using a field coil with current or voltage excitation instead of a permanent magnet.

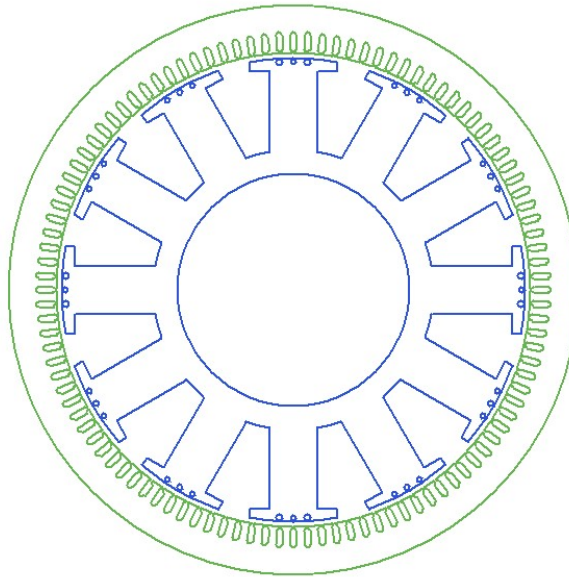


Fig. 4.8 RMxpert model

The dimensioning was followed from a verified work at hydroelectric generator group at Uppsala University, Sweden (Persarvet, 2011). Simulations carried out on the new model (Fig. 4.8). Once the model was verified, for its designed performance, the field winding dimensions were changed to HTS field winding data in RMxpert (Table 4.1).

The model was then, converted to ANSYS MAXWELL model using the inbuilt function in ANSYS. The results for the conventional design were as expected and verified the correctness of the modelling methodology.

RMxpvt model setup quantities:

Table 4.1. 20kVA model setup quantities

| Setup quantities | Value |
|----------------------|-------------|
| Operation type | Generator |
| Operation load | Independent |
| Rated apparent power | 20 kVA |
| Rated voltage | 155.5 V |
| Rated speed | 500 rpm |
| Rated power factor | 0.9 |

The RMxpvt model was converted to ANSYS MAXWELL 2D model and the section of the model thus obtained is shown in Fig. 4.10. The open circuit voltage on the stator conductors was recorded for 3 different types of excitations.

1. Field winding excitation declared as a current excitation with a DC current of 14.484 A. The induced voltage on Phase A is shown in Fig. 4.11
2. Field winding declared as a voltage excitation with source resistance ($R_d=10\ \mu\Omega$ assumed) and zero inductance, with a DC voltage of 65 mV (assumed). The induced voltage on Phase A in this case is shown in Fig. 4.12

3. Field winding declared as a voltage excitation with source resistance ($R_d=10\mu\Omega$, assumed) and inductance ($L=100\text{mH}$ assumed) with a 240Hz FP excitation defined as the dataset. The induced voltage on Phase A in this case is shown in Fig. 4.13.

Fast Fourier Transform (FFT) and Total Harmonic Distortion (THD) calculations were carried out on the induced phase voltage.

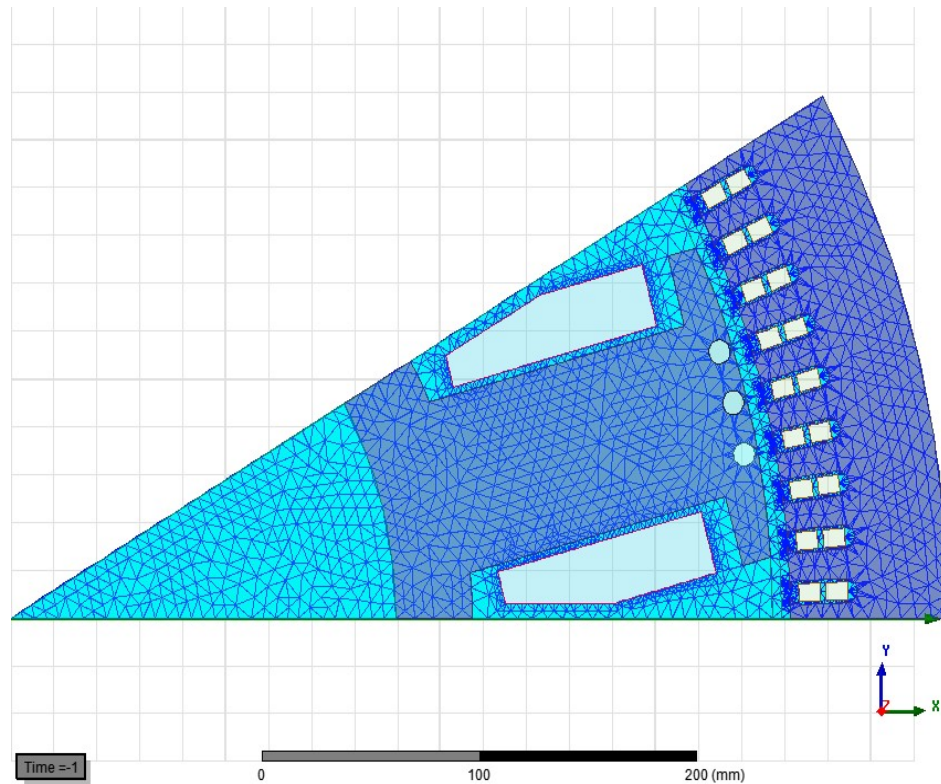


Fig. 4.10 ANSYS MAXWELL 2D model of the 12-pole generator developed using RMxpert.

Voltage plots:

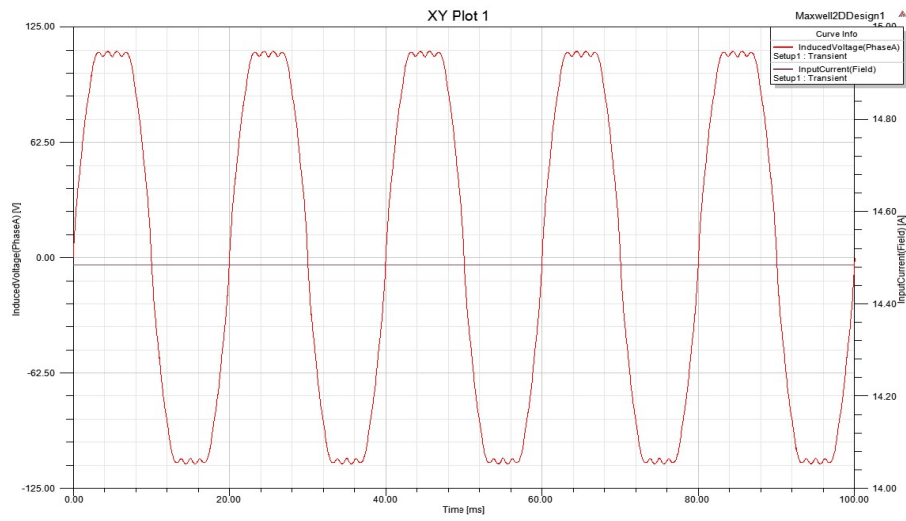


Fig. 4.11 Phase A voltage and field current profile with a DC field current excitation of 14.484A

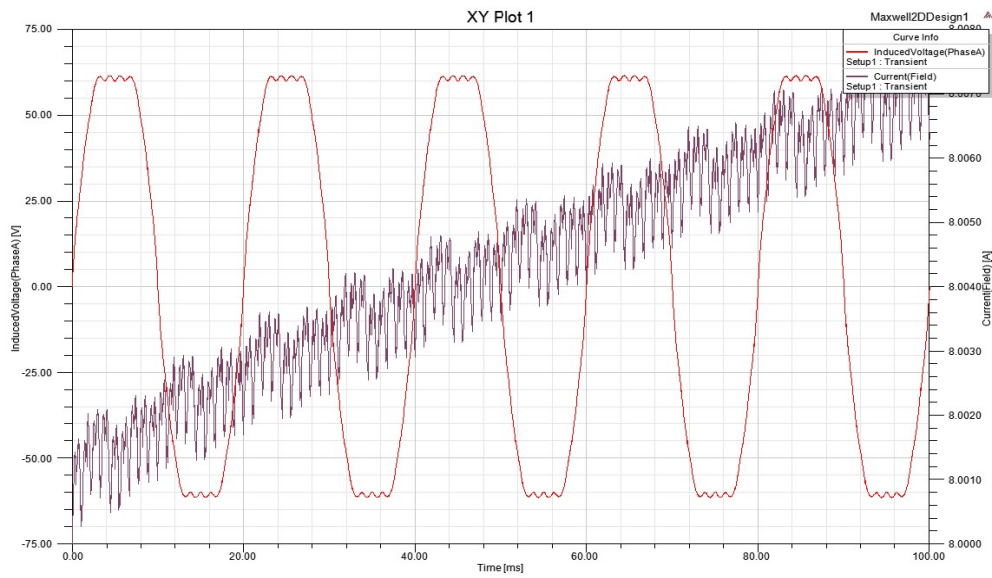


Fig. 4.12 Phase A voltage and field current profiles with a DC voltage excitation of 65mV.

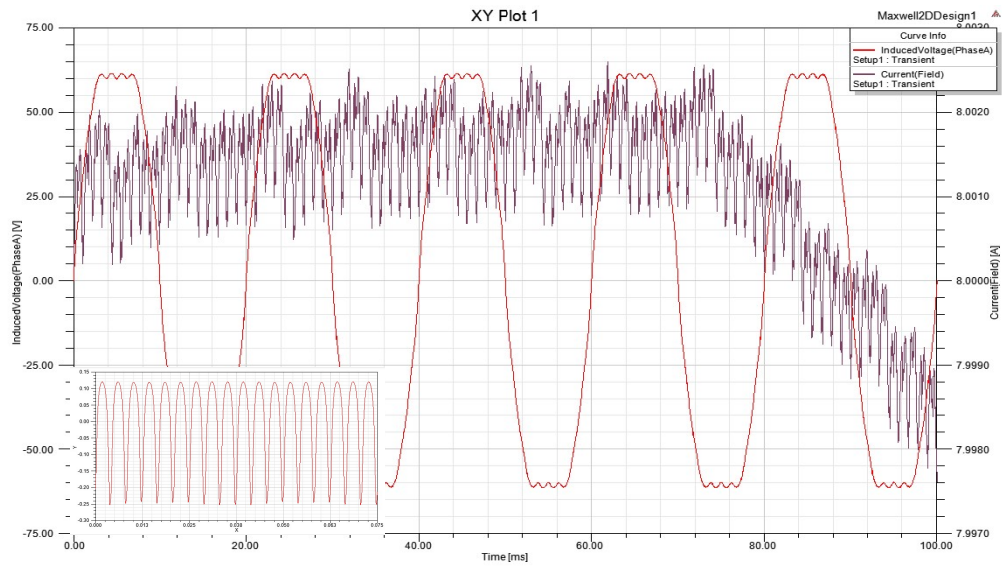


Fig. 4.13 Phase A voltage profile and Field current profile with 240 Hz FP excitation (inset figure)

Table 4.2 Comparison of THDs for the conventional design

| Type of excitation | THD (%) |
|---------------------|---------|
| Current | 13.739 |
| Voltage (DC) | 13.745 |
| Voltage (Flux pump) | 13.749 |

As per standards, THD for a generator is to be within 5% (Ref: IEC:60034-1), the observed value for all types of excitations was found to be at 13.7% the predominant reasons for this were:

1. The absence of damper winding
2. Pole dimensions, which needed further refining.

However, the need for damper windings can be however ignored at this stage, as the proof-of-concept 10 kW HTS generator with flux pump integration is set to have a non-conventional design without the need of conventional damper windings. The pole dimensions also are of no much concern as, G-10 is found to be a suitable pole structure material and it being non-ferromagnetic does not affect the magnetic flux distribution. The drop in the field current was also observed by limiting the excitation until 75 ms (Fig. 4.13).

4.3 Observations

ANSYS MAXWELL along-with RMxpert and MAXWELL Circuit Editor was used for simulations. From the simulation-results, of the basic model, AirX generator model and the salient pole synchronous generator model, it was found that type of meshing and size of mesh element have significant effect on the resolution of the outputs. If the field parameters are not well resolved or if are calculated at the mesh element boundaries, result in sharp transitions in the output. In order to avoid the sharp transitions, time stepping of the analysis and the mesh element sizing have to be carried out in correlation to each other and were considered for in the subsequent simulations.

The time stepping of the analysis determines the smoothness and resolution of the outputs. The time stepping needs to be in accord with the meshing transitions failing which additional spikes are introduced into the output profiles and call for additional normalization to nullify the effect. The % THD values for different types of excitation for the conventional synchronous generator are approximately same, thus justifying that the pulsating flux pump excitation will not have any adverse effect on the harmonic performance of the conventional generator. However, the modelling and simulation for the non-conventional HTS generator with a hexagonal rotor has to be carried out to ascertain the conclusions. When the flux pump excitation is stopped there is linear decrease in the field current. Since the resistances in a flux pump integrated HTS generator would be of the order of $\mu\Omega$, the decay will be extremely slow and allows a possibility to implement band wise operation of flux pump similar to pulse width modulation technique, thus reducing the additional power required for the operation of flux pump.

Chapter 5. 10 kW HTS Generator

5.1 Introduction

The geometric modelling of 10 kW HTS generator was done in SOLIDWORKS and RMXprt. The geometric model included HTS rotor and flux pump stator integration components. The geometric model was converted to finite element model with the application of boundary conditions, meshing and analysis setup, these are discussed in subsequent sections.

5.1.1 Modelling and Simulation Methodology

The geometric modelling and ANSYS simulation methodology adopted in this research work are illustrated in Fig. 5.1. The various steps in the methodology are explained subsequently.

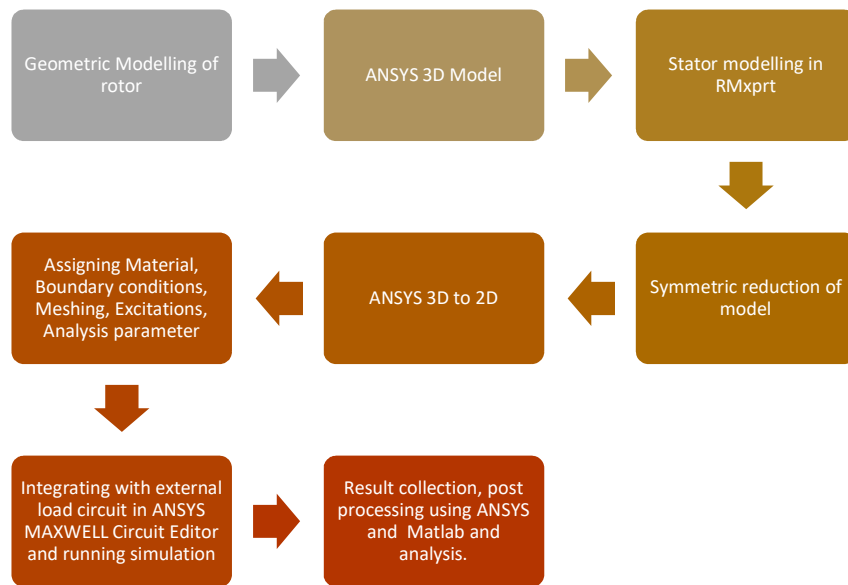


Fig. 5.1 Simulation Methodology-Flow Diagram.

5.1.2 Geometric modelling

The SolidWorks model of the HTS rotor with the flux pump integration is shown in the Fig. 5.2. The HTS rotor of the generator was designed by the research group at Changwon National University, South Korea. The stator for the HTS rotor was custom designed and modelled using the User defined primitives option available in RMxpert, by the author. The geometric design details are provided in the Appendix-D. Simulations were conducted on the FEM model.

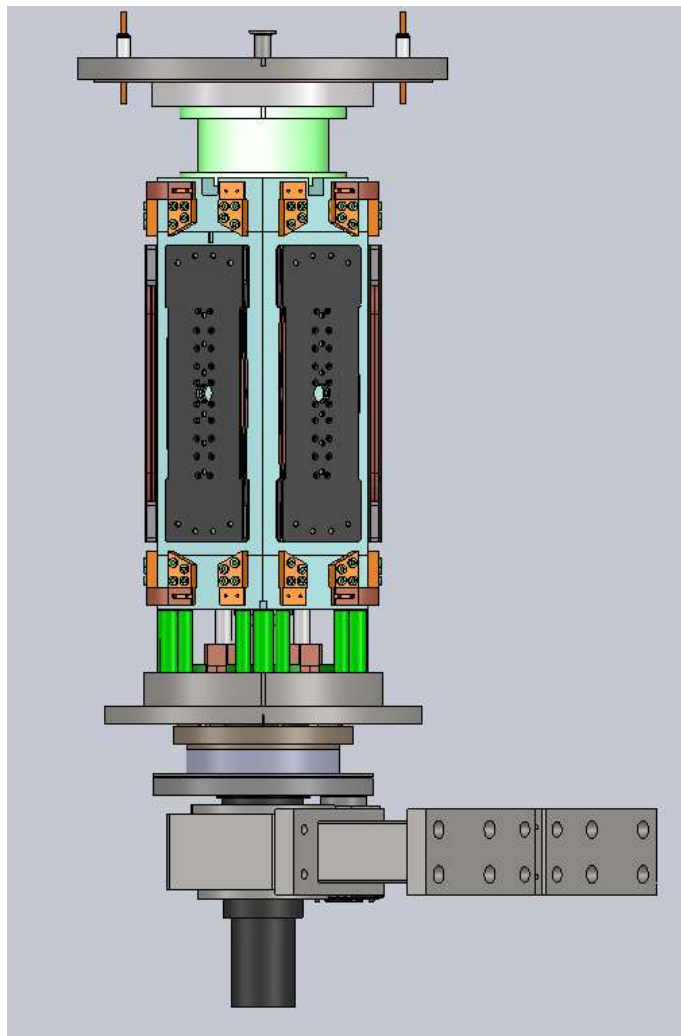


Fig. 5.2 Model of the HTS rotor with flux pump integration ANSYS 3D model

FEM 3D model of the rotor was created by importing the simplified rotor from the SOLIDWORKS model of the 10 kW HTS generator. As the aim of the simulation study revolves around the harmonic performance and stator design, the parts relating to the flux pump integration were suppressed.

5.1.3 Stator modelling

The stator modelling was done in ANSYS by using the User Defined Primitives feature available in RMxprt. The stator yoke dimensions and the stator conductors were set to attain the rated values of the machine. The 3D FEM ANSYS model is shown in the Fig. 5.3.

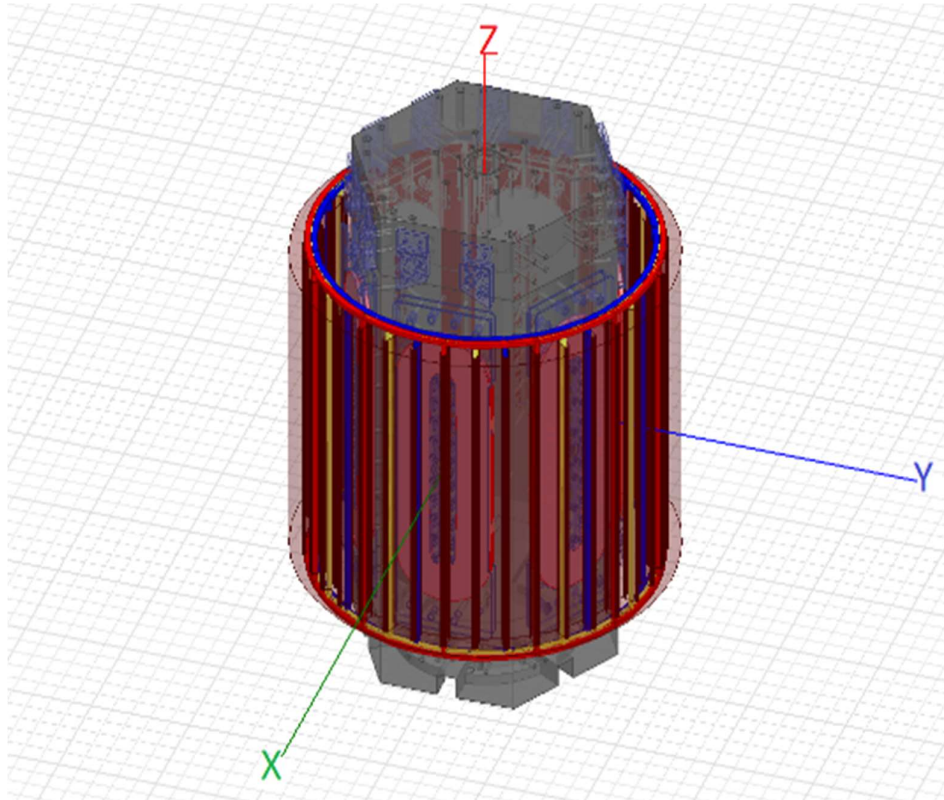


Fig. 5.3 HTS Generator-ANSYS Model.

5.1.4 Symmetric Reduction

The rotating electrical machine is symmetric; therefore, the machine model could be reduced to a pie-section to reduce the computation time and the output for the entire system can be obtained using the symmetry multiplier option in ANSYS. The reduced pie-section of the generator model is shown in Fig. 5.4.

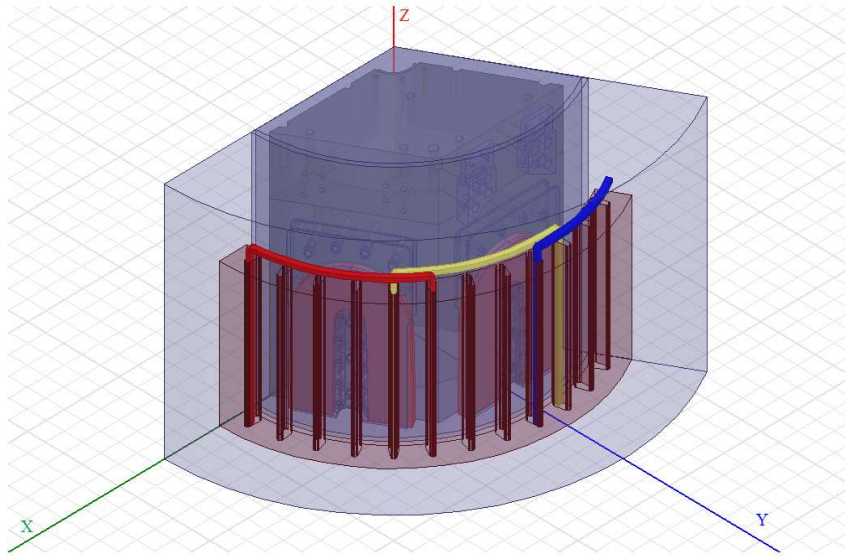


Fig. 5.4 ANSYS MAXWELL 3D FEM pie model of HTS generator.

5.1.5 ANSYS 3D to 2D

In the simulations carried out on the basic models, it was observed that the simulation time for the 3D models took significantly long time. Even with the reduced pie section model, it was observed that the simulation time for an averagely fine mesh and reasonable time step, was of the order of 6 to 7 hours. In order to reduce the simulation time, it was found that converting from 3D to 2D would be a feasible option. The 2D converted model of 3D pie section is shown in Fig. 5.5.

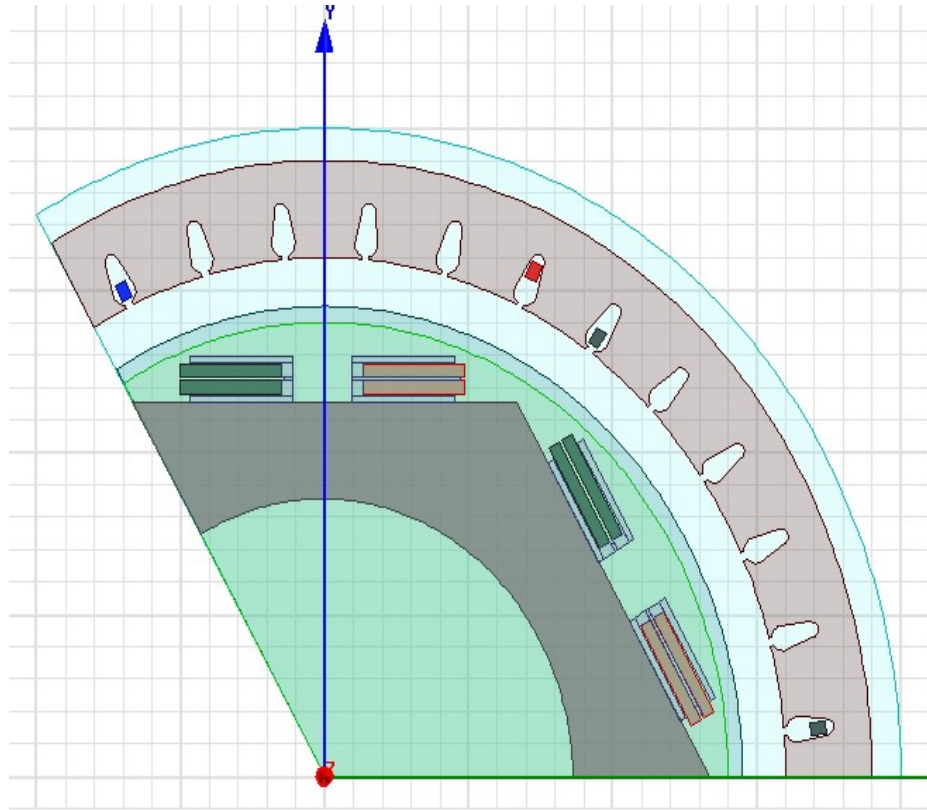


Fig. 5.5 2D Model of the Pie section.

5.1.6 Properties Assignment

Material assignment: ANSYS has a huge range of material repository and can be used for assignments to different parts of the model. There is also a provision for manually entering the values of specific parameters for the material, like conductivity, density *etc...*

Boundary condition assignment: As discussed in section 4.2.3, there is provision for various boundary condition assignments based on the type of Magnetic field and the analysis to be carried out. For 2D transient analysis and the rotational symmetry, Vector Potential and Master-Slave boundary conditions are assigned to the model.

Meshing: Length based meshing was used for the 2D model. A fine mesh was created in critical field parts of the system like rotor coils, stator conductors and in the air gap.

5.1.7 Excitation assignment

The excitations are to be assigned to the parts, which act as sources of electromagnetic, or electric fields. The voltage signals collected as outputs in the flux pump experiments and shown in section 5.2.2 were given as external voltage signal excitation using the ‘External’ excitation property in ANSYS. The stator conductors were integrated to the external circuit through the external circuit integration using MAXWELL Circuit Editor.

5.1.8 Result Collection

The field plots and the rectangular plots can be conveniently, either plotted in ANSYS or exported in .csv format for custom plotting in MSExcel for THD analysis and comparative analysis.

Post processing: FFT plotting and THD analysis of the stator induced voltage is carried out using MATLAB, the .csv exported values from ANSYS were used as inputs. The plotting was done using Origin and MSExcel.

5.2 FEM study of HTS generator

In this section, FEM based study on the performance of a 10 kW proof-of-concept HTS generator, integrated with flux pump to excite the field is reported. From experimental studies discussed in Chapter 3, it is observed that the flux pump can be used to excite a DC current in the HTS windings. To implement the flux pump based excitation for a generator, it is essential that simulation-based system modelling, field analysis and harmonic analysis on the stator induced voltage are done to optimize the prototype design.

In order to accomplish the aforementioned objective, the field windings of the 2D model discussed earlier (see section 5.1.6) were excited at 3 different frequencies of flux-pump voltage excitations (60 Hz, 120 Hz and 240 Hz) modelled using the refined Gen 2a voltage profile shown in Fig. 5.9. Finally, steel and G-10 materials were used as stator yoke and the generator performance compared in terms of induced voltage and THD.

5.2.1 System Modelling

ANSYS MAXWELL provides a very flexible platform for the electromagnetic analysis of rotating machines. With the inclusion of RMXprt features into ANSYS, the analysis of the non-conventional designs becomes convenient and user-friendly compared to earlier versions of ANSYS.

A 10 kW HTS generator model was developed in SOLIDWORKS. A hexagonal rotor core with two layers of HTS racetrack coils per pole made the HTS rotor. The HTS field windings were connected in series. A ConCoil stator (concentric winding) with 36 slots was designed using RMXprt-User Defined Primitives to suit the HTS rotor assembly.

The other specifications of the machine are listed in Table 5.1.

Table 5.1. HTS Generator Parameters

| Rating | 10 kW |
|-----------------------------|--------------|
| Rated Voltage | 400 V |
| Poles | 6 |
| Speed | 300 rpm |
| Frequency | 15 Hz |
| Type of Rotor | HTS |
| HTS Winding | Racetrack |
| HTS Wire | SuNam |
| Coil Thickness | 35.25 mm |
| Turns in field coil | 235 |
| Rated field current | 98 A |
| Field current margin | 40% |

For harmonic analysis, the rotor assembly was simplified and the entire geometry was converted from MAXWELL 3D design model to MAXWELL 2D design model. Simulations were carried out on the 2D FEM model of the 10 kW HTS synchronous generator. For each frequency of excitation, the field values were recorded for every 10 ms and the rectangular plots of the induced voltages of all three phases were plotted and the results were also exported as .csv format files for post processing using MATLAB.

Mesh refinement in FEM analysis is critical - a very fine mesh results in longer simulation time and coarser mesh results in poorly resolved outputs. In Magnetostatics analysis, ANSYS adopts adaptive meshing technique and reaches the set resolution or the best refinement is achieved for a limited number of passes.

In the 3D transient analysis, when a band is assigned, a cylindrical mesh is automatically assigned to the gap between the moving and stationary surfaces whereas, in the 2D transient analysis, the mesh has to be defined by the user. Amongst the available meshing techniques, a trade-off is made in order to achieve reasonable accuracy within a practical period.

Length based mesh with an element size of 1 mm was chosen for field windings, stator conductors and air gap. Coarse mesh with larger element size was chosen for other parts (see Fig. 5.6). The FEM simulation parameters are tabulated in Table 5.2.

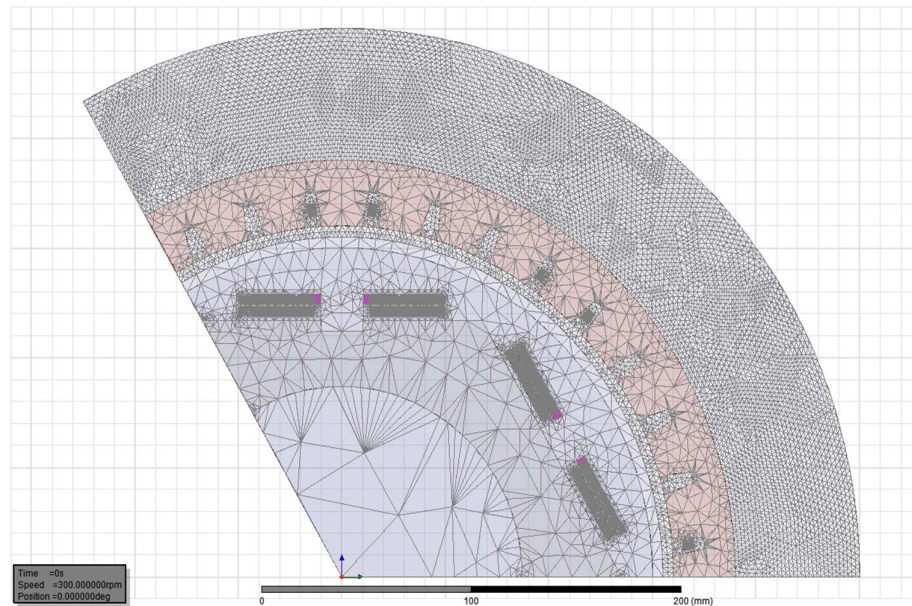


Fig. 5.6 Mesh plot of pie section of the 2D FEM Model.

Table 5.2. FEM Simulation Parameters

| | |
|------------------------------|--------------------|
| Boundary conditions | • Vector potential |
| | • Master-Slave |
| Mesh type | Length based |
| Analysis type | Magnetic transient |
| Time step | 0.0002s |
| Total simulation time | 750 ms |

5.2.2 Field Excitation Inputs

The voltage signals recorded as outputs in one of the flux pump experiments were provided as input to the field windings of the MAXWELL model. The voltage profile of Gen 1 flux pump is shown in Fig. 5.7. The non-zero average waveform results in a quasi-DC emf across the flux pump stator which could then be utilized to pump a DC current up to saturation levels of the Type II HTS stator. The HTS stators are soldered to the HTS rotor windings of the flux pump. The simulation output of induced voltage across the stator conductors was recorded as output. The induced voltage was analysed for the harmonic performance.

The voltage profile of Gen 2a flux pump is shown in Fig. 5.8. There was an unexpected distortion in the peak region of the waveform, which was then investigated and found to be a mechanical disorientation in the test-rig. The issue was rectified and measurement for one of the settings was carried out and the resulting voltage profile output is shown in Fig. 5.9.

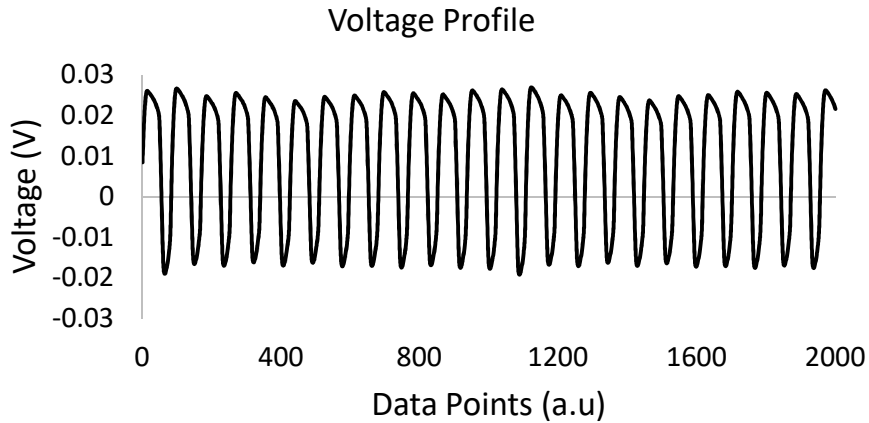


Fig. 5.7 Gen 1 FP Voltage output.

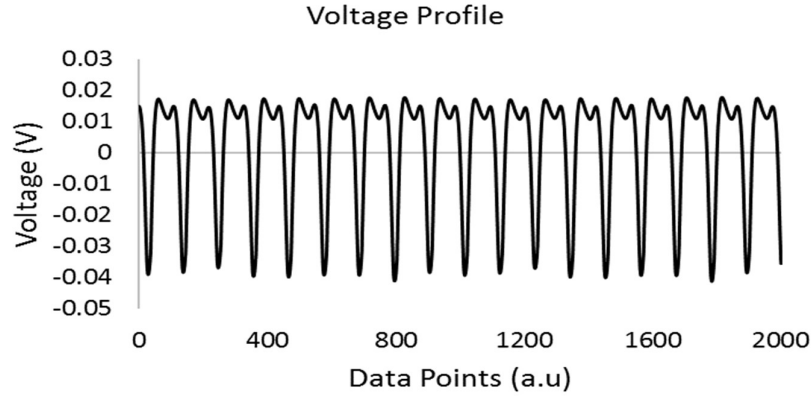


Fig. 5.8 Gen 2a FP Voltage output.

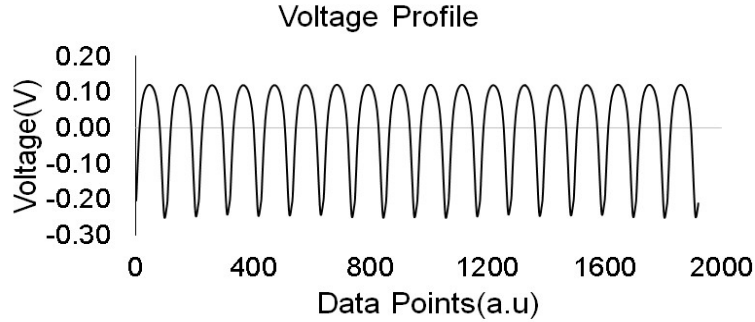


Fig. 5.9 Gen 2a FP Voltage refined output (Courtesy: Robinson Research Institute).

5.2.3 Performance analysis

A dynamic HTS flux pump is integrated with the HTS generator, such that it can be rotated in either direction to that of the field rotor of the generator. The advantage other than the minimization of thermal losses due to the absence of a physical link between cryogenic and non-cryogenic environment is the operation of flux pump intermittently. The operation can be called as a banded operation similar to the pulse width modulation of power converters. The operation can be described as follows; after initial ramp up to the rated field current, the flux pump is put out of operation and since the HTS rotor based field system has ultra-low resistance,

the decay in the field occurs slowly. The flux pump put into operation again, when the field current drops below a threshold value.

In the current simulation scenario, the flux pump is operated when the field current drops below 95 A, during the steady state operation. The frequency of excitation can be varied by controlling the speed of the flux pump rotor. The field windings in the FEM model were excited using the experimental data obtained from flux pump experiments. Since the desired frequency of generated voltage is 15 Hz, 3 different frequencies of flux pump excitation, 60 Hz, 120 Hz and 240 Hz, were used for exciting the field system.

The excitation windings in ANSYS were declared as voltage windings with the assumed flux pump dynamic resistance of $10\ \mu\Omega$. For these investigations, phase voltages were recorded as the output. The field calculations were carried out at an interval of 10 ms.

5.2.4 Field pattern analysis

The field pattern in the HTS generator is observed to be non-uniform and with a high fringing effect, reflected via the high field concentration on the stator of the machine (Fig. 5.10) along the corners of the HTS field coils.

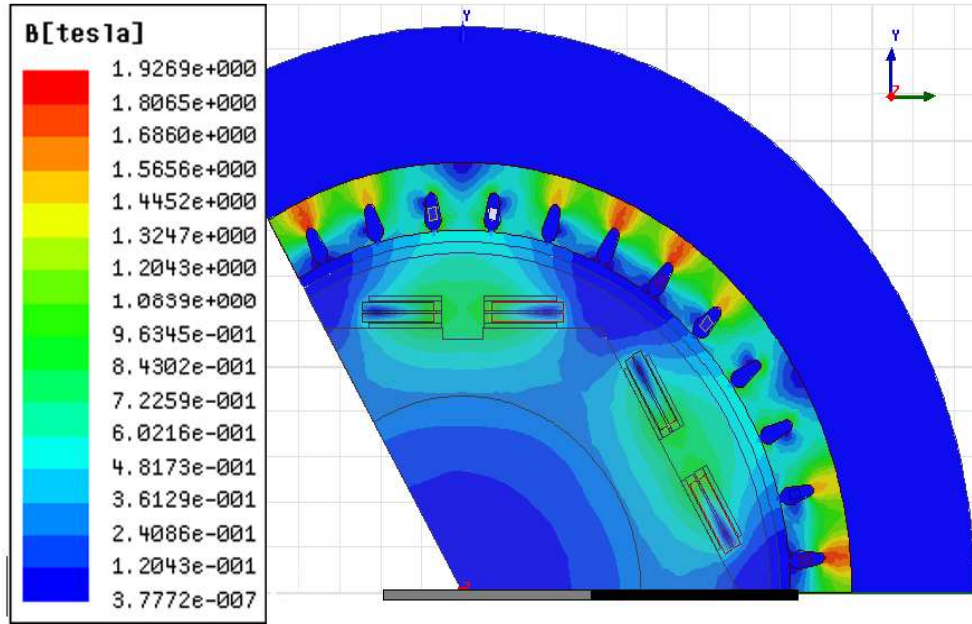


Fig. 5.10 Field pattern with ferromagnetic stator at $t = 0$ s.

The field strength at the centre of the field coil is ~ 1.2 T. Steel1008 material (properties have been provided in Appendix C) used for the stator frame acts as a flux concentrator but there will be hysteresis loss when a ferromagnetic material is used in the varying magnetic field. The field pattern at $t = 10$ ms (Fig. 5.11) also depicts the same fringing effect as observed at $t = 0$ s. The fringing effect is expected as there is no salient or non-salient ferromagnetic rotor pole structure to distribute the field uniformly. The ferromagnetic stator acts as flux concentrator and the field strength at the stator conductors will be higher than the field strength with a non-ferromagnetic stator. Though the ferromagnetic stator concentrates the flux and helps in reducing the number of stator conductors for a rated voltage, it increases the hysteresis loss. The transition from North-pole to South-pole or vice-versa for a particular stator conductor is sharp in the case of ferromagnetic stator than in the case of the non-ferromagnetic stator. The sharp transition manifests as distortion in the induced voltage profile.

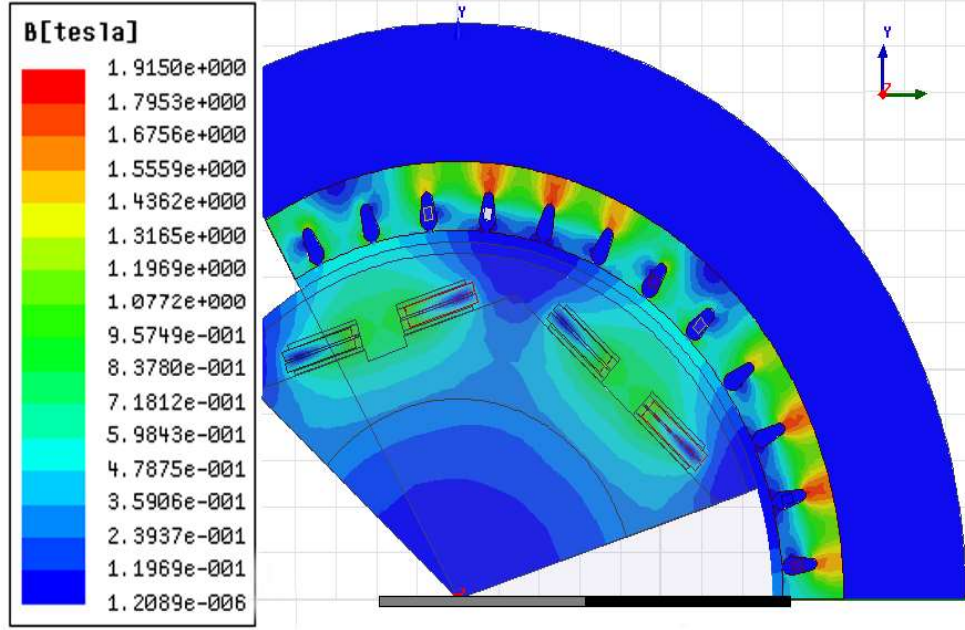


Fig. 5.11 Field pattern with ferromagnetic stator at $t = 10$ ms.

The hysteresis in the ferromagnetic stator increases the ambient temperature around the cryostat of the HTS rotor and increases the ambient thermal load on the cryogenic system. In order to avoid the hysteresis loss, a non-ferromagnetic stator can be used. Hence, to study the effects on the generator performance with a non-ferromagnetic stator, simulations were also carried out with G-10-FRP (Fibre Reinforced Polymer), as the stator material. G-10 is suitable for cryogenic applications with a wide range of operating temperature and good mechanical strength. The iron losses can be approximately expressed as in Eq. 5.1.

$$W_i = K_e f^2 B^2 + K_h f B^2 \quad (5.1)$$

where K_e is the eddy current coefficient of the material, f is the frequency, B is the magnetic field strength and K_h is the hysteresis coefficient of the material (Kulkarni *et al.*, 2016).

For a non-ferromagnetic material, the values of K_e and K_h are zero - hence the iron losses can be reduced to zero with the use of non-ferromagnetic stator frame. G-10 FRP was chosen as the stator material as it will serve the dual purpose of non-conductivity and provide further cryogenic insulation for the HTS rotor. With the use of G-10 FRP, the flux concentration is reduced and the field strength around the stator conductors is correspondingly reduced (see Fig. 5.12).

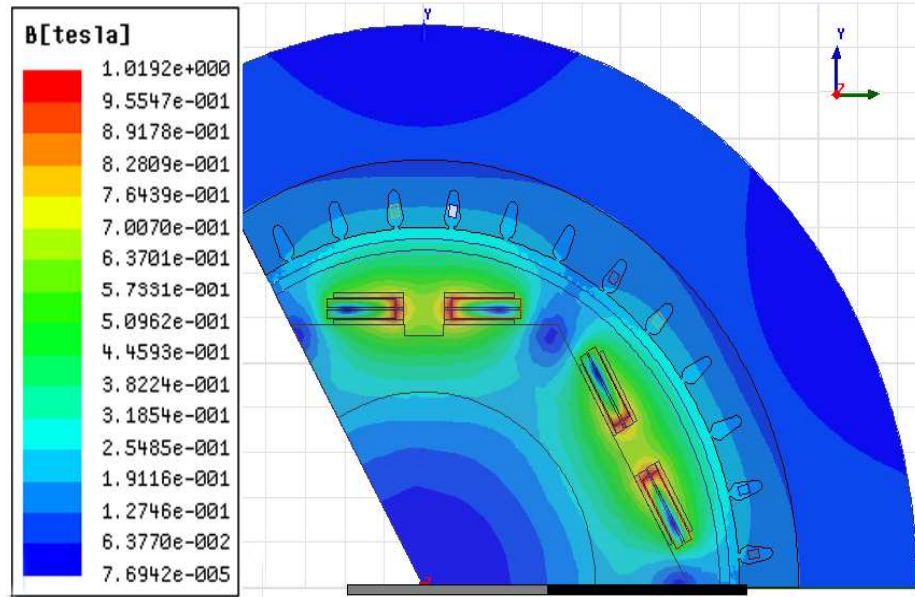


Fig. 5.12 Field pattern with the G-10 stator.

The magnitude of the induced voltages, correspondingly, is lower than the induced voltage with the ferromagnetic stator material. Figs. 5.14 and 5.15 show the induced phase voltages with steel and G-10 stator, respectively.

5.2.5 Excitation Frequency

The excitation frequency of the flux pump has no significant effect on the field distribution of the machine but the rate of increase in field current is observed to be directly proportional to the frequency of excitation. The increase in the field current above the steady state current of 95 A (3 A less than the rated current) versus

the excitation frequency in 750 ms of simulation time is shown in Fig. 5.13. With 60 Hz Flux pump excitation, the increase in field current is 3.1 mA in 750 ms and with 120 Hz the increase is 5.6 mA while the increase is 7.7 mA with 240 Hz excitation.

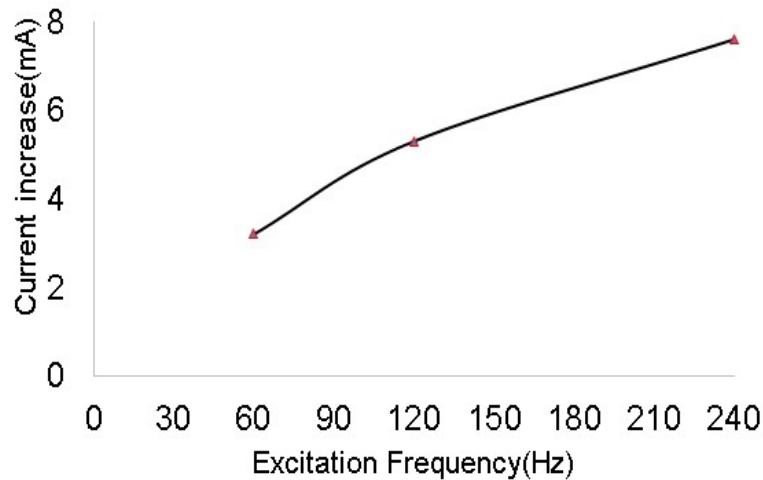


Fig. 5.13 Field current increase versus the excitation frequency.

It is further observed (see section 5.2.6) that the frequency of flux pump excitation has no effect on the THD of the induced voltage but the ramp up rate of field current is seen to be directly proportional to the frequency of excitation.

5.2.6 Harmonic Analysis

The harmonic analysis was carried out on the induced phase voltages, on the same lines as carried out for synchronous generator in 4.3.3. Fast Fourier Transform (FFT) and Total Harmonic Distortion (THD) were computed using MATLAB. FFT and THD provide the quantitative measure of the different frequency components present in the induced voltage waveform.

Total Harmonic Distortion (THD) is given by Eq. 5.2.

$$THD = \frac{\sqrt{\sum_k V_k^2}}{V_1} \quad (5.2)$$

where k is an integer and refers to the harmonic order, $k = 2, 3, 4, \dots$, V_k is the amplitude of k^{th} order harmonic and V_1 is the fundamental frequency component.

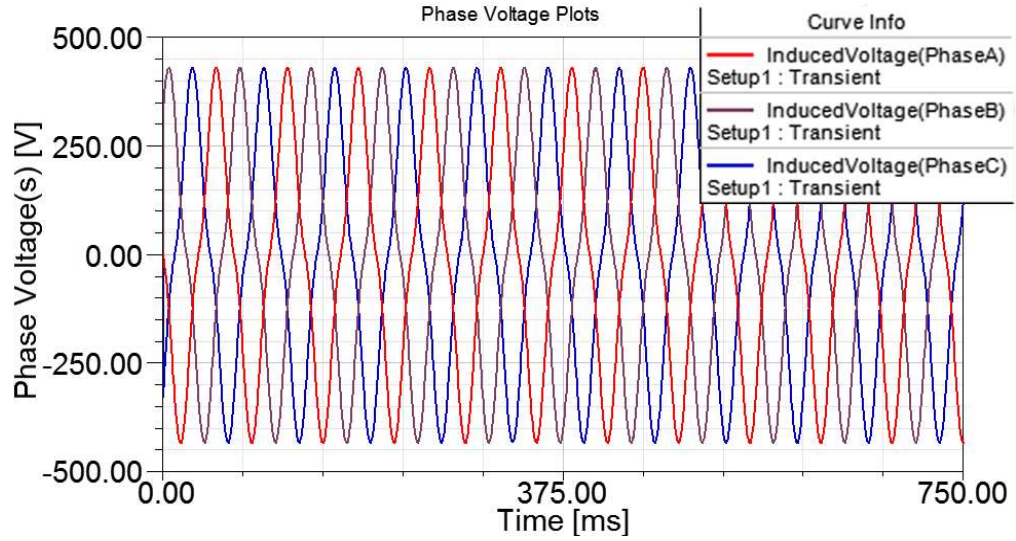


Fig. 5.14 Open circuit phase voltage plots with steel stator.

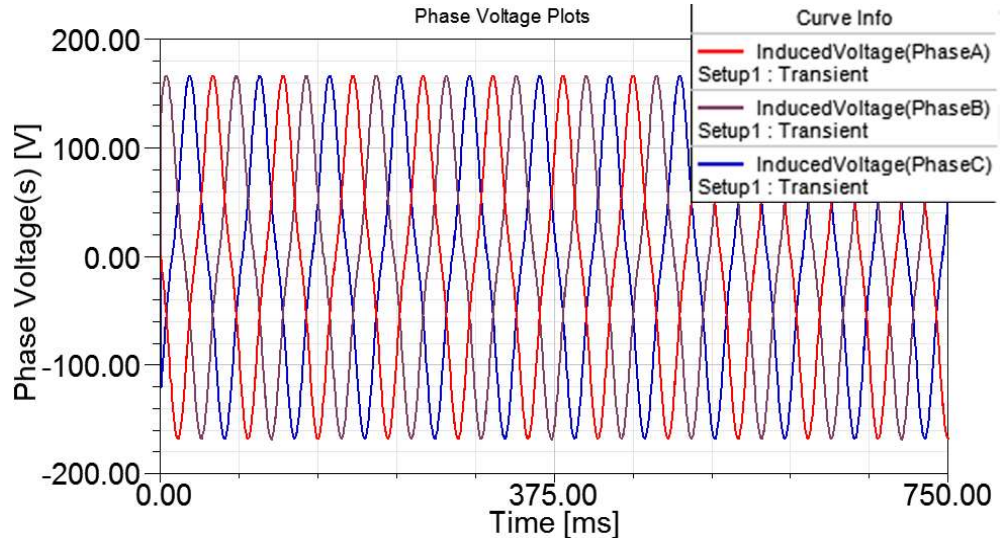


Fig. 5.15 Open circuit phase voltage plots with the G-10 stator.

Table 5.3 gives a comparison between THD values of the Phase voltage FFT with steel stator and with the G-10 stator. It is observed that the THD values with G-10 stator are lower than with the steel stator. The difference in THD values can be attributed to the fringing in the field distribution with steel stator (Fig. 5.10) - the steel stator acts as a flux concentrator. Non-uniformity in the voltage profile observed during the zero crossing of the voltage is higher in the case of steel stator than the G-10 stator. A sharp transition in the field from North-pole to South-pole or vice versa (Figs. 5.10 and 5.11) because of the absence of a ferromagnetic pole structure on the rotor is found to be the reason for the non-uniformity in voltage profile during zero crossing (Kulkarni *et al.*, 2016).

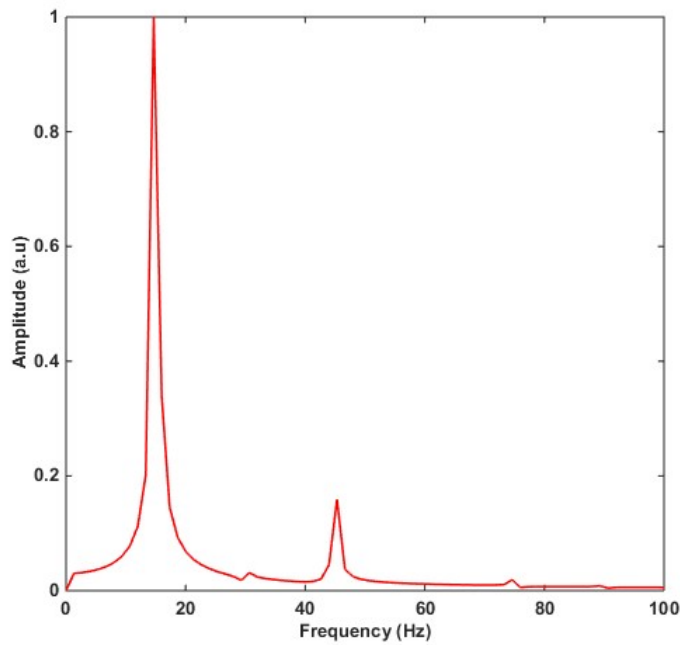


Fig. 5.16 FFT of Phase A voltage plot for steel stator.

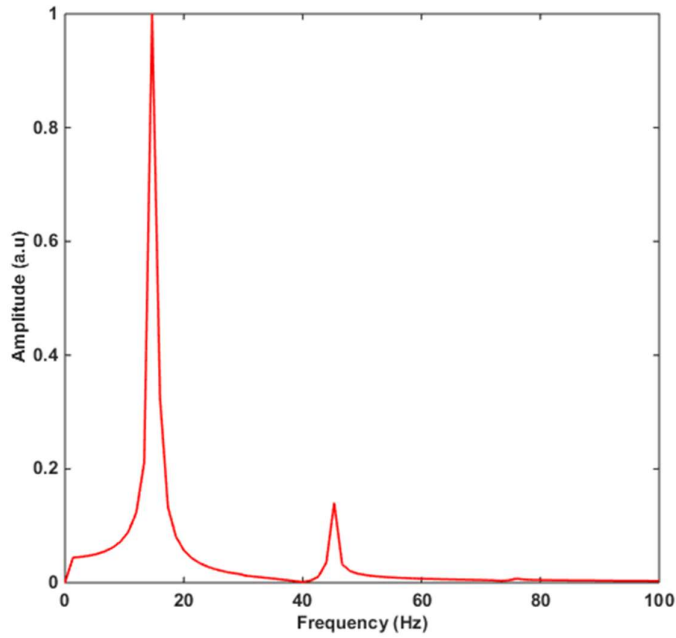


Fig. 5.17 FFT of Phase A voltage plot for the G-10 stator.

Table 5.3. THD Comparison between Steel and G-10 Stator

| THD (%) Comparison | | | | |
|--------------------|---------|---------|---------|---------|
| Excitation | Steel | | G-10 | |
| frequency | Phase A | Phase B | Phase A | Phase B |
| 60 Hz | 15.563 | 15.544 | 13.4066 | 13.4048 |
| 120 Hz | 15.564 | 15.611 | 13.4079 | 13.4077 |
| 240 Hz | 15.578 | 15.584 | 13.4081 | 13.4074 |

The FFT plots of Phase A induced voltage at 240 Hz flux pump excitation with steel stator and G-10 stator are shown in Fig. 5.16 and Fig. 5.17, respectively. A dominant third harmonic is observed in both the cases but the magnitude of the

third harmonic is lower in the case of the G-10 stator and it is reflected in a correspondingly lower THD value as well (Table 5.3).

The third order harmonics on the generators can be eliminated using short pitching and by achieving uniform flux distribution, which is discussed in Chapter 6. However, the unwanted 3rd harmonics on distribution side are generally eliminated using standardized techniques (Schonek, 2001) as follows; 1. Using separate neutral conductor for each phase or doubling the neutral conductor rating. 2. Using star delta transformer. 3. Using transformer with zig-zag secondary. 4. Using zig-zag reactance. 5. Using third order filter in the neutral. 6. Placing filtering devices near the non-linear loads. Since, the research aims at analyzing the harmonic performance of the generator, further discussion on harmonic analysis on distribution side is out of scope for this thesis.

5.3 Concluding Remarks

Flux pump has been successfully seen to be an alternative to DC for exciting the field system in an HTS generator. It avoids the thermal link between the cryogenic and non-cryogenic environment, thus decreasing the thermal loading on the cryogenic system.

Performance analysis was carried out on a 10 kW HTS generator. The field analysis results indicate that there is significant fringing effect in the field pattern and also reflected as distortion in the induced voltage. From the harmonic analysis, it can be concluded that the stator material has a significant effect on the THD of the induced voltage.

With the use of non-ferromagnetic stator material (G-10), the hysteresis loss can be avoided and the THD can be reduced. Optimization of stator configuration will lead to further decrease in THD. The variation in excitation frequencies of the flux pump has negligible effects on the field pattern and the THD of the induced voltage.

The implementation of a series-parallel combination of the flux pump stators can be carried out. Such a configuration, however, calls for a detailed failure analysis of the combination of stators with significant quenching possibilities during the operation. Use of separately excited flux pump stators could possibly resolve the issue but may result in a field current imbalance, this will be discussed in Chapter 6.

Chapter 6. Stator Design and Separate Excitation effects

6.1 Introduction

Chapter 3 discusses the use of flux pump, to avoid the thermal link between the cryogenic and non-cryogenic environments. If the rotor core and stator yoke materials are non-ferromagnetic, then they provide further minimization of losses by eliminating hysteresis and eddy current losses. The use of non-ferromagnetic material such as FRP epoxy for the stator yoke reduced the field concentration at the conductors and the flux distribution was non-uniform over layers for a different phase in each stator slot.

The design of non-conventional electric machines involves the adaptive implementation of the conventional and proven designs (Nick *et al.*, 2002). The 10 kW HTS generator used in this research is one such non-conventional design. Total Harmonic Distortion (THD) is one of the most important performance parameters of a generator. The THD values have to be in accordance with the state regulatory specifications for successful grid connected operation or in stand-alone mode for sensitive electronic loads. Few earlier reports have discussed the potential of flux pumps to replace the DC excitation of field windings (Kulkarni *et al.*, 2015; Bumby *et al.*, 2016).

The no-load harmonic performance of 10 kW HTS generator with two different stator yoke materials has been discussed in chapter 5 and also reported by us earlier (Kulkarni *et al.*, 2016). Use of FRP epoxy (G-10) results in reduced THD as there is no magnetic saturation in the material.

In this chapter, the effects of the stator design on the harmonic performance are discussed and the best-suited design configuration for improved THD performance will be established.

6.2 Performance Analysis

Based on the discussion on conducted studies until now, it is well established that, flux pump offers a unique method of magnetising a superconductor without a physical link between the cryogenic and non-cryogenic environments. Jiang (Jiang *et al.*, 2014) has presented the formulation of dynamic resistance model for an HTS flux pump. The results show a linear relation between the frequency of the flux pump and the rate of current increase. From the voltage profile, it is evident that a net voltage (quasi-DC emf) drop occurs across the superconducting coil (Bumby *et al.*, 2016). Based on the previously reported results by us (Kulkarni *et al.*, 2016), it is well established that the flux pump can be successfully used as an alternative to DC excitation for the field system in a generator.

THD performance of a generator is one of the most critical parameters for the successful implementation of a grid-connected generator or as stand-alone supply for sensitive electronic loads. The range of this work covers the harmonic performance analysis of the proof of concept-10 kW HTS synchronous generator. The harmonic performance of a synchronous generator depends primarily on the rotor and stator construction (Khalf *et. al.*, 2012; Seo *et. al.*, 2014).

The other factors that influence the harmonic performance are nature of field excitation, materials of the ferromagnetic circuit, armature reaction, load configuration, *etc...* System modelling and the no-load harmonic performance of the 10 kW HTS synchronous generator, is discussed in section 4.5. The minimum THD observed with the design was ~13%, which is low enough for stand-alone operation of the generator with only heating load but cannot be used for grid connected operation or electronic loads such as TV, LCD screens *etc.*,

6.3 Design considerations

This research uses an intermediate machine design from an associate research group at Changwon National University, to analyse the effects of flux pump excitation on the harmonic performance of the machine using FEM. However, a brief outline of relevant conventional design considerations has been discussed in this section.

Torque capability of the machine is primarily responsible for the sizing of the electrical machine, the output torque is proportional to the product of rotor volume and the shear stress (Soong, 2008). Torque analysis of the HTS generator considered in this research is touched upon at the end of this chapter. Since this HTS generator is expected to be direct-driven with a wind turbine and the torque in such an electrical machine is related to a magnetic shear stress in the air-gap of the machine given by Eq. 6.1.

$$\sigma_g = \frac{\tau}{2\pi r_r^2 l_r} \quad (6.1)$$

where σ_g is the airgap shear stress, τ is the torque, r_r is the rotor radius and l_r is the rotor core length. The shear stress varies as the square of the flux density.

With a varying air gap between the stator conductor and the rotor core because of the non-conventional rotor structure, the field design is quite critical and challenging for this application. Since, the rotor core and the associated field design is being carried out by the Changwon National University associate group of the international collaboration, only the stator design and the associated design improvisations have been considered in the following sections and the results have been submitted for further optimisation of the proof-of-concept machine.

6.4 Stator Design

In this section of the research, stator design has been studied and proposed considering 3 important parameters; (a) Stator yoke material (b) Winding Pitch Factor (K_p) and (c) Load configuration.

Stator design is one of the important aspects of the design of a synchronous generator (Say, 1976). Using RMXprt a customised stator was designed (see Fig. 6.1) for the HTS rotor. The dimensions of the stator were set to suit the rotor dimensions and the number of stator conductors was set as to attain the rated values. Further details of the stator design are provided in appendix D.

Simulations were conducted with different values for the important parameters (a) Stator yoke material (b) Winding Pitch Factor (K_p) and (c) Load configuration. The results and observations are discussed in the subsequent sections.

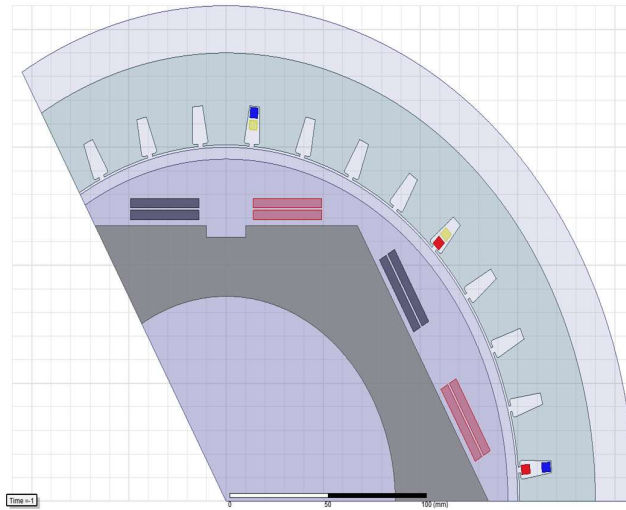


Fig. 6.1 2D Model of stator design 1

6.4.1 Stator Yoke Material

Generally, for cryogenic applications the G-10 material is used. In earlier reports (R. Kulkarni *et al.*, 2016), it is established that FRP epoxy material is a better alternative to the commonly used steel yoke for the proposed flux pump integrated HTS generator instead of a ferromagnetic stator. The hysteresis in the ferromagnetic stator increases the ambient temperature around the cryostat of the HTS rotor and increases the ambient thermal load on the cryogenic system. In order to avoid the hysteresis loss, a non-ferromagnetic stator can be used. Hence, simulations were carried out with G-10-FRP as the stator material to study the effects on the generator performance with a non-ferromagnetic stator.

For a non-ferromagnetic conductor, the values of K_e and K_h in Eq. 6.2,

$$W_i = K_e f^2 B^2 + K_h f B^2 \quad (6.2)$$

reproduced here from chapter 5 for brevity, are zero - hence the iron losses can be reduced to zero with the use of non-conducting stator frame. Use of non-ferromagnetic stator yoke results in a decrease of voltage levels as the field strength around the stator conductors' decreases. The decrease in voltage levels has been compensated with an increase in the number of stator conductors. The increase in the number of stator conductors due to the usage of non-ferromagnetic yoke adds up to the capital cost and requires redesigning of the field coils to make up for the lost power. But use of non-ferromagnetic yoke avoids the recurring hysteresis losses.

6.4.2 Winding Pitch Factor (K_p)

The winding pitch factor is a key factor in determining the magnitude of the fundamental component of the waveform and also in determining the magnitudes

of the higher order harmonics of the waveform. The winding pitch of a generator is the number of slots spanned by each coil in the stator winding over the number of slots per pole (see Fig. 6.2). The winding pitch of generators is generally shortened from full pitch to either 5/6 (Fig. 6.2b) or 2/3 (Fig. 6.2c) in order to change the harmonic content of the output waveform. When the pitch is reduced, the fundamental component of the output voltage is slightly lowered than the full pitch winding. The reduction in the output voltage can be compensated by an increase in the field strength or number of stator conductors. ABB synchronous generators use both 5/6 and 2/3 pitched winding (ABB, 2014). 5/6 is preferred for HV generators where compactness is preferred over reduced THD. The winding pitch factor K_p (Nelson, 2004) gives the variation factor for different harmonics and is expressed as (Eq. 6.3);

$$K_p = \cos \left(\frac{N * 180(1 - \text{pitch})}{2} \right) \quad (6.3)$$

where N is the order of the harmonic. Table 6.1 lists the values of K_p for 2/3 and 5/6 winding pitches. The value of K_p for 3rd harmonic with 2/3 pitch works out to be zero, thus eliminating the third harmonic component. This decreases the overall THD but there is a decrease in the voltage levels and needs compensation.

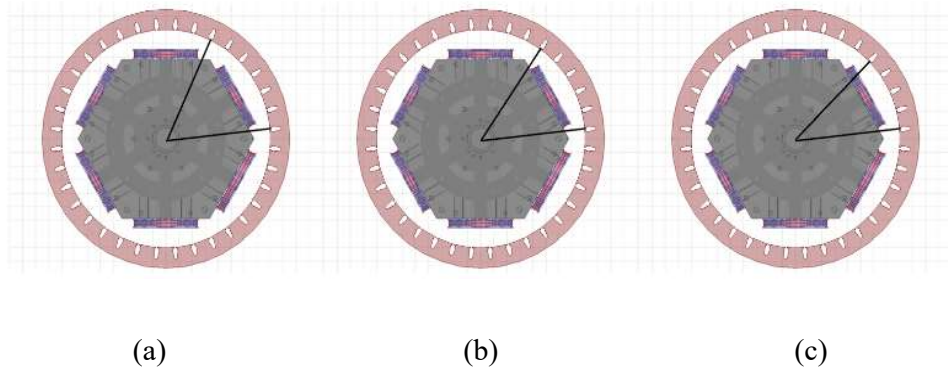


Fig. 6.2 (a) Full pitch, (b) 5/6 pitch and (c) 2/3 pitch.

Table 6.1. Winding Pitch Factor

| Winding Pitch Factor (K_p) | | |
|--------------------------------|-----------|-----------|
| | 2/3 Pitch | 5/6 Pitch |
| Fundamental | 0.87 | 0.97 |
| 3 rd Harmonic | 0.00 | 0.71 |
| 5 th Harmonic | 0.87 | 0.26 |
| 7 th Harmonic | 0.87 | 0.26 |

6.4.3 Load configuration

The harmonic performance of the HTS generator has been examined for “No-Load” and “Rated Load” conditions. HTS generator in the discussion is aimed at the implementation for wind-based power generation. In wind turbines, the best-suited alternator winding configuration is Star at the start-up, to support easy initial spin at high voltage and low current. The winding is switched to Delta once the speed has picked up to boost the current levels (Google patents: Synchronous machines starting systems, 1931). However, for a low-speed generation, as in this case, a fixed Star winding configuration for the alternator windings is deemed suitable.

Simulations were conducted for all possible combinations of alternator winding and load winding configurations as below:

1. Star-Star (S-S)
2. Star-Delta (S-D)
3. Delta-Star

Delta-Delta was not possible with MAXWELL Circuit Editor. From the results, it was found that the configuration 3 gave exceptionally high THD and thus the comparison is shown only for the first two combinations which have

comparable THDs. The THD values for combination 3 are added in Appendix-B. The effect of the change in load configurations on the THD of the induced phase voltage is discussed in section 6.4.

6.5 Results and Observations

The field pattern with G-10 as the stator material and flux pump excitation are observed to be uniform (see Fig. 6.3). The field variation at the stator conductors' location is minimal. The induced voltage waveforms, shown in Fig. 6.4, are consistent with the design expectations and have a lower THD than the designs presented in (Kulkarni *et al.*, 2016) and also reported in this thesis in chapter 5.

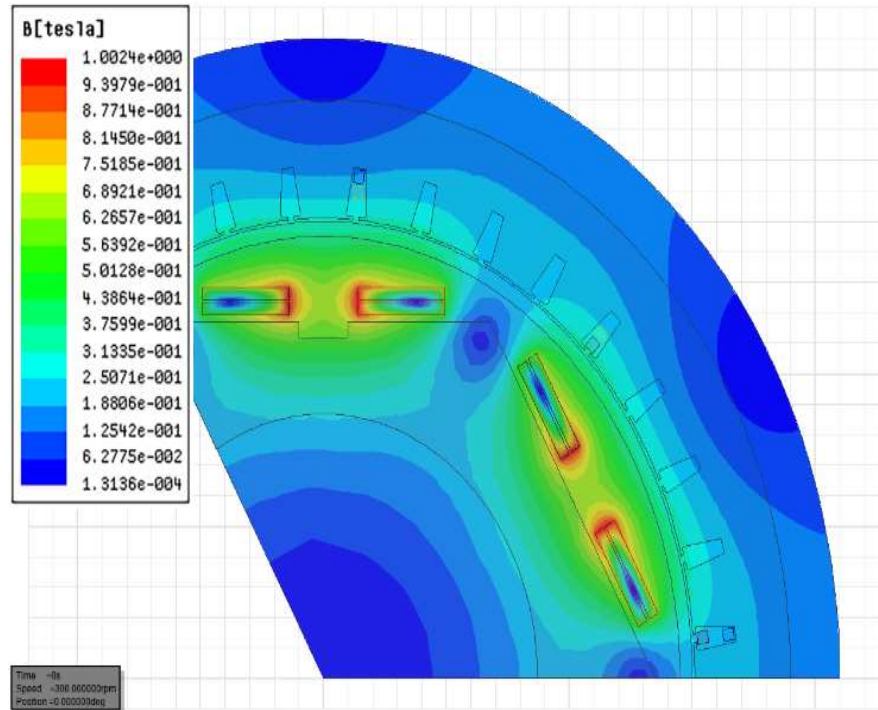


Fig. 6.3 ANSYS field pattern with G-10 Stator Yoke.

The harmonic analysis was carried out on the induced phase voltages. Normalised Fast Fourier Transform (FFT) and THD were computed using MATLAB. FFT and THD provide the quantitative measure of the different

frequency components present in the induced voltage waveform. The importance of THD and the associated mathematical equation has been discussed in sections 1.4 and 5.2.6.

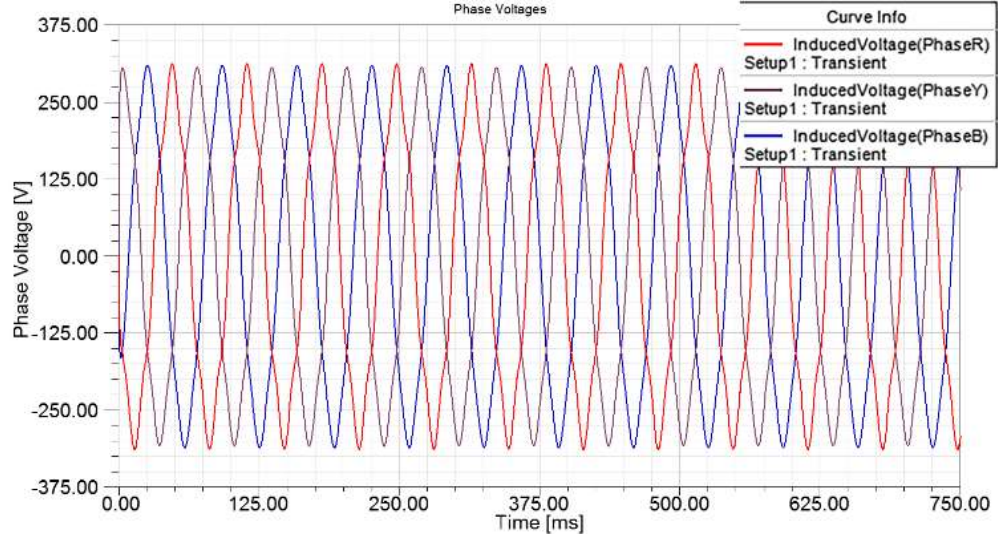


Fig. 6.4 ANSYS plot of induced 3-phase voltage.

The improvement in THD for the 2/3 pitch configuration is clearly seen and this is because of the elimination of the third harmonic component that is present in 5/6 pitch configuration (see Fig. 6.5).

Tables 6.2-6.6 show a comparison between THD values of the induced phase voltage under different conditions. Simulations were carried out for 3 different frequencies of flux pump excitation (60 Hz, 120 Hz and 240 Hz). Under No-Load conditions, it is observed that the THD values with G-10 stator are lower than with the steel stator (see Table 6.2).

- The reduction in THD can be attributed to higher fringing effects and sharper transition of the fields in the case of steel yoke stator for the hexagonal design of rotor without pole shoes.

- The change in the winding pitch resulted in a decrease in the induced voltage levels but improved the harmonic performance. The voltage levels were compensated by increasing the number of stator conductors as mentioned in section 6.3.2.

As discussed in section 6.3.2, the winding pitch is a critical factor in tuning the harmonic performance, results are analysed for two different pitches commonly used in synchronous generators.

Table 6.2. No-Load-THD (V_{ph})

| f (Hz) | Pitch=5/6 | | Pitch=2/3 | |
|----------|-----------|-------|-----------|------|
| | Steel | G-10 | Steel | G-10 |
| 60 | 15.56 | 13.40 | 8.59 | 6.13 |
| 120 | 15.56 | 13.41 | 8.60 | 6.14 |
| 240 | 15.57 | 13.41 | 8.61 | 6.14 |

The THD for 2/3 pitch configuration is significantly reduced when compared to 5/6 pitch configuration for both steel and G-10 stator yokes. The reason for this improvement is the successful elimination of third harmonic component (see Fig. 6.6). Based on these results, for further simulations, the stator yoke material was selected to be G-10 and the winding pitch was selected to be 2/3.

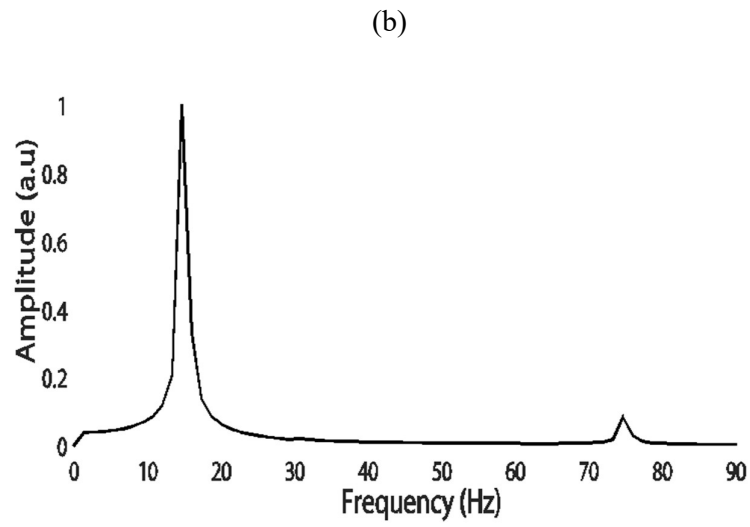
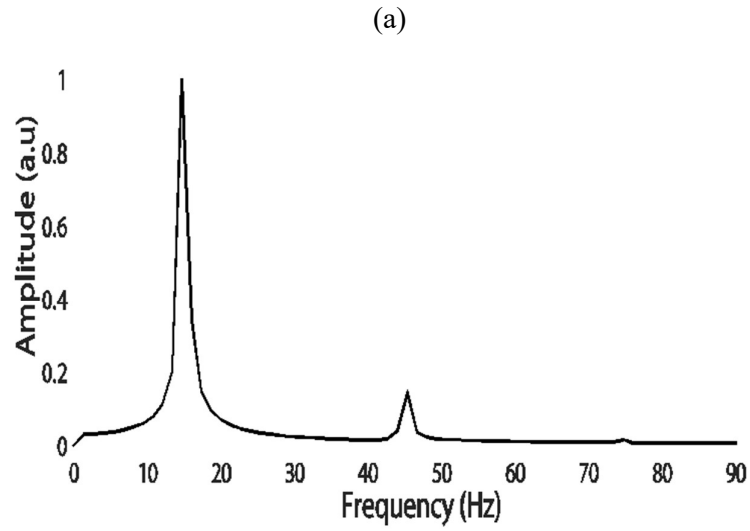


**Fig. 6.5 Normalised FFT plot of Induced Phase Voltage at rated load and
(a) pitch = 5/6. (b) pitch = 2/3.**

Table 6.3. Rated Load-G-10 Stator -2/3 Pitch

| f (Hz) | Star-Star | Star-Delta |
|----------|-----------|------------|
| 60 | 5.91 | 5.21 |
| 120 | 5.91 | 5.22 |
| 240 | 5.98 | 5.22 |

Simulations for different loaded conditions (rated load, $\frac{1}{2}$ rated and $\frac{1}{4}$ rated loads) were carried out for two different configurations. Balanced resistive loads were coupled to the ANSYS MAXWELL model using ANSYS MAXWELL Circuit Editor for these simulations. With S-S configuration, the THD of the induced phase voltage (V_{ph}) is $\sim 3.3\%$ lower than with the No-Load THD values (see Tables 6.2 and 6.3).

Table 6.4. Star-Delta -G-10 Stator -2/3 Pitch

| THD (V_{ph}) | | | |
|------------------|-------|---------------------|---------------------|
| f (Hz) | Rated | $\frac{1}{2}$ Rated | $\frac{1}{4}$ Rated |
| | Load | Load | Load |
| 60 | 5.21 | 5.84 | 6.05 |
| 120 | 5.22 | 5.84 | 6.05 |
| 240 | 5.22 | 5.84 | 6.05 |

On further investigation, it was observed that the field current profiles for the No-Load condition are affected by the pulsating nature of the flux pump

excitation whereas the pulsating nature has not much effect under loaded conditions (see Fig. 6.6).

Though the field current is increasing in both the cases, the field current oscillations in case of the loaded condition have a higher sinusoidal variation than the field currents with the No-load condition. For further simulations, Star-Delta (S-D) was selected as the load configuration. THD values at different levels, Rated, $\frac{1}{2}$ and $\frac{1}{4}$ loads, are tabulated in Table 6.4. Minimum THD is observed at rated load.

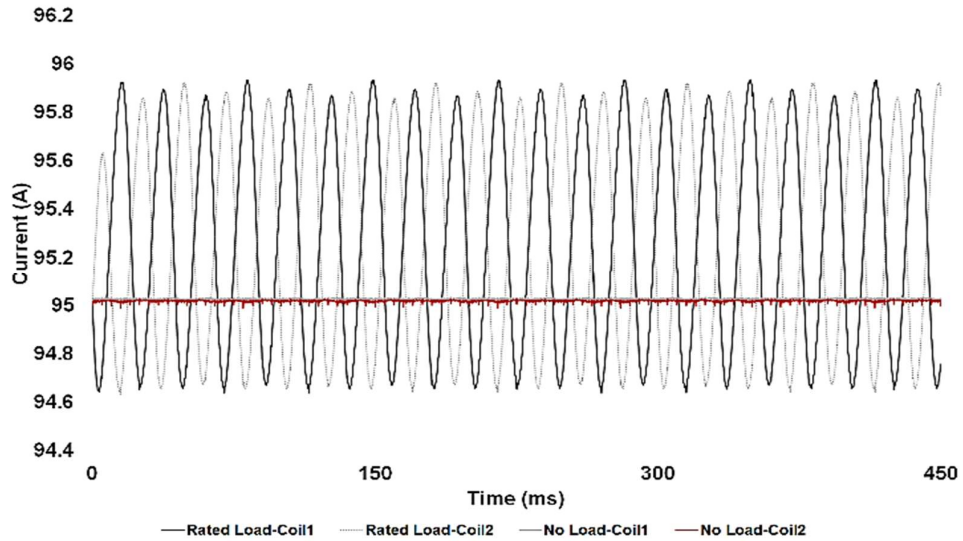


Fig. 6.6 Field current oscillations with the loading condition.

It is also observed that the THD values for S-D configuration are slightly lower than the S-S configuration. This is most likely due to the lower armature reaction in the case of S-D configuration. Studies on armature reaction and analysis of direct axis reactance (X_d) and quadrature axis reactance of the machine (X_q) of the machine are likely to give a better understanding of the ongoing phenomenon from magnetic field interaction.

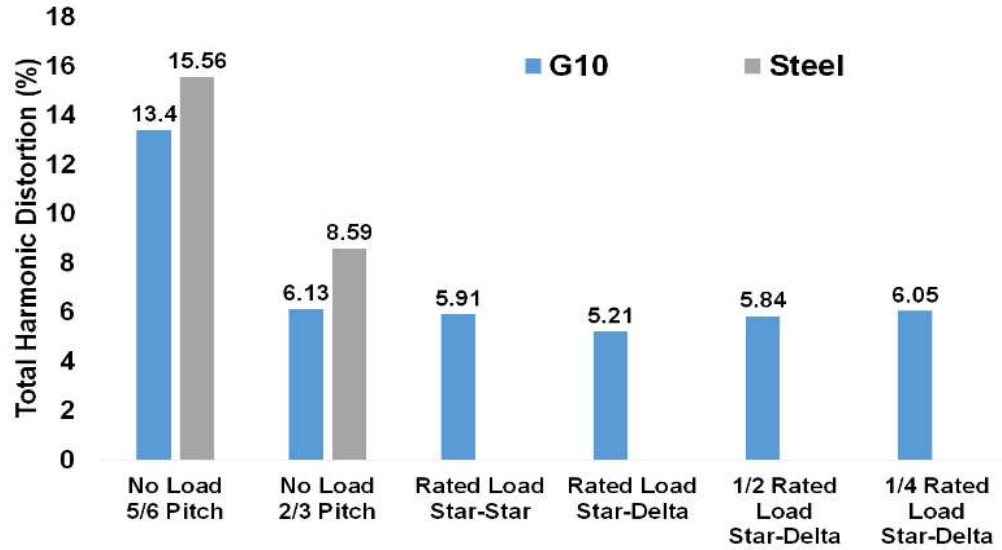


Fig. 6.7 The variation of THD with material, pitch and load configuration.

THD limit as specified in IEEE STD 519-2014 is 5% for a bus voltage < 69 kV at the point of common coupling and the permitted limit is 8% for lower voltage generation < 1 kV. Hence, the proof-of-concept generator to be tested on the field and designed for 400 V meets prescribed standards.

The final commercial product based on this proof-of-concept generator will be a flux pump integrated MW class wind turbine HTS generator and the generated voltage levels for this generator are expected to be > 1 kV and < 69 kV. For this class of generation, the maximum limit of THD is 8% as per the prescribed standard. The observed THD limits are well within this limit and with this design, a tolerance offset of ~3% can be considered for the additional harmonics introduced due to control circuitry and the power electronic switching circuitry, which will be integrated at different points of the generation and transmission.

The results are in consistence with the results observed for similar machines with conventional design approach, thus justifying the approach to evolve a suitable design configuration (Zhang *et al.*, 2012). The overall variation trend of THD

against various design parameters is shown in the bar graphs of Fig. 6.6. It is seen that S-D configuration with a pitch of 2/3 at rated load gives the least THD.

RL Load performance

Simulations were carried out with the balanced RL load as well. The trend observed was same as that with balanced R-load but the RL load gave lesser THD as compared to the R-load and the reason could be identified to be the additional low pass filtering effect as the higher frequency components are reduced.

The effect of load configuration was also similar to that observed with R load. The Star-Star configuration had higher THD as compared to Star-Delta configuration. The results are tabulated in Table 6.5 and Table 6.6.

Table 6.5. Star-Star -G-10 Stator -2/3 Pitch-RL Load

| f (Hz) | THD (V_{ph}) | | |
|----------|------------------|---------------------|---------------------|
| | Rated | $\frac{1}{2}$ Rated | $\frac{1}{4}$ Rated |
| | Load | Load | Load |
| 60 | 5.52 | 5.61 | 5.85 |
| 120 | 5.52 | 5.62 | 6.84 |
| 240 | 5.53 | 5.63 | 6.86 |

Table 6.6. Star-Delta -G-10 Stator -2/3 Pitch-RL Load

| $f(\text{Hz})$ | THD (V_{ph}) | | |
|----------------|------------------|---------------------|---------------------|
| | Rated | $\frac{1}{2}$ Rated | $\frac{1}{4}$ Rated |
| | Load | Load | Load |
| 60 | 4.58 | 4.71 | 5.85 |
| 120 | 4.59 | 4.72 | 5.84 |
| 240 | 4.59 | 4.73 | 5.86 |

6.6 Stator Design Improvisation

As discussed in section 4.5.4, the stator in the 10 kW proof-of-concept HTS generator is air-cored (with no ferromagnetic yoke). The frame of the stator is made of FRP epoxy (G-10). In absence of a ferromagnetic yoke, the field distribution is less concentrated and the drop in the field is higher with small increase in the distance from the centre of the field coil.

6.6.1 Stator Design 1

In earlier work (Kulkarni *et al.*, 2016), parts of which are reported in chapter 5 and section 6.3, a stator design is proposed considering 3 important parameters; (a) The stator yoke material (b) Winding Pitch Factor (K_p) and (c) Load configuration. The 2D FEM model of the earlier design is as shown in Fig. 6.8.

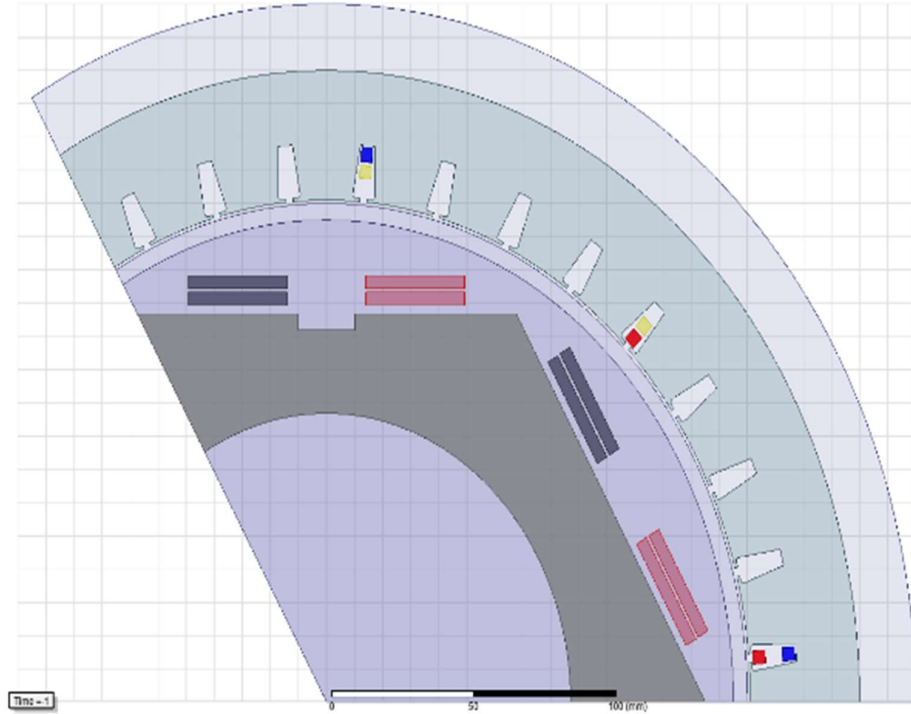


Fig. 6.8 2D model with stator design 1

6.6.2 Stator Design 2

From field and performance analysis of Design 1 reported in section 6.3, it is understood that the conductors corresponding to the same phase are at different field levels - the reason is attributed to the absence of ferromagnetic yoke of the stator. In order to avoid the field non-uniformity, a different stator design is proposed, as shown in Fig. 6.9, wherein the stator conductors could be placed in an adjacent manner rather than stacked manner.

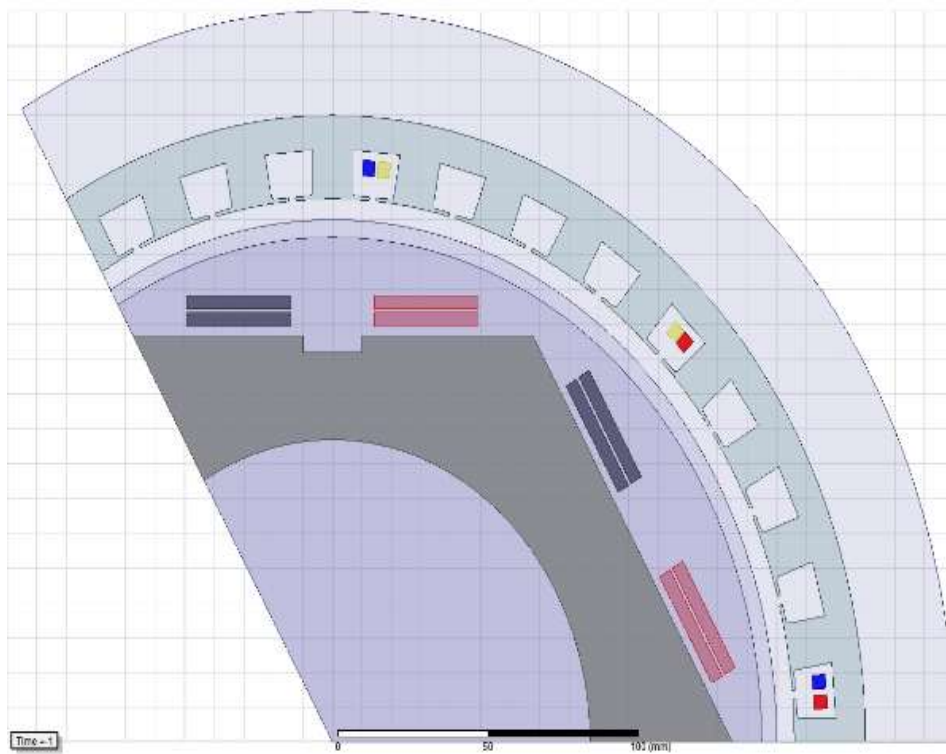


Fig. 6.9 2D model with stator design 2

The two important variations in the design were:

1. Stator slot width
2. Internal diameter of the rotor

The stator slot width was changed from 8 mm to 14 mm to accommodate the adjacent placement of stator conductors. The diameter on the yoke side was reduced from 380 mm to 360 mm and the diameter on gap side was increased from 302 mm to 312 mm. These variations were carried out to place the stator conductors for the same phase at the same field strength for most of the time and decrease the fluctuations in the field level, correspondingly in the induced voltage level as well, thus expected decrease in the THD.

6.7 Results and Observations

The field pattern with Stator Design 1 (Fig. 6.10) shows that the stator conductors corresponding to the same phase are at different field strengths (Fig. 6.11), With the stator design changes, it is observed that the conductors corresponding to the same phase are in the same field strength as required (Figs. 6.12 and 6.13).

The change in stator design resulted in improvement in the harmonic performance of the machine. With the same meshing and boundary conditions as set for stator design 1, the change in the stator dimension and the stator conductor placement strategy for a G-10 stator yoke resulted in a significant improvement in the harmonic performance - they are shown in Table 6.7. The decrease in the harmonic distortion validates that the field uniformity is one of the important factors in ascertaining a better harmonic performance.

Further, with RL load, the THD values are lower than with R-load following the same trend as with stator design 1 discussed in section 6.3.3.

Table 6.7. THD Comparison between Design 1 and Design 2

| f (Hz) | No-Load THD | | Rated Load THD | |
|------------|-------------|----------|----------------|----------|
| | Design 1 | Design 2 | Design 1 | Design 2 |
| 60 | 6.1367 | 4.2915 | 5.2164 | 2.7269 |
| 120 | 6.1378 | 4.3016 | 5.2196 | 2.7366 |
| 240 | 6.1383 | 4.3155 | 5.2243 | 2.7398 |

Table 6.8. THD Comparison between R Load and RL Load with Design 2

| f (Hz) | R load | RL load |
|----------|--------|---------|
| 60 | 2.7269 | 2.4132 |
| 120 | 2.7366 | 2.4099 |
| 240 | 2.7398 | 2.4186 |

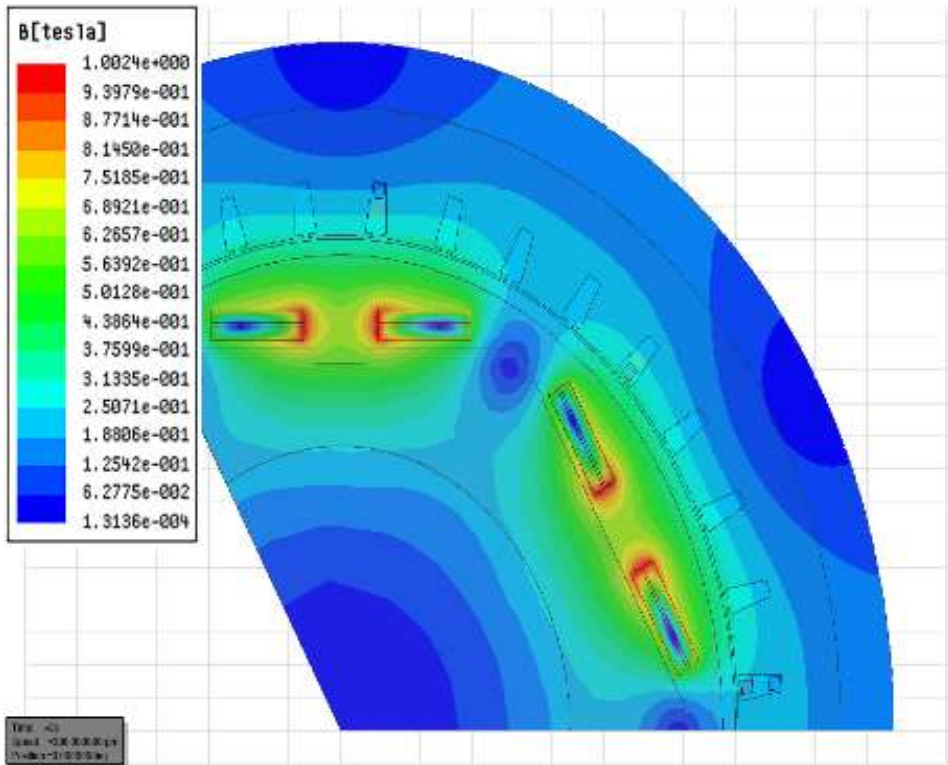


Fig. 6.10 2D field pattern with stator design 1

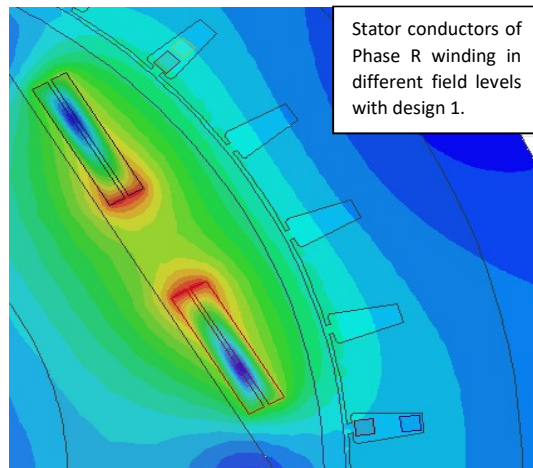


Fig. 6.11 Field pattern around stator conductors with stator design 1

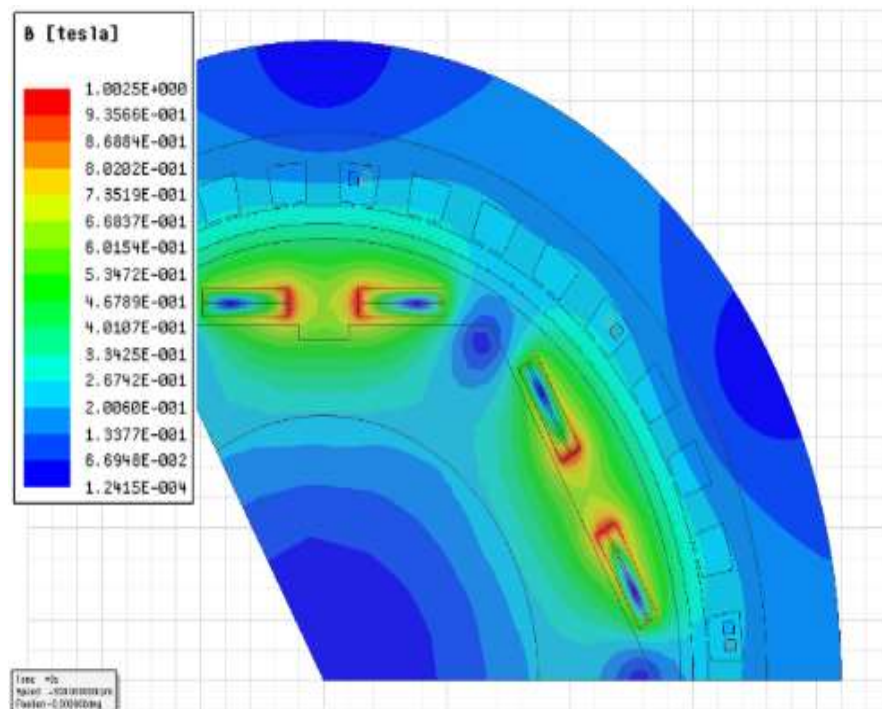


Fig. 6.12 2D field pattern with stator design 2

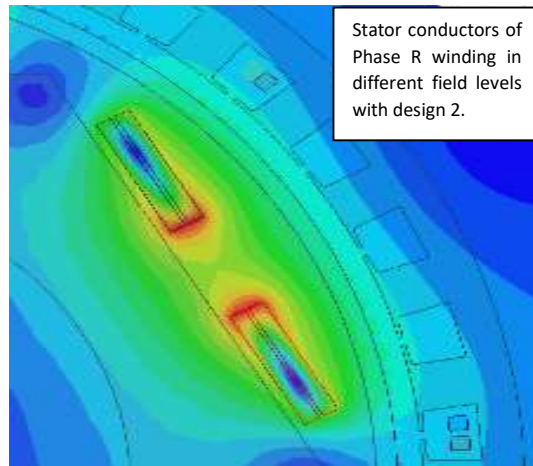


Fig. 6.13 Field pattern around stator conductors with stator design 2

6.8 Separate Excitation

In order to avoid serial field coil damage in the event of quench of one of the coils, separate excitation of coils has been examined as a potential solution. When the coils are separately excited there is a possibility of imbalance in the field currents which is not the case when the coils are connected serially and excited by a single source.

When the HTS rotor coils are excited separately and are not in series, the current in each field coil will not be equal. This imbalance in the field currents causes distortion in the sinusoidal nature of the induced emf. The distortion in the sinusoidal nature of a waveform can be mathematically quantified by calculating the Total Harmonic Distortion (THD) of the waveform.

The field coils in the HTS rotor can be excited separately with the use of flux pump - it would avoid the complete breakdown of the field system associated with the series connection in the event of a quench, this would create an imbalance in the field current levels in the system as the current at any point of time is a complex function of field interaction and frequency of interaction, as in Eq 6.4.

$$I(t) = \frac{\Delta\phi}{\beta} \left(1 - \exp\left(\frac{-\beta ft}{L}\right) \right) \quad (6.4)$$

where, $\Delta\phi$ = the net flux change, β = constant defined by the design parameters of the flux pump.

To analyse the effect of imbalance, simulations were conducted with different current values in the adjacent coils.

The same time duration of 750 ms as the earlier simulations was set to have uniformity and the current in one of the coils was fixed at 95A and current in the other was reduced by 5A for each trial to identify the trend in distortion and also to

study the effect of complete failure of one of the coils for which case, the current was set to 0A.

As anticipated, the effect was quantified notably in the harmonic performance. The results are discussed in the following section.

6.9 Results and Observations

The imbalance in the field current leads to distortion in the effective field around the stator conductors as observed in Figs. 6.14 to 6.16 and the induced voltage waveform gets distorted as well. The distortion is significant with the increase in the field current imbalance as seen in Figs. 6.17 to 6.19. The distortion can be quantified and measured in terms of THD values.

It is also observed that the maximum value of the induced voltage is reduced with the increase in the imbalance of field current. The effect of field current imbalance on the THD is illustrated in the THD plots of Fig. 6.21. As expected, the magnitude of the 2nd harmonic is observed to increase with the increase in the imbalance current magnitude. The corresponding values of THD are tabulated in Table 6.9.

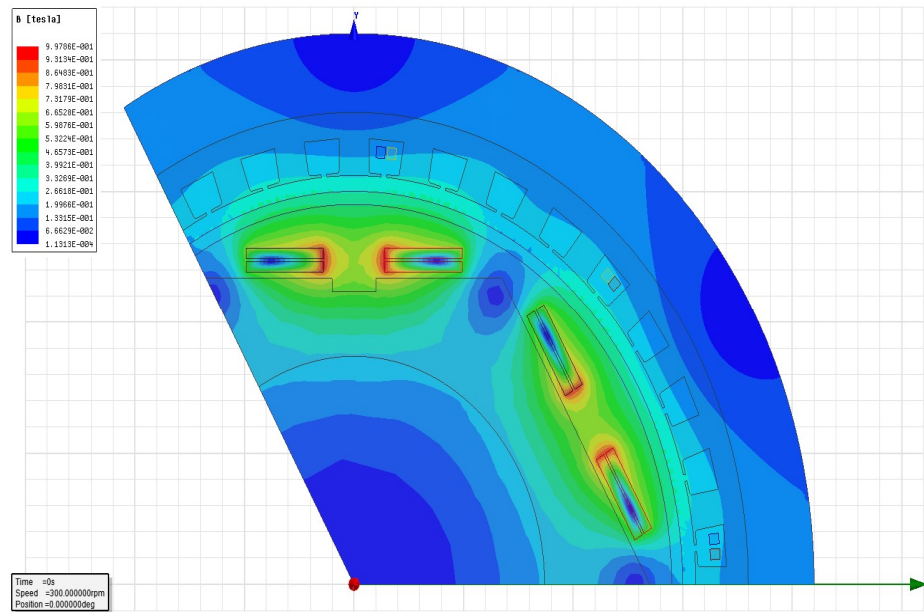


Fig. 6.14 Field pattern with an imbalance current of 5A (95A-90A) in adjacent coils

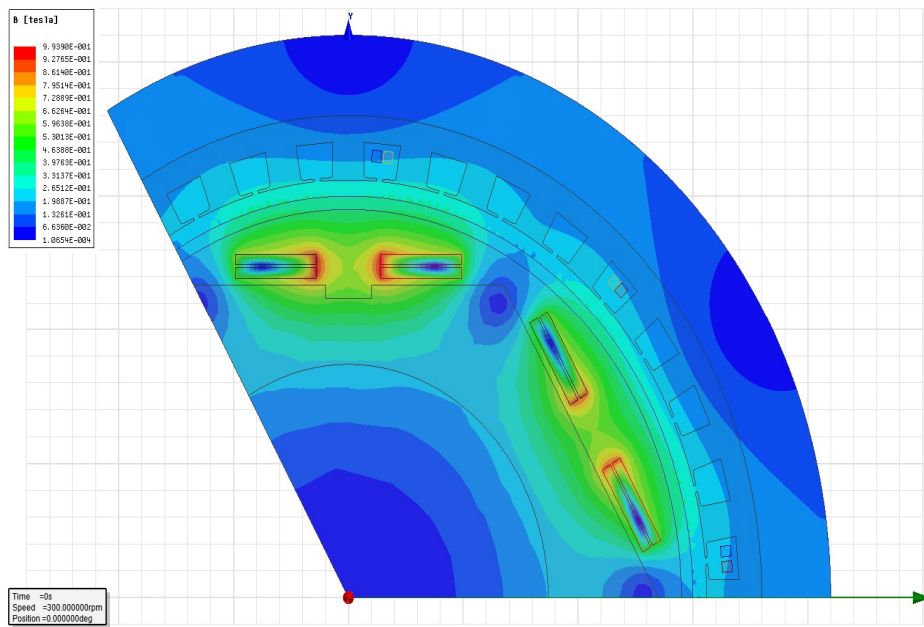


Fig. 6.15 Field pattern with an imbalance current of 10A (95A-85A) in adjacent coils

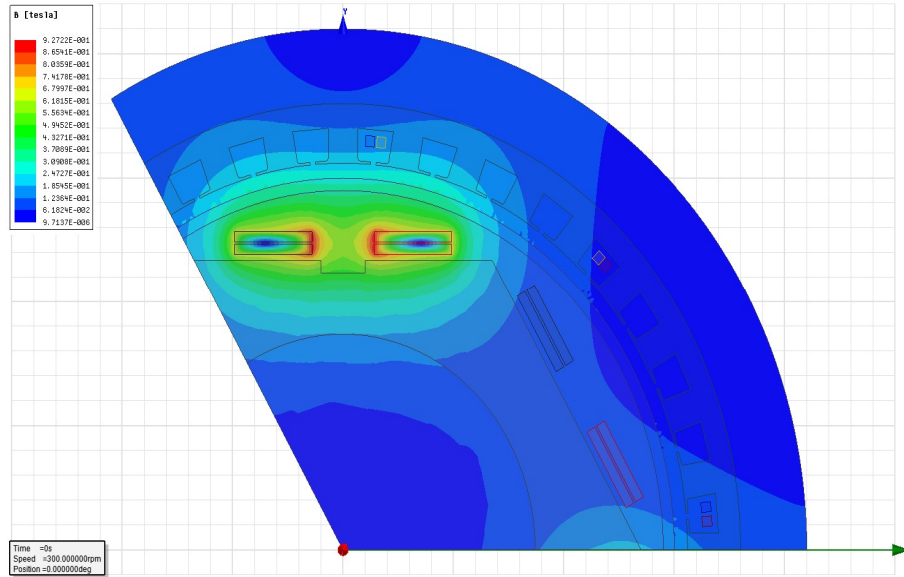


Fig. 6.16 Field pattern with an imbalance current of 95A (95A-0A) in adjacent coils

From the voltage plots, it is evident that an imbalance of 10A does not distort the waveform much but the THD value goes out of the standard limit of 5% for a grid connected operation at the point of common coupling. However, when one of the field coils runs out of operation then it causes a large distortion in the waveform and the THD value is correspondingly the highest.

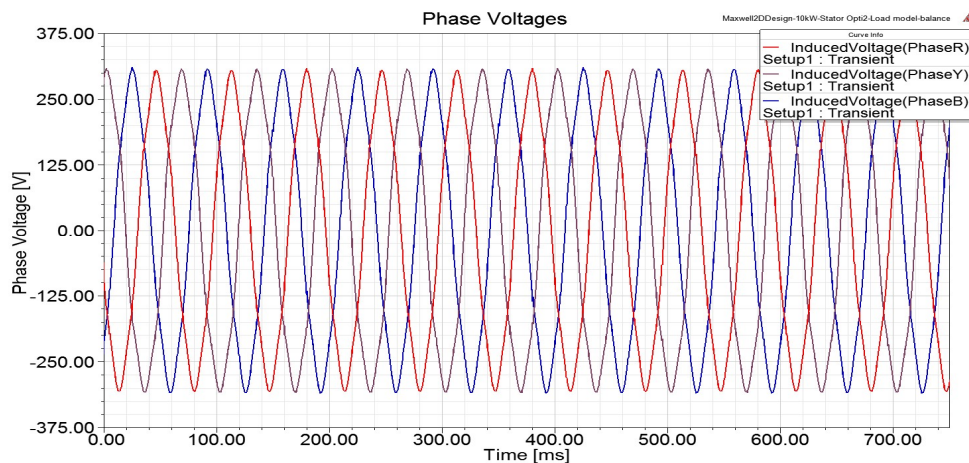


Fig. 6.17 Phase voltage plots with an imbalance current of 5A (95A-90A) in adjacent coils

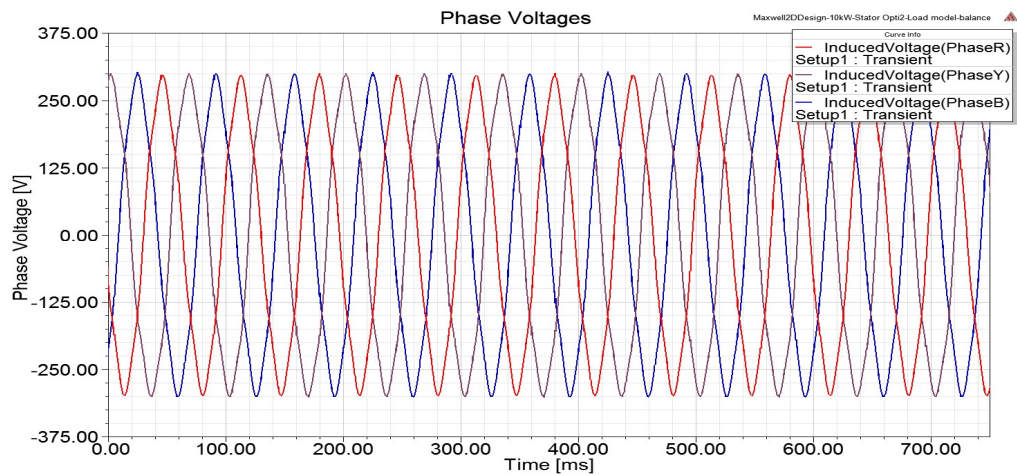


Fig. 6.18 Phase voltage plots with an imbalance current of 10A (95A-85A) in adjacent coils

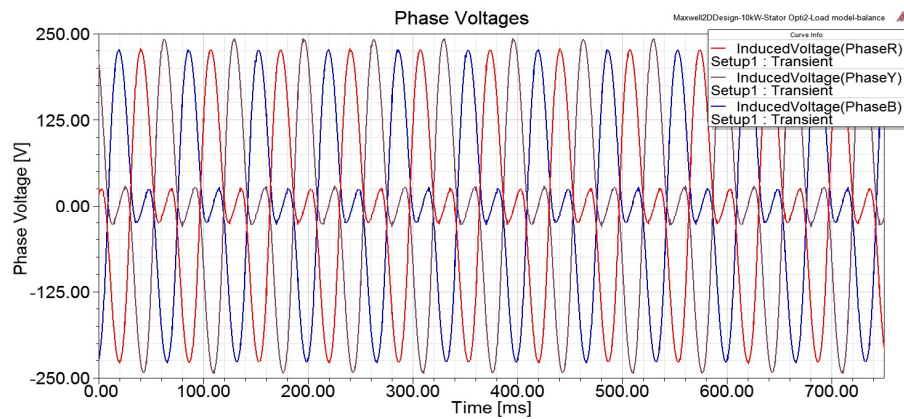


Fig. 6.19 Phase voltage plots with an imbalance current of 95A (95A-0A) in adjacent coils

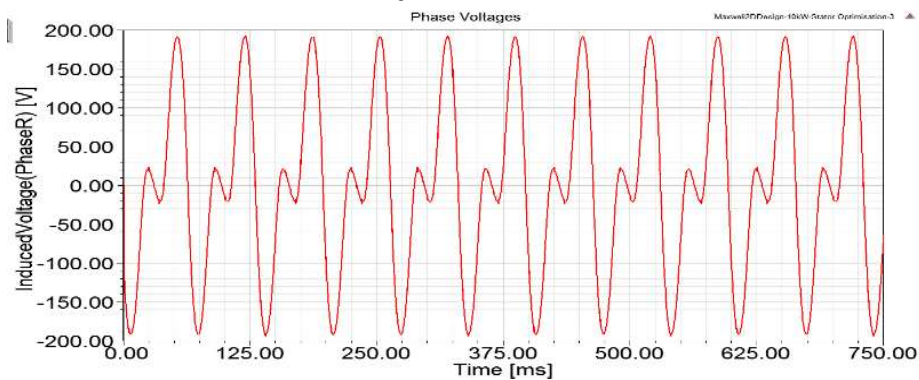


Fig. 6.20 Phase voltage plot of one phase separated, with an imbalance current of 95A (95A-0A) in adjacent coils

**Table 6.9. Imbalance current and Corresponding No-Load THD values for
design 2**

| Condition | THD(%) |
|-------------------------------|---------------|
| Balance | 4.29 |
| 5A Imbalance | 5.78 |
| 10A Imbalance | 7.81 |
| 95A-One coil breakdown | 78 |

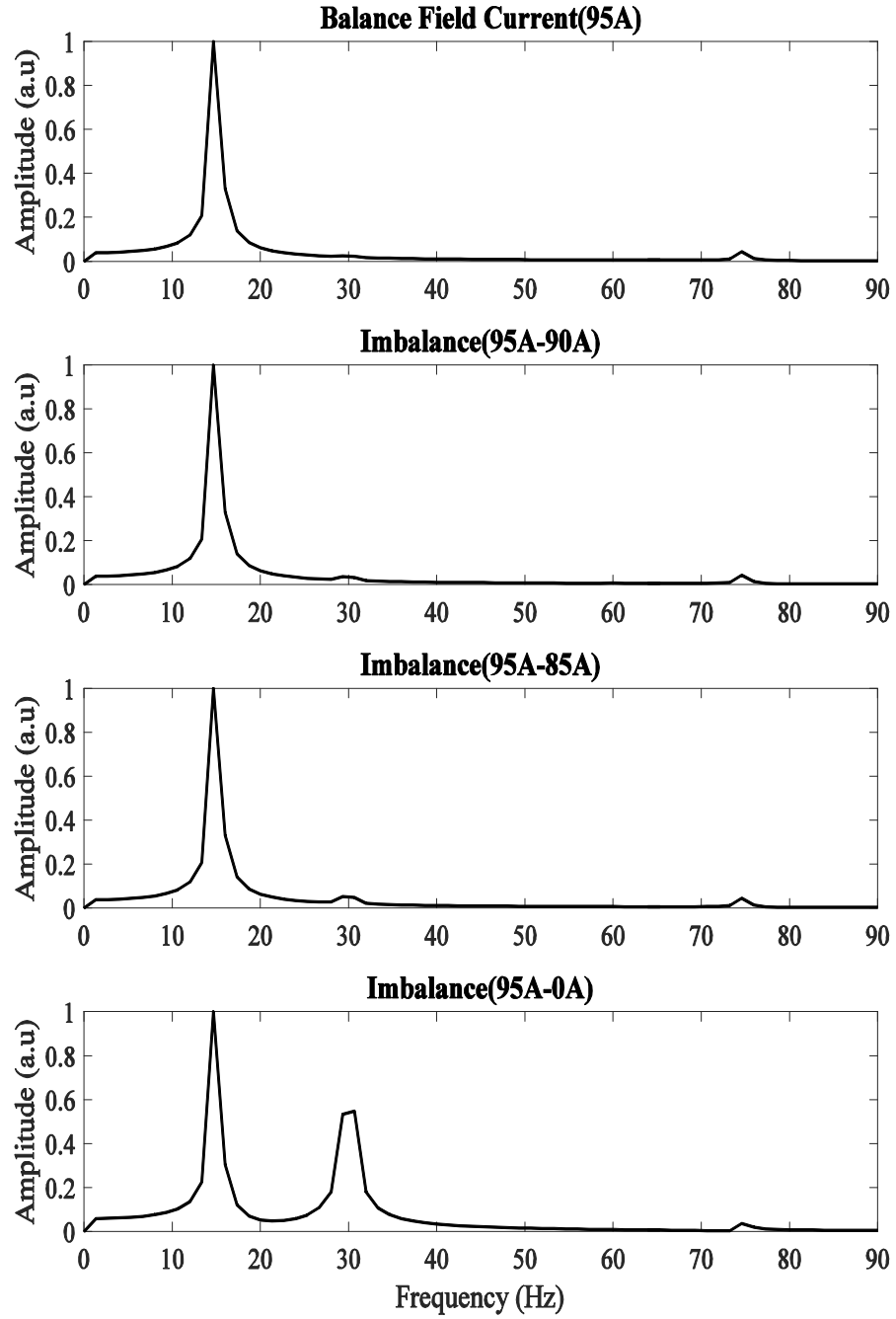


Fig. 6.21 The variation of THD with increased imbalance.

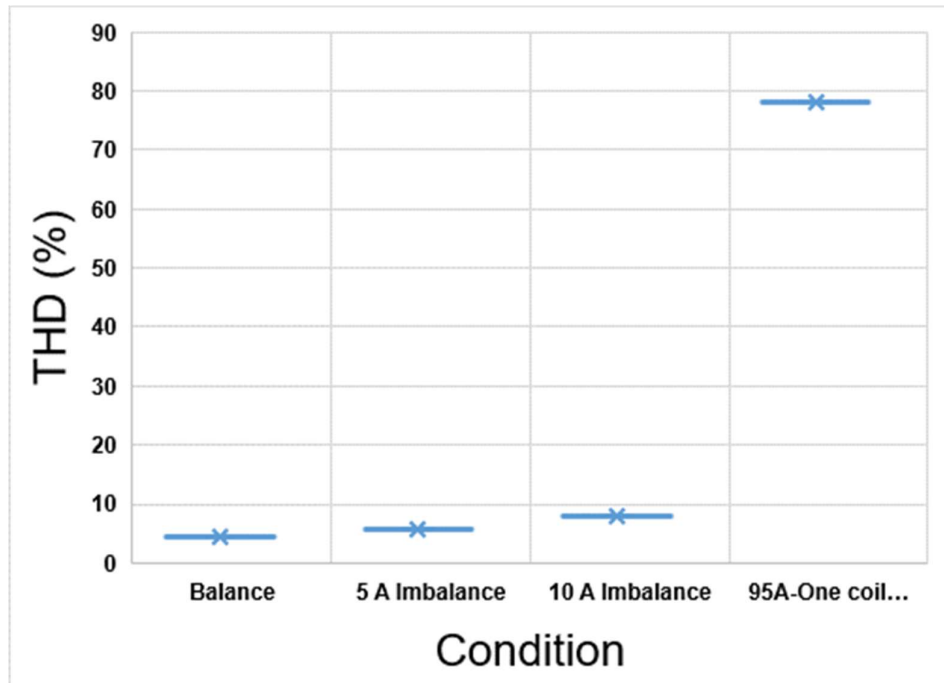


Fig. 6.22 THD (%) versus Imbalance condition(s)

Fig. 6.22 shows the variation of THD with the increase in the imbalance of field current. The imbalance current was increased in steps of 5A till 15A and it is observed that the increase in THD is linear and is within the standard range till an imbalance current of 10A, with an imbalance current of more than 10A the THD value lies outside the prescribed standards. Keeping a tolerance of 10A, the separate excitation mechanism can be implemented.

The presence of 2nd harmonic was anticipated and seemed obvious as the field uniformity determines the uniformity in the stator induced voltage waveform. The percentage increase with every 5A increase in imbalance is found to be 34.7%. At standalone operation, an imbalance of up to 10A can be tolerated. A complete breakdown of one of the coil causes a huge distortion in the induced voltage waveform and results in very large THD (78%) as seen in Table 6.9. This large harmonic distortion is bound to cause cumulative failure if the generator is grid

connected and needs to be identified and isolated at the earliest instance since the coil breakdown. In case, the generator is stand-alone operated, the large 2nd harmonics will affect the operation of sensitive electronic load and may result in failure.

As observed in Fig. 6.5 and in the sub-plots of Fig. 6.21, there is a component of 5th harmonic present in the FFT profile of the phase voltages, this is in accordance with the use of 2/3 pitch (Table. 6.1). However, the magnitude of the 5th harmonic is not affected by the different frequency of flux pump excitation or the imbalance in the field currents.

6.10 Effect of Imbalance on Torque

Torque of the generator is affected by the imbalance in field current, though the analysis and treatment of mechanical aspects of the flux pump excitation lies slightly out of scope for this thesis, a preliminary study on the torque related aspects is presented here and paves way for the future work which could be carried out using ANSYS.

In ANSYS, transient motion simulator generates rotational motion solutions based on the following Eq. 6.4 (ANSYS Online Help Manual, support.ANSYS.com):

$$J\beta + \lambda\omega = T_{em} + T_{load} \quad (6.4)$$

where J is the moment of inertia (kg.m^2), T_{em} is the computed electromagnetic torque (N.m), T_{load} is the external load torque, ω is the angular speed (rad/s), β is the angular acceleration (rad/s^2). λ is the damping factor (N.m.s).

In ANSYS, rotational motion simulation can be carried out in two ways:

- a. Considering mechanical transient
- b. Without considering mechanical transient.

When the simulation is carried out using case (a), the load torque is to be set to the desired value and the electromagnetic torque response can be plotted, the response follows the set load torque and the initial transient response, in this case, is the function of the system parameters. While using case (b) only the moving torque (electromagnetic torque) is calculated and can be plotted using rectangular plot option. The electromagnetic torque of a generator generally has ripples. The source of these ripples is generator side harmonic currents (Xia *et al.*, 2011). Since the harmonic analysis has been carried out in this work, it is logically extrapolated

to carry out preliminary analysis on torque effects as the imbalance in field currents would cause harmonics and the electromagnetic torque is expected to get affected.

6.10.1 Torque plot using condition (a)

The generator torque equation is given by, Eq. 6.5;

$$Torque = \frac{Power * 60}{2\pi * N} \quad (6.5)$$

where N is the speed of the machine in RPM.

For a power of 10 kW and speed 300 rpm, the torque value works out to be ~318 Nm. Setting the load torque value as 318 Nm in the motion setting the transient simulation is conducted and the electromagnetic moving torque is plotted. Fig. 6.23 shows the variation of moving-torque with respect to time for imbalance currents increasing in steps of 5A till 15A and then for the one coil breakdown scenario. It is observed that the initial transient response of torque is similar for all the imbalance conditions but for one coil breakdown, it is observed that the torque profile has sharp high spikes and this anomalous behaviour needs further detailed investigation.

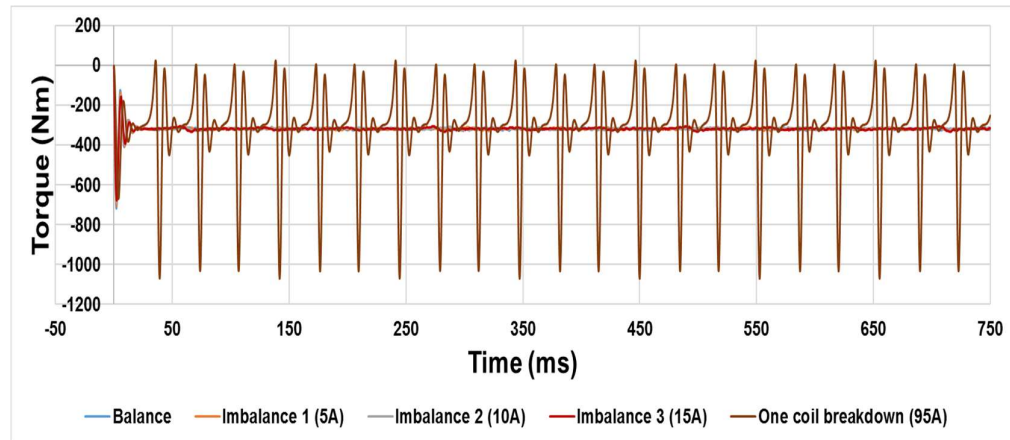


Fig. 6.23 Torque response comparison for various conditions of imbalance considering mechanical transient

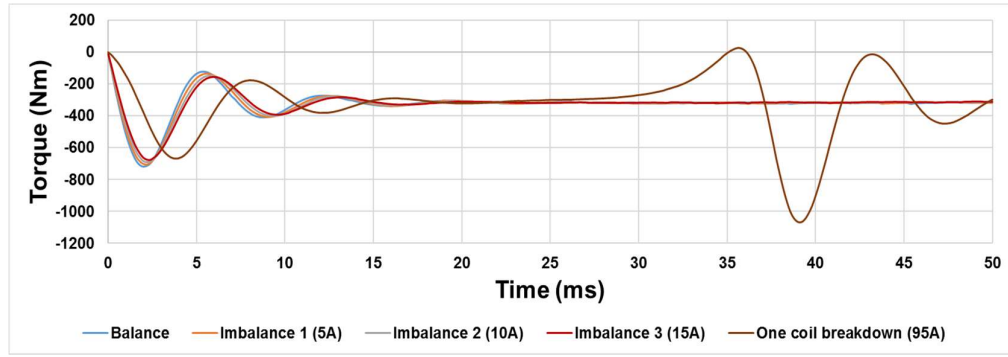


Fig. 6.24 Initial torque transients under different imbalance conditions

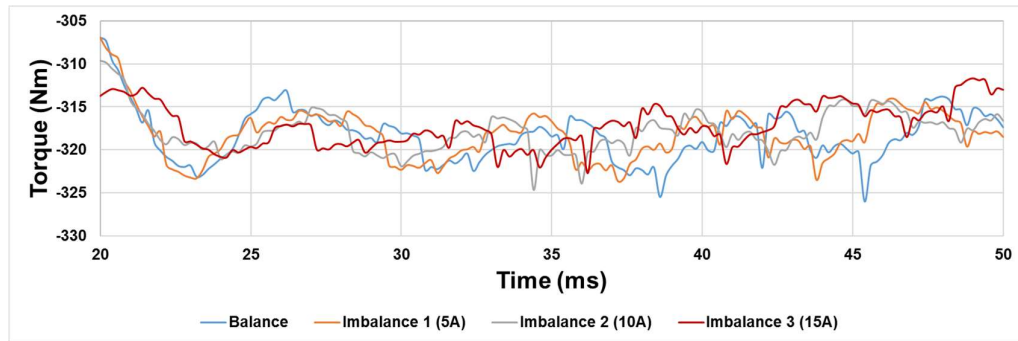


Fig. 6.25 Steady state torque ripples under lower imbalance conditions

From Fig. 6.24 it can be seen that the settling time for the torque is almost same for lower imbalances but increases by a large value for the largest imbalance condition. There is also a large spike observed for the largest imbalance and it needs further investigation. Fig. 6.25 shows the close up of torque ripple profile during the steady state condition for the lower imbalance currents. It can be observed they are periodic as expected and some intermediate spikes in the profile are the result of the meshing transitions.

6.10.2 Torque plot using condition (b)

When the mechanical transient is not considered, the load torque is not initialized to a particular value, and in such condition, torque varies as shown in Fig. 6.26, which shows the variation of torque with respect to time for imbalance currents increasing in steps of 5A till 15A and then for the one coil breakdown

scenario. It is observed that the torque oscillation is minimum with balanced field current and gradually increases with the increase in imbalance current.

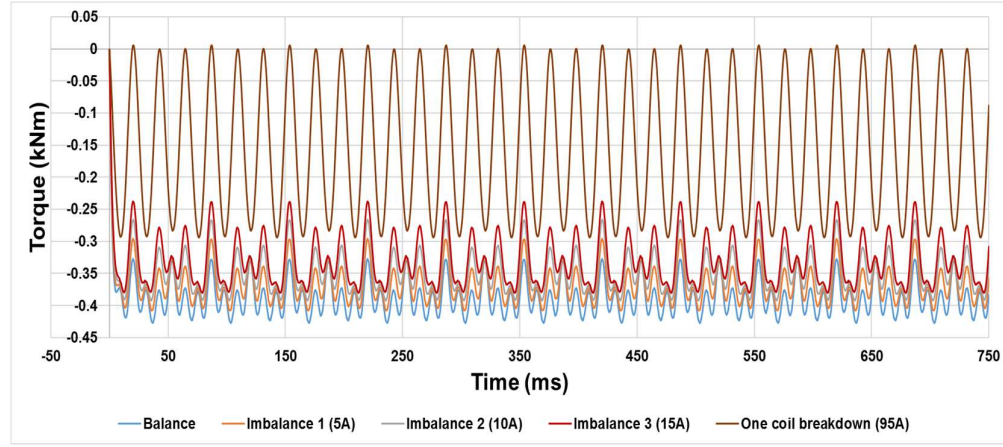


Fig. 6.26 Torque response comparison for various conditions of imbalance without considering mechanical transient

The worst-case scenario of one coil complete breakdown gives maximum torque oscillation and as seen with the THD plots (Fig. 6.22) the THD in such a situation is the highest, this condition can cause catastrophic failure of the system due to severe transients. The peak-to-peak ripple of the torque is also found to be increasing with the increase in imbalance current.

A preventive mechanism to avoid the complete breakdown has to be established in order to safeguard the system. Research on the design of HTS circuit breakers to prevent such catastrophic failure with the desired response in order to isolate the system in case of field coil breakdown is in progress by other research teams in the research group.

6.11 Concluding Remarks

6.11.1 Stator Design

The study of stator design effects on harmonic performance of the generator was carried out. It was observed that the flux pump could be successfully implemented as an alternative to DC source for exciting the field system in an HTS generator. The results indicate that the variation in the parameters such as stator yoke material, winding pitch and loading configuration affect the harmonic performance significantly.

The stator material has a significant effect on the THD of the induced voltage as well. The use of non-ferromagnetic stator material (G-10) led to a decrease in the THD. The different excitation frequencies of the flux pump had negligible effects on the THD of the induced voltage.

Based on the simulations with different winding pitches, a winding pitch of $2/3$ is the best suited for this machine. Use of $2/3$ pitch introduced a significant percentage of 5th harmonic, but from the results, it is seen that this does not increase the overall THD significantly and is not affected by the different frequencies of excitation.

The simulations on the load configurations indicate that S-D configuration would result in the smallest value of THD. THD is lesser with RL load than with R load. The stator design improvement measures carried out in order to place the stator conductors corresponding to the same phase in the same field strength has resulted in improvement in THD.

Stator design 2 resulted in lower THD with both R load and RL load. The load configuration also followed the same trend as Stator design 1. Most suitable

configuration to affirm minimum THD for a10 kW HTS generator has been suggested and is as outlined in Table 7.2

Table. 7.2 Machine configuration

| Parameter | Value |
|-------------------------------|--------------------------------------|
| 1. Stator Yoke Material | <i>FRP epoxy polymer (G-10)</i> |
| 2. Stator conductor placement | <i>Adjacent arrangement</i> |
| 3. Stator coil winding pitch | <i>2/3</i> |
| 4. Type of FP excitation | <i>Separate & Control band</i> |
| 5. Load configuration | <i>Star-Delta</i> |
| 6. Generator Operation | <i>Standalone and Grid connected</i> |

6.11.2 Separate Excitation

In order to avoid serial field coil damage in the event of a quench of one of the coils, separate excitation of coils has been examined as a potential solution. When the coils are separately excited, there is a possibility of imbalance in the field currents which is not the case when the coils are connected serially and excited by a single source. In order to understand the performance of the system in such condition, simulations were carried out with different values of field current in adjacent coils, and worst case scenario was simulated as well.

It was observed that the imbalance in field current due to separate excitation of the field coils results in the occurrence of 2nd harmonic which was not seen in the balanced case. The magnitude of the 2nd harmonic increases with the increase in the field current imbalance. Complete failure of one of the field coils results in a colossal THD and would affect the grid stability and the electronic loads.

It is also observed that the imbalance of $\sim 10\%$ of rated field current causes a THD increase of 3.5%. This can be considered as a tolerance level and further research on establishing a preventive mechanism to avoid imbalance and quench mechanism for the generator field coils has to be carried out.

The effect of imbalance of field current on the electromagnetic torque is dealt briefly in the next chapter. It is observed that torque is profoundly affected by the breakdown of one of the coils and can cause significant damage to the system. The initial observation paves the way for mechanical analysis of the system keeping torque and thermal aspects as focus points.

The effects of stator design on the harmonic performance of the generator were carried out. It has been observed that the flux pump can be an alternative to DC source for exciting the field system in an HTS generator, even for loaded conditions such as S-S or S-D configurations. The results indicate that the variation in the parameters such as stator yoke material, winding pitch and loading configuration affect the harmonic performance significantly.

The stator material has a significant effect on the THD of the induced voltage. The use of non-ferromagnetic stator material (G-10), leads to a decrease in the THD. The different excitation frequencies of the flux pump have negligible effects on the THD of the induced voltage. Based on the simulations with different winding pitches, a winding pitch of $2/3$ is the best suited for this machine. Though the use of $2/3$ pitch introduces a high percentage 5th harmonic (Table. 6.1), from the results it is seen that this does not increase the overall THD significantly and is not affected by the frequencies of excitation.

The simulations on the load configurations indicate that S-D configuration would result in the smallest value of THD. THD is lesser with RL load than with R load. Most suitable configuration with respect to the stator yoke material, winding pitch and load configuration to minimise THD of 10 kW HTS generator has been established and is presented in the concluding chapter.

The stator design improvement measures carried out in order to place the stator conductors corresponding to the same phase in the same field strength has resulted in improvement in THD. Stator design 2 resulted in lower THD with R load and RL load both. The load configuration also followed the same trend as Stator design 1.

It is observed that the imbalance in field current due to separate excitation of the field coils results in the occurrence of 2nd harmonic which is not observed in the balanced case. The magnitude of the 2nd harmonic increases with the increase in the field current imbalance, complete failure of one of the field coils results in a very large THD and would cause damage to the grid stability and the electronic loads.

The effect of imbalance of field current on the electromagnetic torque has been briefly dealt. It is observed that torque is highly affected by the breakdown of one of the coils and can cause significant damage to the system. The initial observation paves way for mechanical analysis of the system keeping torque and thermal aspects as focus points. Studies to prevent the complete breakdown of field coils due to quenching or isolate the system in case of such failure is essential to implement the separately excited system efficiently. These studies are outside the scope of this thesis and put forth the indicators for future work.

Chapter 7. Conclusions and Future Work

In this chapter, the summary of results and conclusions of the research are provided. With the successful completion of the research work and accomplished objectives, the findings are provided as inputs to the ongoing HTS Rotating Machinery international project being executed in collaboration with research groups in New Zealand, South Korea and China.

7.1 Conclusions

The research work presented in this thesis has involved experimental, and simulation work with the output(s) of the experimental work provided as input(s) to the simulation models. This section summarises results and provides a comparative analysis of results observed at various stages of the research.

The experimental study on two different types of flux pump has provided a thorough understanding of the behaviour of flux pump excitation with two completely different configurations, measurement of the open circuit voltage of the flux pump stator is one of the important contributions of this work. The measured voltage signals of the flux pump stators were utilised as inputs to the FEM model in the subsequent phases of the research. It is seen that the rate of rising of current varies directly with the frequency of excitation both in cold rotor flux pump and warm rotor flux pump. The saturation current in both the configurations of flux pump varies inversely with the distance of separation. Despite a reduction in the maximum output current at increased flux gaps with warm rotor flux pump, the device was still capable of injecting current into the experimental circuit at (gaps) $d > 10$ mm. The result was significant because the mechanical strength and thermal performance of a composite cryostat wall are closely related to its physical dimensions.

In the case, of warm rotor flux pump, practical values of stator currents for an HTS application were achieved at higher separation distances. The reason was the presence of a ferromagnetic yoke on the stator side of the flux pump which causes flux concentration. The presence of a ferromagnetic yoke will lead to additional heat in the system due to eddy current and hysteresis.

In an HTS application, the presence of a heat source in the system or surroundings is to be avoided as much as possible to reduce the load on the cryogenic system. Fibre Reinforced Epoxy polymer, also called G-10, was checked as an alternative to the ferromagnetic yoke. Due to its lower thermal conductivity property, G-10 is a suitable material for cryogenic applications. As the plan is to use the flux pump technology for an HTS synchronous generator with a wind turbine, the quality of power would not be good if there is no stable field in the rotor coils and would need a customised power converter to make it usable, which may not be economical.

The voltage profile and the dynamic resistance aspects of the flux pump were studied, and it was found from the experimental and analytical results that the magnitude of dynamic resistance and the frequency dependencies of dynamic resistance do not affect the performance of the flux pump as the excitation source for the HTS generator. The anomalous voltage profile observed across the flux pump stator indicated quasi-dc emf and the current oscillations did not affect the field stability in the FEM study of HTS generator.

An analytical study based on FEM was carried out, and it reflects that the non-conventional HTS generator design can be operated in standalone and grid-connected modes by utilizing the suggested configuration and mechanical optimizations suggested in the Future work.

The experimental and simulation results prove flux pump to be an alternative to DC for exciting the field system in an HTS generator. Use of flux pump for exciting the HTS field coils of a generator avoids the thermal link between the cryogenic and non-cryogenic environment, thus decreasing the thermal loading on the cryogenic system.

A performance analysis was carried out on a 10 kW HTS generator, and it was established that with the use of ferromagnetic yoke on the stator side, there is significant fringing effect in the field pattern and was reflected as distortion in the induced voltage. From the harmonic analysis, it was seen that the stator material has a significant effect on the THD of the induced voltage. The variation in excitation frequencies of the flux pump had negligible effects on the field pattern and the THD of the induced voltage.

Development of FEM model of the 10 kW HTS generator has resulted in carrying out studies keeping various factors in consideration and has aided in proposing a suitable optimum configuration to obtain minimal THD value and avoid a serial system failure in the event of a quench.

7.2 Future Work

HTS based power applications are a potential solution for applications requiring high power densities and recent research and development in the domain reaffirms the possibilities and promises commerciality of HTS applications.

The effect of various parameters of flux pump that affect the scalability of the flux pump for different rating of the generator is another potential research work. The torque imbalance and other mechanical aspects associated with the HTS generator need to be studied in detail in order to facilitate the commercialization of HTS generators. Field based testing and grid connected operation of the generator needs to be analysed from power system operation and stability perspective.

References

- A, B.C., Synchronous machine starting system, 1931, Google Patents.
- ABB, "Technical Note," (2014). [Online]. Available: library.e.abb.com/public/8d5deb3fe4638051c1257c9400508282/Technical%20note%20Winding%20pitch%20LR_040214.pdf. [Accessed 18 February 2016]
- Appleton, A. D., and Prothero, D. H., (1998), An introduction to the power applications of superconductivity. In B. Seeber (Ed.), Handbook of applied superconductivity (Vol. 2, pp. 1487-1495). Bristol, UK : Institute of Physics Publishing.
- Arepoc, (2007), High Linearity Hall Probes for Room and Cryogenic Temperatures. Arepoc s.r.o.
- Bai, Z., Yan, G., Wu, C., Ding, S., Chen, C., (2010), "A novel high temperature superconducting magnetic flux pump for MRI magnets", Cryogenics, Volume 50, Issue 10, Pages 688-692, ISSN 0011-2275.
- Barnes, P. N., Sumption, M. D., Rhoads, G. L., (2005), "Review of high power density superconducting generators: Present state and prospects for incorporating YBCO windings." Cryogenics 45(10–11): 670-686.
- Bean, C. P., (1964), "Magnetization of High-Field Superconductors." Reviews of Modern Physics 36(1): 31-39.
- Bednorz, J. G. and Müller, K. A., (1986), "Possible highT_c superconductivity in the Ba–La–Cu–O system." Zeitschrift für Physik B Condensed Matter 64(2): 189-193.
- Bondarev, B., (2015), "New Theory of Superconductivity. Method of Equilibrium Density Matrix. Magnetic Field in Superconductor.", Open Access Library Journal, 2, 1-20.
- Brambilla, F. G. R., (2009), "Simulating Superconductors in AC Environment: Two Complementary COMSOL Models". COMSOL Conference.

Bumby, C. W., Jiang, Z., Storey, J. G., Pantoja, A. E and Badcock, R. A., (2016), "Anomalous open-circuit voltage from a high-T_c superconducting dynamo." *Applied Physics Letters* 108(12): 122601

Bumby, C. W., Badcock, R. A., Sung, H. J., Kim, K. M., Jiang, Z., Pantoja, A. E., Bernardo, P., Park, M., and Buckley, R. G., (2016), "Development of a brushless HTS exciter for a 10 kW HTS synchronous generator." *Superconductor Science and Technology* 29(2): 024008.

Bumby, C. W., Pantoja, A. E., Sung, H. J., Jiang, Z., Kulkarni R. and Badcock, R. A., (2016), "Through-Wall Excitation of a Magnet Coil by an External-Rotor HTS Flux Pump." *IEEE Trans. on Applied Superconductivity* 26(4): 1-5.

Chen, Z. and Spooner, E., (2001), "Grid Power Quality with Variable Speed Wind Turbines." *IEEE Trans. on Energy Conversion*, Vol.16, No. 2.

Coombs, T., Hong, Z., Zhu, X., (2008), "A thermally actuated superconducting flux pump." *Physica C: Superconductivity* 468(3): 153-159.

Cyrot. M., 1973, *Rep. Prog. Phys.* 36 103

Ferendeci, A.; Mawardi, O.; Melfi, M.; Laquer, H. Flux pump excited brushless alternator. *IEEE Trans. on Magnetics*. 1981, 17, 146–148.

Gerlando, A. Di, Foglia, G., Iacchetti, M. F., and Perini, R., (2010), "Simulation and test results of grid connected WECSs with diode rectifiers and modular PMSGs," *The XIX International Conference on Electrical Machines - ICEM*, Rome, 2010, pp. 1-6.

Gupta, R., *et al.*, (2013), "High Field HTS Solenoid for a Muon Collider - Demonstrations, Challenges and Strategies," *IEEE Trans. on Applied Superconductivity*, vol. 24, pp. 4301705.

Hazelton, D. W., Selvamanickam, V., (2009). "Recent Developments in 2G HTS Coil Technology." *IEEE Trans. on Applied Superconductivity*, 19(3): 2218-2222.

Hoffmann, C., Pooke. D and Caplin. A. D., (2011), "Flux Pump for HTS Magnets." IEEE Trans. on Applied Superconductivity, 21(3): 1628-1631.

Hoffmann, C., Walsh, R., Karrer-Mueller, E., and Pooke. D., (2012), "Design Parameters for an HTS Flux Pump." Physics Procedia 36(0): 1324-1329.

http://www.sensorsportal.com/HTML/DIGEST/may_2014/Vol_170/P_2067.pdf

<https://support.ANSYS.com/portal/site/ANSYSCustomerPortal/template.fss?file=%2Fsolutions%2Fattach%2FMAXWELL.pdf>

Hughes, A., (2013), "Electric Motors and Drives: Fundamentals, Types and Applications", Elsevier Science.

Ishmael, S., Goodzeit, C., Masson, P., Meinke, R., and Sullivan, R., (2008), "Flux Pump Excited Double-Helix Rotor for Use in Synchronous Machines." IEEE Trans. on Applied Superconductivity, 18(2): 693-696.

Jensen, B. B and Abrahamsen, A. B., (2011), "Modelling, construction, and testing of a simple HTS machine demonstrator," 2011 IEEE Energy Conversion Congress and Exposition, Phoenix, AZ, pp. 1636-1640.

Jeong, S., and Kim, Y., (2010). "Thermal anchoring of conduction-cooled current leads for superconductivity applications near liquid nitrogen temperature." Cryogenics 50(4): 287-291.

Jiang, Z., Hamilton, K., Amemiya, N., Badcock, R. A., and Bumby, C. W., (2014), "Dynamic resistance of a high- T_c superconducting flux pump." Applied Physics Letters 105(11): 112601-112601-112604.

Jones, H., (2008), "Superconductors in the transmission of electricity and networks", Energy Policy, 36(12), 4342-4345.

K. Ogasawara, K. Yasukochi, S. Nose, and H. Sekizawa, "Effective resistance of current-carrying superconducting wire in oscillating magnetic fields 1: Single core composite conductor," Cryogenics, vol. 16, no. 1, pp. 33–38, Jan. 1976.

Kalsi, S. S, (2011), Application of High Temperature Superconductors to Electric Power Equipment, Wiley.

Kalsi, S. S, Henderson, N., Gritter, D., Nayak, O., and Gallagher, C., (2005), “Benefits of HTS technology to ship systems”, IEEE Symposium on Electric Ship Technologies. Philadelphia PA: 437-443.

Kalsi, S. S, Weeber, K., Takesue, H., Lewis, C., Neumueller, H. W., and Blaugher, R. D., (2004), “Development status of rotating machines employing superconducting field windings,” Proceedings of the IEEE 92(10): 1688-1704.

Karmaker, H., Ho, M., and Kulkarni, D., (2015), “Comparison Between Different Design Topologies for Multi-Megawatt Direct Drive Wind Generators Using Improved Second Generation High Temperature Superconductors,” IEEE Trans. on Applied Superconductivity, vol.25, no.3, pp. 1-5.

Khalf, M. A., Wamkeue, R., and Aguglia, D., (2012), “Finite element approach for performances prediction of a small synchronous generator using ANSYS software,” (CCECE), 25th IEEE Canadian Conference on Electrical & Computer Engineering, Montreal, QC, pp. 1-4.

Kim, Y. B., Hempstead, C. F., and Strnad, A. R., (1963), “Magnetization and Critical Supercurrents”, Physical Review, 129(2): 528-535.

Kim, Y. B., Ko, J., Jeong, S., and Lee, S.S., (2006), “Experiment and analysis for a small-sized flywheel energy storage system with a high-temperature superconductor bearing”, Superconductor Science and Technology 19(2): 217.

Ko, T. K., and Mawardi, O. K., (1989), “Parametric representation of a superconducting high-current generator.” IEEE Trans. on Magnetics on 25(5): 4346-4349.

Kostas, Gavroglu, B., (2010), “Dirk van Delft. Freezing Physics: Heike Kamerlingh Onnes and the Quest for Cold.” Isis 101(1): 247-249.

Kulkarni, R., Prasad, K., and Lie, T.T., (2015), "Flux pump for HTS rotating machinery applications," 2015 IEEE Eindhoven PowerTech, Eindhoven, pp. 1-5.

Kulkarni, R., Prasad, K., Lie, T.T., Badcock, R. A., Bumby, C.W., and Sung, H. J., (2016), "FEM and performance analysis of 10 kW HTS generator with flux pump excitation," 2016 IEEE International Conference on Power System Technology (POWERCON), Wollongong, NSW, pp. 1-6.

Lewis, C., and Muller, J., "A direct drive wind turbine HTS generator," IEEE Power Engineering Society General Meeting, Tampa FL, the United States, pp. 1-8, 2007.

Liang, Y., and Yang, Y., (2016), "Performance Analysis of 10 MW HTS Wind Generator based on 2D Transient FEA," IEEE Power and Energy Technology Systems Journal, vol. 4, no. 1, pp. 10-15.

Liu, T., Huang, S., Deng, Q., Pu, Q., and Huang, K., (2011), "Effect of the number of slots per pole on performance of permanent magnet generator direct-driven by wind turbine," 2011 International Conference on Electrical Machines and Systems, Beijing, pp. 1-4.

Lousberg, G. P., Ausloos, M., Vanderbemden, Ph., and Vanderheyden, B., (2008), "Bulk high- T_c superconductors with drilled holes: how to arrange the holes to maximize the trapped magnetic flux?," Superconductor Science and Technology 21(2): 025010.

Lukasik, B., Goddard, K. F and Sykulski, J. K., (2011), "Finite Element Assisted Method of Estimating Equivalent Circuit Parameters for a Superconducting Synchronous Generator with a Coreless Rotor," IEEE Trans. on Magnetics, vol.45, no.3, pp.1226-1229.

M. P. Oomen et al., "HTS flux pump for cryogen free HTS magnets," IEEE Trans. Appl. Supercond., vol. 15, no. 2, pp. 1465–1468, Jun. 2005.

M. P. Oomen, J. Rieger, M. Leghissa, B. ten Haken, and H. H. J. ten Kate, "Dynamic resistance in a slab-like superconductor with $J_c(B)$ dependence," Supercond. Sci. Technol., vol. 12, no. 6, pp. 382–387, Jun. 1999

Mawardi, O.; Muelder, S.; Michelotti, R. Brushless superconducting alternators. IEEE Trans. on Magnetics. 1977, 13, 780–783.

McConnell, B. W., (2000), "Transformers-a successful application of high temperature superconductors," IEEE Trans. on Applied Superconductivity, 10(1), 716- 720.

McConnell. B. W, Mehta. S.P., and Walker, M. S., (2000). "HTS transformers," in IEEE Power Engineering Review, vol. 20, no. 6, pp. 7-11.

Mehta, S. P., Aversa, N., and Walker, M. S., (1997), "Transforming transformers [superconducting windings]," in IEEE Spectrum, vol. 34, no. 7, pp. 43-49.

Min, Z., *et al.* (2012). "Design Methodology of HTS Bulk Machine for Direct-Driven Wind Generation." IEEE Trans. on Applied Superconductivity, 22(3): 5201804-5201804.

Mulholland, T. P. S. a. B. M. Joseph., (2003). "Analysis of Future Prices and Markets for High Temperature Superconductors", U.S. Department of Energy.

Murakami, K. T. a. M. (2003). "High-temperature superconductor bulk magnets that can trap magnetic fields of over 17 Tesla at 29 K.", Nature (421): 4.

Muta, I.; Tsukiji, H.; Hoshino, T.; Mukai, E. Electrical characteristics of fully superconducting synchronous generator in persistent excitation mode. IEEE Trans. on Magnetics. 1992, 28, 434–437.

Muta, I.; Tsukiji, H.; Hoshino, T.; Mukai, E. Output power limit of 200 MW class brushless superconducting generator excited with magnetic flux-pump. IEEE Trans. on Applied Superconductivity. 2001, 11, 2335–2338.

Nakamura, T., Sugano, M., Doi, T., and Amemiya, N., (2010), “Flux Pumping Effect of HTS Films in a Traveling Magnetic Field.” IEEE Trans. on Applied Superconductivity, 20(3): 1033-1036.

Nakano, M., Kometani, H., and Kawamura, M., (2006), “A study on eddy-current losses in rotors of surface permanent-magnet synchronous machines”, IEEE Trans. on Industrial Applications, vol. 42, no. 2, pp. 429-435.

Nelson, J. P., (2004). “A better understanding of harmonic distortion in the petrochemical industry,” IEEE Trans. on Applied Superconductivity, 40(1), pp. 220-231. doi: 10.1109/TIA.2003.821802

Nick, W., Nerowski, G., Neumüller, H.-W., Frank, M., Hasselt, P van., Frauenhofer, J., Steinmeyer, F., (2002). “380 kW synchronous machine with HTS rotor windings—development at Siemens and first test results.”, Physica C: Superconductivity 372–376, Part 3(0): 1506-1512.

Pantoja. A. E, Jiang, Z., Badcock, R. A., and Bumby, C. W., (2016) , “Impact of stator wire width on output of a dynamo-type HTS flux pump,” IEEE Trans. on Applied Superconductivity, vol. 26, no. 8, art. no. 4805208.

Park, M., Jo, Y-S., Ryu, K-S., (2007), “Recent Activities of HTS Power Application in Korea.” International Journal of Applied Ceramic Technology 4(3): 217-224.

Parkinson, B. J., Slade, R., Mallett, M. J. D., and Chamritski, V., (2013), “Development of a Cryogen Free 1.5 T YBCO HTS Magnet for MRI,” IEEE Trans. on Applied Superconductivity, vol. 23, pp. 4400405-4400405.

Persarvet, G. “Evaluation of Finite Element Method Based Software for Simulation of Hydropower Generator - Power Grid Interaction”. Sweden, Uppsala University. Master Programme in Engineering Physics: 47.

Pina, J. M., *et al.* (2011). “Research and Development of Alternative Concepts in HTS Machines.” IEEE Trans. on Applied Superconductivity 21(3): 1141-1145.

Polinski, J. (2010, 08 30). "Materials in cryogenics. Geneva: European Course in Cryogenics 2010", CERN.

Poole, C. P., (2000). "Handbook of superconductivity". ed. San Diego, Calif;, London: Academic Press.

Qu, R., Liu, Y., and Wang. J., (2013), "Review of Superconducting Generator Topologies for Direct-Drive Wind Turbines," IEEE Trans. on Applied Superconductivity, 23(3): 5201108-5201108.

R. C. Duckworth, Y. F. Zhang, T. Ha, and M. J. Gouge, "Dynamic resistance of YBCO-coated conductors in applied AC fields with DC transport currents and DC background fields," IEEE Trans. Appl. Supercond., vol. 21, no. 3, pp. 3251–3256, Jun. 2011

Reis. C. T., Mehta, S. P., McConnell. B. W., and Jones, R.H., (2002), "Development of high temperature superconducting power transformers," IEEE Power Engineering Society Winter Meeting. Conference Proceedings (Cat. No.02CH37309), 2002, pp. 151-156 vol.1.

Say, M.G., "Alternating Current Machines" (4th.ed.) Pitman Publishing Ltd. 1976

Schonek., J, "Cahier technique no. 202 The singularities of the third harmonic", ECT 202(e) Feb 2001, Schneider Electric.

Seo, J. H., Chung, T. K., Lee, C. G., Jung, S. Y., and Jung, H. K., (2009), "Harmonic iron loss analysis of electrical machines for high-speed operation considering driving condition", IEEE Trans. on Magnetics., vol. 45, no. 3, pp. 4656-4659, Oct. 2009.

Seo, J. H., Han, K. J., Choi, H. S., Lee, S. H., Hahn, S., and Lee, H., (2014), "Comparison Study on Harmonic Loss of MW-Class Wind Generators With HTS Field Winding," IEEE Trans. on Applied Superconductivity 24(3): 1-5.

Seo, J. H., Han, K. J., Choi, H.S., Lee, S. H., Hahn, S., and Lee, H., (2014), "Comparison Study on Harmonic Loss of MW-Class Wind Generators with HTS Field Winding," IEEE Trans. on Applied Superconductivity. 24(3): p. 1-5

Seo, J. H., Kwak, S. Y., Jung, S. Y., Lee, C. G., Chung, T. K., and Jung, H. K., (2009), "A research on iron loss of IPMSM with a fractional number of slot per pole", IEEE Trans. on Magnetics, vol. 45, no. 3, pp. 1824-1827, Mar. 2009.

Shafaie, R., and Kalantar, M., (2013), "Design of a 10-MW-Class Wind Turbine HTS Synchronous Generator With Optimized Field Winding," IEEE Trans. on Applied Superconductivity 23(4).

Sung, H. J., Badcock, R. A., Jiang, Z., Choi, J., Park, M., and Yu, I. K., (2016), "Design and heat load analysis of a 12 MW HTS wind power generator module employing a brushless HTS exciter," IEEE Trans. on Applied Superconductivity, vol. 26, no. 4, Art. no. 5205404.

Sung, H. J., Go, B. S., Jiang, Z., Park, M., Yu, I. K., (2016), "Heat loss analysis-based design of a 12 MW wind power generator module having an HTS flux pump exciter," Phys. C, vol. 530, pp. 133–137.

T. Ackermann, "Wind Power in Power Systems", ISBN: 0-470-85508-8, J. Wiley&Sons, Chichester (UK), 2005

Tsukamoto, O., (2005), "Roads for HTS power applications to go into the real world cost issues and technical issues", 1st Asian Conference on Applied Superconductivity and Cryogenics (ASAC 2003). Japan, Elsevier. 45: 3-10.

van de Klundert, L. J. M., ten Kate, H. H. J., (1981), "Fully superconducting rectifiers and fluxpumps Part 1: Realized methods for pumping flux." Cryogenics 21(4): 195-206.

Van Sciver, S., (2012), "Low-Temperature Materials Properties in Helium", Cryogenics (pp. 17-58). Springer Science+Business Media.

Wang, J., *et al.* (2002). "The first man-loading high temperature superconducting Maglev test vehicle in the world." Physica C: Superconductivity 378–381, Part 1(0): 809-814.

Wang, J., Qu, R., and Liu, Y., (2013), "Comparison Study of Superconducting Generators with Multiphase Armature Windings for Large-Scale Direct-Drive

Wind Turbines," in IEEE Trans. on Applied Superconductivity, vol. 23, no. 3, pp. 5201005-5201005.

Wipf, S., (1968), "Flux pumps with moving magnetic fields," IEEE Trans. on Magnetism, 4(3): 493-493.

Wolfus, Y., Fleger, Y., Friedman, A., Kopansky, F., Kalisky, B., Yeshurun, Y., Bar-Haim, Z., Ron, Z., Ying, L., Pundak, N., (2004), "Estimation of the critical current of BSCCO coils based on the field dependent I-V curves of BSCCO tapes," Physica C: Superconductivity, vol. 401, pp. 222-226.

Wu, M. K., Ashburn, J. R., Torng, C. J., Hor, P. H., Meng, R. L., Gao, L., Huang, Z. J., Wang, Y. Q., and Chu, C. W., "Superconductivity at 93 K in a new mixed-phase Y-Ba-Cu-O compound system at ambient pressure," Physical Review Letters 58(9): 908-910.

Zakarian, V. L., Kaiser, M. J., (1999), "Computer-aided design of synchronous generators with comb rotors," Applied Mathematical Modelling 23(1): 1-18.

Zhang, G., Campbell, A. M., Rastogi, A., Coombs, T., and Dai, S., (2006), "Numerical Simulation of Magnetic Fields in YBCO High Temperature Superconducting Flywheel Model," IEEE Trans. on Applied Superconductivity 16(2): 1578.

Zhang, W., Xia, D., Zhang, D., and Zhang, G., (2014), "Parameter Design by a Novel Method and Optimization of the Field Coil for a 500 kW Air-Gap HTS Generator." IEEE Trans. on Applied Superconductivity, 24(3): 1-4.

Zhang, Z., Matveev, A., Øvrebø, S., Nilssen, R., and Nysveen, A., (2011), "State of the art in generator technology for offshore wind energy conversion systems," Proc. of IEMDC, Canada, May, pp.1131-1136.

Zhang, Z., Molinas, M., Matveev, A., Nilssen, R., and Nysveen, A., (2012), "Efficiency calculation and improvement of a large-diameter ironless permanent magnet generator," 15th International Conference on Electrical Machines and Systems (ICEMS), Sapporo, pp. 1-6.

Appendices

Appendix-A: Conference Proceedings and Journal publication

Appendix- B: Additional Results

Appendix-C: Datasheets

Appendix-D: Stator Design Data & Material properties

Appendix- A

Conference Proceedings and Journal publication

1. IEEE-Powertech, Eindhoven 2015

Flux pump for HTS rotating machinery applications

Ravichandra Kulkarni¹, Krishnamachar Prasad, Tek Tjing Lie

School of Engineering, Auckland University of Technology, Private Bag 92006, Auckland 1142

(¹email:rkulkarn@aut.ac.nz).

Abstract— High Temperature Superconducting (HTS) machines offer several benefits over the conventional machines. With the advent of YBCO materials, research and development in HTS applications has gained significant impetus. The application of flux pump has its own advantages over the conventional mechanism for magnetic field generation in superconductors. This paper reviews few relevant works and presents preliminary results from experiments carried out to provide justification on the application of flux pump for generating magnetic flux in a rotating machine.

Keywords: High Temperature Superconductors (HTS), Low Temperature Superconductors (LTS), YBCO (Yttrium Barium Cupric Oxides), Flux pump, Superconducting generator

INTRODUCTION

(a) HTS materials

High temperature superconductivity has been the limelight of research groups in the domain of superconductivity. HTS materials have evolved to a great extent since their discovery and few of the applications incorporating their outstanding features have reached commercial stage [1]. Taking cryogenics into account, these materials can be suitably used, with a trade-off between size and efficiency. HTS materials exhibit superconductivity at relatively high temperatures (> 35K) compared to the LTS materials (< 35K) [1, 2].

Design of magnets using LTS is an old technology and dominates the Magnetic Resonance Imaging (MRI) applications to date. HTS magnets have also been designed and have proven to trap high strength magnetic fields [3]. The high current densities (~ 106 - 108 A/m²) and high magnetic field capabilities (4 - 5 T) of the 2G HTS (YBCO) wires make them outstandingly 'super' [3-5].

(b) HTS rotating machinery and thermal loading

HTS based generators are predicted to capture 50% of the present market of rotating electrical machines by the year 2020 [6]. As the year is nearing, it will be socially beneficial if this prediction turns out to be a reality.

Low weight, small size and high efficiency are the characteristics of superconducting generators with LTS materials. Various types have been studied since 1960s [7]. Seemingly, HTS based rotating machinery are new and possess better commerciality than LTS machines [2, 8, 9].

Reliance Electric/Rockwell Automation is reported to be the first corporation to have started development of HTS motors in the United States. A 200-hp motor was built and tested in

1996, followed by a larger 1000-hp motor tested in year 2000. Both motors were four-pole 60-Hz using conventional copper armatures with HTS field coils [2]. In 2002, Siemens developed and presented results of 380 kW synchronous machine with HTS rotor windings.[10].

Kalsi *et al.* [2] discuss different topologies of superconducting generator for direct driven wind turbines. One of the claims in this work is that when referred to overall size, efficiency and drivetrain costs, the HTS generator concept is superior to permanent magnet direct drive generator. Application of HTS materials in the design of rotating machinery puts in the advantages of the HTS materials into the rotating machinery but also poses its own design challenges.

One of the common concern of most of the work on HTS rotating machines is the thermal interaction between the cryogenic and non-cryogenic parts of the system. This interaction loads the cryogenic system with thermal load and results in good amount of loss and reduces overall efficiency of the system[11].

(c) Flux pump

The feasibility of superconductor applications is dependent on the heat leak produced by current feed-through and the dissipation in the normal parts of the current leads. For commercial operation of superconducting systems, reduction of these losses is inevitable. Flux pump is one potential solution for this problem [12, 13].

Flux pump offers a unique method of magnetizing a superconductor without a physical link between the cryogenic and non-cryogenic environment. If suit-fitted properly for an application, it can resolve the problem of thermal link between the cryogenic and non-cryogenic environment.

Application of flux pump to energize an HTS magnet with a current ramp rate of 0.44A/s with a maximum current of 49 A in a 2.7mH HTS coil has been successfully demonstrated[14]. It is also observed that the rate of rise of current is dependent on the number of tapes (Fig 1) and also on the frequency of rotation of the flux pump (Fig 2).

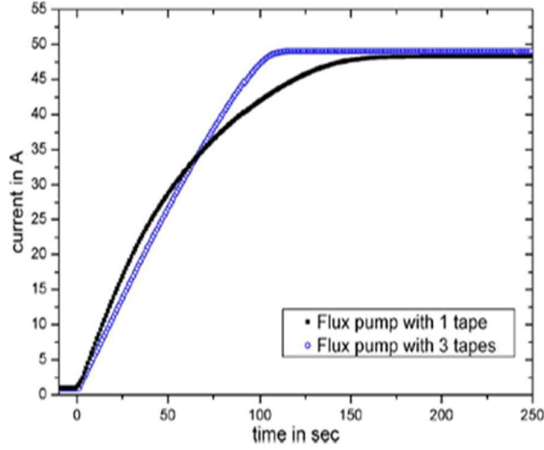


Fig 1. Ramping up of current in the flux pump based HTS magnet.

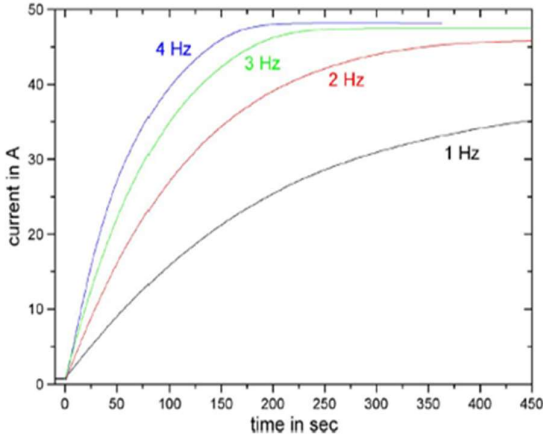


Fig 2. Ramping up of current in the flux pump based HTS magnet at different frequencies.

A thermally actuated flux pump has been proposed by Coombs *et al.*, and the technique used enables the creation of a high magnetic field limited by the characteristic features of the super conductor and not the magnetizing system [15]. The method applied here acts on the surface of the superconductor and offers shaping and patterning of the magnetic field with use of multiple pumps on the surface of superconductor.

The authors, however, have not commented on the suitability of this method to a HTS rotating machine. Though it is worth investigating, we believe a simpler method would conveniently solve the issue and this will be discussed later.

FLUX PUMP AND HTS ROTATING MACHINERY

One of the complex design challenges is to maintain isolation between the cryogenic and non-cryogenic environment in a superconducting application. This becomes far more complex when the superconducting application involves a dynamic component.

Work on improving the current leads from cryogenic environment to non-cryogenic environment has been carried out [11]. We propose a simple method of thermal anchoring of the conduction-cooled current leads and report a decrease in cooling load on the cryogenic system. Despite having reduced the load on the cryocooler, a thermal link exists and loading does occur in this system.

EXPERIMENTS AND OBSERVATIONS

Formulation of dynamic resistance model for a high temperature superconducting flux pump has been presented [16]. The current and voltage profiles with a gap of 1 mm, reported in [16] are as shown in Fig 3.

The results show a linear agreement between the frequency of the flux pump and the rate of current increase.

From the voltage profile, it is evident that a net voltage (quasi DC emf) drop occurs across the superconducting coil.

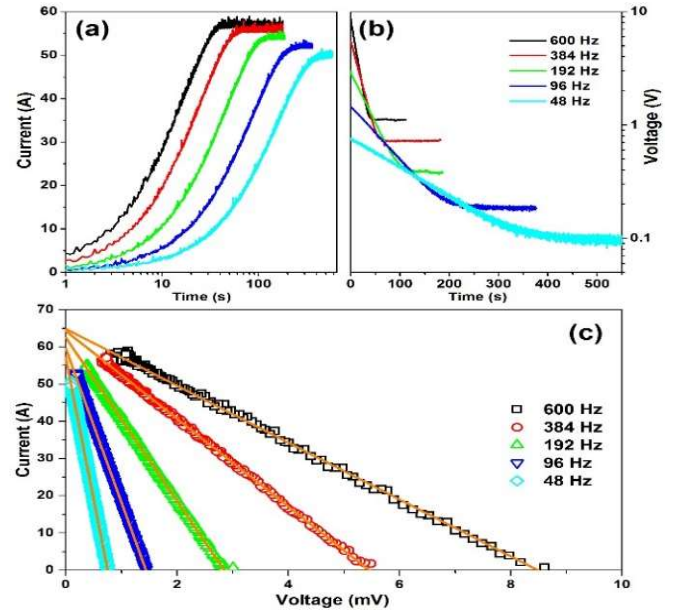


Fig 3. (a) Plots of Current, (b) Voltage against time and (c) Current vs Voltage of an HTS flux pump. ([Jiang et al., 2014](#))

The time dependent current $I(t)$ ($< I_c$, critical current) has been derived in previous works [16] and is given by

$$I(t) = \frac{\Delta\phi}{\beta} \left(1 - \exp\left(\frac{-\beta f t}{L}\right) \right) \text{-----} 1$$

where,

$\Delta\phi$ = the net flux change

β = constant defined by the design parameters of the flux pump

Experiments were carried out by us on an HTS flux pump, with mechanical rotor that contained 12 NdFeB magnets and a type II HTS stator.

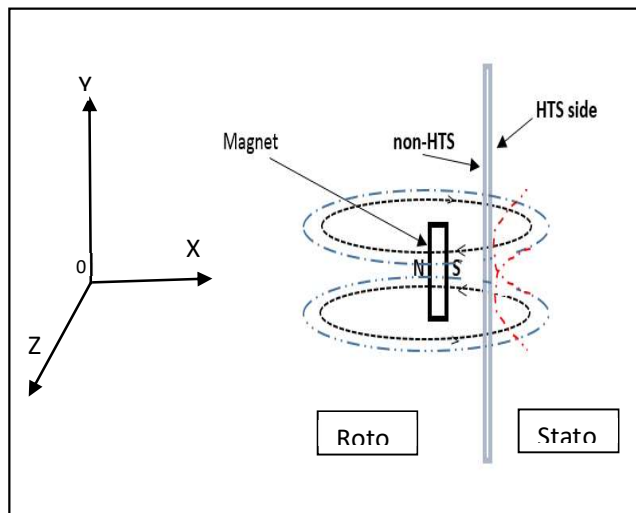
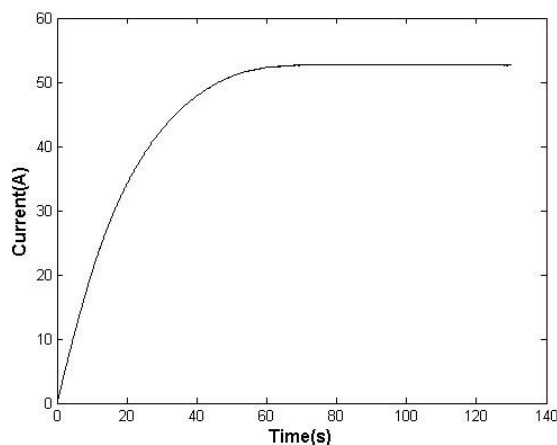


Fig 4. Flux interaction between the rotor magnets and HTS stator

Figure 4 illustrates the interaction between the magnetic field lines and the HTS stator. When the magnet moves with respect to the HTS stator in the XZ-plane, the flux lines are cut by the HTS stator and a current is induced in the HTS stator.

Type I superconductor repels all the magnetic lines (Meissner effect), whereas type II superconductor operates in a mixed state when the applied magnetic field strength lies between the 1st critical field and 2nd critical field thus causing an induced emf and current in the HTS stator.

The current in the HTS stator was measured using a solenoid coil and Hall sensor arrangement. The hall sensor senses the variation in the magnetic field and provides a proportional voltage as output. This voltage is in the range of millivolts. Lettech amplifier was used to amplify the hall voltages.



A high rate data acquisition system was designed using LABVIEW and NI-DAQ cards. The frequency of data

acquisition was selected based on the frequency of flux interaction between the rotor and the stator of the flux pump.

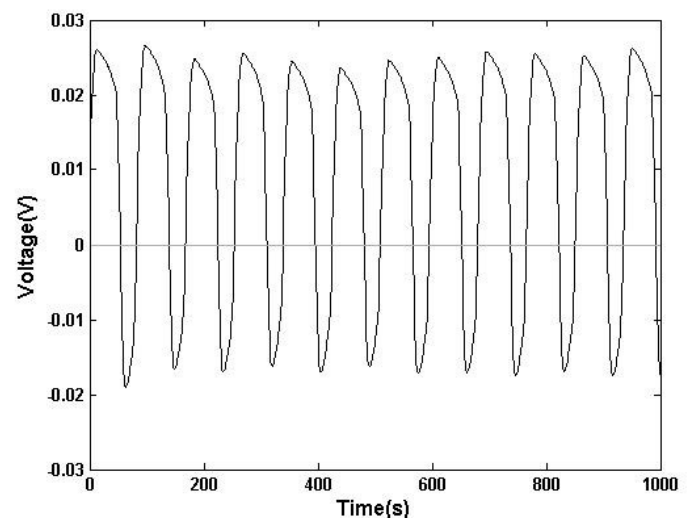
The amplified hall voltage signals were acquired by LABVIEW program via NI-DAQ cards and stored in TDMS file format to facilitate large data management.

In the experiment, the speed N of the flux pump rotor was set as per the following equation;

$$N = (60 * f) / P \text{ -----2}$$

where,

f = frequency (Hz)



P = Number of permanent magnets

In order to avoid resonance with the line voltage, the frequency was set at 598 Hz and the corresponding speed was set at 2990 rpm for a 12 NdFeB magnets rotor. The speed of the rotor was controlled and varied using OMRON Servo driver and TRIO Motion Coordinator.

The results observed are in agreement with the previous results [16]. The voltage across the HTS stator of flux pump is as shown in Fig. 5. The voltage across the HTS stator is asymmetric over the reference line. The

The averaging of the voltage profile shown in Fig. 5 gives a non-zero value hence justifying a quasi-DC emf across the HTS stator.

Fig 5. Voltage (598 Hz) across the HTS stator during flux pump operation.

The averaged current for 1 mm separation and 598 Hz frequency is shown in Fig 6. The ramp up rate is around 0.875A/s. The maximum current reached is 52.5A. The steady state is reached in 65s.

Fig 6. The averaged current for 1 mm separation and 598 Hz.

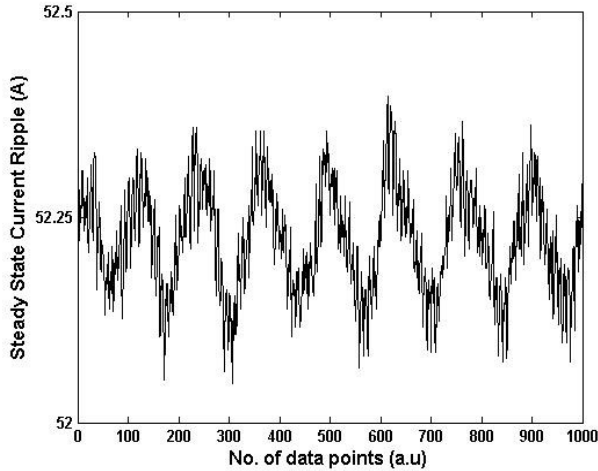


Fig 7. Steady state current ripple (598 Hz)

It can be inferred from the current ripple that the field fluctuation would be similar to the current ripple as the field due to a current carrying conductor is proportional to the current flowing through it. Further experimentation and Finite Element Modelling (FEM) studies are needed to critically analyze the field pattern and fluctuations in the field taking into account the shielding currents, demagnetizing and cross magnetizing effects.

The FFT of the voltage across HTS stator is shown in the Fig 7.

The normalized FFT of the voltage signal across the HTS stator showed the presence of 2nd and 4th harmonics. The presence of even harmonics are because of the asymmetry in the voltage and this has never been reported. However, an interesting factor is the magnitude of the harmonics.

The magnitude of 2nd and 4th harmonics are observed to be 30% and 4% of the fundamental, respectively. The 3rd harmonic is found to be smaller than the 4th harmonic. Further investigation and analysis with a larger data set is currently in progress to understand the nature and magnitude of various harmonics in the voltage profile.

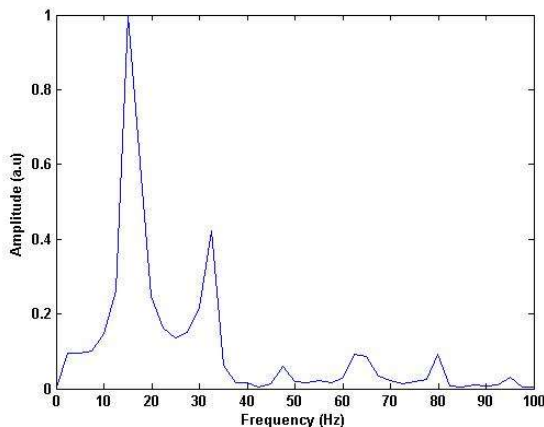


Fig 8. Normalized FFT of the Voltage (16 Hz) across the HTS stator.

From the results of our flux pump experiments in magnetizing a superconductor, it is clear that the flux pump can be utilized in generating magnetic field in an HTS rotating machinery.

Some of the concerns that need to be addressed such as

- An efficient magnetic circuit to bridge the magnetic flux between flux pump magnets and the superconductor.
- Harmonic analysis of the system in conjunction with the synchronous generator operating conditions.
- Demagnetizing and cross-magnetizing effects of armature conductors on the flux link between flux pump magnets and superconductor

CONCLUSION

An empirical formula for the rate of rise of current and its dependency on the shape and size of the magnets used in the flux pump and choice of material of the magnetic circuit are some of the aspects for improvising the design of the flux pump in order to suit-fit it to a rotating machinery application. Based on the earlier results and preliminary results from this work, it can be concluded that application of flux pump is suitable for exciting rotor (HTS conductors) in a synchronous generator.

ACKNOWLEDGMENTS

The authors would like to thank Rod Badcock, Chris Bumby and Zhenan Jiang of Robinson Research Institute, Victoria University of Wellington, for their cooperation and help in carrying out this study.

REFERENCES

- [1] S. S. Kalsi, Dave Gritter, Om Nayak and Chuck Gallagher, "Benefits of HTS technology to ship systems " presented at the IEEE Symposium on Electric Ship Technologies, Philadelphia PA, 2005.
- [2] S. S. Kalsi, K. Weeber, H. Takesue, C. Lewis, H. W. Neumueller, and R. D. Blaugher, "Development status of rotating machines employing superconducting field windings," *Proceedings of the IEEE*, vol. 92, pp. 1688-1704, 2004.
- [3] K. T. A. M. Murakami, "High-temperature superconductor bulk magnets that can trap magnetic fields of over 17 Tesla at 29 K," *Nature*, p. 4, 2003.
- [4] S. Kalsi, *Application of High Temperature Superconductors to Electric Power Equipment*: Wiley, 2011.
- [5] P. N. Barnes, M. D. Sumption, and G. L. Rhoads, "Review of high power density superconducting generators: Present state and prospects for incorporating YBCO windings," *Cryogenics*, vol. 45, pp. 670-686, 10// 2005.
- [6] T. P. S. A. B. M. Joseph Mulholland, "Analysis of Future Prices and Markets for High Temperature Superconductors," U.S. Department of Energy June 2003.
- [7] Q. Ronghai, L. Yingzhen, and W. Jin, "Review of Superconducting Generator Topologies for Direct-

- Drive Wind Turbines," *Applied Superconductivity, IEEE Transactions on*, vol. 23, pp. 5201108-5201108, 2013.
- [8] B. B. Jensen and A. B. Abrahamsen, "Modeling, construction, and testing of a simple HTS machine demonstrator," in *Energy Conversion Congress and Exposition (ECCE), 2011 IEEE*, 2011, pp. 1636-1640.
 - [9] Z. Min, W. Wei, Y. R. Chen, and T. Coombs, "Design Methodology of HTS Bulk Machine for Direct-Driven Wind Generation," *Applied Superconductivity, IEEE Transactions on*, vol. 22, pp. 5201804-5201804, 2012.
 - [10] W. Nick, G. Nerowski, H. W. Neumüller, M. Frank, P. van Hasselt, J. Frauenhofer, *et al.*, "380 kW synchronous machine with HTS rotor windings—development at Siemens and first test results," *Physica C: Superconductivity*, vol. 372–376, Part 3, pp. 1506-1512, 8// 2002.
 - [11] S. Jeong and Y. Kim, "Thermal anchoring of conduction-cooled current leads for superconductivity applications near liquid nitrogen temperature," *Cryogenics*, vol. 50, pp. 287-291, 4// 2010.
 - [12] L. J. M. van de Klundert and H. H. J. ten Kate, "Fully superconducting rectifiers and fluxpumps Part 1: Realized methods for pumping flux," *Cryogenics*, vol. 21, pp. 195-206, 4// 1981.
 - [13] C. Hoffmann, R. Walsh, E. Karrer-Mueller, and D. Pooke, "Design Parameters for an HTS Flux Pump," *Physics Procedia*, vol. 36, pp. 1324-1329, // 2012.
 - [14] C. Hoffmann, D. Pooke, and A. D. Caplin, "Flux Pump for HTS Magnets," *Applied Superconductivity, IEEE Transactions on*, vol. 21, pp. 1628-1631, 2011.
 - [15] T. Coombs, Z. Hong, and X. Zhu, "A thermally actuated superconducting flux pump," *Physica C: Superconductivity*, vol. 468, pp. 153-159, 2/1/ 2008.
 - [16] Z. Jiang, K. Hamilton, N. Amemiya, R. A. Badcock, and C. W. Bumby, "Dynamic resistance of a high-Temperature superconducting flux pump," *Applied Physics Letters*, vol. 105, pp. 112601-112601-4, 2014.

2. MT24, South Korea, 2015

Through-Wall Excitation of a Magnet Coil by an External-Rotor HTS Flux Pump

Chris W. Bumby, Andres E. Pantoja, Hae-Jin Sung, Zhenan Jiang, Ravi Kulkarni, and Rodney A. Badcock

Abstract—High-temperature superconducting (HTS) magnet systems conventionally require normal-conducting current leads, which connect between the HTS circuit and an external power supply located at room temperature. These current leads form a thermal bridge across the cryostat wall, and they represent the dominant heat load for many magnet applications. The use of a superconducting flux pump device is an alternative approach to exciting a magnet coil, which can eradicate this parasitic heat load, as such devices do not require direct physical connection to the HTS circuit. However, earlier proposed flux pump designs have required power-dissipating active components to be located within the cryogenic envelope, thus imposing their own parasitic heat load. Here, we report the successful demonstration of a mechanically rotating HTS flux pump, which operates entirely outside of the cryogenic envelope. This prototype device projects flux across a cryostat wall, leading to the injection of a direct current into a thermally isolated closed HTS circuit. This is achieved through the implementation of a flux-concentrating magnetic circuit employing ferromagnetic yoke pieces, which enables flux penetration of the HTS circuit at large flux gaps. We have demonstrated the injection of direct currents of > 30 A into a closed HTS circuit while operating this device across a cryostat wall.

Index Terms—Coated conductor, current leads, flux pump, HTS dynamo, superconducting generator, YBCO.

I. INTRODUCTION

NORMAL-CONDUCTING current leads are a ubiquitous component of high- T_c superconducting (HTS) magnet systems [1]. These leads form metal conducting paths which bridge across the cryostat wall in order to transfer large DC currents from a power supply located at room temperature. However, heat conduction and ohmic dissipation within these current leads impose a substantial heat load on the cryostat. In some cases, this heat load can form more than half the total cooling power required by the system [2].

An alternative method to excite a DC transport current in an HTS circuit is to employ a superconducting flux pump [3]–[8]. One such device is the rotating HTS flux pump [9]–[15], which

comprises a set of rotating permanent magnets that traverse a coated conductor HTS wire, such that a time-averaged DC output voltage is developed [12], [13]. This DC output voltage can drive large currents through a series-connected HTS coil. However, previously reported flux pumps have required that the flux gap between the rotor magnets and the stator is ≤ 7 mm, which has necessitated that the rotor be placed inside the cryogenic environment. This leads to additional parasitic heat loads due to turbulence and friction, as well as requiring unreliable and hard-to-source cryogenic bearings. It would be much more preferable to locate the rotor of the flux pump outside of the cryostat, and hence eliminate any form of penetration through the cryostat wall.

Here we report a rotating HTS flux pump which achieves this goal through the use of ferromagnetic rotor and stator yokes, which form a magnetic circuit that focuses flux upon the HTS stator wire. We show that this device can operate at flux gaps of up to 14.5 mm, which is sufficient to accommodate a thermally insulating cryostat wall. For the first time, we have demonstrated the excitation of an HTS coil by a flux pump in which all active parts are located outside the cryogenic environment.

II. EXPERIMENTAL APPARATUS

A. Design of the External-Rotor HTS Flux Pump

Fig. 1(a) shows the external-rotor HTS flux pump built and tested in this work, and its arrangement within a composite cryostat liquid nitrogen bath. The custom-built G10 composite cryostat was fabricated by Fabrum Solutions Ltd (NZ).

An iron stator yoke was placed directly upon the base of the cryostat above a thin (3 mm) section of the cryostat wall. A 12 mm wide coated-conductor stator wire was wrapped around the stator yoke and threaded through a hole to enable a closed electrical circuit to be formed through soldered connection to an HTS double pancake coil (DPC). The DPC was measured to have a critical current of $I_{c,coil} = 95$ A at the $1 \mu\text{V cm}^{-1}$ criterion, and had a measured inductance $L = 1.97$ mH. The stator wire was manufactured by Superpower Inc. [16], and had a measured I_c at the $1 \mu\text{V cm}^{-1}$ criterion of 292 A. An iron rotor disc (yoke) was placed opposite the stator yoke, but outside (beneath) the cryostat, such that the composite cryostat wall was accommodated in the flux gap between the rotor and stator yoke. The rotor yoke housed 9 Nd-Fe-B (N42) permanent magnets which were arranged in a homopolar orientation with the axis of magnetization directed across the flux gap. The N42 magnets had dimensions of $1'' \times (1/2)'' \times (1/4)''$ and

Manuscript received October 17, 2015; accepted January 18, 2016. Date of publication February 8, 2016; date of current version March 14, 2016. This work was supported by the New Zealand Ministry of Business, Innovation, and Employment under Contract RTVU1401.

C. W. Bumby, A. E. Pantoja, Z. Jiang, and Rodney A. Badcock are with the Robinson Research Institute, Victoria University of Wellington, Lower Hutt, 5046, New Zealand (e-mail: chris.bumby@vuw.ac.nz).

H.-J. Sung is with the Department of Electrical Engineering, Changwon National University, Changwon 641-733, Korea.

R. Kulkarni is with the School of Engineering, Auckland University of Technology, Auckland, 1142, New Zealand.

Color versions of one or more of the figures in this paper are available online at <http://ieeexplore.ieee.org>.

Digital Object Identifier 10.1109/TASC.2016.2526605

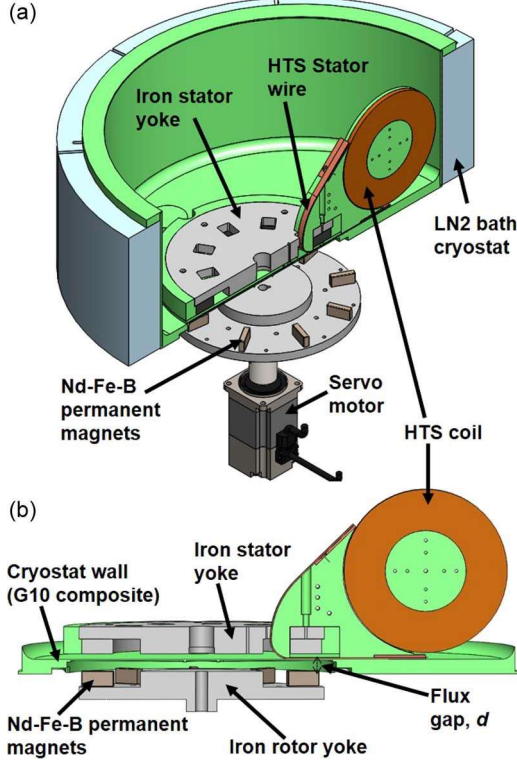


Fig. 1. (a) Three-dimensional view of the external-rotor flux pump, the composite cryostat bath, and the HTS coil. (b) Cross-sectional view of the cryostat wall and flux pump rotor and stator showing magnetic circuit formed between the rotor and the stator.

the magnetization axis was oriented perpendicular to one of the $1'' \times (1/4)''$ faces. The iron rotor yoke was mounted on a steel shaft which was directly driven by a speed-controlled servo-motor. This controlled the frequency, f , at which the rotor magnets crossed the coated-conductor stator wire. The flux gap between the rotor and stator yokes could be adjusted through the use of a set of interchangeable spacer plates which inserted beneath the rotor mounting collar. As the flux gap is increased the peak amplitude of the applied perpendicular magnetic field at the stator wire decreases [13], [14]. In this work the flux gap, d , was varied between 7.5 mm and 14.5 mm, and in each case the operating behaviour of the flux pump was characterized at 77 K.

B. Electrical Measurement of Superconducting Circuit

The output voltage of the flux pump was measured using voltage taps placed on either side of the coated conductor stator wire. Voltage measurements were made using a sample integration time of between 8 s and 16 s. The current in the HTS circuit was inferred from the magnetic field measured at the centre of the coil using a fixed cryogenic Hall sensor (Arepoc type HHP-NA). A programmable current source (Agilent 6680 A) was used to calibrate the Hall sensor signal with the current flowing through the coil.

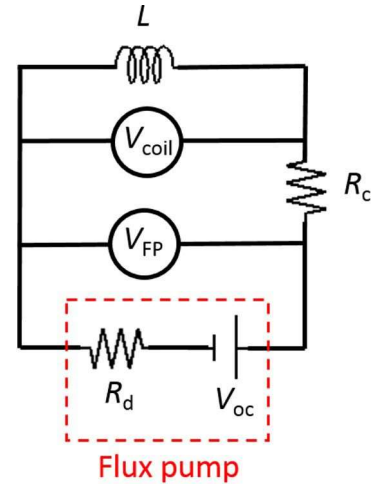


Fig. 2. Equivalent electrical circuit for a flux pump connected in series with an HTS coil.

III. ELECTRICAL CIRCUIT MODEL

We have previously shown that the behaviour of a rotating HTS flux pump connected in series with a superconducting coil can be described by the equivalent circuit shown in Fig. 2 [12], [13]. Here R_c denotes the resistance of normal-conducting soldered joints between the coated conductor wires in the circuit, L is the inductance of the HTS coil, and V_{oc} is the open-circuit voltage of the flux pump. The internal resistance of the flux pump, R_d , is understood to be due to the effect of *dynamic resistance* within the superconducting stator. *Dynamic resistance* is a hysteretic loss caused by the interaction of the oscillating magnetic field applied by the rotor magnet with a DC transport current [17]–[19] in the stator wire. The measured output voltage from the flux pump is denoted, $V_{FP} = V_{oc} - IR_d$, where I is the current flowing in the circuit. Similarly, $V_{coil} = V_{FP} - IR_c$ is the measured voltage across the HTS coil during ramping. From Fig. 2, we can then describe the evolution of the current in the coil in the following manner:

$$I = I_0 [1 - \exp(-(R_d + R_c)t/L)] \quad (1)$$

Here t is the time since the flux pump started operating, and $I_0 = V_{oc}/(R_d + R_c)$. Equation (1) assumes that $I < I_{c,coil}$. The voltage across the coil can be similarly expressed as:

$$V_{coil} = V_{oc} \exp(-(R_d + R_c)t/L) \quad (2)$$

From equation (1) we see that the maximum current that can be injected into the coil is limited by the total resistance of the circuit during flux pump operation, $R_c + R_d$. The joint resistance, R_c can be obtained from the decay time constant, (L/R_c) of the current in the circuit once the flux pump has been turned off (as both R_d and V_{oc} are zero when there is no oscillating applied field). The circuit studied in this work was found to have a joint resistance, $R_c = 3.2 \mu\Omega$ which was stable over multiple cooling-warming cycles.

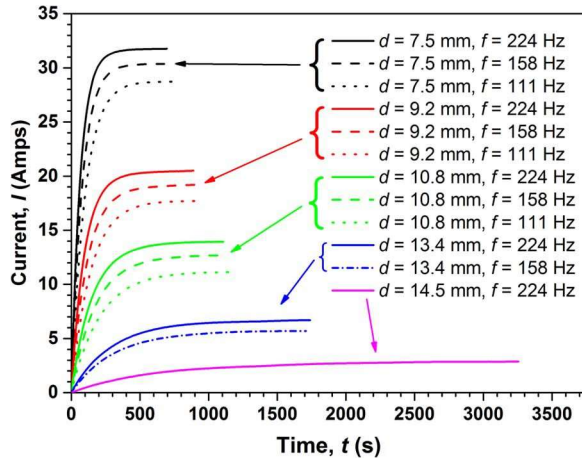


Fig. 3. Evolution of the current in the HTS coil as a function of time since the flux pump started operating.

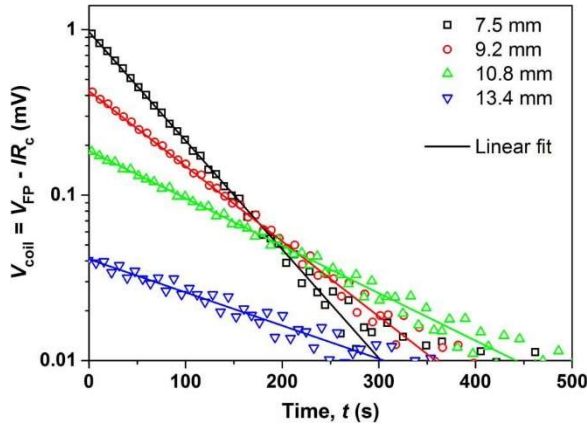


Fig. 4. Voltage across the HTS coil, V_{coil} , versus time t during the first 500 s of the flux pump operation at $f = 224$ Hz (ramp-up). Solid lines show linear fits to data points shown.

IV. RESULTS

Fig. 3 shows the time evolution of current in the coil over time during operation of the flux pump. At $d = 7.5$ mm, the flux pump is capable of injecting > 30 A into the HTS coil at $f = 224$ Hz. At each flux gap value, we observe a distinct “family” of curves which saturate at a different maximum current. At larger flux gaps the required ramp-up time became very long and data was only acquired at the higher operating frequencies. Fig. 4 shows the voltage across the coil, V_{coil} , as a function of time during the ramping of current by the flux pump. This data is shown on a log-linear plot and the straight-line relationship observed between V_{coil} and t indicates an exponential decay consistent with equation (2). The gradient of each line is determined by the time constant $L/(R_d + R_c)$ for each case. We see that this gradient changes with distance (and frequency) which indicates that R_d is a function of both d and f (as L and R_c are constant at all times).

The effect of the flux gap and operating frequency on ramping behavior can be more clearly understood by considering the output voltage of the flux pump as a function of current. This is shown in Fig. 5. For any pair of fixed operating parameters, the $I - V$ relationship is described by a

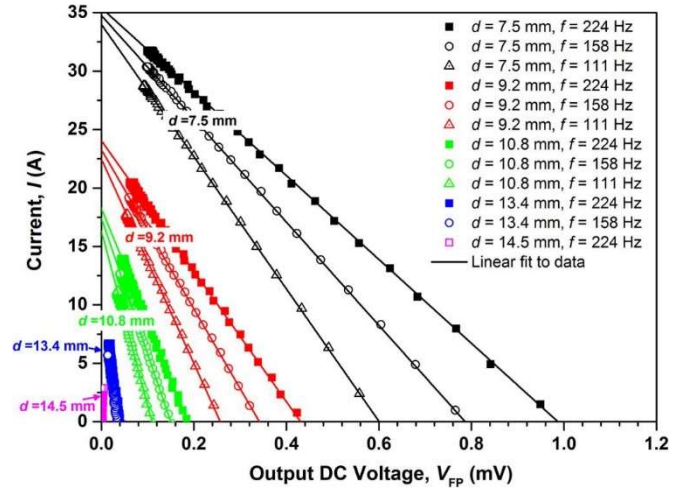


Fig. 5. Plots showing dc output voltage of flux pump versus current for various operating frequencies and flux gaps.

line, again as expected from Fig. 2. V_{oc} is obtained from the intercept on the x -axis, and the gradient of each line describes the internal resistance, $R_d = -dV_{\text{FP}}/dI$ at the corresponding operating parameters. It is clear that R_d varies with frequency which reflects that dynamic loss is a hysteretic loss [17]–[19] whereby R_d is expected to be proportional to f . In fact in this case we observe a slightly non-linear relationship between R_d and f , which we attribute to the effect of eddy currents within the iron stator yoke.

The intercept of each line on the y -axis of Fig. 5 gives the short-circuit current, I_{sc} , where

$$I_{\text{sc}} = \frac{V_{\text{oc}}}{R_d}. \quad (3)$$

I_{sc} represents the maximum current that the flux pump is capable of delivering to a fully superconducting circuit for which $R_c = 0 \Omega$. We see that for each fixed flux gap, I_{sc} is approximately independent of operating frequency. This is a straightgeneral characteristic of HTS rotating flux pumps [12]–[15], which reflects that both V_{oc} and R_d are approximately proportional to the operating frequency, such that this dependency cancels in equation (3).

V. DISCUSSION

From Fig. 5 we can extract values of V_{oc} , I_{sc} and R_d for each operating frequency and flux gap. These values are shown in Fig. 6, where the frequency-normalised values of V_{oc} and R_d are plotted. In this figure, “Forwards” and “Reverse” refer to the direction of rotation of the flux pump rotor. Also plotted in Fig. 6(a) is the peak applied magnetic field B_{\perp} , experienced at the HTS stator wire as a function of flux gap, d , which has been calculated using finite-element software [21].

Fig. 6(b) shows the frequency-normalised value, R_d/f , which enables comparison of data taken at different frequencies. We find that R_d drops with increasing flux gap, which reflects the corresponding drop in B_{\perp} . The direction of rotation does not appear to systematically affect the R_d values obtained at each flux gap. This is consistent with the effect of dynamic

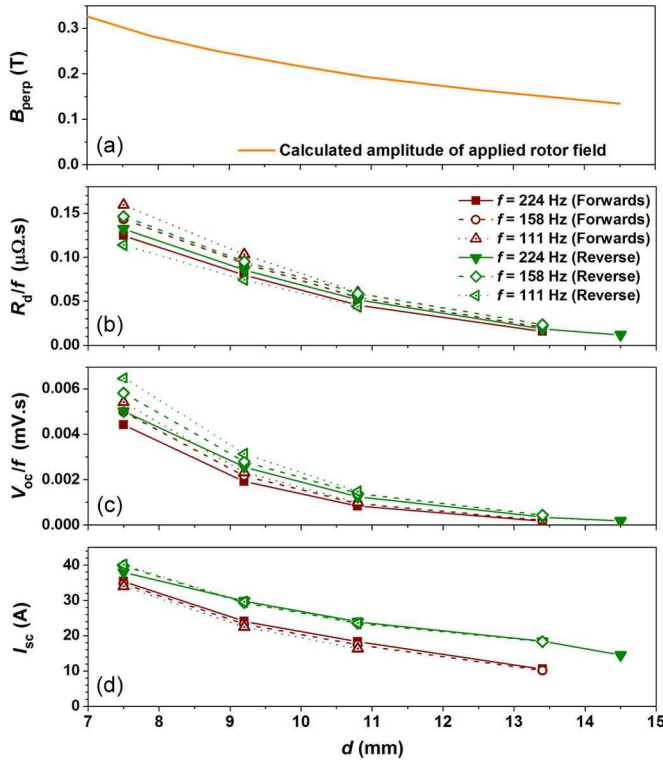


Fig. 6. (a) Peak applied perpendicular magnetic field B_{\perp} ($=B_{\text{perp}}$) experienced at a stator wire, calculated using FEMM software [22]. (b) Frequency normalized internal resistance R_d/f versus flux gap d . (c) Frequency normalized open-circuit voltage V_{oc}/f versus flux gap d . (d) Short-circuit current I_{sc} versus flux gap d . Data is shown for operation of rotor in both “Forwards” and “Reverse” directions.

resistance, which is expected to be a function of B_{\perp} and f only [17]–[19].

Fig. 6(c) shows the frequency-normalised open-circuit voltage, V_{oc}/f , which also decreases with increasing flux gap. In this case, the direction of rotation does appear to have a small effect on the open-circuit voltage, with V_{oc} in the “Reverse” direction being approximately 15% more than that obtained in the “Forwards” direction. This observation is slightly surprising given that the total rate at which flux cuts the stator wire is the same irrespective of rotational direction. However, the physical origin of the DC output voltage from a rotating HTS flux pump is still a matter of some conjecture [11], [13], [14]. The device has an identical device topology to a homopolar AC generator, and hence it is not expected to output a DC voltage. Indeed, the DC output voltage measured in the normal-conducting state (i.e. at 293 K) is zero. Giaever [20] has previously proposed a model for a unipolar superconducting DC generator in which partial rectification occurs due to the presence of time-varying circulating eddy currents which form a superconducting shunt leakage path as the rotor magnet passes across the stator wire [21]. Misalignment of the rectangular magnets upon the flux pump rotor could give rise to symmetry differences in the geometry of such circulating currents during the rotor cycle, and this effect would be exacerbated if J_c across the tape were not uniform. We suggest that these are the two most likely causes of the observed differences between “Forward” and “Reverse” behaviour of V_{oc} for our device.

Fig. 6(d) emphasises that I_{sc} is independent of frequency at each flux gap for a given rotor direction. However, the asymmetry in V_{oc} with rotor direction is also observed in the I_{sc} values, such that we obtain distinct and separate curves for I_{sc} in the forwards and reverse directions respectively. This follows directly from the values shown Fig. 6(c) and equation (3). At larger flux gaps, the difference between the two rotor directions becomes highly significant, such that at $d = 13.4$ mm, I_{sc} in the “Reverse” direction is almost twice that obtained in the “Forwards” direction. If misalignment is the primary cause of the asymmetry then it appears that the device is highly sensitive to the rotor magnet geometry.

In both rotor directions it can be seen that I_{sc} decreases with increasing flux gap. This occurs because V_{oc} drops more quickly than R_d with decreasing applied magnetic field amplitude, B_{\perp} . The dynamic resistance, R_d will be more than zero for all values of $B_{\perp} > 0$ [17]. However there is a maximum flux gap, d_{max} , beyond which B_{\perp} is excluded from the centre of the HTS stator by screening currents, and beyond this point $V_{oc} = 0$ [13]. Therefore, as the applied field amplitude is decreased we find that V_{oc} decreases faster than R_d and hence $I_{sc} \rightarrow 0$ as $d \rightarrow d_{\text{max}}$ (from equation (3)).

Despite this inherent reduction in output current at increased flux gaps, our device is still capable of injecting current into our experimental circuit at $d = 14.5$ mm. This result is significant because the mechanical strength and thermal performance of a composite cryostat wall is closely related to its physical dimensions. Wall thicknesses of more than 7.5 mm allow space for both vacuum insulation and MLI in a G10 composite cryostat wall.

VI. CONCLUSION

For the first time, we have demonstrated that an HTS magnet circuit can be excited by an HTS flux pump in which all active parts are located outside of the cryostat. We have achieved this through the use of a ferromagnetic circuit to focus flux across the cryostat wall and hence increase the applied field-intensity experienced at the coated-conductor stator wire. This approach is highly attractive for applications where quasi-persistent current operation is required, as duty-cycle operation of the flux pump leads to a substantially lower heat load than that imposed by a pair of metal current leads [12], [14]. It should be noted that the stator geometry employed here allows for up to 12 HTS stator wires to be installed in parallel. In this way the reported device could deliver operating currents of more than 360 A at a flux gap of 7.5 mm. One application of particular interest is the excitation of HTS rotor coils within a superconducting generator. In this application, the external-rotor HTS flux pump can act as a “brushless exciter” which also eliminates the need for rotating slip-rings to transfer DC excitation current onto the rotor [14]. We are currently investigating the application of our external rotor flux pump as a brushless exciter within a superconducting generator designed for large-scale wind turbine applications [23], [24].

REFERENCES

- [1] A. Ballarino, "Current leads, links and buses," in *Proc. CAS-CERN Accel. School, Supercond. Accel.*, Erice, Italy, 2013, pp. 1–12.
- [2] S. Kalsi, *Applications of High Temperature Superconductors to Electric Power Equipment*. Hoboken, NJ, USA: IEEE Press, 2011, pp. 49–59.
- [3] L. J. M. van de Klundert and H. H. J. ten Kate, "Fully superconducting rectifiers and flux pumps. Part 1: Realized methods for pumping flux," *Cryogenics*, vol. 21, no. 4, pp. 195–206, Apr. 1981.
- [4] M. P. Oomen *et al.*, "HTS flux pump for cryogen free HTS magnets," *IEEE Trans. Appl. Supercond.*, vol. 15, no. 2, pp. 1465–1468, Jun. 2005.
- [5] Z. Bai, C. Chen, Y. Wu, and Z. Zhen, "Effect of various pulse wave forms for pulse-type magnetic flux pump," *Cryogenics*, vol. 51, no. 9, pp. 530–533, Jul. 2011.
- [6] Z. Bai *et al.*, "A newly developed pulse-type microampere magnetic flux pump," *IEEE Trans. Appl. Supercond.*, vol. 20, no. 3, pp. 1667–1670, Jun. 2010.
- [7] L. Fu, K. Matsuda, M. Baghdadi, and T. Coombs, "Linear flux pump device applied to high temperature superconducting (HTS) magnets," *IEEE Trans. Appl. Supercond.*, vol. 25, no. 3, Jun. 2015, Art. no. 4603804.
- [8] T. Nakamura, M. Sugano, T. Doi, and N. Amemiya, "Flux pumping effect of HTS films in a travelling magnetic field," *IEEE Trans. Appl. Supercond.*, vol. 20, no. 3, pp. 1033–1036, Jun. 2010.
- [9] R. M. Walsh, R. Slade, D. Pooke, and C. Hoffmann, "Characterisation of current stability in an HTS NMR system energised by an HTS flux pump," *IEEE Trans. Appl. Supercond.*, vol. 24, no. 3, Jun. 2014, Art. no. 46007805.
- [10] C. Hoffmann, D. Pooke, and A. D. Caplin, "Flux pump for HTS magnets," *IEEE Trans. Appl. Supercond.*, vol. 21, no. 3, pp. 1628–1631, Jun. 2011.
- [11] T. A. Coombs, J. F. Fagnard, and K. Matsuda, "Magnetization of 2-G coils and artificial bulks," *IEEE Trans. Appl. Supercond.*, vol. 24, no. 5, Oct. 2014, Art. no. 8201005.
- [12] Z. Jiang, K. Hamilton, N. Amemiya, R. A. Badcock, and C. W. Bumby, "Dynamic resistance of a high-Tc superconducting flux pump," *Appl. Phys. Lett.*, vol. 105, Sep. 2014, Art. no. 112601.
- [13] Z. Jiang *et al.*, "Impact of flux gap upon dynamic resistance of a rotating HTS flux pump," *Supercond. Sci. Technol.*, vol. 28, no. 11, Sep. 2015, Art. no. 115008.
- [14] C. W. Bumby *et al.*, "Development of a brushless HTS exciter for a 10 kW HTS synchronous generator," *Supercond. Sci. Technol.*, vol. 29, no. 2, Jan. 2016, Art. no. 024008.
- [15] Z. Jiang, C. W. Bumby, R. A. Badcock, and H.-J. Sung, "A novel rotating HTS flux pump incorporating a ferromagnetic circuit," *IEEE Trans. Appl. Supercond.* [Online]. Available: <http://dx.doi.org/10.1109/TASC.2016.2521332>.
- [16] 2G HTS Wire Specifications, accessed on Oct. 6, 2015. [Online]. Available: http://www.superpower-inc.com/system/files/SP_2G+Wire+Spec+Sheet_2014_web_v1_0.pdf.
- [17] M. P. Oomen, J. Rieger, M. Leghissa, B. ten Haken, and H. H. J. ten Kate, "Dynamic resistance in a slab-like superconductor with $J_c(B)$ dependence," *Supercond. Sci. Technol.*, vol. 12, no. 6, pp. 382–387, Jun. 1999.
- [18] K. Ogasawara, K. Yasukochi, S. Nose, and H. Sekizawa, "Effective resistance of current-carrying superconducting wire in oscillating magnetic fields 1: Single core composite conductor," *Cryogenics*, vol. 16, no. 1, pp. 33–38, Jan. 1976.
- [19] R. C. Duckworth, Y. F. Zhang, T. Ha, and M. J. Gouge, "Dynamic resistance of YBCO-coated conductors in applied AC fields with DC transport currents and DC background fields," *IEEE Trans. Appl. Supercond.*, vol. 21, no. 3, pp. 3251–3256, Jun. 2011.
- [20] I. Giaever, "A DC transformer," *IEEE Spectr.*, vol. 3, no. 9, pp. 117–122, Sep. 1966.
- [21] C. W. Bumby, Z. Jiang, A. E. Pantoja, and R. A. Badcock, "Anomalous open-circuit voltage from a high-Tc superconducting dynamo," *Appl. Phys. Lett.*, to be published.
- [22] D. C. Meeker, Finite Element Method Magnetics, Version 4.2 (Nov. 15, 2013 Build). [Online]. Available: <http://www.femm.info>.
- [23] H.-J. Sung *et al.*, "Design of a 12 MW HTS wind power generator using a flux pump exciter," *IEEE Trans. Appl. Supercond.*, to be published.
- [24] H.-J. Sung *et al.*, "Design and heat load analysis for a 12 MW HTS wind power generator module employing brushless HTS exciter," *IEEE Trans. Appl. Supercond.*, to be published.

3. IEEE-Powercon, Australia

FEM and Performance Analysis of 10 kW HTS Generator with Flux Pump excitation

R. Kulkarni, K. Prasad and T.T.

Lie

Department of Electrical and Electronic
Engineering, Auckland University of
Technology,
Auckland 1010, New Zealand
e-mail: rkulkarni@aut.ac.nz

R.A. Badcock and C.W. Bumby

Robinson Research Institute, Victoria
University of Wellington, Wellington,
New Zealand.

H.J. Sung

Department of Electrical Engineering,
Changwon National University,
Changwon,
South Korea

Abstract-- High Temperature Superconductor (HTS) based rotating electrical machines offer the advantages of lighter weight, smaller size, better efficiency and lower noise compared to conventional machines. For a generator with HTS rotor, the interaction between the cryogenic rotor and non-cryogenic room environment occurs because of the use of feedthrough current leads to excite the field in the machine. The use of flux pump for exciting the field system of HTS coil will avoid a physical link between the cryogenic and non-cryogenic environment. This reduces the thermal load on the system. This paper presents Finite Element Modelling (FEM) based study on the steady state performance of HTS synchronous generator with flux pump excitation. The experimental results of a single stator HTS flux pump are used as the input for exciting the field of HTS synchronous generator in ANSYS simulation environment. Total Harmonic Distortion (THD) calculations are performed on the output phase voltage of the generator. A comparison between steel and G10-FRP (Fibre Reinforced Polymer) as stator material is made. Choice of G10 as a stator material leads to smaller THD values.

Index Terms-- Current leads, FEM, Flux pump, HTS, Harmonics, YBCO.

I. INTRODUCTION

High Temperature Superconductors (HTS) have evolved to a great extent since they first came into existence in 1986 and few of the power systems applications have reached a commercial stage [1]. HTS materials exhibit superconductivity at relatively high temperatures (> 35 K). Design of magnets using Low Temperature Superconductors (LTS) still dominates the Magnetic Resonance Imaging (MRI) applications to-date. The HTS magnets have also been designed and proven to trap high strength magnetic fields. The high current densities (~ 106 - 108 A/m²) and high magnetic field capabilities (4 - 5 T) of the 2G HTS (Yttrium Barium Cupric Oxides-YBCO) wires make them outstandingly 'super' [2]. Electrical generators with HTS on rotor or stator can produce very high power density. The design of HTS generators is application-specific and various topologies have

been reported [3-7]. With optimization, HTS machines would be more commercially attractive than LTS machines.

In most HTS applications, the feed-through current leads, used to maintain unidirectional current in the HTS windings, thermally load the cryogenic system [8]. Up to 50% of the total thermal load on the cryogenic system is reported to be due to these leads [1]. The use of a flux pump for exciting the HTS windings can effectively reduce the thermal link between the cryogenic and non-cryogenic environment, thus reducing the thermal load on the cryogenic system by almost 80% [9,19]. Although a conceptual design on the use of flux pump for rotor excitation has been proposed, the practicality of the design and applicability of the design has not yet been reported [10].

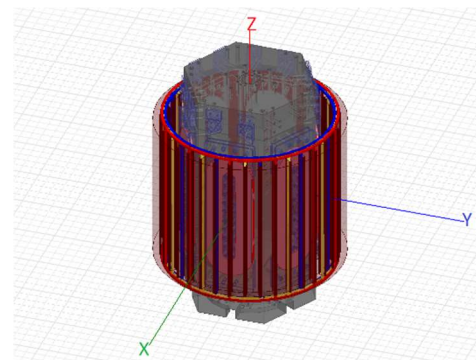


Fig. 1. HTS Generator-ANSYS Model.

Few results exist on the effects of rotor configuration and field windings on the harmonics of the induced voltage in the stator conductors [11, 12]. However, there are no reports on the effects of field distortion in a non-conventional design of HTS rotor with a non-ferromagnetic stator such as G10 FRP epoxy.

In this paper, analysis of the performance of a HTS generator, integrated with flux pump to excite the field is reported. It will be shown that the flux pump can be used to excite a DC current in the HTS windings. Electromagnetic

field analysis on the model and harmonic analysis on the stator induced voltage at 3 different frequencies of flux-pump excitation (60Hz, 120Hz and 240Hz) are carried out on the model. Finally, steel and G10 are used as stator core materials and the generator performance will be compared in terms of induced voltage and THD.

II. FLUX PUMP

Flux pumping offers a unique method of magnetizing a superconductor without a physical link between the cryogenic and non-cryogenic environment [13-15]. If designed suitably for an application, it can resolve the problem of thermal loading on the cryogenic system by avoiding such a physical link. An application of a flux pump to energize a HTS magnet with a current ramp rate of 0.44 A/s with a maximum current of 49 A in a 2.7 mH HTS coil has been successfully demonstrated [13]. It is also reported that the rate of rise of current is dependent on the number of tapes and also on the frequency of rotation of the flux pump.

A thermally actuated flux pump has been proposed by Coombs *et al.* [16] and the technique used enables the creation of a high magnetic field limited by the characteristic features of the super conductor and not the magnetizing system. The method applied here acts on the surface of the superconductor and offers shaping and patterning of the magnetic field with the use of multiple pumps on the surface of superconductor. However, no comments are made on any suitability of this method to a HTS rotating machine.

In superconductivity applications, one of the complex design challenges is to maintain isolation between the cryogenic and non-cryogenic environment. This becomes even more complex when the superconducting application involves a dynamic component. Results on improving the current leads from cryogenic environment to non-cryogenic environment have been reported [8]. Here, a simple method of thermal anchoring of the conduction-cooled current leads is proposed and a decrease in the cooling load on the cryogenic system is demonstrated. Despite having reduced the load on the cryogenic system, a thermal link still exists and loading does occur in this system.

Formulation of a dynamic resistance model for a HTS flux pump has been presented by Jiang *et al.* [17]. The results show a linear relation between the frequency of the flux pump and the rate of current increase. From the voltage profile, it is evident that a net voltage (quasi-DC emf) drop occurs across the superconducting coil [18]. In our experiments with the flux pump, we have observed the same trend and the non-uniform voltage profile observed across the HTS stator for a configuration of 5S-3P configuration is similar to that of Bumby *et al.* [19] and is shown in Fig. 2.

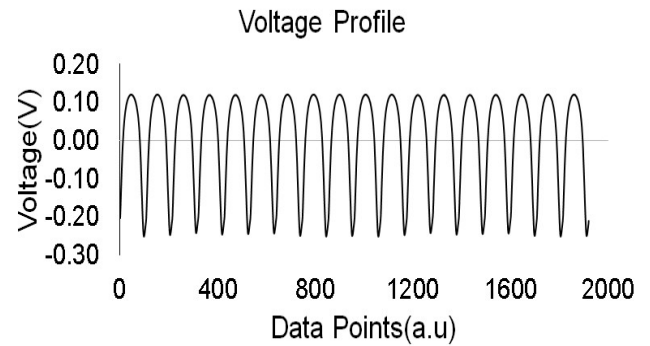


Fig. 2. HTS Stator Voltage profile

III. FEM MODELLING OF HTS GENERATOR

ANSYS MAXWELL provides a very flexible platform for the electromagnetic analysis of rotating machines. With the inclusion of RMxpert features into ANSYS, the analysis of the non-conventional designs is convenient and user friendly compared to earlier versions of ANSYS.

A 6-pole, 10 kW HTS generator model was developed in SOLIDWORKS. A hexagonal rotor core with 2 layers of HTS racetrack coils per pole made the HTS rotor. The HTS field windings were connected in series. A ConCoil stator (concentric winding) with 36 slots was designed using RMxpert-User Defined Primitives to suit the HTS rotor assembly. The other details of the machine are listed in Table I. The rotor assembly was simplified and the entire geometry was converted from MAXWELL 3D design (Fig. 3) model to MAXWELL 2D design model (Fig. 4) to reduce the simulation time. Simulations were carried out on the 2D FEM model of the 10 kW HTS synchronous generator.

TABLE I
HTS GENERATOR PARAMETERS

| | |
|-----------------------------|--------------|
| Rating | 10 kW |
| Rated Voltage | 400 V |
| Poles | 6 |
| Speed | 300 rpm |
| Frequency | 15 Hz |
| Type of Rotor | HTS |
| HTS Winding | Racetrack |
| HTS Wire | SuNam |
| Coil Thickness | 35.25 mm |
| Turns in field coil | 235 |
| Rated field current | 98A |
| Field current margin | 40% |

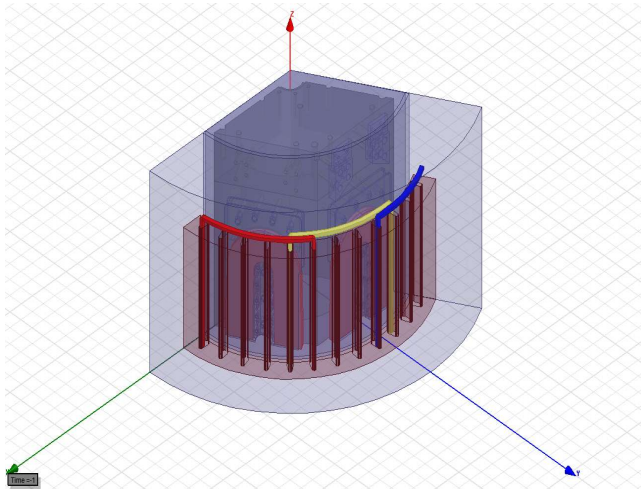


Fig. 3. ANSYS MAXWELL 3D FEM pie model of HTS generator.

Mesh refinement in FEM analysis is critical - a very fine mesh results in longer simulation time and coarser mesh results in poorly resolved outputs. A trade-off has to be made in order to achieve reasonable accuracy within a practical time frame. Length based mesh with an element size of 1 mm was chosen for field windings, stator conductors and air gap. Coarse mesh with larger element size was chosen for other parts (see Fig. 4).

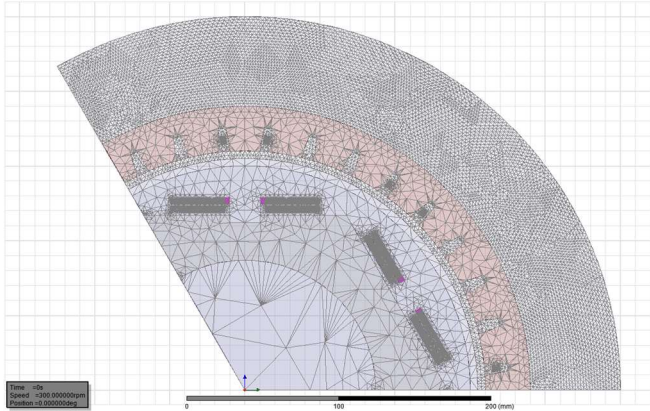


Fig. 4. Mesh plot of pie section of the 2D FEM Model.

The FEM simulation parameters are listed in Table II.

TABLE II

| FEM SIMULATION PARAMETERS | |
|------------------------------|--|
| Boundary conditions | <ul style="list-style-type: none"> • Vector potential • Master-Slave |
| Mesh type | Length based |
| Analysis type | Magnetic transient |
| Time step | 0.0002s |
| Total simulation time | 750 ms |

IV. PERFORMANCE ANALYSIS

A dynamic HTS flux pump is integrated with the HTS generator and can be rotated in either direction to that of the field rotor of the generator. After initial ramp up to the rated field current, the flux pump is put out of operation and since the HTS rotor based field system has ultra-low resistance, the decay in the field occurs really slow. The flux pump is again brought into operation when the field current drops below a threshold value. In this case, the flux pump is operated when the field current drops below 95A, during the steady state operation. The frequency of excitation can be varied by controlling the speed of the flux pump rotor. The field windings in the FEM model were excited using the experimental data obtained from flux pump experiments. Since the desired frequency of generated voltage is 15 Hz, 3 different frequencies of flux pump excitation, 60Hz, 120Hz and 240Hz, were used for exciting the field system. The excitation windings in ANSYS were declared as voltage windings with assumed flux pump dynamic resistance of $10 \mu\Omega$. For these investigations, open circuit phase voltages were recorded as the output. The field calculations were carried out at an interval of 10 ms.

A. Field Analysis

The field pattern in the HTS generator is observed to be non-uniform and with a high fringing effect, reflected via the high field concentration on the stator of the machine (Fig. 5) along the corners of the HTS field coils.

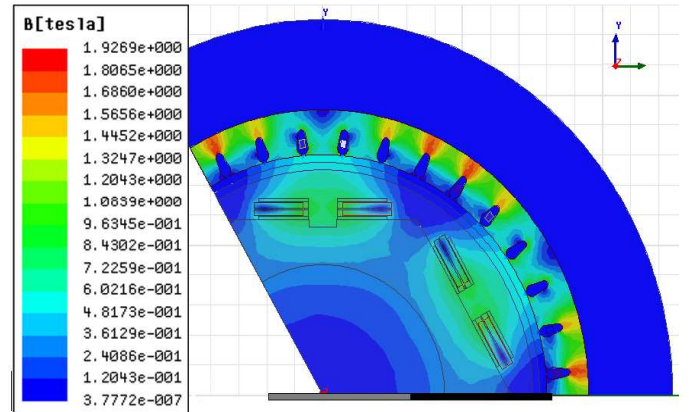


Fig. 5. Field pattern with ferromagnetic stator at $t = 0$ s.

The field strength at the centre of the field coil is ~ 1.2 T. Steel1008 material used for the stator frame acts as a flux concentrator but there will be hysteresis loss when a ferromagnetic material is used in varying magnetic field. The field pattern at $t = 10$ ms (Fig. 6), also depicts the same fringing effect as observed at $t = 0$ s. This fringing effect is expected as there is no salient or non-salient ferromagnetic rotor pole structure to distribute the field uniformly. The ferromagnetic stator acts as flux concentrator and the field strength at the stator conductors will be higher than the field strength with

a non-ferromagnetic stator. Though the ferromagnetic stator concentrates the flux and helps in reducing the number of stator conductors for a rated voltage, it increases the hysteresis loss. The transition from North- pole to South-pole or vice-versa for a particular stator conductor is sharp in the case of ferromagnetic stator than in the case of non-ferromagnetic stator. This sharp transition manifests as distortion in the induced voltage profile.

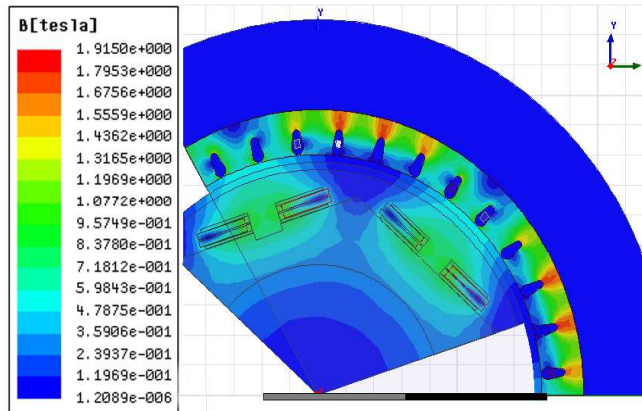


Fig. 6. Field pattern with ferromagnetic stator at t = 10 ms.

The hysteresis in the ferromagnetic stator increases the ambient temperature around the cryostat of the HTS rotor and increases the ambient thermal load on the cryogenic system. In order to avoid the hysteresis loss, a non-ferromagnetic stator can be used. Hence, simulations were also carried out with G10-FRP as the stator material to study the effects on the generator performance with a non-ferromagnetic stator.

The iron losses can be approximately expressed as follows:

$$W_i = K_e f^2 B^2 + K_h f B^2, \quad (1)$$

where K_e is the eddy current coefficient of the material

f is the frequency

B is the magnetic field strength

K_h is the hysteresis coefficient of the material.

For a non-conductor, the values of K_e and K_h are zero - hence the iron losses can be reduced to zero with the use of non-conducting stator frame.

G10-FRP was chosen as the stator material, as it will serve the dual purpose of non-conductivity and provide further cryogenic insulation for the HTS rotor. But with the use of G10-FRP, the flux concentration is reduced and the field strength around the stator conductors is correspondingly reduced (see Fig. 7). The magnitude of the induced voltages, correspondingly, is lower than the induced voltage with the ferromagnetic stator material. Figs. 9 and 10 show the induced phase voltages with steel and G10 stator, respectively.

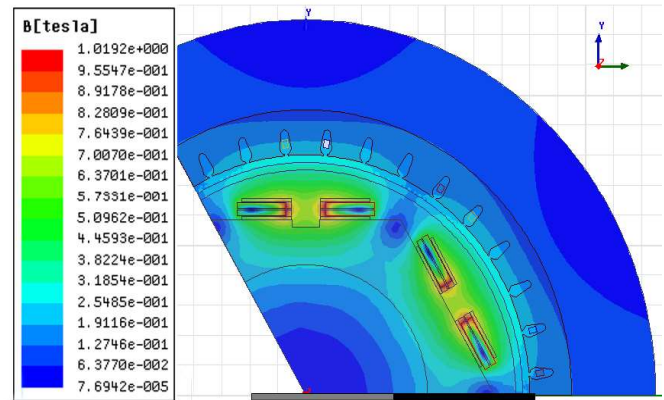


Fig. 7. Field pattern with G10 stator.

B. Excitation Frequency

The excitation frequency of the flux pump has no significant effect on the field distribution of the machine but the rate of increase in field current is observed to be directly proportional to the frequency of excitation. The increase in the field current above the steady state current of 95 A (3 A less than the rated current) versus the excitation frequency in 750 ms of simulation time is shown in Fig. 8. With 60 Hz Flux pump excitation, the increase in field current is 3.1mA in 750 ms and with 120 Hz the increase is 5.6mA while the increase is 7.7 mA with 240 Hz. It is further observed that the frequency of flux pump excitation has no effect on the THD of the induced voltage but the ramp up rate of field current is seen to be directly proportional to the frequency of excitation.

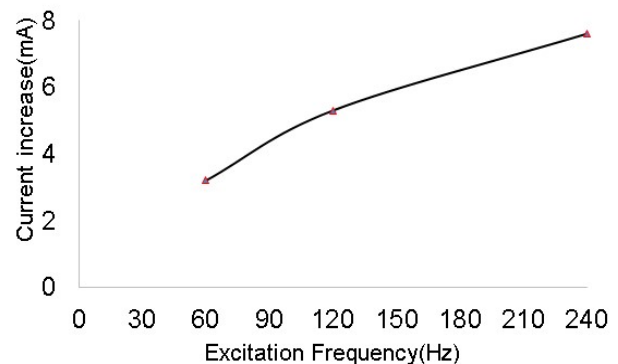


Fig. 8. Field current increase versus the excitation frequency.

C. Harmonic Analysis

The harmonic analysis was carried out on the induced Phase voltages. Fast Fourier Transform (FFT) and THD were computed using MATLAB. FFT and THD provide the quantitative measure of the different frequency components present in the induced voltage waveform.

THD is given by the following equation:

$$THD = \frac{\sqrt{\sum_k V_k^2}}{V_1}, \quad (2)$$

where k is an integer and refers to the harmonic order, $k = 2, 3, 4, \dots$, V_k is the amplitude of k^{th} order harmonic, and V_1 is the fundamental frequency component.

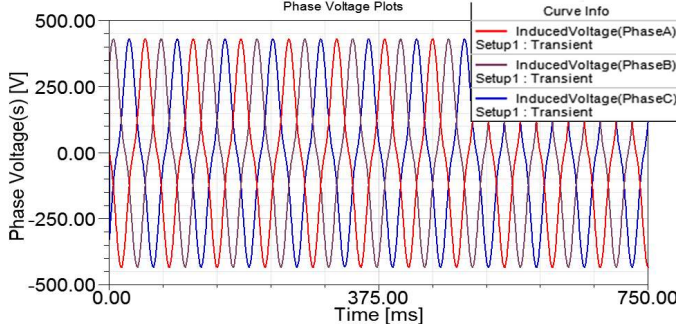


Fig. 9. Open circuit phase voltage plots with steel stator.

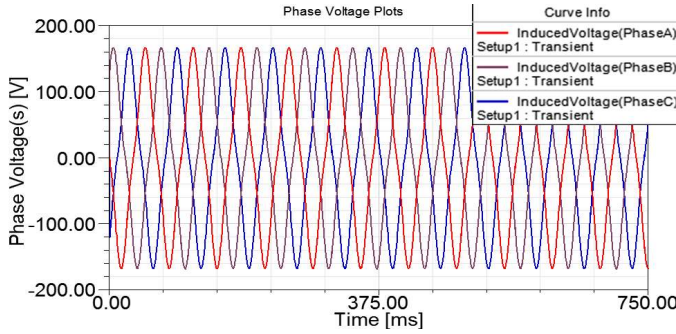


Fig. 10. Open circuit phase voltage plots with G10 stator.

Table III gives a comparison between THD values of the Phase voltage FFT with steel stator and with G10 stator. It is observed that the THD values with G10 stator are lower than with the Steel stator. This difference can be attributed to the fringing in the field distribution with steel stator (Fig. 5) - the steel stator acts as flux concentrator. Non-uniformity in the voltage profile observed during the zero crossing of the voltage is higher in the case of steel stator than the G10 stator. A sharp transition in the field from North-pole to South-pole or vice versa (Figs. 5 and 7) because of absence of a ferromagnetic pole structure on the rotor is found to be the reason for the non-uniformity in voltage profile during zero crossing.

The FFT plots of Phase A induced voltage at 240 Hz flux pump excitation with steel stator and G10 stator are shown in Fig. 11 and Fig. 12, respectively. A dominant third harmonic is observed in both the cases but the magnitude of the third harmonic is lower in case of G10 stator and this is reflected in a correspondingly lower THD value (Table III) as well.

TABLE III

| THD COMPARISON BETWEEN STEEL AND G10 STATOR | | | | |
|---|---------|---------|---------|---------|
| THD (%) Comparison | | | | |
| Excitation frequency | Steel | | G10 | |
| | Phase A | Phase B | Phase A | Phase B |
| 60 Hz | 15.563 | 15.544 | 13.4066 | 13.4048 |
| 120 Hz | 15.564 | 15.611 | 13.4079 | 13.4077 |
| 240 Hz | 15.578 | 15.584 | 13.4081 | 13.4074 |

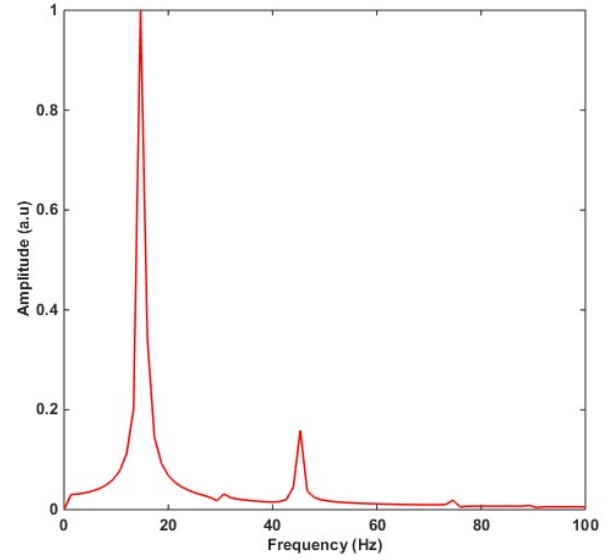


Fig. 11. FFT of Phase A voltage plot for steel stator.

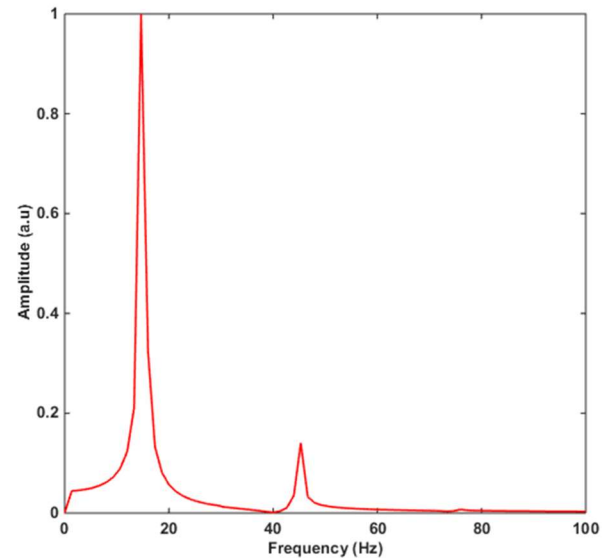


Fig. 12. FFT of Phase A voltage plot for G10 stator.

V. CONCLUSIONS

Flux pump has been successfully shown to be an alternative to DC for exciting the field system in a HTS generator. This avoids the thermal link between the cryogenic and non-cryogenic environment, thus decreasing the thermal loading on the cryogenic system. In addition, performance analysis was carried out on a 10 kW HTS generator. The field analysis results indicate that there is significant fringing effect in the field pattern. This is also reflected as distortion in the induced voltage. From the harmonic analysis, it can be concluded that the stator material has significant effect on the THD of the induced voltage. With the use of non-ferromagnetic stator material (G10), the hysteresis loss can be avoided and the THD can be reduced, optimization of stator configuration will lead to decrease in THD. The different excitation frequencies of the flux pump have negligible effects on the field pattern and the THD of the induced voltage. The implementation of a series parallel combination of the flux pump stators can be carried out but that calls for a detailed failure analysis of (such a) combination of stators with significant quenching possibilities during the operation. Use of separately excited flux pump stators could possibly resolve the issue but may result in a field current imbalance and these studies are currently in progress.

REFERENCES

- [1] S. S. Kalsi, *Application of High Temperature Superconductors to Electric Power Equipment*, New York: Wiley, 2011
- M. Tomita and K. Murakami, "High-temperature superconductor bulk magnets that can trap magnetic fields of over 17 Tesla at 29 K", *Nature*, 2003(421), pp 517–520
- P. N. Barnes, M.D. Sumption, and G.L. Rhoads, "Review of high power density superconducting generators: Present state and prospects for incorporating YBCO windings," *Cryogenics*, 2005. **45**(10–11): pp. 670–686
- Q. Ronghai, L. Yingzhen, and W. Jin, "Review of Superconducting Generator Topologies for Direct-Drive Wind Turbines," *IEEE Trans. on Applied Superconductivity*, , 2013. **23**(3): p. 5201108-5201108.
- S. S. Kalsi, N.H., D. Gritter, O. Nayak and C. Gallagher, "Benefits of HTS technology to ship systems," IEEE Symposium on Electric Ship Technologies, Philadelphia PA, 27 July 2005.
- S. S. Kalsi, K. Weeber, H. Takesue, C. Lewis, H. W. Neumueller and R. D. Blaugher, "Development status of rotating machines employing superconducting field windings," in *Proc. 2004 IEEE*, vol. 92, no. 10, pp. 1688-1704.
- W. Nick, G. Nerowski, H.-W. Neumüller, M. Frank, P. van Hasselt, J. Frauenhofer, F. Steinmeyer, "380 kW synchronous machine with HTS rotor windings—development at Siemens and first test results," *Physica C: Superconductivity*, 2002. **372–376**, Part 3(0): p. 1506-1512
- S. Jeong and Y. Kim, Thermal anchoring of conduction-cooled current leads for superconductivity applications near liquid nitrogen temperature, *Cryogenics*, 2010. **50**(4): p. 287-291.
- T. Nakamura, M. Sugano, T. Doi and N. Amemiya, "Flux Pumping Effect of HTS Films in a Traveling Magnetic Field," *IEEE Trans. on Applied Superconductivity*, 2010. **20**(3): p. 1033-1036
- S. Ishmael, C. Goodzeit, P. Masson, R. Meinke and R. Sullivan, "Flux Pump Excited Double-Helix Rotor for Use in Synchronous Machines," *IEEE Trans. on Applied Superconductivity*, 2008. **18**(2): p. 693-696.
- R. Shafaie and M. Kalantar, Design of a 10-MW-Class Wind Turbine HTS Synchronous Generator With Optimized Field Winding, *IEEE Trans. on Applied Superconductivity*, 2013. **23**(4): p. 5202307-5202307
- H. Seo, K. J. Han, H. S. Choi, S. H. Lee, S. Hahn and H. Lee, "Comparison Study on Harmonic Loss of MW-Class Wind Generators With HTS Field Winding," *IEEE Trans. on Applied Superconductivity*, 2014. **24**(3): p. 1-5
- C. Hoffmann, D. Pooke, and A. D. Caplin, "Flux Pump for HTS Magnets," *IEEE Trans. on Applied Superconductivity*, 2011. **21**(3): p. 1628-1631
- C. Hoffmann, R. Walsh, E. Karrer-Mueller, D. Pooke, "Design Parameters for an HTS Flux Pump," *Physics Procedia*, 2012. **36**(0): p. 1324-1329.
- R. Kulkarni, K. Prasad, and T.T. Lie, "Flux pump for HTS rotating machinery applications," *PowerTech 2015 IEEE Eindhoven*. 2015.
- T. Coombs, Z. Hong, and X. Zhu, "A thermally actuated superconducting flux pump," *Physica C: Superconductivity*, 2008. **468**(3): p. 153-159.
- Z. Jiang, K. Hamilton, N. Amemiya, R. A. Badcock and C. W. Bumby, Dynamic resistance of a high-Tc superconducting flux pump, *Applied Physics Letters*, 2014. **105**(11): p. 112601-112601-4
- C. W. Bumby, A. E. Pantoja, H. J. Sung, Z. Jiang, R. Kulkarni and R. A. Badcock, "Through-Wall Excitation of a Magnet Coil by an External-Rotor HTS Flux Pump," *IEEE Trans. on Applied Superconductivity*,, 2016. **26**(4): p. 1-5
- C. W. Bumby, R. A. Badcock, H. J. Sung, K. M. Kim, Z. Jiang, A. E. Pantoja, P. Bernardo, M. Park and R. G. Buckley, "Development of a brushless HTS exciter for a 10 kW HTS synchronous generator," *Superconductor Science and Technology*, 2016. **29**(2): p. 024008

4. Energies Journal, MDPI

Design Improvisation for Reduced Harmonic Distortion in a Flux Pump-Integrated HTS Generator

Ravichandra Kulkarni ^{1,*}, Krishnamachar Prasad ¹, Tek Tjing Lie ¹, Rodney A. Badcock ², Chris W. Bumby ² and Hae-Jin Sung ²

¹ Department of Electrical and Electronic Engineering, Auckland University of Technology, Auckland 1010, New Zealand; kprasad@aut.ac.nz (K.P.); tlie@aut.ac.nz (T.T.L.)

² Robinson Research Institute, Victoria University of Wellington, Wellington 5010, New Zealand; rod.badcock@vuw.ac.nz (R.A.B.); chris.bumby@vuw.ac.nz (C.W.B.); haejin0216@gmail.com (H.-J.S.)

* Correspondence: rkulkarn@aut.ac.nz; Tel.: +64-210-850-1580

Received: 29 May 2017; Accepted: 22 August 2017; Published: 5 September 2017

Abstract: This paper presents a design improvisation of a flux pump-integrated 10 kW high-temperature superconducting (HTS) proof of concept generator for reduced harmonic distortion. To carry out the design improvisation, a finite element analysis (FEA) model of the 10 kW HTS generator is developed, and time-stepped magnetic transient simulations are conducted on the 2D model. The effects of stator yoke material, winding pitch factors, and load configurations on total harmonic distortion (THD) are investigated. The results showed that fibre-reinforced polymer (FRP) epoxy (G10) can be used as the stator yoke material to effectively avoid the hysteresis and eddy current losses. In addition, the study results show that for the non-conventional design of the machine, a winding pitch of 2/3 and the armature-load configuration of Star-Delta gives THD values within the standard limit defined by IEEE Standard 519-2014. The THD values indicate that the machine design configuration is suitable for the development of machines for both stand-alone and grid-connected operations, according to IEEE STD 519-2014.

Keywords: current leads; finite element method (FEM); flux pump; HTS; harmonics; yttrium barium copper oxide (YBCO)

1. Introduction

The success of an electromechanical design modelling is in its ability to predict the performance of the system accurately. The penetration of computation software in pre-determining the outcome of the design has become incredibly large. The finite element analysis (FEA) is one such computational method that can be applied to the complex design problems, and maximum improvisation can be carried out before the field test deployment. In this paper, FEA-based simulations on a flux pump-integrated 10 kW high-temperature superconducting (HTS) generator are conducted to analyse the harmonic contents under different operating conditions. Though 10 kW is a low-end rating for a HTS-based machine, it is developed as a proof-of-concept system.

Technologies to deliver higher power wind turbines are sought for efficient renewable generation. Higher power density machines are one solution. High current densities of 106–108 A/mm² and high magnetic field capabilities of 4–5 T of the second-generation (2G) HTS (Yttrium Barium Copper Oxide-YBCO) materials make them attractive for power-dense electric machine applications [1–3]. HTS-based generators are being designed and developed to meet this power demand [4–6]. In the design of HTS machines, thermal loss considerations are key to minimising cryogenic load and the local instability of the HTS winding. One way of reducing thermal losses is to minimise the components causing thermal loading on the cryogenic system [7,8]. The use of flux pump avoids the thermal link between the cryogenic and non-cryogenic environments [8–10].

The use of flux pumps to excite HTS coils for various applications has come a long way and evolved significantly. To be specific, the application of a flux pump as an excitation alternative for rotating machines has been proven and studied by various research groups across the world [11–20]; this research has thoroughly described the various characteristics of the machine as well as conducted performance analysis. The independent and novel finding of the voltage profile across the flux pump stator is our unique contribution. The study on the influence of flux-pump excitation on the induced voltage in a generator, as against a conventional DC excitation source is the first of its kind. Along with the nature of excitation, the load configuration and stator material have also been taken into consideration to make the study more comprehensive.

If non-ferromagnetic rotor core and stator yoke materials are chosen, they provide further minimisation of losses by eliminating hysteresis and eddy current losses. The usage of non-ferromagnetic material such as fibre-reinforced polymer (FRP) epoxy as the stator yoke reduces the field concentration at the conductors, and the flux distribution is non-uniform over the layers for different phases in each stator slot. The design of non-conventional electric machines involves the adaptive implementation of both conventional and proven designs [5]. The 10 kW HTS generator used in this research is one such non-conventional design.

Total harmonic distortion (THD) is one of the most important performance parameters of a generator. THD gives a measure of overall integral multiple frequency components in a periodic waveform. The higher frequency harmonic components cause an increase in iron loss and reduction in the efficiency of electrical machines [21,22]. The THD values have to be in accordance with the standard specifications (IEEE STD 519-2014) for a stable grid-connected operation or in stand-alone mode. Earlier reports have discussed the potential of flux pumps to replace the DC excitation of field windings [8,9]. Another substantial contributing factor in harmonic performance is the stator yoke material. For HTS-based rotating machines' applications, air-cored stator suits best [23,24]. A study outlining the harmonic distortion effects of the use of an air-cored stator or a non-ferromagnetic stator for a non-conventional machine design with flux pump excitation, as presented in this paper, is first of its kind. We have reported the no-load harmonic performance of a 10 kW HTS generator with two different stator yoke materials [25]. The use of FRP epoxy (G10) results in reduced THD as there is no magnetic saturation in the material. In this paper, the effects of the stator design on the harmonic performance will be reported, and the best-suited design configuration for improved THD performance will be established.

2. FEA Modelling of HTS Generator

The engineering design friendly finite element simulation package-ANSYS Maxwell, provides a flexible platform for the electromagnetic analysis of rotating machines.

The inclusion of RMxpert features into ANSYS has made the analysis of the non-conventional designs more convenient and user friendly than earlier versions of ANSYS [26]. A six-pole, 10 kW HTS generator model was developed in SolidWorks. A hexagonal rotor core with two layers of HTS racetrack coils per pole made the HTS rotor. The HTS field windings were connected in a series. A ConCoil stator (concentric winding) with 36 slots was designed using RMxpert-User Defined Primitives to suit the HTS rotor assembly.

The other details of the machine are listed in Table 1. The rotor assembly was simplified and the entire geometry was converted from a Maxwell 3D design (Figure 1) model to a Maxwell 2D design model (Figure 2) to reduce the simulation time. Simulations were carried out on the 2D finite element model (FEM) of the 10 kW HTS synchronous generator.

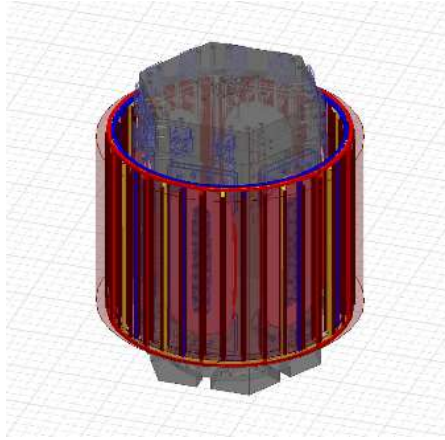
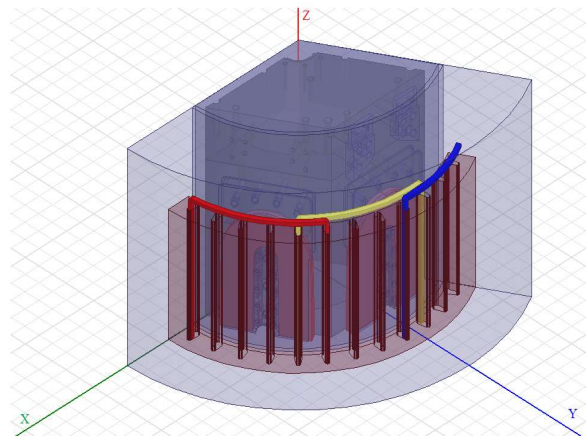


Figure 1. High-temperature superconducting (HTS) generator-ANSYS 3D model.

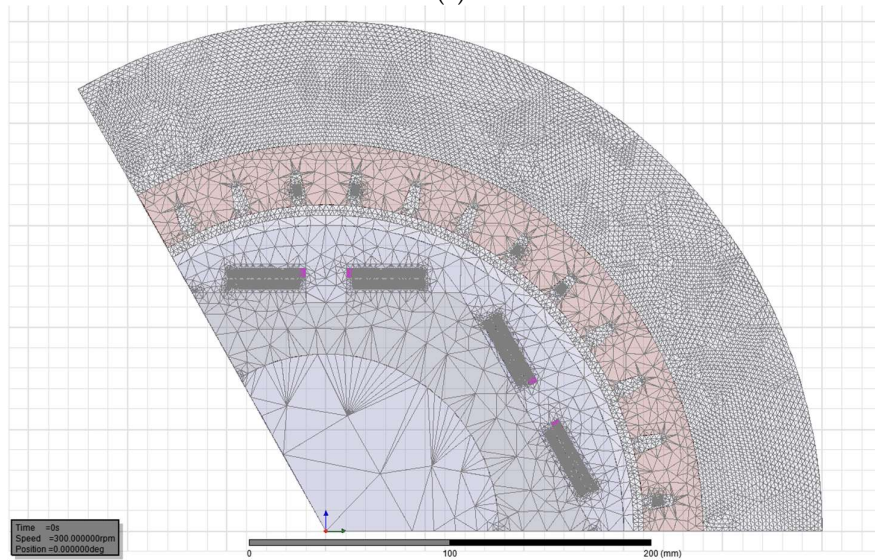
Table 1. HTS Generator Parameters.

| Parameter | | Value |
|---------------------|------|-----------|
| Rating | | 10 kW |
| HTS Temperature | Coil | 30K |
| Rated Voltage | | 400 V |
| Poles | | 6 |
| Speed | | 300 rpm |
| Frequency | | 15 Hz |
| Type of Rotor | | HTS |
| HTS Winding | | Racetrack |
| HTS Wire | | SuNam |
| Coil Thickness | | 35.25 mm |
| Turns in field coil | | 235 |

| | |
|----------------------|--------|
| Rated field current | 98 A |
| Field current margin | 40% |
| Rotor shaft length | 315 mm |
| Total diameter | 497 mm |



(a)



(b)

Figure 2. (a) ANSYS Maxwell 3D finite element model (FEM) pie model of a HTS generator; (b) mesh plot of pie section of the 2D FEM model.

Mesh refinement in FEM analysis is critical, as a very fine mesh results in longer simulation time, and coarser mesh results in poorly resolved outputs. A trade-off was made in order to achieve reasonable accuracy within a practical time frame. Length-based mesh with an element size of 1 mm was chosen for field windings, stator conductors, and air gap. Coarse mesh with a larger element size

of 3.5 mm was chosen for other parts (Figure 2b). The rotor core was left at the default mesh size set by ANSYS at > 3.5 mm, as it does not influence the effects being studied. The FEM simulation parameters are listed in Table 2. The use of the master-slave boundary condition helped with reducing the model size by making use of the symmetrical geometry of the machine [27].

Table 2. FEM Simulation Parameters.

| Boundary Conditions | | Vector Potential & Master Slave |
|-----------------------|--|---------------------------------|
| Mesh type | | Length based |
| Analysis type | | Magnetic transient |
| Time step | | 0.2 ms |
| Total simulation time | | 750 ms |

3. Performance Analysis

The flux pump offers a unique method of magnetising a superconductor without a physical link between the cryogenic and non-cryogenic environment [9–14]. Jiang et al. [15] have presented a formulation of a dynamic resistance model for a HTS flux pump, wherein the results show a linear relation between the frequency of the flux pump and the rate of current increase. From the voltage profile, it is evident that a net voltage (quasi-DC emf) drop occurs across the superconducting coil [7].

In the present study with the flux pump, the same trend was observed and the non-uniform voltage profile observed across the HTS stator (see Figure 3) is similar to that of Bumby et al. [16]. Based on the previous reported results [9], it is well established that the flux pump can be successfully used as an alternative to DC excitation for the field system in a generator. The voltage profiles obtained from experiments with flux pumps were used as excitation inputs to the FEM model discussed in Section 2.

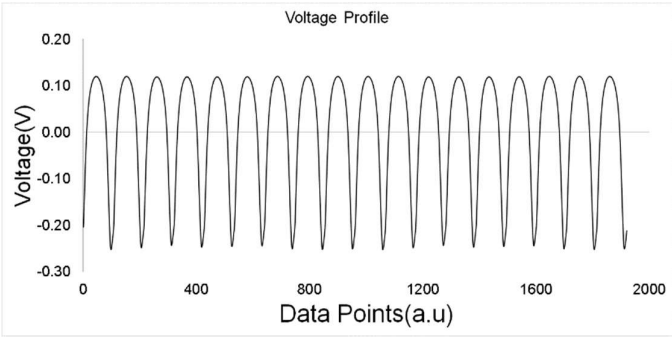


Figure 3. Voltage profile across the flux pump stator.

As outlined in Section 1, the THD performance of a generator is one of the most critical parameters for the successful implementation of either a grid-connected generator or one used as a stand-alone supply for sensitive electronic loads. The range of this study covers the harmonic performance analysis of the proof of concept 10 kW HTS synchronous generator. The harmonic performance of a synchronous

generator depends primarily on the rotor and stator construction [28,29].

The other factors that influence the harmonic performance are the nature of field excitation, the materials of the ferromagnetic circuit, armature reaction, load configuration, etc. In a previous work, we investigated and reported the no-load harmonic performance of the 10 kW HTS synchronous generator [25]. The minimum THD observed with the design was ~13%, which is low enough for the stand-alone operation of the generator with only heating load, but could not be used for grid-connected operation or electronic loads such as TV, Liquid Crystal Displays etc.

In this paper, we propose a stator design that considers three important parameters; (a) the stator yoke material, (b) winding pitch factor (K_p), and (c) load configuration.

3.1. Effect of Stator Yoke Material

In the above-mentioned work [25], we realized that FRP epoxy material is a better alternative to the commonly used steel yoke. The hysteresis in the ferromagnetic stator increases the ambient temperature around the cryostat of the HTS rotor and the ambient thermal load on the cryogenic system. In order to avoid the hysteresis loss, a non-ferromagnetic stator can be used. Hence, simulations were carried out with G10-FRP as the stator material in order to study the effects on the performance of generators with non-ferromagnetic stators.

The iron losses can be approximately expressed as follows:

$$W_i = K_e f^2 B^2 + K_h f B^2 \quad (1)$$

where K_e is the eddy current coefficient of the material, f is the frequency, B is the magnetic field strength, and K_h is the hysteresis coefficient of the material.

For a non-conductor, the values of K_e and K_h are zero; hence, the iron losses can be reduced to zero with the use of a non-conducting stator frame. The use of non-ferromagnetic stator yoke results in a decrease of voltage levels as the field strength around the stator conductors decreases. The decrease in voltage levels has been compensated with an increase in the number of stator conductors. The increase in the number of stator conductors due to the usage of non-ferromagnetic yoke adds up to the capital cost, but avoids the recurring hysteresis losses.

3.2 Effect of Winding Pitch Factor (K_p)

The winding pitch of a generator is the number of slots spanned by each coil in the stator winding over the number of slots per pole (Figure 4). The winding pitch of generators is generally shortened from full pitch to either 5/6 (Figure 4b) or 2/3 (Figure 4c) in order to change the harmonic content of the output waveform. At the same time, the fundamental component of the output voltage is slightly lower than the full pitch winding. The reduction in the output voltage can be compensated by an increase in the field strength or the number of stator conductors. One of the leading manufacturers of synchronous generators-ABB uses both 5/6 and 2/3 pitched winding [30]. 5/6 is preferred for HV generators where compactness is preferred over reduced THD. The winding pitch factor K_p [31] gives the variation factor for different harmonics and is expressed as:

$$K_p = \cos\left(\frac{N \times 180(1 - \text{pitch})}{2}\right) \quad (2)$$

where N is the order of the harmonic.

Table 3 lists the values of K_p for 2/3 and 5/6 winding pitches. The value of K_p for the third harmonic with 2/3 pitch works out to be zero, thus eliminating the third harmonic component. This decreases the overall THD, but there is also a decrease in the voltage levels, which needs compensation.

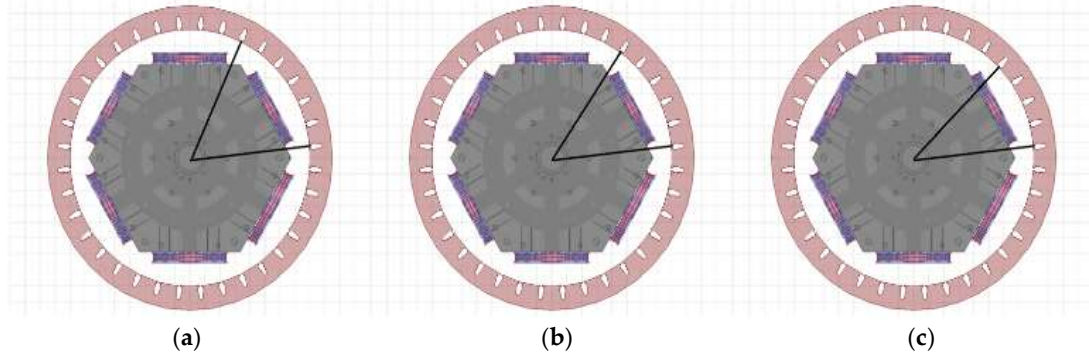


Figure 4. Stator conductor placement: (a) full pitch; (b) 5/6 pitch; (c) 2/3 pitch.

Table 3. Winding Pitch Factor.

| Winding Pitch Factor (K_p) | | |
|--------------------------------|-----------|-----------|
| Component | 2/3 Pitch | 5/6 Pitch |
| Fundamental | 0.87 | 0.97 |
| 3rd Harmonic | 0.00 | 0.71 |
| 5th Harmonic | 0.87 | 0.26 |
| 7th Harmonic | 0.87 | 0.26 |

3.3. Effect of Load Configuration

The harmonic performance of the HTS generator has been examined for “no load” and “rated load” conditions. The HTS generator in this discussion is aimed at implementation for wind-based power generation. In wind turbines, the best-suited alternator winding configuration is Star at the start-up in order to support an easy initial spin at high voltage and low current. The winding is switched to Delta once the speed has picked up to boost the current levels [32]. However, for low speed generation, as in this case, a fixed Star winding configuration for the alternator windings is deemed suitable.

Simulations were conducted for two different alternator winding and load winding configurations.

4. Star-Star (S-S)
5. Star-Delta (S-D)

The effect of the change in load configurations on the THD of the induced phase voltage will be discussed in the next section. The change in the load configuration has an effect on the field current as well; this effect is also discussed in next section.

4. Results and Discussion

4.1 Field Pattern

The field pattern with G10 as the stator material and flux pump excitation is observed to be uniform (Figure 5). The field variation at the stator location is minimal. The induced voltage waveforms (Figure 6) are consistent with the design expectations and have a lower THD than the designs we reported previously [25]. The harmonic analysis was carried out on the induced phase voltages. Normalised fast Fourier transform (FFT) and THD were computed using MATLAB 2015b. FFT and THD provide the quantitative measure of the different frequency components present in the induced voltage waveform.

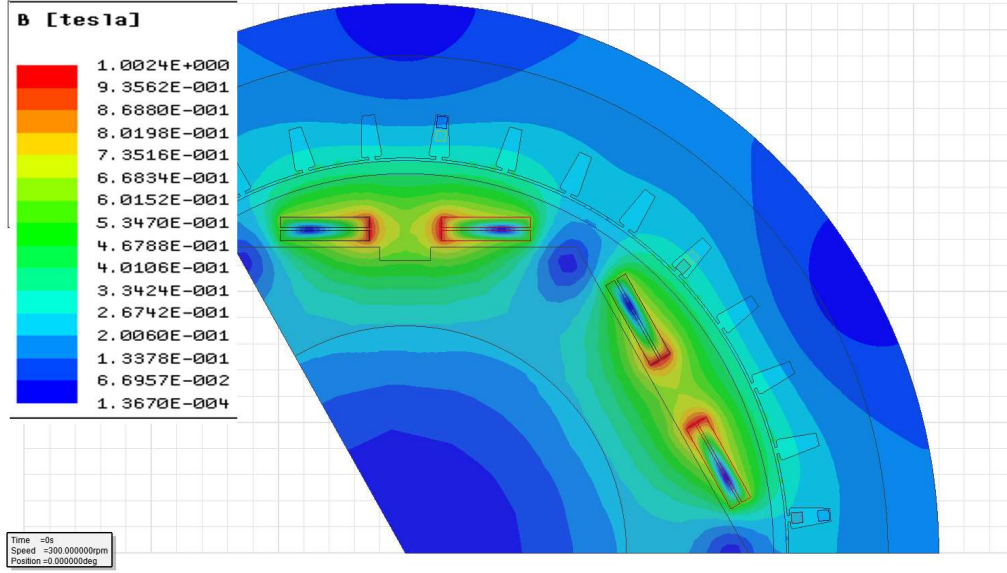


Figure 5. ANSYS field pattern with G10 stator yoke (stator design 1).

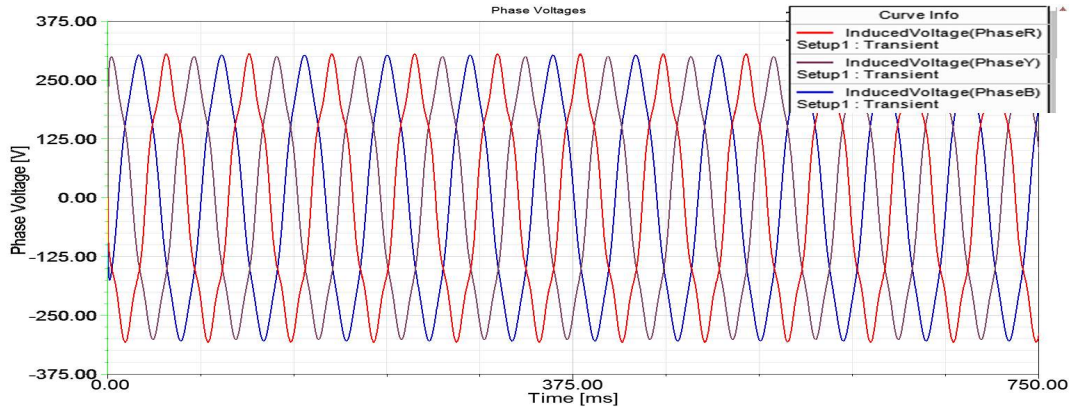


Figure 6. ANSYS plot of induced three-phase voltage.

4.2 Total Harmonic Distortion

THD is given by the following equation:

$$\text{THD} = \frac{\sqrt{\sum_k V_k^2}}{V_1} \quad (3)$$

where k is an integer and refers to the harmonic order ($k = 2, 3, 4 \dots$), V_k is the amplitude of k th order harmonic, and V_1 is the fundamental frequency component. The improvement in THD for the 2/3 pitch configuration is clearly seen, and this is because of the elimination of the third harmonic component that is present in the 5/6 pitch configuration (see Figure 7).

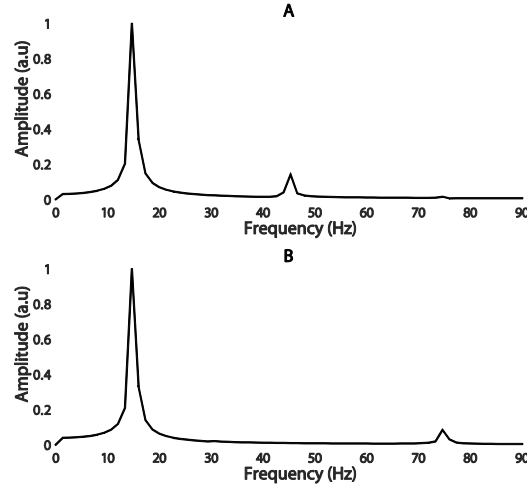


Figure 7. Normalised fast Fourier transform (FFT) plot of induced phase voltage at rated load: (a) pitch = 5/6; (b) pitch = 2/3.

Tables 4–6 show a comparison between the THD values of the induced phase voltage under different conditions. Simulations were carried out for three different frequencies of flux pump excitation (60 Hz, 120 Hz and 240 Hz). Under “no load” conditions, it was observed that the THD values with G10 stator were lower than those with the steel stator (Table 4). This reduction in THD can be attributed to higher fringing effects and sharper transition of the fields in the case of steel yoke stator for the hexagonal design of the rotor without pole shoes. The change in the winding pitch resulted in a decrease in the induced voltage levels, but improved the harmonic performance. The voltage levels were compensated by increasing the number of stator conductors, as mentioned in Section 3.

Table 4. No load THD (V_{ph}) [22].

| f (Hz) | Pitch = 5/6 | | Pitch = 2/3 | |
|----------|-------------|-------|-------------|------|
| | Steel | G10 | Steel | G10 |
| 60 | 15.56 | 13.40 | 8.59 | 6.13 |
| 120 | 15.56 | 13.41 | 8.60 | 6.14 |
| 240 | 15.57 | 13.41 | 8.61 | 6.14 |

Table 5. Rated load G10 Stator 2/3 Pitch.

| f (Hz) | Star-Star | Star-Delta |
|----------|-----------|------------|
| 60 | 5.91 | 5.21 |
| 120 | 5.91 | 5.22 |
| 240 | 5.98 | 5.22 |

Table 6. Star-Delta G10 Stator 2/3 Pitch

| f (Hz) | THD (V _{ph}) | | |
|----------|------------------------|----------------|----------------|
| | Rated Load | 1/2 Rated Load | 1/4 Rated Load |
| 60 | 5.21 | 5.84 | 6.05 |
| 120 | 5.22 | 5.84 | 6.05 |
| 240 | 5.22 | 5.84 | 6.05 |

As discussed in Section 3, since the winding pitch is a critical factor in tuning the harmonic performance [33–36], results are analysed for two different pitches. The THD for the 2/3 pitch configuration is significantly reduced when compared to the 5/6 pitch configuration for both steel and G10 stator yokes. The reason for this improvement is the successful elimination of the third harmonic component (Figure 7). Based on these results, for further simulations, the stator yoke material was selected to be G10, and the winding pitch was selected to be 2/3.

Simulations for different loaded conditions (rated load, 1/2 rated and 1/4 rated loads) were carried out for two different configurations. Balanced resistive loads were coupled to the ANSYS Maxwell model using ANSYS Maxwell Circuit Editor for these simulations. With S-S configuration, the THD of the induced phase voltage (V_{ph}) is ~3.3% lower than with the “no load” THD values (see Tables 4 and 5).

On further investigation, it was observed that the field current profiles for the “no load” condition are affected by the pulsating nature of the flux pump excitation, whereas the pulsating effect does not have much of an effect under loaded conditions (see Figure 8). However, the field current is increasing in both of the cases; the field current oscillations in the case of the loaded condition have a higher sinusoidal variation than the field currents with the “no load” condition. For further simulations, Star-Delta (S-D) was selected as the load configuration. The THD values at different levels (Rated, 1/2 and 1/4 loads) are as tabulated in Table 6. Minimum THD is observed at rated load.

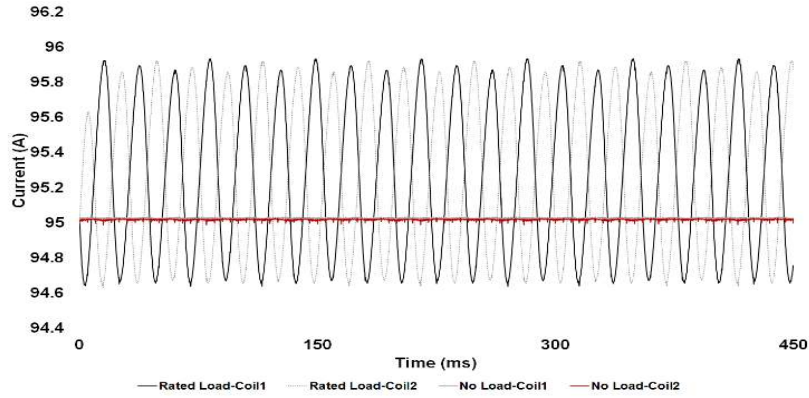


Figure 8. Field current oscillations with respect to the loading condition.

It is also observed that the THD values for the S-D configuration are slightly lower than the S-S configuration. This is most likely due to the lower armature reaction in the case of the S-D configuration. Studies on armature reaction and analyses of direct axis reactance (X_d) and quadrature axis reactance of the machine (X_q) of the machine are likely to give a better understanding of the ongoing phenomenon from magnetic field interaction. The THD limit as specified in IEEE STD 519-2014 is 5% for a bus voltage <69 kV at the point of common coupling, and the permitted limit is 8% for lower voltage generation <1 kV. Hence, the proof of concept generator to be tested in field and designed for 400 V meets prescribed standards.

The final commercial product based on this proof of concept generator will be a flux pump-integrated MW class wind turbine HTS generator, and the generated voltage levels for this generator are expected to be >1 kV and <69 kV. For this class of generation, the maximum limit of THD is 8%, as per the prescribed standard.

The observed THD limits are well within this limit, and with this design, a tolerance offset of ~3% can be considered for the additional harmonics introduced due to control circuitry and the power electronic switching circuitry, which will be integrated at different points of the generation and transmission. The overall variation trend of THD against various design parameters is shown in the bar graphs of Figure 9. It is seen that the S-D configuration with a pitch of 2/3 at rated load gives the least THD. The results are in consistence with the results observed for similar ironless machines [37].

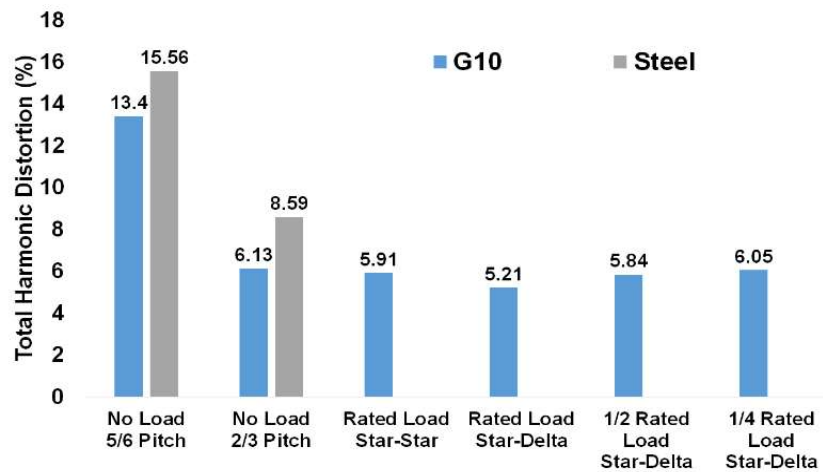


Figure 9. The variation of total harmonic distortion (THD) with material, pitch and load configurations.

As discussed in Section 3, the stator made of FRP epoxy (G-10) is better suited in cryogenic applications. In the absence of a ferromagnetic yoke, the field distribution is less concentrated and the drop in the field is higher, with a small increase in the distance from the centre of the field coil. To improve the THD performance, design modifications were carried out on the stator geometry, and are discussed in the following sections.

4.3 Stator Design Improvement

4.3.1. Stator Design 1

In our earlier work [24], we proposed a stator design considering three important parameters: (a) the stator yoke material (b), winding pitch factor (K_p), and (c) load configuration. The 2D FEM model of the earlier design is as shown in Figure 10.

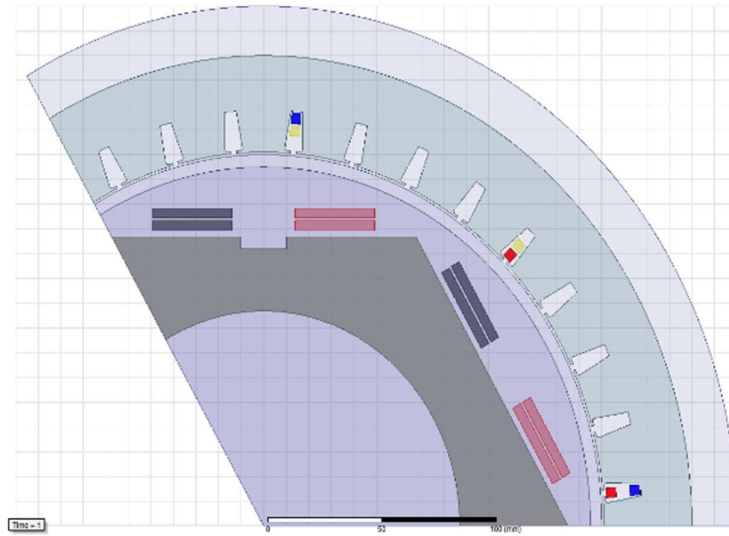


Figure 10. 2D model with stator design 1.

4.3.2. Stator Design 2

From field and performance analysis of Design 1, it is understood that the conductors corresponding to the same phase are at different field levels. The reason is attributed to the absence of the ferromagnetic yoke of the stator. In order to avoid field non-uniformity, a different stator design is proposed, as shown in Figure 11, wherein the stator conductors could be placed in an adjacent manner rather than a stacked manner.

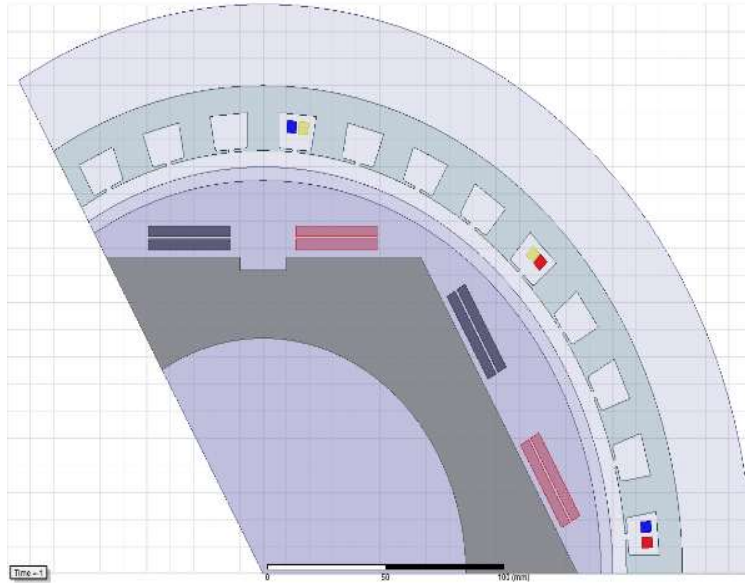


Figure 11. 2D model with stator design 2.

The two important variations in the design were:

Stator slot width, and
Internal diameter of the rotor.

The stator slot width was changed from 8 mm to 14 mm to accommodate the adjacent placement of all three phase stator conductors. The diameter on the yoke side was reduced from 380 mm to 360 mm, and the diameter on the gap side was increased from 302 mm to 312 mm. These variations were carried out to place the stator conductors for the same phase at the same field strength for most of the time, and decrease the fluctuations in the field level as well as the correspondingly in the induced voltage level. Thus, there was an expected decrease in the THD.

The field pattern with stator design 1 shows that the stator conductors corresponding to the same phase are at different field strengths (Figure 5). When the stator design changes, it is observed that the conductors corresponding to the same phase are in the same field strength, as required (Figure 12). The change in stator design resulted in an improvement in the harmonic performance of the machine. With the same meshing and boundary conditions as set for stator design 1, the change in the stator dimension and conductor placement strategy for a G-10 stator yoke resulted in a significant improvement in the harmonic performance; these results are shown in Table 7. The decrease in the harmonic distortion validates that field uniformity is one of the important factors in ascertaining a better harmonic performance.

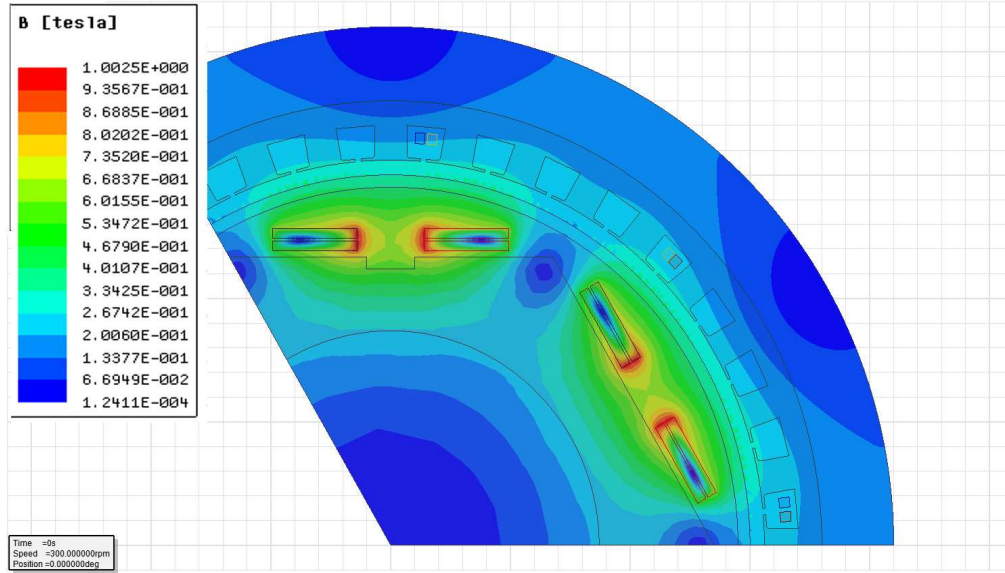


Figure 12. ANSYS field pattern with G10 stator yoke (stator design 2).

Table 7. THD Comparison between Design 1 and Design 2.

| f (Hz) | No Load THD | | Rated Load THD | |
|----------|-------------|----------|----------------|----------|
| | Design 1 | Design 2 | Design 1 | Design 2 |
| 60 | 6.1367 | 4.2915 | 5.2164 | 2.7269 |
| 120 | 6.1378 | 4.3016 | 5.2196 | 2.7366 |
| 240 | 6.1383 | 4.3155 | 5.2243 | 2.7398 |

5. Conclusions

The effects of stator design on the harmonic performance of the generator were carried out. It has been successfully shown that the flux pump can be an alternative to DC source for exciting the field system in an HTS generator, even for loaded conditions such as S-S or S-D configurations. The results indicate that the variation in the parameters such as stator yoke material, winding pitch, and loading configuration affect the harmonic performance significantly. The stator material has a significant effect on the THD of the induced voltage. The use of non-ferromagnetic stator materials (G10) leads to a decrease in the THD. The different excitation frequencies of the flux pump have negligible effects on the THD of the induced voltage. Based on the simulations with different winding pitches, a winding pitch of 2/3 is the best suited for this machine. The simulations on the load configurations indicate that the S-D configuration would result in the smallest value of THD. The most suitable configuration with respect to the stator yoke material, winding pitch, and load configuration to minimize the THD of a 10 kW HTS generator has been established. A better stator conductors' placement and stator design strategy to reduce harmonic distortion have been analytically deduced. Further work on the geometrical design improvisation of the stator windings, and separately excited field coils to avoid quenching and total failure of the system, are currently in progress.

Acknowledgments: The authors would like to acknowledge the support from Robinson Research Institute, Victoria University of Wellington, New Zealand, Auckland University of Technology, New Zealand and Changwon National University, South Korea.

Author Contributions: Ravichandra Kulkarni, Krishnamachar Prasad and Tek Tjing Lie conceived and designed the simulation study and experiments; Ravichandra Kulkarni, Rodney A Badcock, Chris W Bumby and Hae Jin Sung conducted flux pump experiments and analyzed the data; Rodney A Badcock, Hae Jin Sung provided the solidworks model of the HTS generator; Ravichandra Kulkarni wrote the paper.

Conflicts of Interest: The authors declare no conflict of interest.

References

1. Kalsi, S.S. Application of High Temperature Superconductors to Electric Power Equipment; John Wiley & Sons: Hoboken, NJ, USA, 2011.
2. Qu, R.; Liu, Y.; Wang, J. Review of Superconducting Generator Topologies for Direct-Drive Wind Turbines. *IEEE Trans. Appl. Supercond.* **2013**, *23*, 5201108–5201108.
3. Kalsi, S.S.; Henderson, N.; Gritter, D.; Nayak, O.; Gallagher, C. Benefits of HTS technology to ship systems. In Proceedings of the IEEE Symposium on Electric Ship Technologies, Philadelphia, PA, USA, 27 July 2005.
4. Kalsi, S.S.; Weeber, K.; Takesue, H.; Lewis, C.L.; Neumueller, H.W.; Blaugher, R.D. Development status of rotating machines employing superconducting field windings. *Proc. IEEE.* **2004**, *92*, 1688–1704.
5. Nick, W.; Nerowski, G.; Neumüller, H.W.; Frank, M.; Van Hasselt, P.; Frauenhofer, J.; Steinmeyer, F. 380 kW synchronous machine with HTS rotor windings—development at Siemens and first test results. *Phys. C Supercond.* **2002**, *372–376*, 1506–1512.
6. Barnes, P.N.; Sumption, M.D.; Rhoads, G.L. Review of high power density superconducting generators: Present state and prospects for incorporating YBCO windings. *Cryogenics* **2005**, *45*, 670–686.
7. Jeong, S.; Kim, Y. Thermal anchoring of conduction-cooled current leads for superconductivity applications near liquid nitrogen temperature. *Cryogenics* **2010**, *50*, 287–291.
8. Bumby, C.W.; Pantoja, A.E.; Sung, H.J.; Jiang, Z.; Kulkarni, R.; Badcock, R.A. Through-Wall Excitation of a Magnet Coil by an External-Rotor HTS Flux Pump. *IEEE Trans. Appl. Supercond.* **2016**, *26*, 1–5.
9. Kulkarni, R.; Prasad, K.; Lie, T.T. Flux pump for HTS rotating machinery applications, In Proceedings of the 2015 IEEE Eindhoven PowerTech 2015, Eindhoven, The Netherlands, 29 June–2 July 2015.
10. Nakamura, T.; Sugano, M.; Doi, T.; Amemiya, N. Flux Pumping Effect of HTS Films in a Traveling Magnetic Field. *IEEE Trans. Appl. Supercond.* **2010**, *20*, 1033–1036.
11. Ishmael, S.; Goodzeit, C.; Masson, P.; Meinke, R.; Sullivan, R. Flux Pump Excited Double-Helix Rotor for Use in Synchronous Machines. *IEEE Trans. Appl. Supercond.* **2008**, *18*, 693–696.
12. Hoffmann, C.; Walsh, R.; Karrer-Mueller, E.; Pooke, D. Design Parameters for an HTS Flux Pump. *Phys. Procedia* **2012**, *36*, 1324–1329.
13. Hoffmann, C.; Pooke, D.; Caplin, A.D. Flux Pump for HTS Magnets. *IEEE Trans. Appl. Supercond.* **2011**, *21*, 1628–1631.
14. Coombs, T.; Hong, Z.; Zhu, X. A thermally actuated superconducting flux pump. *Phys. C Supercond.* **2008**, *468*, 153–159.
15. Jiang, Z.; Hamilton, K.; Amemiya, N.; Badcock, R.A.; Bumby, C.W. Dynamic resistance of a high-Tc superconducting flux pump. *Appl. Phys. Lett.* **2014**, *105*, 112601.
16. Bumby, C.W.; Badcock, R.A.; Sung, H.J.; Kim, K.M.; Jiang, Z.; Pantoja, A.E.; Buckley, R.G. Development of a brushless HTS exciter for a 10 kW HTS synchronous generator. *Supercond. Sci. Technol.* **2016**, *29*, 024008.
17. Mawardi, O.; Muelder, S.; Michelotti, R. Brushless superconducting alternators. *IEEE Trans. Magn.* **1977**, *13*, 780–783.
18. Muta, I.; Tsukiji, H.; Hoshino, T.; Mukai, E. Electrical characteristics of fully superconducting synchronous generator in persistent excitation mode. *IEEE Trans. Magn.* **1992**, *28*, 434–437.
19. Muta, I.; Tsukiji, H.; Hoshino, T.; Mukai, E. Output power limit of 200 MW class brushless superconducting generator excited with magnetic flux-pump. *IEEE Trans. Appl. Supercond.* **2001**, *11*, 2335–2338.
20. Ferendeci, A.; Mawardi, O.; Melfi, M.; Laquer, H. Flux pump excited brushless alternator. *IEEE Trans. Magn.* **1981**, *17*, 146–148.
21. Vashi, A. Harmonic Reduction in Power System. Master's Degree, California State University, Sacramento, CA, USA, 8 June 2010.
22. Wakileh, G.J. Harmonics in rotating machines. *Electr. Power Syst. Res.* **2003**, *66*, 31–37.
23. Miller, T.J.E.; Hughes, A. Comparative design and performance analysis of air-cored and iron-cored synchronous machines. *Proc. Inst. Electr. Eng.* **1977**, *124*, 127–132.

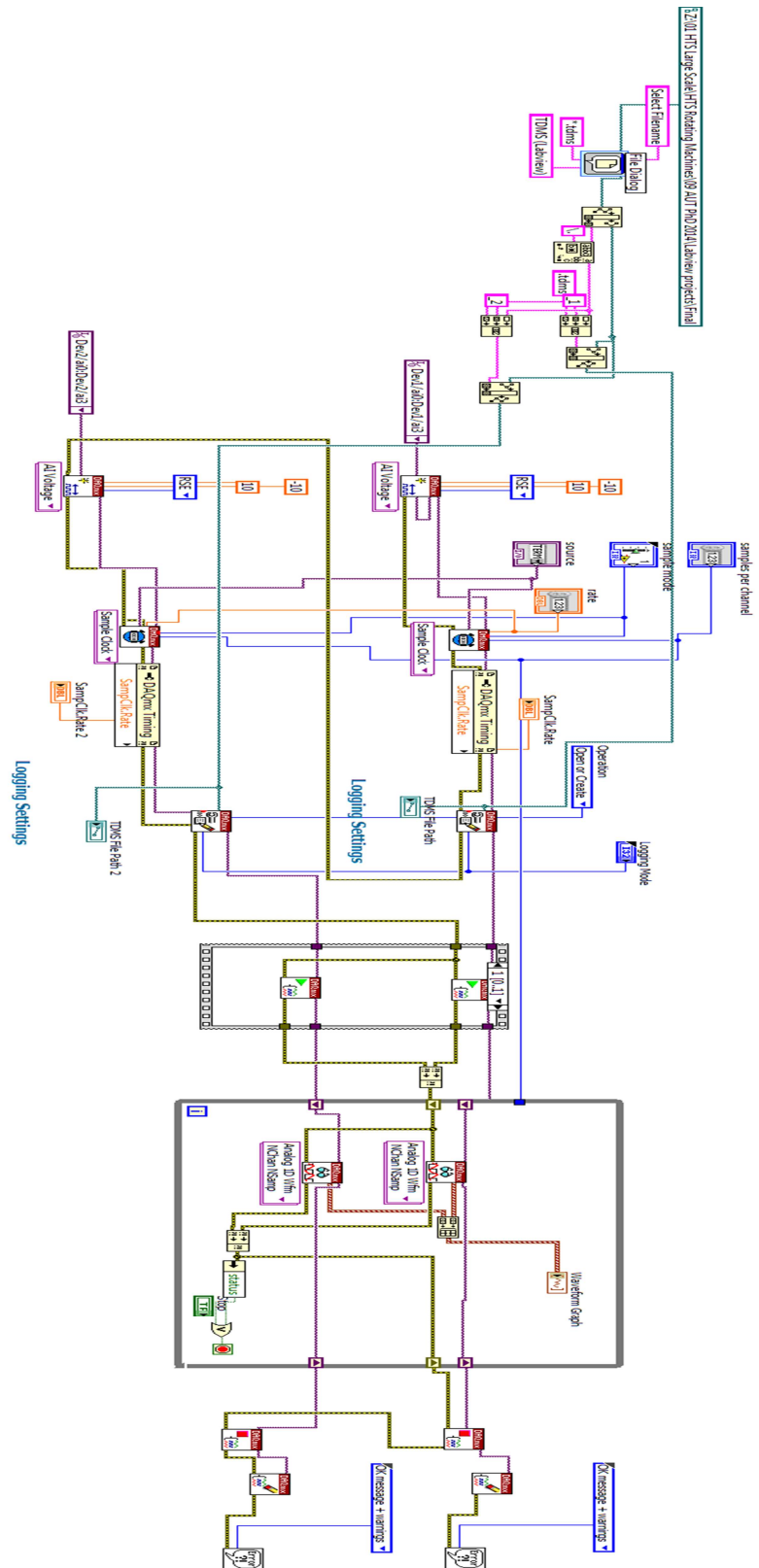
24. Hughes, A.; Miller, T.J.E. Analysis of fields and inductances in air-cored and iron-cored synchronous machines. *Proc. Inst. Electr. Eng.* **1977**, *124*, 121–126.
25. Kulkarni, R.; Prasad, K.; Lie, T.T.; Badcock, R.A.; Bumby, C.W.; Sung, H.J. FEM and performance analysis of 10 kW HTS generator with flux pump excitation. In Proceedings of the 2016 IEEE International Conference on Power System Technology (POWERCON), Wollongong, Australia, 28 September–1 October 2016.
26. Khalf, M.A.; Wamkeue, R.; Aguglia, D. Finite element approach for performances prediction of a small synchronous generator using ANSYS software. In Proceedings of the 25th IEEE Canadian Conference on Electrical & Computer Engineering (CCECE), Montreal, QC, Canada, 29 April–2 May 2012.
27. ANSYS Maxwell Manual. Available online: <https://support.ANSYS.com/portal/site/ANSYSCustomerPortal/template.fss?file=%2Fsolutions%2Fattach%2FMAXWELL.pdf> (accessed on 29 August 2017).
28. Shafaie, R.; Kalantar, M. Design of a 10-MW-Class Wind Turbine HTS Synchronous Generator with Optimized Field Winding. *IEEE Trans. Appl. Supercond.* **2013**, *23*, 5202307.
29. Seo, J.H.; Han, K.J.; Choi, H.S.; Lee, S.H.; Hahn, S.; Lee, H. Comparison Study on Harmonic Loss of MW-Class Wind Generators with HTS Field Winding. *IEEE Trans. Appl. Supercond.* **2014**, *24*, 1–5.
30. Technical Note. Available online: library.e.abb.com/public/8d5deb3fe4638051c1257c9400508282/Technical%20note%20Winding%20pitch%20LR_040214.pdf (accessed on 25 August 2017).
31. Nelson, J.P. A better understanding of harmonic distortion in the petrochemical industry. *IEEE Trans. Ind. Appl.* **2004**, *40*, 220–231.
32. Butcher Charles A. Synchronous Machine Starting System. U.S. Patent 1,804,591, 12 May 1931.
33. Zhang, L.; Huang, Y.; Dong, J.; Guo, B.; Zhou, T. Stator winding design of induction motors for high efficiency. In Proceedings of the 17th International Conference on Electrical Machines and Systems (ICEMS), Hangzhou, China, 22–25 October 2014.
34. Smith, R.; Layton, J.M. Harmonic elimination in poly-phase machines by graded windings. *Proc. Inst. Electr. Eng.* **1963**, *110*, 1640–1648.
35. Alternator Winding Pitch and Power System Design. Available online: <https://power.cummins.com/technical-papers> (accessed on 29 August 2017).
36. Say, M.G. *Alternating Current Machines*, 4th ed.; Pitman Publishing Ltd: London UK, 1976.
37. Zhang, Z.; Molinas, M.; Matveev, A.; Nilssen, R.; Nysveen, A. Efficiency calculation and improvement of a large-diameter ironless permanent magnet generator. In Proceedings of the 2012 15th International Conference on Electrical Machines and Systems (ICEMS), Sapporo, Japan, 21–24 October 2012.



© 2017 by the authors. Licensee MDPI, Basel, Switzerland. This article is an open access article distributed under the terms and conditions of the Creative Commons Attribution (CC BY) license (<http://creativecommons.org/licenses/by/4.0/>).

Appendix-B : Additional Results

B1.LabVIEW Block Diagram



B2.Sample High rate data acquisition CSV files

The tdms format was used for storing the raw data as it is suitable for large data management and is a built-in file format in LabVIEW. The following overview description from the National Instruments white paper (<http://www.ni.com/white-paper/3727/en/>) provides more clarity and is followed by sample file from the acquired data during experimentation.

Overview of the TDMS File Structure

The single, most important feature to understand about the internal format of the TDMS file structure is its inherent hierarchical organization. The TDMS file format is structured using three levels of hierarchy, as shown in Figure 1 – file, group, and channel. The file level can contain an unlimited number of groups, and each group can contain an unlimited number of channels. Because of this channel grouping, you can choose how to organize your data to make it easier to understand. For example, you may have one group for your raw data and another group for your analyzed data within one single file. Or, you may have multiple groups that correspond to sensor types or locations.

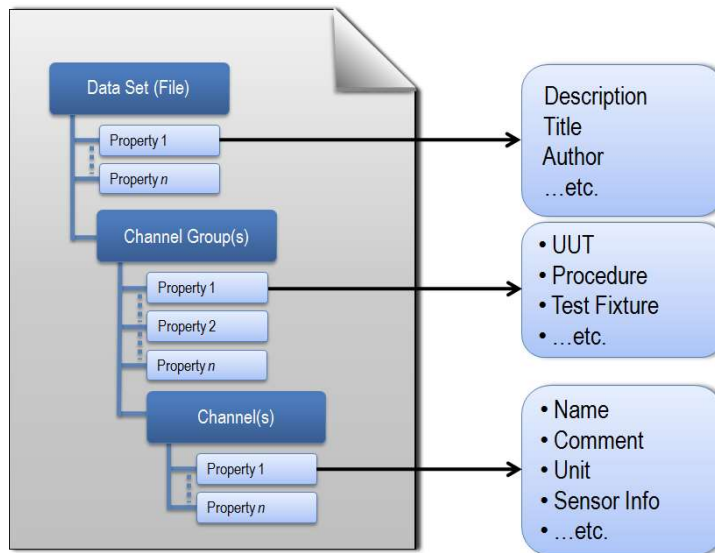


Figure 1. Each TDMS file contains descriptive information on the file, group, and channel levels.

At each level of the hierarchy, you can store an unlimited number of custom scalar properties. Each level accepts an unlimited number of custom-defined attributes to achieve well-documented and search-ready data files. The descriptive information located in the file, a key benefit of this model, provides an easy way to document the data without having to design your own header structure. As your documentation requirements increase, you do not have to redesign your application; you simply extend the model to meet your specific needs. The more custom properties you use to document your measurement data, the more easily it can be located later by using an NI DataFinder client that abstracts complex database communication from the user.

TDMS files also automatically generate a complimentary *.tdms_index file. This file provides consolidated information on all the attributes and pointers in the bulk data file that

drastically speeds up read access to the data on larger data sets. This index file is not required for storage or distribution and automatically regenerates

3. Writing and Reading TDMS Files with NI Software

The NI TDMS file format is a National Instruments platform-supported file format. All NI software development environments interface with TDMS files as part of their native function palettes or libraries. These interfaces abstract the complexity of storing structured data while making it easy to add descriptive information along with captured measurement or simulation data.

LabVIEW

There are multiple interfaces to NI TDMS files from NI LabVIEW software. The easiest way to get started writing TDMS files in LabVIEW is with the Write to Measurement File Express VI. This Express VI offers the ease of dialog-based configuration but sacrifices performance and is not suitable for high-speed streaming or real-time applications.

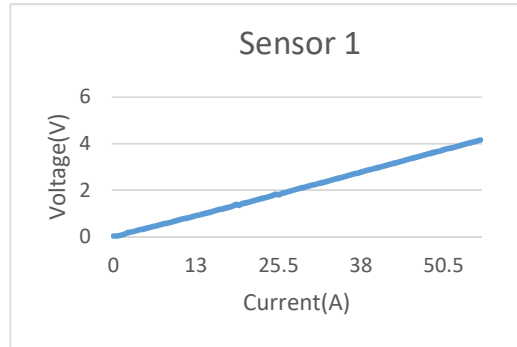
For more flexibility and to achieve the best performance, use the TDMS primitive VIs from the File I/O palette. With these VIs, you can read and write TDMS files and their properties in the most efficient manner possible. This method of accessing TDMS files is real-time-capable using the LabVIEW Real-Time Module. The TDM Streaming palette was introduced in LabVIEW 8.2.

Installation of LabVIEW or drivers released in August 2010 or later includes access to a brand new TDMS Advanced palette for extremely low-level control of TDMS files, so you can perform advanced techniques such as asynchronous writes and reads.

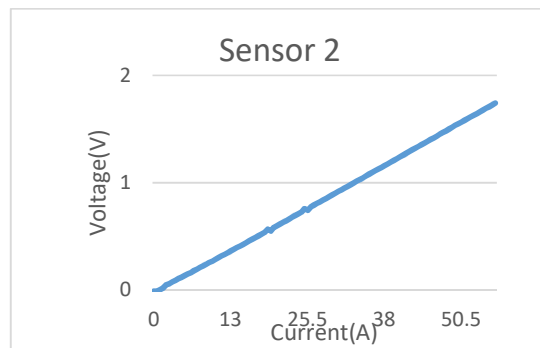
| 1 | Root Name | Title | Author | Date/Time |
|---|--------------------------------------|----------|-------------|-----------|
| 2 | 2990rpm-6mm-initial-gen1-241014-v1_2 | | | |
| 3 | | | | |
| 4 | Group | Channels | Description | |
| 5 | Sensors 4,3,2,1 | 4 | | |
| 6 | | | | |

| | | | | | | | | |
|----|-----------------|-----------|-------|-----------|----------------|--------------------|--------------|------------|
| 6 | | | | | | | | |
| 7 | Sensors 4,3,2,1 | | | | | | | |
| 8 | Channel | Datatype | Unit | Length | NI_ChannelName | NI_UnitDescription | wf_increment | wf_samples |
| 9 | Dev2/ai0 | DT_DOUBLE | Volts | 267142279 | Dev2/ai0 | Volts | 0.00002 | 1 |
| 10 | Dev2/ai1 | DT_DOUBLE | Volts | 267142279 | Dev2/ai1 | Volts | 0.00002 | 1 |
| 11 | Dev2/ai2 | DT_DOUBLE | Volts | 267142279 | Dev2/ai2 | Volts | 0.00002 | 1 |
| 12 | Dev2/ai3 | DT_DOUBLE | Volts | 267142279 | Dev2/ai3 | Volts | 0.00002 | 1 |

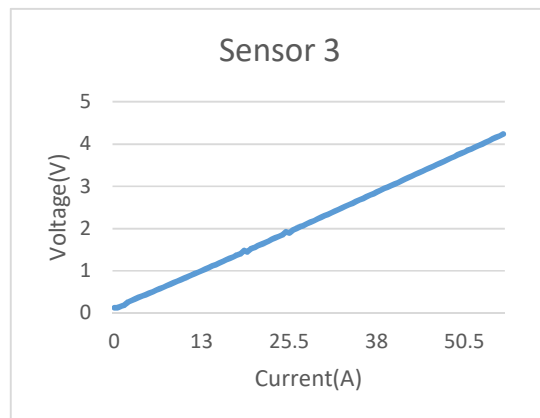
B3.Hall sensor current coil calibration curves and corresponding quadratic fit equations for unknown current by change of subject in the quadratic fit equation:



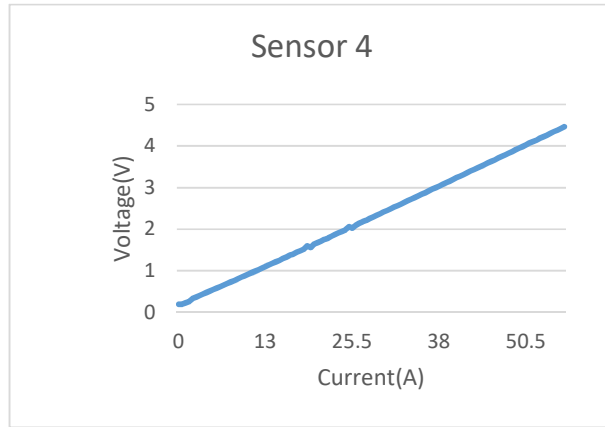
$$i_1 = -0.203x^2 + 14.3x \quad (B.1)$$



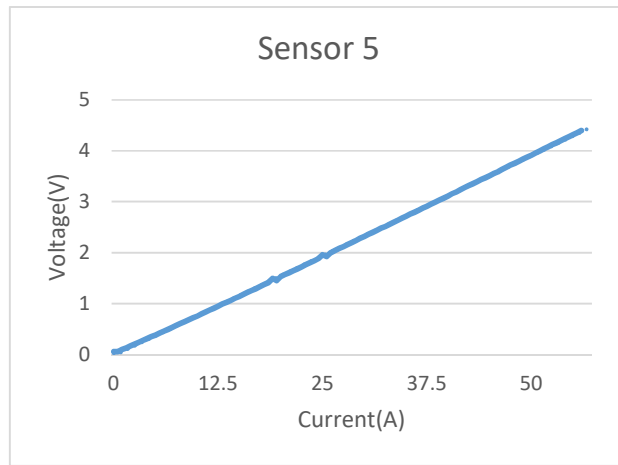
$$i_2 = -1.92x^2 + 14.3x \quad (B.2)$$



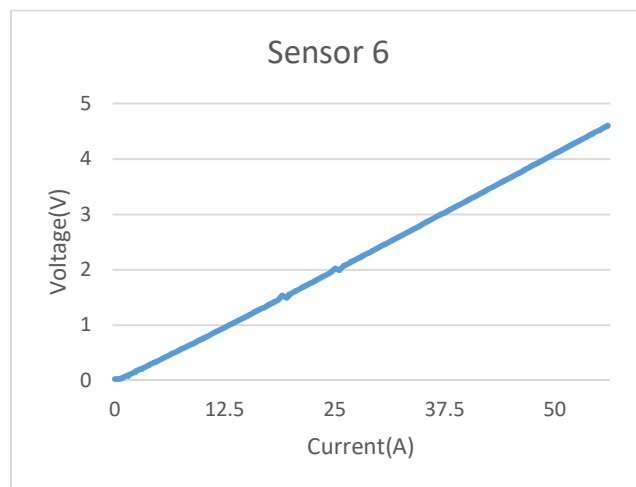
$$i_3 = 0.05x^2 + 13.1x \quad (B.3)$$



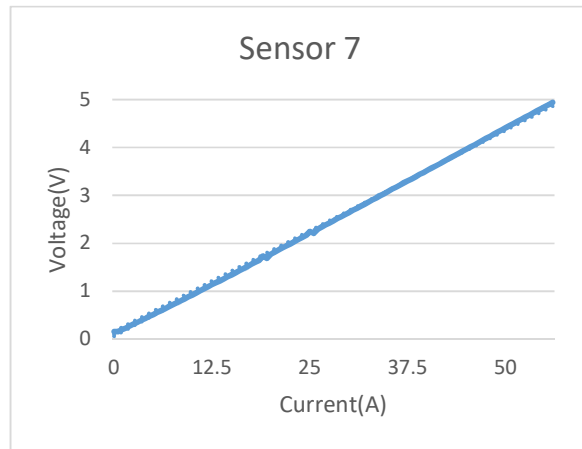
$$i_4 = 0.167x^2 + 11.9x \quad (B.4)$$



$$i_5 = -0.12x^2 + 13.2x \quad (B.5)$$



$$i_6 = -0.18x^2 + 13x \quad (B.6)$$



$$i_7 = -0.18x^2 + 13x \quad (\text{B.7})$$

B4. THD values for different load configurations

Table 1.

| Unloaded(Un-optimized, Shortpitch=1)) | | |
|---------------------------------------|---------|---------|
| Frequency (Hz) | THD (%) | |
| | Steel | G10 |
| 60 | 15.563 | 13.4066 |
| 120 | 15.564 | 13.4079 |
| 240 | 15.578 | 13.4081 |

Table 2.

| Unloaded(optimized, Shortpitch=2)) | | |
|------------------------------------|---------|--------|
| Frequency (Hz) | THD (%) | |
| | Steel | G10 |
| 60 | 8.5991 | 6.1367 |
| 120 | 8.6053 | 6.1378 |
| 240 | 8.6059 | 6.1383 |

Table 3.

| Loaded(R Load) | G10-Star-Star |
|----------------|---------------|
| Frequency | THD (Vph) |
| 60 | 5.9089 |
| 120 | 5.9137 |
| 240 | 5.9843 |

Table 4.

| Loaded(R Load) | Star-Delta |
|----------------|------------|
| Frequency | THD(Vph) |
| 60 | 5.2164 |
| 120 | 5.2196 |
| 240 | 5.2243 |

Table 5.

| Loaded(R Load) | Delta-Star |
|----------------|------------|
| Frequency | THD(Vph) |
| 60 | 6.1345 |

| | |
|-----|--------|
| 120 | 6.1388 |
| 240 | 6.1424 |

Table 6.

| Loaded(RL load) | Star-Star |
|-----------------|-----------|
| Frequency | THD(Vph) |
| 60 | 5.5218 |
| 120 | 5.5239 |
| 240 | 5.5277 |

Table 7.

| Loaded (R-L Load) | Star-Delta |
|-------------------|------------|
| Frequency | THD(Vph) |
| 60 | 4.5855 |
| 120 | 4.5844 |
| 240 | 4.5863 |

Table 8.

| Loaded (R-L Load) | Delta-Star |
|-------------------|------------|
| Frequency | THD(Vph) |
| 60 | 6.3865 |
| 120 | 6.3988 |
| 240 | 6.4004 |

Table 9.

Stator Design 2

| Frequency | Star Delta | | |
|-----------|------------|--------------|---------------|
| | THD (Vph) | | |
| | No Load | Rated R load | Rated RL-load |
| 60 | 4.2915 | 2.7269 | 2.4132 |
| 120 | 4.3016 | 2.7366 | 2.4099 |
| 240 | 4.3155 | 2.7398 | 2.4186 |

B5. ANSYS MAXWELL Magnetic Field Formulation

Magnetic field formulation is the basis function of any finite element analysis based software package. There are various electromagnetic field formulations using FEA to numerically solve maxwell's equations. When choosing the right formulation to be implemented in FEA, special mathematical handling is required in order to avoid non-physical solutions and to provide numerical stability and computational efficiency. This section from the ANSYS Online Help Manual (support.ansys.com) reproduced here for brevity, describes the basis for formulation employed in ANSYS MAXWELL.

ANSYS MAXWELL magnetic field formulation is founded on MAXWELL's equations starting with the basic field equations:

Faraday's law:
$$\nabla \times \mathbf{E} = -\frac{\partial \mathbf{B}}{\partial t} \quad (\text{B5.1})$$

Gauss's law:
$$\nabla \cdot \mathbf{B} = 0 \quad (\text{B5.2})$$

Ampere's law:
$$\nabla \times \mathbf{H} = \mathbf{J} \quad (\text{B5.3})$$

in which, \mathbf{E} is the electric field strength, \mathbf{B} is the magnetic flux density, \mathbf{H} is the magnetic field strength, and \mathbf{J} is the electric current density. Obviously, these equations are considered together with the constitutive material equations for both electric fields as $\mathbf{E} = f(\mathbf{J})$ and magnetic field as $\mathbf{B} = f(\mathbf{H})$. Numerical solution of such equations is based on T- Ω formulation in which Ω is nodal-based magnetic scalar potential, defined in the entire solution domain and T is edge-based electrical vector potential, defined only in the conducting eddy-current region (Fig. 2.10).

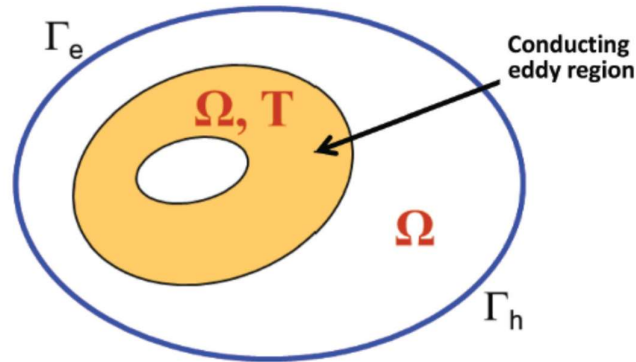


Fig. B5.1 Domain representation for T- Ω formulation (Courtesy: ANSYS).

There are several advantages of T- Ω formulation:

- Avoid unphysical solution due to utilization of edge elements to model a source component and induced eddy current.
- Computationally efficient because in the non-conducting region, only scalar potential is employed.

- Numerical stability because no gauging is required to obtain unique solutions.

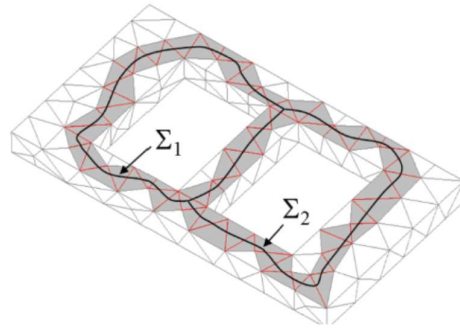


Fig. B5.2 Identification of multiple connected region and creation of cutting domain are all done automatically based on tree/cotree technology (Courtesy: ANSYS).

In T - Ω formulation, the key to allow the use of scalar potential is that the solution domain has to be single connected. In the eddy-conducting region, field H is described by both electrical vector potential T and magnetic scalar potential Ω , and curl of the electrical vector potential T is the induced eddy-current density. In the source conductor region, field H is described by both applied source field H_p and magnetic scalar potential Ω , in which curl of H_p is the source current density J .

In the non-source, non-eddy-conductor region, since $\nabla \times H = 0$ and curl of any gradient is always zero, then H can be represented by the gradient of the magnetic scalar potential as long as the domain is single connected. To make the domain single connected, one needs to introduce a cut so that Ampere's law can hold with respect to T in the cut region. This means in the non-conducting cut region, even though there is no current, field H is also described by both Ω and T , not just by Ω alone. Therefore, for the T - Ω formulation with multiple connected domains, one identifies the non-conducting cut domain. In ANSYS MAXWELL, the process of cut domain generation is automatically done based on the automatic identification of tree and co-tree algorithm (MAXWELL 3D and 2D Help Manuals, support.ansys.com).

B5.1 Introduction

In this section, for brevity, some of the sections from the ANSYS 3D and 2D Online Help Manuals (support.ansys.com) relevant to the study are reproduced. These sections describe the basis for formulation employed in ANSYS MAXWELL and RMXprt.

The study involves analysis of a rotating electrical machine and the effect of a pulsating flux pump excitation on the performance of the machine. This chapter describes about the Finite Element Analysis-modelling and simulation that needs to be carried out in order to, achieve the objectives of the study.

ANSYS MAXWELL and RMXprt software package are chosen, to carry out the study using FEA technique. ANSYS MAXWELL is the premier electromagnetic field simulation software for engineers tasked with designing and analysing 2-D and 3-D electromagnetic and electromechanical devices, including motors, actuators, transformers, sensors and coils.

MAXWELL uses the accurate finite element method to solve static, frequency-domain, and time varying electromagnetic and electric fields.

A key benefit of ANSYS MAXWELL is its automated solution process, which requires one to specify only the geometry, material properties and desired output. From this point, MAXWELL automatically generates an appropriate, efficient and accurate mesh for solving the problem. This proven automatic adaptive meshing process removes complexity from the analysis process, giving out a highly efficient, easy-to-use design flow.

ANSYS MAXWELL generates high fidelity, reduced-order models from the finite element solution for use in ANSYS Simpler, a multi-domain system simulation software. This advanced functionality creates a powerful electromagnetics-based design flow that combines complex circuits with accurate component models to design complete, high-performance electromechanical, mechatronic and power electronic systems.

ANSYS MAXWELL Circuit Editor is used, to implement the load circuit and the load circuit can be integrated as a part of excitation with the ANSYS MAXWELL model. The output of the simulation is stored as .csv file, which can be analysed in MS Excel and MATLAB conveniently (MAXWELL 3D and 2D Help Manuals, support.ansys.com).

B5.2 ANSYS MAXWELL and RMxpert

Using ANSYS MAXWELL, the following computations are possible:

- Static electric fields, forces, torques, and capacitances caused by voltage distributions and charges.
- Static magnetic fields, forces, torques, and inductances caused by DC currents, static external magnetic fields, and permanent magnets.
- Time-varying magnetic fields, forces, torques, and impedances caused by AC currents and oscillating external magnetic fields.
- Transient magnetic fields caused by electrical sources and permanent magnets.

In this study, modelling and simulations for two different stator geometries and stator materials, are conducted, and then the performances compared. The description of all the features of ANSYS MAXWELL and RMxpert are out of scope and relevance of this thesis and hence, only the essential features are discussed in the following sections.

7.2.1 Transient Solver

The transient field simulator computes the time-domain magnetic fields in 2D or 3D. The source of the magnetic fields can be:

- Moving or non-moving time varying currents and voltages.
- Moving or non-moving permanent magnets and/or coils.
- Moving or non-moving external circuit coupling.

The quantities for which the transient field simulator solves are the magnetic field, H , and the current distribution, J ; the magnetic flux density, B , is automatically calculated from the H -field. Derived quantities such as - forces, torques, energy, speed, position, winding flux linkage, and winding induced voltage may be calculated from these basic field quantities.

B5.2.1 Meshing

Meshing is an integral part of the computer aided engineering simulation process. The mesh influences the accuracy, convergence and speed of the solution. Furthermore, the time it takes to create and mesh a model is often a significant portion of the time it takes to get results from a CAE solution. Therefore, the better and more automated the meshing tools, the better the solution.

From easy, automatic meshing to a highly crafted mesh, ANSYS provides the ultimate solution. In MAXWELL, mesh operations are optional mesh refinement settings that provide MAXWELL with mesh construction guidance. The technique of guiding MAXWELL's mesh construction is referred to as "seeding" the mesh. Seeding is performed using the Mesh Operations commands on the MAXWELL 3D or MAXWELL 2D menu.

When defining a mesh, typically, the mesh operations are assigned first and then the mesh is created. However, the mesh can also be refined after the initial mesh has been created. The length of tetrahedral elements on a surface or within a volume can be refined until they are below a certain value (length-based mesh refinement) or the surface triangle length of all tetrahedral elements on a surface or volume can be refined to within a specified value (skin depth-based mesh refinement).

In some circumstances, a mesh operation that modifies MAXWELL's surface approximation settings for one or more faces can also be created. In some circumstances involving curved surfaces, a cylindrical gap treatment mesh operation can be assigned.

For MAXWELL 2D, when the TAU mesher is selected in the Initial Mesh Settings dialog, the Skin Depth Layers mesh setting corresponding to the selected edges can be defined. Surface approximation settings are only applied to the initial mesh (the mesh that is generated the first time a design variation is solved). The other types of mesh operations (refining the mesh) can be performed on either the initial mesh or on the most recently generated mesh (the current mesh) if a previously created mesh is being updated. Meshing plays an important role in generating solutions. A very fine mesh results in good results but takes significant computation time and resources, whereas a coarse mesh takes less simulation time but the geometry is not well resolved.

In this study, length based meshing technique is used and the different lengths for the elements was set depending on the resolution required at different points of the machine. The details of the specific meshing and associated setting will be discussed in the corresponding sections (MAXWELL 3D and 2D Help Manuals, support.ansys.com).

B5.2.2 Boundary conditions

The boundary conditions are the field variable values or related variables such as derivatives on the boundaries of the field, specifically defined. The transient field solver discussed in 1.2.1 allows us to define the following boundary conditions:

| Boundary Type | H-Field Behavior |
|---------------|------------------|
|---------------|------------------|

| | |
|---|--|
| Default Boundary Conditions (Natural and Neumann) | <p>Field behaves as follows:</p> <ul style="list-style-type: none"> • Natural boundaries — Tangential H and normal B are continuous across surfaces without current density distribution. Tangential H has a jump if the surface has current density distribution. • Neumann boundaries — Magnetic field is normal to the boundary. |
| Vector Potential | Sets the magnetic vector potential on the boundary. |
| Symmetry | <p>Field behaves as follows:</p> <ul style="list-style-type: none"> • Odd Symmetry (Flux Tangential) — Magnetic Field is tangential to the boundary; its normal components are zero. • Even Symmetry (Flux Normal) — Magnetic Field is normal to the boundary; its tangential components are zero. |
| Balloon | Models the case where the structure is “infinitely” far away from other magnetic fields, permanent magnets, or current sources. |
| Master and Slave (Matching) | The Magnetic Field on the slave boundary is forced to match the magnitude and direction (or the negative of the direction) of the Magnetic Field on the master boundary. |

In this study, Vector Potential boundary condition and Master Slave boundary condition are used. Master-Slave Boundary condition helps in breaking down a symmetrical model such as an electrical machine, into smaller sections, and this reduces the simulation time.

B5.2.3 ANSYS 2D Sources/Excitations

To compute fields for a structure, a source of charge must be defined, voltage, current, or electric or magnetic fields for the model. At least one object or edge is to be defined as either a source (such as a current, charge, or voltage) or a value boundary.

Permanently polarized or magnetized materials can also act as sources of charge or magnetic field (respectively). If some type of source is not identified and declared, the MAXWELL 2D will not be able to generate a solution.

The field quantities computed by each solver — and the required electromagnetic are as follows:

| Field Solver | Sources | Field Computed | Derived Field Quantities |
|----------------------|--|--|--|
| Electrostatic | Voltages Charges Charge density Floating | ϕ | E, D |
| Magnetostatic | DC current Current density | A_z (XY models), A_ϕ (RZ models) | H, B |
| Eddy Current | AC currents Current density | $A_z(\omega t)$ (XY models), $A_\phi(\omega t)$ (RZ models) | $J_z(\omega t)$ (XY models), $J_\phi(\omega t)$ (RZ models), H (ωt), B (ωt), |
| DC Conduction | DC voltages | ϕ | E, D, J |
| AC Conduction | AC voltages | $\phi(\omega t)$ | E (ωt), J (ωt) |
| Transient | Transient voltages and currents through External Circuit connection. Current; current density; coil; end connection | A_z (XY and RZ models) | H, B |

where:

- **A** is the magnetic vector potential.
- **H** is the magnetic field.
- **B** is the magnetic flux density.
- ϕ is the electric potential.
- **E** is the electric field.
- **D** is the electric flux density.
- **J** is the current density.

B5.2.4 MAXWELL Circuit Editor

The Schematic editor is the Ansoft tool for creating circuit schematics, or designs for a transient solution type. A design graphically represents and captures the electrical structure and characteristics of a circuit. Such a design is created by starting the schematic editor and placing components, ports, connectors, and wires into a default empty schematic.

Schematic Editor Window: The Schematic Editor window allows to place components and wire them together. The components can be moved by simply selecting and dragging them. Copy and paste can be used on components and their wires within the schematic editor.

7.2.2 RMxpert

Rotational Machine Expert (RMxpert) is an integrated interactive software package with ANSYS, used for designing and analysing electrical machines. The basic modelling of the 10kW HTS rotor was done in SOLIDWORKS and it was imported through RMxpert, for the stator of the machine, User Defined Primitive feature of RMxpert was used to design a suitable stator.

RMxpert is template-based electrical machine design tool that provides fast, analytical calculations of machine performance and 2-D and 3-D geometry creation for detailed finite element calculations in ANSYS MAXWELL. In this study, RMxpert has been used to create a custom designed stator for the HTS rotor of the proof-of-concept 10 kW HTS generator (MAXWELL 3D and 2D Help Manuals, support.ansys.com).

Appendix C: Data Sheets

C1. Hall sensor data sheet

ELECTRICAL SPECIFICATIONS OF THE HALL PROBE

HIGH LINEARITY HALL PROBE FOR ROOM AND CRYOGENIC TEMPERATURES

| | | | |
|-------|---------|-----------------|---|
| TYPE: | THV-MOD | PRODUCT NUMBER: | 2 |
|-------|---------|-----------------|---|

| PARAMETER | UNIT | 300 K | 77 K | 4.2 K |
|--|----------|-------|------|-------|
| Nominal control current, I_n | mA | 20 | 20 | 20 |
| Maximum control current | mA | 22 | 25 | 25 |
| Input resistance | Ω | 63 | 61 | |
| Linearity error up to 1 T | % | < 0.2 | | |
| Change of sensitivity due to reversing of the magnetic field | % | < 1 | | |

| Hall probe No. | Sensitivity at I_n [mV/T] | Offset at I_n [μ V] | | Output resistance [Ω] | |
|----------------|-----------------------------|----------------------------|-------|--------------------------------|------|
| # | 300 K | 300K | 77 K | 300 K | 77 K |
| 1 | 36.8 | < -20 | < 30 | 14 | 13 |
| 2 | 35.5 | < -60 | < 20 | 14 | 12 |
| 3 | 33.9 | < -40 | < -50 | 14 | 12 |
| 4 | 33.1 | < 50 | < 20 | 13 | 12 |
| 5 | 32.4 | < 20 | < 50 | 13 | 12 |
| 6 | 31.6 | < -50 | < -10 | 13 | 12 |
| 7 | 31.0 | < -60 | < -40 | 13 | 11 |

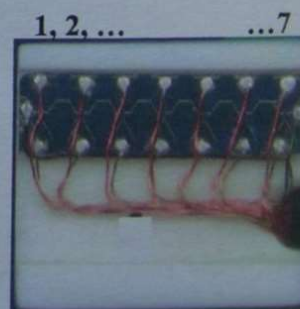
Overall dimensions: 10.2 x 10.9 x 15 mm

Distance between sensors = 1.5 mm

Color code:

Current leads: green, black

Hall leads: red, yellow



C2. Lettech Amplifier datasheet

LETTECH DESIGN AND DEVELOPMENT LTD

109 TIROHANGA ROAD
LOWER HUTT 5010
NEW ZEALAND
PH & FX: (04) 569-3983

SERVICES: ELECTRONIC EQUIPMENT DESIGN AND DEVELOPMENT, CONSULTING, ROBOTICS, AUTOMATION.

7-December-2007.

Attention: Dr ROD BADCOCK and SEBASTIAN
INDUSTRIAL RESEARCH LTD.
69 Gracefield Rd,
P.O.Box 31-310
Lower Hutt 5040

DETAILS OF FIRST EIGHT AMPLIFIER UNIT

CONFIGURATION:

The unit in general, is configured for use with a single block of seven Hall effect detectors where the block has a resistance of approximately 67ohms. The constant current supply delivers current into that 67ohms with an adjustable range of 10mA to 30mA.

Eight identical differential low noise amplifiers are available to amplify the low millivolt signals from the individual Hall sensors within the common block. One amplifier channel, being spare, may be used for other purposes.

INPUT and OUTPUT:

Amplifier input impedance is set at 75ohms, and the amplifier gain is set at 1,500. Output to an external plug is taken directly from the amplifier chip, which is the Texas TLE2141CD. All outputs have been loaded with 10Kohm on the circuit board. The chip has internal output current limiting and the maker claims outputs can be shorted to either power supply rail.

Access to the amplifier inputs is by pulling the end cover in the direction of the longitude axis of the case. This cover is held in place with Velcro. Input is made by screw connection to a pluggable socket. One pluggable socket has 10 pins where there are four groups of two differential input connections, plus two connections to supply a constant current to the Hall probe. Another similar pluggable socket has eight pins to provide the second set of four differential input connections.

Output connections are provided at the top of the case with a pluggable socket with screw terminals. There are eight single ended output terminals plus two zero volt terminals.

Maximum output voltage range is + or - 10volts.

Input connections of pins1,2 go to output pin1. Input connections pins3,4 go to output pin 2.
Input connections pins5,6 go to output pin 3. Input connections pins7,8 go to output pin 4.

On the second set of input connections, pins1,2 go to output pin 5, pins 3,4 go to output pin6, pins5,6 go to output pin 7, pins7,8 go to output pin 8.

CASE:

Overall dimensions are 248mm long, 112mm wide, 67mm high.

The case has been designed to provide easy access to the amplifier input terminals, while preventing free air flow over the terminals to avoid thermally generated potentials which would cause erroneous DC offset to the sensor signals.

The case is divided into two sections. One section houses the power supply with its transformer and dual power supply regulator. 240Volt mains input is via an IEC chassis mounted plug with incorporated filter. A 250mA fuse protects mains voltage components. The transformer is mounted as far away as possible from the amplifier circuit boards, and has a steel shield around it to reduce magnetic field induction of 50Hz noise to the amplifiers and wiring.

The other section of case houses the eight amplifiers and constant current regulator.

A shield separates the two sections of case to reduce electrical/Rf noise transfer from power supply section to amplifiers. Exchange of heated air is also greatly reduced.

AMPLIFIERS:

Each amplifier has an 'OFFSET' trimpot plus a 'COMMON MODE REJECTION' trimpot.

All these trimpots have been adjusted prior to delivery to IRL. The common mode rejection trimpots are able to be finely adjusted because they are 100Kohm in a 1M5ohm circuit.

AMPLIFIER BANDWIDTH LIMITING:

The IRL suggested cut off frequency of 40Hz is impractical when the amplifiers must have a flat response from DC to 20Hz. Thus rejection of mains 50Hz with RC filters is not possible when the two frequencies are so close. Several octaves of frequency separation is required for a flat response from 20Hz and below.

It was found that adding RC bandwidth limiting increased the noise level on the amplifier outputs by five times the level without bandwidth limiting. With low noise being a key requirement, it was decided to omit add-on bandwidth limiting. Allowance has been made on the circuit boards for those extra components should they be needed in the future. The TLE2141CD amplifier chips incorporate internal frequency compensation. No oscillation has been observed during testing of these amplifiers.

C3.Typical generator datasheet

1 PERFORMANCE DATA (Calculated values)

TYPE

Type designation: AMG 0400ES04

PERFORMANCE DATA

| | | | | | | | | |
|---|---|----------|----------|----------|-----------------------|----------|----------|----------|
| Main standard | IEC 60034 | | | | | | | |
| Rated power factor | 0.8 | | | | | | | |
| Insulation class | H | | | | | | | |
| Temperature rise | H | | | | | | | |
| Ambient temperature | 40 °C | | | | | | | |
| Altitude over sea level | ≤ 1000 m | | | | | | | |
| Cooling/Protection | IC0A1/IP23 | | | | | | | |
| | Single bearing | | | | Double bearing | | | |
| Mounting arrangement | IM 2105 | | | | IM 1001 | | | |
| Weight without/with PMG | 2700/2715 kg | | | | 2750/2765 kg | | | |
| Inertia (no diff. with PMG) | 22.1 kgm ² | | | | 20.7 kgm ² | | | |
| Direction of rotation | CW (Facing drive end) | | | | | | | |
| Maximum overspeed | 2250 rpm | | | | | | | |
| Winding pitch | Two thirds (2/3) | | | | | | | |
| Stator winding resistance | 0.00167 Ω per phase at 20 °C series star connection | | | | | | | |
| Rotor winding resistance | 0.603 Ω at 20 °C | | | | | | | |
| Ex. stator winding resistance | 17.308 Ω at 20 °C | | | | | | | |
| Ex. rotor winding resistance | 0.0452 Ω at 20 °C | | | | | | | |
| Total Harmonic Distortion | THD<3.5% at no load operation or rated Linear balanced load | | | | | | | |
| Voltage regulation | ±1 % | | | | | | | |
| Telephone Interference | THF<2% | | | | TIF<50 | | | |
| Frequency | 50 Hz | | | | 60 Hz | | | |
| Speed | 1500 rpm | | | | 1800 rpm | | | |
| Cooling Air | 1.28 m³/sec | | | | 1.53 m³/sec | | | |
| Voltage series star 3 ph. | 380/220 | 400/231 | 415/240 | 440/254 | 415/240 | 440/254 | 460/266 | 480/277 |
| Voltage series delta 3 ph. | 220 | 230 | 240 | 254 | 240 | 254 | 266 | 277 |
| Rated continuous output | 1190 kVA | 1250 kVA | 1250 kVA | 1190 kVA | 1300 kVA | 1375 kVA | 1440 kVA | 1500 kVA |
| Xd(u) | 3.479 | 3.298 | 3.064 | 2.595 | 3.824 | 3.598 | 3.448 | 3.298 |
| Xd(s) | 2.869 | 2.563 | 2.189 | 1.595 | 3.39 | 3.066 | 2.82 | 2.53 |
| Xq(u) | 1.544 | 1.463 | 1.36 | 1.151 | 1.697 | 1.596 | 1.53 | 1.463 |
| Xq(s) | 0.283 | 0.269 | 0.25 | 0.211 | 0.311 | 0.293 | 0.281 | 0.269 |
| X'd(u) | 0.257 | 0.245 | 0.227 | 0.192 | 0.283 | 0.266 | 0.255 | 0.245 |
| X'd(s) | 0.188 | 0.178 | 0.164 | 0.137 | 0.208 | 0.195 | 0.186 | 0.178 |
| X''d(u) | 0.171 | 0.162 | 0.149 | 0.125 | 0.189 | 0.177 | 0.169 | 0.162 |
| X''q(u) | 0.205 | 0.194 | 0.18 | 0.153 | 0.225 | 0.212 | 0.203 | 0.194 |
| X''q(s) | 0.186 | 0.177 | 0.164 | 0.139 | 0.204 | 0.192 | 0.184 | 0.176 |
| X1(u) | 0.109 | 0.103 | 0.096 | 0.081 | 0.12 | 0.113 | 0.108 | 0.103 |
| X2(u) | 0.196 | 0.186 | 0.172 | 0.145 | 0.216 | 0.203 | 0.194 | 0.186 |
| X2(s) | 0.179 | 0.169 | 0.157 | 0.132 | 0.197 | 0.185 | 0.177 | 0.169 |
| X0(u) | 0.028 | 0.027 | 0.025 | 0.021 | 0.031 | 0.03 | 0.028 | 0.027 |
| Xp(s) | 0.212 | 0.202 | 0.188 | 0.158 | 0.233 | 0.22 | 0.211 | 0.202 |
| SCR (short circuit ratio), Ir0/Xd (u) | 0.35 | 0.39 | 0.46 | 0.63 | 0.29 | 0.33 | 0.35 | 0.40 |
| s=saturated value, u=unsaturated value, values are p.u. at rated voltage and power. | | | | | | | | |
| Td0' | 3.739 s | | | | | | | |
| Td' | 0.239 s | | | | | | | |
| Td'' | 0.020 s | | | | | | | |
| Ta | 0.0361 s | | | | | | | |
| CE-Marking | Generator fulfills the requirements of Low Voltage Directive (2006/95/EC) Generator supplied to EEA-area will be CE-marked | | | | | | | |

| | | | | | |
|------------|---------------------|-------------------------|-------|-----------|-------|
| ABB | ABB Generators Ltd. | Document identification | Lang. | Rev. ind. | Sheet |
| | | SAMG 5861260 | en | C | 3 |

TEMPLATE: TECHNICALSPECIFICATION.DOT; FILENAME: 5861260-C-AMG 0400ES04 TECHNICAL SPECIFICATION.DOC; PRINTDATE: 5/31/2012 1:24:00 PM; SAVE DATE: 5/30/2012 2:37:00 PM

Appendix-D

Stator Design Data and Material properties

D1. Stator Design 1

ANSYS allows custom design of the model parts by the use of RMxpert. The evaluated values in the properties windows are the values entered by the user.

Properties: 10kW HTS - Maxwell2DDesign-10kW-Optimised stator-Rated-load - Modeler


| Command | | | | | |
|---------|-------------------|-----------------------|------|-----------------|--|
| | Name | Value | Unit | Evaluated Value | Description |
| | Command | CreateUserDefinedPart | | | |
| | Coordinate Sys... | RelativeCS1 | | | |
| | Name | RMxpert/SlotCore.dll | | | |
| | Location | syslib | | | |
| | Version | 12.1 | | | |
| | DiaGap | 302 | mm | 302mm | Core diameter on gap side, DiaGap<DiaYoke for outer cores |
| | DiaYoke | 380 | mm | 380mm | Core diameter on yoke side, DiaYoke<DiaGap for inner cores |
| | Length | 300 | mm | 300mm | Core length |
| | Skew | 0 | deg | 0deg | Skew angle in core length range |
| | Slots | 36 | | 36 | Number of slots |
| | Slot Type | 4 | | 4 | Slot type: 1 to 6 |
| | Hs0 | 1 | mm | 1mm | Slot opening height |
| | Hs01 | 0 | mm | 0mm | Slot closed bridge height |
| | Hs1 | 1 | mm | 1mm | Slot wedge height |
| | Hs2 | 15 | mm | 15mm | Slot body height |
| | Bs0 | 2.5 | mm | 2.5mm | Slot opening width |
| | Bs1 | 8 | mm | 8mm | Slot wedge maximum width |
| | Bs2 | 5 | mm | 5mm | Slot body bottom width, 0 for parallel teeth |
| | Rs | 0 | mm | 0mm | Slot body bottom fillet |
| | Fillet Type | 0 | | 0 | 0: a quarter circle; 1: tangent connection; 2&3: arc bottom. |
| | HalfSlot | 0 | | 0 | 0 for symmetric slot, 1 for half slot |
| | SegAngle | 15 | deg | 15deg | Deviation angle for slot arches (10~30, <10 for true surface). |
| | LenRegion | 200 | mm | 200mm | Region length |
| | InfoCore | 0 | | 0 | 0: core; 100: region. |

D2. Stator Design 2

Properties: 10kW-A HTS - - Maxwell2DDesign-10kW-Stator Opti2-Load model-balance - Modeler

| Command | | | | |
|-------------------|-----------------------|------|-----------------|--|
| Name | Value | Unit | Evaluated Value | Description |
| Command | CreateUserDefinedPart | | | |
| Coordinate Sys... | RelativeCS1 | | | |
| Name | RMxprt/SlotCore.dll | | | |
| Location | syslib | | | |
| Version | 12.1 | | | |
| DiaGap | 312 | mm | 312mm | Core diameter on gap side, DiaGap<DiaYoke for outer cores |
| DiaYoke | 360 | mm | 360mm | Core diameter on yoke side, DiaYoke<DiaGap for inner cores |
| Length | 300 | mm | 300mm | Core length |
| Skew | 0 | deg | 0deg | Skew angle in core length range |
| Slots | 36 | | 36 | Number of slots |
| Slot Type | 4 | | 4 | Slot type: 1 to 6 |
| Hs0 | 1 | mm | 1mm | Slot opening height |
| Hs01 | 0 | mm | 0mm | Slot closed bridge height |
| Hs1 | 1 | mm | 1mm | Slot wedge height |
| Hs2 | 12 | mm | 12mm | Slot body height |
| Bs0 | 2.5 | mm | 2.5mm | Slot opening width |
| Bs1 | 14 | mm | 14mm | Slot wedge maximum width |
| Bs2 | 0 | mm | 0mm | Slot body bottom width, 0 for parallel teeth |
| Rs | 0 | mm | 0mm | Slot body bottom fillet |
| Fillet Type | 0 | | 0 | 0: a quarter circle; 1: tangent connection; 2&3: arc bottom. |
| HalfSlot | 0 | | 0 | 0 for symmetric slot, 1 for half slot |
| SegAngle | 15 | deg | 15deg | Deviation angle for slot arches (10~30, <10 for true surface). |
| LenRegion | 200 | mm | 200mm | Region length |
| InfoCore | 0 | | 0 | 0: core; 100: region. |

D3. Steel 1008


 View / Edit Material

Material Name: Material Coordinate System Type:

Properties of the Material

| Name | Type | Value | Units |
|-----------------------|-------------|--------------|-------------|
| Relative Permeability | Nonlinear | B-H Curve... | |
| Bulk Conductivity | Simple | 2000000 | siemens/m |
| Magnetic Coercivity | Vector | | |
| - Magnitude | Vector Mag | 0 | A_per_meter |
| - X Component | Unit Vector | 1 | |
| - Y Component | Unit Vector | 0 | |
| - Z Component | Unit Vector | 0 | |
| Core Loss Model | | None | w/m^3 |
| Mass Density | Simple | 7872 | kg/m^3 |
| Composition | | Solid | |

D4. FR4Epoxy


 View / Edit Material

Material Name: Material Coordinate System Type:

Properties of the Material

| Name | Type | Value | Units |
|-----------------------|------------|-------|-------------|
| Relative Permeability | Simple | 1 | |
| Bulk Conductivity | Simple | 0 | siemens/m |
| Magnetic Coercivity | Vector | | |
| - Magnitude | Vector Mag | 0 | A_per_meter |
| Core Loss Model | | None | w/m^3 |
| Mass Density | Simple | 1900 | kg/m^3 |
| Composition | | Solid | |

D5. Perfect conductor-HTS material

View / Edit Material

Material Name

perfect-conductor

Material Coordinate System Type:

Cartesian

Properties of the Material

| Name | Type | Value | Units |
|-----------------------|------------|----------|-------------|
| Relative Permeability | Simple | 0.999991 | |
| Bulk Conductivity | Simple | 1e+029 | siemens/m |
| Magnetic Coercivity | Vector | | |
| - Magnitude | Vector Mag | 0 | A_per_meter |
| Core Loss Model | | None | w/m^3 |
| Mass Density | Simple | 6300 | kg/m^3 |
| Composition | | Solid | |
